UC Santa Cruz

UC Santa Cruz Electronic Theses and Dissertations

Title

Beyond the Standard Model Physics, from the LHC to Fixed Target Experiments and Astrophysical Probes

Permalink

Author

Hamer, Nick

Publication Date

2024

Copyright Information

Peer reviewed|Thesis/dissertation

UNIVERSITY OF CALIFORNIA

SANTA CRUZ

**BEYOND THE STANDARD MODEL PHYSICS, FROM THE LHC
TO FIXED TARGET EXPERIMENTS AND ASTROPHYSICAL
PROBES**

A dissertation submitted in partial satisfaction of the
requirements for the degree of

DOCTOR OF PHILOSOPHY

in

PHYSICS

by

Nick Hamer

June 2024

The Dissertation of Nick Hamer
is approved:

_____

Professor Stefania Gori, Chair

_____

Professor Stefano Profumo

_____

Professor Wolfgang Altmannshofer

_____

Peter Biehl
Vice Provost and Dean of Graduate Studies

Table of Contents

List of Figures

List of Tables

xiii

Abstract

Beyond the standard model physics, from the LHC to fixed target experiments

and astrophysical probes

by

Nick Hamer

The Standard Model (SM) of particle physics, while excruciatingly consistent under precision testing, is not a complete theory. Theories of new physics beyond the Standard Model (BSM) thrive beyond its shortcomings. This thesis will explore several complementary avenues of investigation in this realm.

The first part concerns CP violation (CPV) in the theory of a two Higgs doublet model (2HDM), and the signature of electric dipole moments (EDMs) is considered. Subject to constraints on EDMs set by experiments, collider phenomenology is explored and a benchmark is elaborated.

An astrophysical interlude proceeds with a statistical treatment proposed to distinguish microlensing events in which lensing objects are drawn from populations of free floating planets (FFPs) or from populations of primordial black holes (PBHs). The Nancy Grace Roman Space Telescope, set to launch in 2027, will observe a sufficient number of events during its Galactic Bulge Time Domain Survey to enable such statistical tools.

The third part discusses a pair of BSM models where additional particles contribute to the muon anomalous moment, a_μ. First, the flavorful supersymmetric

Standard Model (FSSM) is described, and its contributions to a_μ are computed. It is shown that sleptons in the multi-TeV range can ameliorate the recently measured tension in a_μ. Second, a minimal extension to the SM with an addition scalar coupling to muons is described, and the detection reach of the proposed DarkQuest experiment is computed. Mitigation strategies on various sources of backgrounds are discussed in detail.

Acknowledgments

Thanks to everyone who had any sort of contact with me, for putting up with me.

Part I

Introduction

The Standard Model (SM) of particle physics, can be understood as a low-energy effective theory. Not to say that it captures all low energy phenomena, rather that it suggests a regime for known unknowns. Theories of new physics beyond the Standard Model (BSM) are a complementary ingredient in the effectiveness of the SM. This thesis will explore several complementary avenues of investigation in this realm. There are BSM theories that can be probed across an extreme spectrum of energies, of which this thesis will explore a handful. Models will be presented which can be tested at relatively low energy beam dump experiments, much higher energy experiments at the LHC, and in the astrophysical laboratory.

Chapter 1

Standard Model background

The standard model of particle physics is a theory of gauge symmetries and particle content describing the known fundamental interactions (strong, weak, and electromagnetic) and matter fields (quarks, leptons, and Higgs). The discovery of the Higgs boson at the LHC in 2012 [13] completed its catalog of particles alongside 6 quarks, 6 leptons, 3 weak gauge bosons, 8 gluons, and one photon. Their interactions are described by the group $SU(3)_C \times SU(2)_L \times U(1)_Y$. The first subgroup of that tensor product separately describes QCD while the remaining two describe the electroweak interactions. These symmetries are gauged, a resulting term in the covariant derivative of the Langrangian then describes the interactions between fields charged under these symmetries and their respective gauge bosons. Through the Higgs mechanism, the electroweak piece of this group is broken into a resulting $U(1)_{EM}$ group describing electromagnetic interactions. The only fermions charged under $SU(3)_C$ are quarks, while the particular fermions charged under the $SU(2)_L$ (weak) gauge group are the left-handed fermions

(left-handed as in transforming under a certain representation of the Lorentz group as opposed to possessing a specific helicity). The masses of the fermions in the SM necessarily come from interactions with the Higgs field after it acquires a non-zero vacuum expectation value (VEV). To include a Dirac mass term for the fermions would violate the gauge symmetry laid out. Thus, since the SM does not include right-handed neutrinos, it cannot account for neutrino masses inferred from the phenomenon of neutrino oscillations[52, 53, 228].

The forces of the standard model are mediated by gauge bosons, spin-1 particles associated with each of the subgroups of the full gauge symmetry. In particular they are associated with the adjoint representation of those particular groups, and so there are 8 gluon fields, G_μ^a, 3 weak gauge bosons, W_μ^a, and one gauge boson associated with the $U(1)_Y$ (hypercharge), B_μ. After electroweak symmetry breaking (EWSB) in which the neutral component of the Higgs field acquires a nonzero VEV, the electrically neutral weak gauge boson, W_μ^3, mixes with the B_μ, yielding the physical eigenstates of the Z boson and the photon. The dynamics of these bosons appears in the Lagrangian as,

$$\mathcal{L}_{\text{gauge}} = -\frac{1}{4} G_{\mu\nu}^a G^{\mu\nu a} - \frac{1}{4} W_{\mu\nu}^a W^{\mu\nu a} - \frac{1}{4} B_{\mu\nu} B^{\mu\nu} + i\overline{\psi_j} \slashed{D} \psi_j, \qquad (1.1)$$

4

where,

$$G^a_{\mu\nu} = \partial_\mu G^a_\nu - \partial_\nu G^a_\mu + g_S f^{abc} G^b_\mu G^c_\nu, \tag{1.2}$$

$$W^a_{\mu\nu} = \partial_\mu W^a_\nu - \partial_\nu W^a_\mu + g \epsilon^{abc} W^b_\mu W^c_\nu, \tag{1.3}$$

$$B_{\mu\nu} = \partial_\mu B_\nu - \partial_\nu B_\mu, \tag{1.4}$$

$$D_\mu = \partial_\mu - i g_1 B_\mu Y - \frac{1}{2} i g \sigma_a W^a_\mu - i g_S t_a G^a_\mu, \tag{1.5}$$

where a runs over the appropriate adjoint index, f and ϵ are the structure constants of $SU(3)$ and $SU(2)$ respectively, and t and σ are the generators in the fundamental representation of those groups. The strength of the gauge interactions is encoded in g_1, g, and g_S. It is evident in these equations that gauge bosons of nonabelian symmetries interact between themselves, a feature not present for abelian symmetries.

The Higgs is a complex scalar doublet which transforms under the fundamental representation of $SU(2)_L$. It has a hypercharge such that one component has unit electric charge and one component is electrically neutral. After EWSB, the Higgs doublet can be written,

$$\Phi = \frac{1}{\sqrt{2}} \begin{pmatrix} 0 \\ v + h \end{pmatrix} \tag{1.6}$$

, where v is the vacuum expectation value, and h is identified with the physical Higgs boson. The terms in the Lagrangian involving the Higgs doublet look like,

$$\mathcal{L}_{\text{Higgs}} = |D_\mu \Phi|^2 - \left(\mu^2 |\Phi|^2 + \lambda |\Phi|^4 \right), \tag{1.7}$$

with the terms in brackets being the scalar potential. The minimization of the potential

is dependent on μ and λ. Specifically, for $\mu^2 < 0$, and $\lambda > 0$ the potential is minimized at nonzero $|\Phi|^2$. In order to have a theory with a massless photon, we ascribe the nonzeroness to the lower component [433],

$$v^2 = -\mu^2/\lambda \tag{1.8}$$

$$m_H^2 = 2\lambda v^2 \tag{1.9}$$

A motivation for a theory of spontaneously broken gauge symmetry is that it results in massive gauge bosons. The other components of the complex scalar doublet Φ are identified with longitudinal degrees of freedom of the $W^\pm$ and Z. Their masses are then,

$$m_W = \frac{1}{2}gv \tag{1.10}$$

$$m_Z = \frac{1}{2}v\sqrt{g_1^2 + g^2} \equiv \frac{m_W}{\cos\theta_W} \tag{1.11}$$

with θ_W being the weak mixing angle.

The masses of the SM fermions can now be described in terms of their couplings to the Higgs field. An example Lagrangian term from the Yukawa sector reads,

$$-y_{ij}^d \overline{Q_L^i} \Phi d_R^j \supset -\overline{d_L} d_R m_d (1 + \frac{h}{v}). \tag{1.12}$$

On the left are flavor eigenstates where i and j are flavor indices, with (ignoring color charge) Q_L a sextuplet of quarks - up and down types over three generations. d_R is a triplet of down type quarks over three generations (down, strange, bottom). Isolated on the right, after a diagonalization, is a single term for the mass eigenstate down quark. A factor of $v/\sqrt{2}$ has been factored out leaving a mass term as well as an interaction with the Higgs boson. All fermions' coupling to the Higgs boson is proportional to their

6

mass in this way. The diagonalization of all quarks from the flavor basis to the mass basis has its information encoded in the mass matrix and the CKM matrix. The CKM matrix describes mixing across different generations of quarks, additionally it contains a complex phase which gives rise to CP violation in the weak sector. Historically, it was CP violation which gave rise to hypotheses of a third generation, as two generations was insufficient to confer independent phases (field redefinitions could absorb them) [318, 375]. Some quantities, like electric dipole moments, rely on CP violation, and so are sensitive to the phases in the CKM matrix.

Electric dipole moments (EDMs) are described by a term in the Lagrangian,

$$\mathcal{L} \supset -\frac{i}{2} d \overline{\psi} \sigma^{\mu\nu} \gamma_5 F_{\mu\nu} \psi, \qquad (1.13)$$

in the limit of vanishing momentum transfer. The standard model prediction for the electron EDM is on the order $|d_e| \sim 10^{-38}$e cm [390]. A positive result of any EDM at a greater magnitude than predicted by the SM would directly indicate the existence of physics beyond the standard model (BSM). The electron EDM is sensitive to a broad range of new physics models containing new sources of CP violation. The experimental prospects of the electron EDM are weak compared to the prediction of the SM, though they are improving. The most stringent constraint is from JILA at $|d_e| < 4.1 \times 10^{-30}$e cm at the 90% C.L., proceeding the result of the ACME collaboration at $|d_e| < 1.1 \times 10^{-29}$e cm. While being many orders of magnitudes from testing the SM itself, they can be powerful constraints on new models. In the following section, these constraints are quantified for a specific model, the complex two Higgs doublet model, so that new

collider phenomenology can be expressed while respecting the non-measurement of an

electron EDM.

Part II

Complex two Higgs doublet

phenomenology

Chapter 2

Introduction

The SM hosts a Higgs doublet which necessarily participates in EWSB, giving rise to the masses of the weak gauge bosons and a single Higgs boson. There is room for passengers, additional Higgs field content, who can interact with the particles of the SM. Despite searches, no additional scalars have been found, providing constraints on classes of models with extra Higgs content. To avoid an obvious constraint, flavor changing neutral currents (FCNC), which are not present at tree-level in the SM, it is common to introduce an additional Z_2 symmetry in models with two Higgs doublets. In some basis, henceforth called the Z_2 basis, the doublets are given opposite charges, and the right-handed quark and charged lepton fields are also assigned charges. The configuration of the right-handed field charges (relative to the charges of the Higgs doublets) define the "type" of a particular model, e.g. the particles charged under the "Type 2" configuration are described in Tab. 2.1. The basis in which all of the EW VEV is in a single doublet, called the Higgs basis, differs from the Z_2 basis by a rotation of an angle

β. Put another way, in the Z_2 basis, each doublet has some fraction of the EW VEV described by the equations,

$$\frac{v_2}{v_1} \equiv \tan \beta \qquad v_1^2 + v_2^2 = v^2 \qquad \text{with } v = 246 \text{ GeV.} \tag{2.1}$$

To have a theory with an accessible decoupling limit (defined below) [258, 263], we need to allow a soft breaking of the Z_2 symmetry, meaning a term is present in the Lagrangian which has a net Z_2 charge and positive mass-dimension, the m_{12}^2 term below [221]. The scalar potential reads,

$$-\mathcal{L} \supset \frac{1}{2} \left[m_{11}^2 |\Phi_1|^2 + m_{22}^2 |\Phi_2|^2 - \left(m_{12}^2 \Phi_1^\dagger \Phi_2 + h.c. \right) \right] \tag{2.2}$$
$$+ \frac{1}{2} \lambda_1 |\Phi_1|^4 + \frac{1}{2} \lambda_2 |\Phi_2|^4 + \lambda_3 |\Phi_1|^2 |\Phi_2|^2 + \lambda_4 |\Phi_1^\dagger \Phi_2|^2$$
$$+ \frac{1}{2} (\lambda_5 (\Phi_1^\dagger \Phi_2)^2 + h.c.)$$

Complex phases can be present in m_{12}^2 or λ_5 and this can give rise to CP violation.

Classes of 2HDM can be defined by the explicit (dis)allowance of CP violation in the Higgs sector. CP conserving models necessarily have physical Higgs bosons which are CP eigenstates, while CP violating models can have the physical bosons be admixtures of CP eigenstates. Such models can contribute to sizeable EDMs, and have additional decay modes not present in a complementary CP conserving theory. If such a decay was observed (or multiple in tandem) it would directly indicate a CP violating theory.

Diagonalization of the CP conserving theory into the mass basis, yields 5 phys-

ical Higgs bosons: two charged states, $H^\pm$, one neutral pseudoscalar, A, and two scalars which are mixtures of the scalar states in a previously defined basis, h and H. In particular, starting from the Z_2 basis, the diagonalization is performed by a rotation of an angle α. The quantity, $\cos(\beta - \alpha) \equiv x$, then (subject to convention and doublet construction) describes the overlap between the unphysical scalar which belongs to the doublet in the Higgs basis containing the VEV and the physical 125 GeV Higgs boson measured at the LHC. The limit of $x \to 0$ is called the alignment limit [113], and in this limit the other neutral scalar Higgs boson does not decay into two weak gauge bosons. Another important limit of 2HDM theories is called the decoupling limit, where the mass scale of the additional Higgs bosons is much higher (in the limit, infinite) than the EW scale, and the physics at the two different scales decouples. This leads to $x \to 0$, with a distinction that the alignment limit does not require the other mass scale to be heavy.

A CP violating 2HDM allows more mixing between the scalar particles. Two additional rotation angles participate in the diagonalization to the mass basis: here called $\alpha_{2,3}$. They are related through a minimization condition of the scalar potential such that there is one independent source of CP violation. The angle α_2 provides a CP-odd component to the 125 GeV Higgs boson (and CP-even component to the third Higgs boson). The angle α_3 is most easily described in the limit of small angles, in which it mixes the second (otherwise CP-even) and third (otherwise CP-odd) bosons together. A decay that would be forbidden in a CP conserving 2HDM, e.g. $H \to Zh$ would be allowed, in the notation of the CPV theory (and subject to some convention):

12

$h_2 \to Zh_1$. Measuring this decay alone wouldn't demonstrate CP violation, but together with a measurement like $h_2 \to ZZ$ or $h_3 \to Zh_1$ would be sufficient since these pairs of decays could not belong to a CP conserving theory. A single channel that would demonstrate a CP violating theory would be $h_3 \to Zh_2 \to ZZh_1$.

Fermions can couple to the Higgs bosons with scalar and pseudoscalar couplings. With some defined configuration of Z_2 charges in the model, the parameter β thus influences these couplings as do the rotation angles involved in diagonalization. The Yukawa couplings to the physical Higgs bosons can be written,

$$\mathcal{L}_{\text{Yuk}} = -\frac{m_{f_i}}{v} \sum_k (\overline{f_i}\kappa_f^{(k)}f_i + i\overline{f_i}\gamma_5\tilde{\kappa}_f^{(k)}f_i)h_k \tag{2.3}$$

The κ and $\tilde{\kappa}$ are the scalar and pseudoscalar couplings respectively. There are many two-loop diagrams that contribute to the electron EDM that involve a pseudoscalar coupling of a fermion to a Higgs boson, which given non-negligible couplings would produce an EDM much, much larger than predicted by the SM and possibly large enough to be in contradiction to null measurements at existing experiments.

up-type	+
down-type	-
charged leptons	-
Φ_1	-
Φ_2	+

Table 2.1: Example charges of a Type-II 2HDM. Only relative signs matter, so it can be read from this table that e.g. Φ_2 couples to up-type quarks

Chapter 3

Electron EDM in the complex two-Higgs doublet model

This chapter is based on [67].

3.1 Introduction

The discovery of a non-vanishing electric dipole moment (EDM) of any fundamental particle in next generation experiments would unambiguously signal the existence of new sources of CP-violation beyond the Standard Model (SM) of particle physics. Indeed, many such models predict EDMs of elementary particles that are within reach of current experiments, with the SM contribution estimated to lie several orders of magnitude lower [392, 452, 453]. Such a discovery could supply a crucial ingredient towards solving the long standing problem of the origin of the cosmic baryon asymmetry [214, 391]. Currently, the most stringent limit on the electron EDM is

provided by the ACME collaboration [75] and reads $d_e < 1.1 \times 10^{-29} e$ cm at a 90%

confidence level. The collaboration expects an improvement in sensitivity by an order

of magnitude in the near future [75]. A further significant improvement in sensitivity

might come in the future from the EDM[3] experiment [444].

Two-Higgs doublet models (2HDMs) are among the most popular extensions

of the SM and can contain new sources of CP-violation. 2HDMs arise in many well-

motivated theories beyond the SM, such as in the Minimal Supersymmetric Standard

Model (MSSM). The most general form of a 2HDM allows for new sources of CP-

violation both in the scalar potential and in the Higgs-Yukawa interactions. However,

it generically exhibits flavor changing neutral currents, which are strongly constrained

by experiments. By imposing a softly broken $\mathbb{Z}_2$ symmetry [241] to yield the complex

two-Higgs doublet model (C2HDM), flavor changing neutral currents at tree-level are

naturally eliminated. The $\mathbb{Z}_2$ symmetric C2HDM still accommodates new sources of

CP-violation in the scalar potential to generate EDMs of fundamental particles.

Analyses of electric dipole moments in the C2HDM have a long history, starting

with the calculation of two loop Barr-Zee diagrams [91], followed by several extensions,

e.g. [157, 257, 331]. However, the results of these previous works only include a subset

of all two loop contributions and are not gauge-invariant. More recently, Ref. [42]

employed the pinch technique to calculate the Barr-Zee diagrams gauge invariantly. Still,

as indicated by the authors, not all contributions to the electron EDM were included.

In this chaper, we present for the first time the complete calculation of the

electron EDM by systematically accounting for all Feynman diagrams that contribute

at two loop order. Due to the recurrent issue of gauge-invariance, we perform the calculation in both the background field gauge *and* in the conventional 't Hooft R_ξ gauge keeping the gauge parameter ξ arbitrary. We algebraically establish ξ-independence and reach agreement in both gauges providing strong validation for our results. Our final formula for the electron EDM in the C2HDM is given in (3.43). This is the main equation that should be used in phenomenological exploration of the electron EDM. For convenience, we provide a *Mathematica* notebook containing the necessary formulae as an ancillary file.

The presentation of our work is organized as follows. In Sec. 3.2, we introduce the C2HDM, establishing the notation we use in this chaper. In Sec. 3.3, we present the electron EDM in background field gauge. Our main results are contained in this section. In Sec. 3.4, we reevaluate the EDM in the conventional Feynman-'t Hooft gauge and explain how we reach agreement with the background field evaluation. In Sec. 3.6, we compare our results with the recent evaluation of the electron EDM presented in [42]. We also introduce a set of benchmark parameters to carry out a numerical exploration of the electron EDM. In Sec. 3.5, we explain how our results may be adapted to obtain EDMs of light quarks. In Sec. 3.7, we present an asymptotic expansion of the electron EDM near the decoupling limit and discuss its relationship to the formula derived from an effective field theory. Sec. 3.8 is reserved for our conclusions. Finally, in the appendix, we collect useful equations on the 2HDM scalar potential.

3.2 Formulation of the C2HDM

The C2HDM is the most general CP-violating two-Higgs doublet model that possesses a softly-broken $\mathbb{Z}_2$ symmetry. In our discussion, we will closely follow the notation of [133, 264], to which we refer the reader for a detailed description of its formulation.

The SM scalar sector is extended by an additional scalar doublet with identical quantum numbers as the SM Higgs. The scalar potential is

$$
\begin{aligned}
V(\Phi_1, \Phi_2) = {}& m_{11}^2 \Phi_1^\dagger \Phi_1 + m_{22}^2 \Phi_2^\dagger \Phi_2 - \left(m_{12}^2 \Phi_1^\dagger \Phi_2 + \text{c.c.} \right) \\
& + \tfrac{1}{2}\lambda_1 \left(\Phi_1^\dagger \Phi_1 \right)^2 + \tfrac{1}{2}\lambda_2 \left(\Phi_2^\dagger \Phi_2 \right)^2 + \lambda_3 \left(\Phi_1^\dagger \Phi_1 \right) \left(\Phi_2^\dagger \Phi_2 \right) \\
& + \lambda_4 \left(\Phi_1^\dagger \Phi_2 \right) \left(\Phi_2^\dagger \Phi_1 \right) + \left(\tfrac{1}{2}\lambda_5 \left(\Phi_1^\dagger \Phi_2 \right)^2 + \text{c.c.} \right) .
\end{aligned} \tag{3.1}
$$

Apart from the soft-breaking term proportional to m_{12}^2, the potential exhibits invariance under the $\mathbb{Z}_2$ transformation $\Phi_2 \to -\Phi_2$. Generally, both doublets may acquire a vacuum expectation value. Assuming the parameters are chosen to respect U(1)_{EM} in the vacuum, they take the form

$$
\langle \Phi_1 \rangle = \frac{1}{\sqrt{2}} \begin{pmatrix} 0 \\ v_1 \end{pmatrix}, \qquad \langle \Phi_2 \rangle = \frac{1}{\sqrt{2}} \begin{pmatrix} 0 \\ v_2 e^{i\zeta} \end{pmatrix}, \tag{3.2}
$$

where $v \equiv \sqrt{v_1^2 + v_2^2} = 246$ GeV, and ζ is a possible relative phase between them. The values of v_1, v_2, and ζ are given in terms of the potential parameters in the appendix. We use rephasing invariance to work in the basis where $\zeta = 0$ throughout the chaper.

It is convenient to transform to the Higgs basis

$$
\begin{pmatrix} \Phi_1 \\ \Phi_2 \end{pmatrix} = \begin{pmatrix} \cos\beta & -\sin\beta \\ \sin\beta & \cos\beta \end{pmatrix} \begin{pmatrix} H_1 \\ H_2 \end{pmatrix}, \tag{3.3}
$$

with $\tan\beta = v_2/v_1$ so that the vacuum expectation value is contained entirely in H_1.

In this new basis the potential reads

$$
\mathcal{V}(H_1, H_2) = Y_1 H_1^\dagger H_1 + Y_2 H_2^\dagger H_2 + \left(Y_3 H_1^\dagger H_2 + \text{c.c.} \right)
$$

$$
+ \tfrac{1}{2} Z_1 \left(H_1^\dagger H_1 \right)^2 + \tfrac{1}{2} Z_2 \left(H_2^\dagger H_2 \right)^2 + Z_3 \left(H_1^\dagger H_1 \right) \left(H_2^\dagger H_2 \right)
$$

$$
+ Z_4 \left(H_1^\dagger H_2 \right) \left(H_2^\dagger H_1 \right) + \left(\tfrac{1}{2} Z_5 \left(H_1^\dagger H_2 \right)^2 \right.
$$

$$
\left. + \left(Z_6\, H_1^\dagger H_1 + Z_7\, H_2^\dagger H_2 \right) H_1^\dagger H_2 + \text{c.c.} \right), \quad (3.4)
$$

where the new parameters Y_i, Z_i are linear combinations of the original parameters m_{ij}^2, λ_i given the appendix. Analysis of small fluctuations around the vacuum shows that the components of the scalar fields in the Higgs basis are given by

$$
H_1 = \begin{pmatrix} G^+ \\ \frac{1}{\sqrt{2}} \left(v + \varphi_1^0 + iG^0 \right) \end{pmatrix} \qquad H_2 = \begin{pmatrix} H^+ \\ \frac{1}{\sqrt{2}} \left(\varphi_2^0 + ia^0 \right) \end{pmatrix},
$$

where G^+, G^0 are the would-be Goldstone modes supplying the longitudinal modes of the massive W, Z gauge bosons, and H^+ is a physical charged Higgs, of mass squared $m_{H^+}^2 = Y_2 + \tfrac{1}{2} Z_3 v^2$. The remaining scalars—the CP-even φ_1^0 and φ_2^0, and CP-odd a^0—mix, with the Higgs squared-mass matrix $\mathcal{M}^2$ given by

$$
\frac{\mathcal{M}^2}{v^2} = \begin{pmatrix} Z_1 & \mathrm{Re}(Z_6) & -\mathrm{Im}(Z_6) \\ & Y_2/v^2 + \tfrac{1}{2} Z_{345}^+ & -\tfrac{1}{2}\mathrm{Im}(Z_5) \\ & & Y_2/v^2 + \tfrac{1}{2} Z_{345}^- \end{pmatrix}, \tag{3.5}
$$

19

where $Z_{345}^{\pm} = Z_3 + Z_4 \pm \mathrm{Re}(Z_5)$. The mass matrix is diagonalized by a special orthogonal matrix R

$$R\mathcal{M}^2 R^{\top} = \mathrm{diag}(m_1^2, m_2^2, m_3^2) \tag{3.6}$$

$$\begin{pmatrix} h_1 \\ h_2 \\ h_3 \end{pmatrix} = R \begin{pmatrix} \varphi_1^0 \\ \varphi_2^0 \\ a^0 \end{pmatrix}, \tag{3.7}$$

where we parameterize the elements of R as

$$R = \begin{pmatrix} q_{11} & \mathrm{Re}(q_{12}) & \mathrm{Im}(q_{12}) \\ q_{21} & \mathrm{Re}(q_{22}) & \mathrm{Im}(q_{22}) \\ q_{31} & \mathrm{Re}(q_{32}) & \mathrm{Im}(q_{32}) \end{pmatrix}. \tag{3.8}$$

Elements of R are subject to orthonormality conditions

$$\sum_{k=1}^{3} q_{k1}^2 = \frac{1}{2} \sum_{k=1}^{3} |q_{k2}|^2 = 1, \tag{3.9}$$

$$\sum_{k=1}^{3} q_{k2}^2 = \sum_{k=1}^{3} q_{k1} q_{k2} = 0, \tag{3.10}$$

which prove indispensable in the calculation of the electron EDM. Inserting the linear combinations (3.7) into the scalar potential (3.4) generates the interaction vertices in terms of mass eigenstate fields, for which we point the reader to [264] for a complete listing. For reference, we reproduce here the three-point coupling of the neutral Higgs bosons with two charged Higgs bosons

$$h_k \text{----} \Big\langle \begin{matrix} H^- \\ H^+ \end{matrix} = -iv\lambda_{kH^+H^-}$$

where

$$\lambda_{kH^+H^-} = q_{k1}Z_3 + \mathrm{Re}(Z_7 q_{k2}), \tag{3.11}$$

which appears in the final result for the EDM.

In the mass-eigenstate basis, the Yukawa Lagrangian governing the coupling of Higgs fields h_k and $H^\pm$ to the SM fermions f is

$$\mathcal{L}_{\text{Yuk}} =$$

$$-\frac{m_f}{v}\sum_k h_k \bar{f}\big[q_{k1} - 2T_3^f c_f \mathrm{Re}(q_{k2}) + i\, c_f \mathrm{Im}(q_{k2})\gamma_5\big]f$$

$$-\sqrt{2}\Big[H^+ \bar{f}'\big(\frac{m_{f'}c_{f'}}{v}\,P_L + \frac{m_f c_f}{v}P_R\big)V_{f'f}\,f + \text{c.c.}\Big], \tag{3.12}$$

where $T_3^f = \pm\frac{1}{2}$ is the third component of weak isospin, and $V_{f'f}$ is a CKM matrix element for quarks and the Kronecker delta for leptons. The coupling coefficients c_f are controlled by the $\mathbb{Z}_2$ charges assigned to the quarks and leptons. The possible assignments yield the four 2HDM types:

$$\text{Type I}: \quad c_d = c_\ell = \cot\beta, \tag{3.13}$$

$$\text{Type II}: \quad c_d = c_\ell = -\tan\beta, \tag{3.14}$$
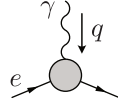
$$\text{Lepton Specific}: \quad \begin{cases} c_d = \cot\beta \\ c_\ell = -\tan\beta, \end{cases} \tag{3.15}$$

$$\text{Flipped}: \quad \begin{cases} c_d = -\tan\beta \\ c_\ell = \cot\beta, \end{cases} \tag{3.16}$$

and $c_u = -\cot\beta$ for all types.

21

3.3 Background field evaluation

The electron EDM, d_e, is derived from the $q^2 = 0$ limit of the CP-odd Pauli form factor in the electromagnetic vertex function

$$\supset i d_e \bar{u}(\mathbf{p}')\sigma^{\mu\nu}q_\nu\gamma_5 u(\mathbf{p}) \,. \qquad (3.17)$$

The unsuppressed contributions to the electron EDM in the C2HDM start at two loop order. In what follows, we present the leading order behavior of the EDM in the asymptotic limit $m_e \to 0$, adopt a normalization that sets the overall scale

$$\frac{d_e}{e} = \frac{\sqrt{2}\alpha G_F m_e}{64\pi^3}\delta_e \qquad (3.18)$$

$$\approx (6.5 \times 10^{-28} \,\text{cm}) \times \delta_e \,,$$

where we used $\alpha(m_Z) \approx 1/129$, and report our results in terms of the dimensionless electric dipole moment, δ_e.

Before presenting the results of our calculation, we briefly review relevant aspects of the background field method. In the background field method, the electromagnetic vector potential is shifted in the Lagrangian to its background field value $\bar{A}_\mu(x)$ corresponding to the classical electric field coupled to the electron EDM. Terms linear in the quantum field A_μ incurred by this shift are cancelled by a suitable choice for the source $J^\mu_{\text{em}}(x)$. In passing to the quantum theory, we choose the background field gauge condition [192]

$$\mathcal{L} = -\frac{1}{2\xi}\Big[\big(\partial^\mu A_\mu\big)^2 + \big(\partial^\mu Z_\mu + \xi m_Z G^0\big)^2$$

$$+ 2\big|(\partial^\mu + ie\bar{A}^\mu)W^+_\mu - i\xi m_W G^+\big|^2\Big], \quad (3.19)$$

22

which generalizes the conventional 't Hooft R_ξ gauges (see (3.44) below) by maintaining

covariance with respect to gauge transformations of the background field $\bar{A}_\mu$. Compared

to the conventional 't Hooft R_ξ gauges, the background field gauge modifies the tree-

level triple gauge vertex

$$\Delta \left(\begin{array}{c} \bar{A}_\mu \\ p_+ \quad p_- \\ W_\nu^+ \quad W_\rho^- \end{array} \right) = \frac{-ie}{\xi} \left(g^{\mu\nu} p_-^\rho + g^{\rho\mu} p_+^\nu \right), \qquad (3.20)$$

includes a gauge-ghost four-point vertex

$$\begin{array}{c} \bar{A}_\mu \otimes \\ Z_\nu \end{array} = \frac{ie^2 c_\mathrm{W}}{s_\mathrm{W}} g^{\mu\nu}, \qquad (3.21)$$

and features the absence of the $\bar{A}_\mu$-induced W gauge-Goldstone transition, substantially

reducing the number of contributing Feynman diagrams. For this reason, we provide

a detailed account of our results in the background field gauge, and only provide an

outline of the calculation in the conventional 't Hooft R_ξ gauge in section 3.4.

With the help of FEYNARTS [266], we generated all possible two loop dia-

grams for the electromagnetic vertex function. Table 3.1 organizes the diagrams that

contribute to the electron EDM in the background field gauge. Groups of non-vanishing

diagrams that trivially sum to zero are not shown, but are briefly mentioned in Sec. 3.4

in the context of the Feynman-'t Hooft gauge in which they do contribute. The Barr-

Zee diagrams in the first three rows form the largest class, and are defined by containing

insertions of one-loop three-point vertex functions inside the electron form factor. Tra-

ditionally, these contributions have been classified according to the kind of three-point

function that enters into the Barr-Zee diagram (rows of Table 3.1). However consider-

ations of gauge-invariance and scaling in the decoupling limit suggest that it is more

23

natural to group them by degrees of freedom entering in the loop, (columns of Table 3.1). The remaining diagrams (which we call "kite diagrams") are shown in the last two rows of Table 3.1, and make up a smaller set of diagrams. Nevertheless, they formally contribute at the same order, and their inclusion is essential for gauge-independence of the final result.

In our calculations, we dimensionally regulated all Feynman integrals, and employed a naively anticommuting definition of γ_5 in the Dirac algebra. As the EDM is UV finite to the order we work, no ambiguities associated with this definition arise. We made extensive use of an in-house version of PACKAGE-X [382] to automate the evaluation of the two loop Feynman integrals. In the results below, we express the contributions in terms of squared mass ratios with respect to the k-th neutral Higgs: $r_k = m_f^2/m_k^2$, $w_k = m_W^2/m_k^2$, $z_k = m_Z^2/m_k^2$, and $h_k = m_{H^+}^2/m_k^2$. We also make frequent use of the Davydychev-Tausk vacuum integral function [185]

$$
\begin{aligned}
\Phi(x,y) = \mathrm{Re}\bigg\{ &\frac{2}{\sqrt{\lambda}}\Big[\frac{\pi^2}{6} - \frac{1}{2}\ln x \ln y \\
&+ \ln\Big(\frac{1+x-y-\sqrt{\lambda}}{2}\Big)\ln\Big(\frac{1-x+y-\sqrt{\lambda}}{2}\Big) \\
&- \mathrm{Li}_2\Big(\frac{1+x-y-\sqrt{\lambda}}{2}\Big) - \mathrm{Li}_2\Big(\frac{1-x+y-\sqrt{\lambda}}{2}\Big)\Big]\bigg\}, \quad (3.22)
\end{aligned}
$$

where $\lambda = (1-x-y)^2 - 4xy$ is the Källén polynomial, and Li_2 is the dilogarithm
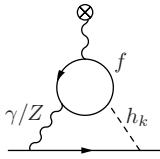
Figure 3.1: Representative fermion loop contribution to electromagnetic δ_f^{EM} (photon exchange) and neutral current δ_f^{NC} (Z exchange) Barr-Zee diagrams. The symbol '$\otimes$' denotes the background electromagnetic field $\bar{A}_\mu$. Additional diagrams are obtained by reflections along the vertical axis, or by exchanging the γ/Z and h_k lines attached to the external electron.

function. The special equal-mass case is given by

$$
\begin{aligned}
\Phi(x) &= \Phi(x,x) \\
&= \frac{2}{\sqrt{1-4x}}\Big[\frac{\pi^2}{6} + \ln^2\Big(\frac{1-\sqrt{1-4x}}{2}\Big) \\
&\quad - \frac{\ln^2 x}{2} - 2\,\mathrm{Li}_2\Big(\frac{1-\sqrt{1-4x}}{2}\Big)\Big].
\end{aligned}
\tag{3.23}
$$

Fermion loop contributions. The contributions with a fermion f in the loop are shown in Fig. 3.1, and give gauge-independent results. The four electromagnetic Barr-Zee diagrams were originally considered in [91] and are given by

$$
\begin{aligned}
\delta_f^{\mathrm{EM}} = &-4 N_C^f (Q_{\mathrm{EM}}^f)^2 Q_{\mathrm{EM}}^\ell \sum_k \mathrm{Im}(q_{k2})\Big\{ c_f\big(q_{k1} - 2T_3^\ell c_\ell \mathrm{Re}(q_{k2})\big) r_k \Phi(r_k) \\
&+ \big(q_{k1} - 2T_3^f c_f \mathrm{Re}(q_{k2})\big) c_\ell r_k \Big[4 + 2\ln(r_k) + (1-2r_k)\Phi(r_k)\Big]\Big\},
\end{aligned}
\tag{3.24}
$$

where $N_C^f = 3$ for quarks and $N_C^f = 1$ for leptons, and Q_{EM}^f and $T_3^f = \pm\frac{1}{2}$ are the electric charge and third component of weak isospin, respectively. The four neutral current diagrams give

$$\delta_f^{\mathrm{NC}} = -\frac{N_C^f Q_{\mathrm{EM}}^f Q_{\mathrm{W}}^f Q_{\mathrm{W}}^\ell}{4 c_{\mathrm{W}}^2 s_{\mathrm{W}}^2} \sum_k \mathrm{Im}(q_{k2}) \Big\{ c_f \big(q_{k1} - 2T_3^\ell c_\ell \mathrm{Re}(q_{k2}) \big) \frac{r_k}{1 - z_k} \Big(\Phi(r_k) - \Phi\big(\tfrac{r_k}{z_k}\big) \Big)$$

$$+ \big(q_{k1} - 2T_3^f c_f \mathrm{Re}(q_{k2}) \big) c_\ell \frac{r_k}{1 - z_k} \Big(2 \ln(z_k) + (1 - 2r_k)\Phi(r_k) - \big(1 - \tfrac{2r_k}{z_k}\big)\Phi\big(\tfrac{r_k}{z_k}\big) \Big) \Big\}, \tag{3.25}$$

where $s_{\mathrm{W}} = \sin(\theta_W)$, $c_{\mathrm{W}} = \cos(\theta_W)$, and $Q_{\mathrm{W}}^f = 2T_3^f - 4Q_{\mathrm{EM}}^f s_{\mathrm{W}}^2$ is the weak charge of fermion f.

All fermion species should be added to obtain the complete contribution to the EDM. Practically, it suffices to only include the third generation fermions t, b and τ, since other fermion contributions are suppressed by their much smaller masses. For the lighter fermions, b and τ, it may be more convenient to expand δ_f^{EM} and δ_f^{NC} in small fermion masses, which can be obtained with the help of the small-argument expansion of the Davydychev-Tausk function (3.23)

$$\Phi(x) = \Big(\ln^2(x) + \frac{\pi^2}{3} \Big) + 2x \Big(\ln^2(x) + 2\ln(x) + \frac{\pi^2}{3} - 2 \Big) + \mathcal{O}(x^2). \tag{3.26}$$
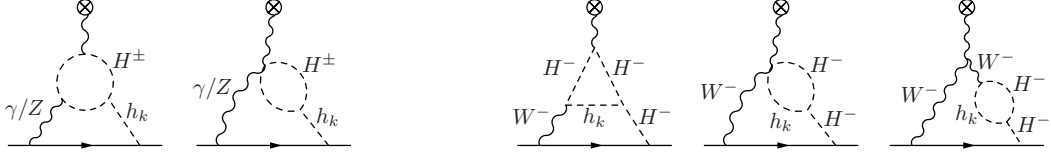
Figure 3.2: Representative charged Higgs contributions to **left:** electromagnetic $\delta_{H^+}^{\text{EM}}$ and neutral current $\delta_{H^+}^{\text{NC}}$ Barr-Zee diagrams, and **right:** charged current $\delta_{H^+}^{\text{CC}}$ Barr-Zee diagrams.

Charged Higgs loop contributions. Representative Feynman diagrams involving charged Higgs loops are shown in Fig. 3.2. Like the fermion loop contributions, these are all gauge-independent. For the electromagnetic Barr-Zee diagrams we find

$$\delta_{H^+}^{\text{EM}} = \frac{2Q_{\text{EM}}^\ell s_{\text{w}}^2}{\pi\alpha} c_\ell \sum_k \text{Im}(q_{k2})\lambda_{kH^+H^-}\, w_k \Big[2 + \ln(h_k) - h_k\Phi(h_k) \Big], \tag{3.27}$$

where $\lambda_{kH^+H^-}$ is the triple Higgs coupling given (3.11). The neutral current Barr-Zee diagrams give a result proportional to Q_{w}^ℓ:

$$\delta_{H^+}^{\text{NC}} = \frac{Q_{\text{w}}^\ell c_{2\text{w}}}{4\pi\alpha} c_\ell \sum_k \text{Im}(q_{k2})\lambda_{kH^+H^-}\frac{z_k}{1-z_k}\Big[\ln(z_k) - h_k\Phi(h_k) + \frac{h_k}{z_k}\Phi\big(\tfrac{h_k}{z_k}\big) \Big], \tag{3.28}$$

where $c_{2\text{w}} = \cos(2\theta_W)$. Finally, for the charged current Barr-Zee diagrams we find

$$\begin{aligned}
\delta_{H^+}^{\text{CC}} = \frac{(-2T_3^\ell)}{4\pi\alpha} c_\ell \sum_k \text{Im}(q_{k2})\lambda_{kH^+H^-} & \Big[2 - \frac{2}{h_k} + \frac{2\ln(h_k)}{h_k} - \frac{2-2h_k+w_k}{h_k-w_k}\ln\Big(\frac{h_k}{w_k}\Big) \\
& - \frac{1+h_k^2-h_k(2+w_k)}{w_k(h_k-w_k)}\ln(h_k)\ln\Big(\frac{h_k}{w_k}\Big) - \frac{2(h_k-2h_k^2+h_k^3+w_k-2h_kw_k)}{h_k^2 w_k}\text{Li}_2\Big(1-\frac{1}{h_k}\Big) \\
& + \frac{w_k(1-4h_k+2h_k^2)}{h_k^2(h_k-w_k)}\Phi(h_k) - \frac{1-h_k^3-w_k+h_k^2(3+2w_k)-h_k(3+w_k+w_k^2)}{w_k(h_k-w_k)}\Phi(h_k,w_k) \Big].
\end{aligned} \tag{3.29}$$

The overall sign $-2T_3^\ell$ arises from isospin ladder operators that assemble to form the commutator $[T_-,T_+]$ upon combining each charged current diagram of Fig. 3.2 with its mirror image.

W boson loop contributions. The groups of Barr-Zee diagrams with W boson loop shown in Fig. 3.3 are the largest set contributing to the electron EDM. The 36 electromagnetic and neutral current Barr-Zee diagrams yield the gauge-dependent expressions

$$\delta_W^{\text{EM}}(\xi) = \delta_W^{\text{EM}} + Q_{\text{EM}}^\ell c_\ell \sum_k \text{Im}(q_{k2}) q_{k1} \left[2\ln(\xi) + F_\xi(w_k) \right], \tag{3.30}$$

$$\delta_W^{\text{NC}}(\xi) = \delta_W^{\text{NC}} + \frac{Q_{\text{w}}^\ell}{4s_{\text{w}}^2} c_\ell \sum_k \text{Im}(q_{k2}) q_{k1} \left[\xi(1 - 2s_{\text{w}}^2)\Phi(\xi c_{\text{w}}^2) + F_\xi(w_k) \right], \tag{3.31}$$

with

$$\delta_W^{\text{EM}} = Q_{\text{EM}}^\ell c_\ell \sum_k \text{Im}(q_{k2}) q_{k1} \left[4(1 + 6w_k) + 2(1 + 6w_k)\ln(w_k) - (3 - 16w_k + 12w_k^2)\Phi(w_k) \right], \tag{3.32}$$

$$\delta_W^{\text{NC}} = \frac{Q_{\text{w}}^\ell}{4s_{\text{w}}^2} c_\ell \sum_k \text{Im}(q_{k2}) q_{k1} \left[-\frac{3 - 16w_k + 12w_k^2}{1 - z_k} \Phi(w_k) + \frac{1 - 2s_{\text{w}}^2 + 2(5 - 6s_{\text{w}}^2)w_k}{c_{\text{w}}^2(1 - z_k)} \ln(z_k) \right.$$
$$\left. - \frac{(1 + 8s_{\text{w}}^2 - 12s_{\text{w}}^4)z_k}{1 - z_k} \Phi(c_{\text{w}}^2) \right]. \tag{3.33}$$

Gauge-dependence is contained within the mass-dependent function,

$$F_\xi(w_k) = -\xi \ln^2(\xi) - 2(1 - \xi)^2 w_k \text{Li}_2(1 - \xi) - [3 + \xi - (1 - \xi)^2 w_k] \ln(\xi) \ln(w_k)$$
$$+ \xi(1 - 2\xi w_k)\Phi(\xi w_k) + \left[3 - \xi - 2(2 - \xi - \xi^2)w_k + (1 - \xi)^3 w_k^2 \right] \Phi(w_k, \xi w_k). \tag{3.34}$$

The result for the charged current Barr-Zee diagrams with the W boson in loop is more complicated because of the presence of another mass scale from the charged Higgs. The 12 diagrams give

$$\delta_W^{\text{CC}}(\xi) = \delta_W^{\text{CC}} + \frac{(-2T_3^\ell)}{4s_{\text{w}}^2} c_\ell \sum_k \text{Im}(q_{k2}) q_{k1} G_\xi(w_k), \tag{3.35}$$

$$\delta_W^{\text{CC}} = \frac{(-2T_3^\ell)}{4s_{\text{w}}^2} c_\ell \sum_k \text{Im}(q_{k2}) q_{k1} \left[\frac{2}{w_k} - \frac{2(1 - w_k)^2}{h_k w_k} - \frac{2(1 - w_k)w_k^2 + (2 + w_k)h_k^2 - h_k(2 - w_k - 7w_k^2)}{h_k w_k(h_k - w_k)} \ln(w_k) \right.$$
$$+ \frac{h_k^2 - 2(1 - w_k)^2 + h_k(1 + 7w_k)}{h_k(h_k - w_k)} \ln(h_k) - \frac{(1 - w_k)^3 - 3h_k^2 w_k - h_k(1 + 3w_k - 4w_k^2)}{h_k^2(h_k - w_k)} \ln\left(\frac{h_k}{w_k}\right) \ln(w_k)$$
$$- \frac{2w_k(1 - w_k)^3 + h_k(2 - 8w_k + 6w_k^3)}{h_k^2 w_k^2} \text{Li}_2\left(1 - \frac{1}{w_k}\right) - \frac{1 - 6w_k + 6w_k^2 + 4w_k^3}{(h_k - w_k)w_k^2} \Phi(w_k)$$
$$+ \frac{(1 - w_k)^4 - 3h_k^3 w_k - h_k(2 + 5w_k)(1 - w_k)^2 + h_k^2(1 + 7w_k^2)}{h_k^2(h_k - w_k)} \Phi(h_k, w_k) \right], \tag{3.36}$$

28
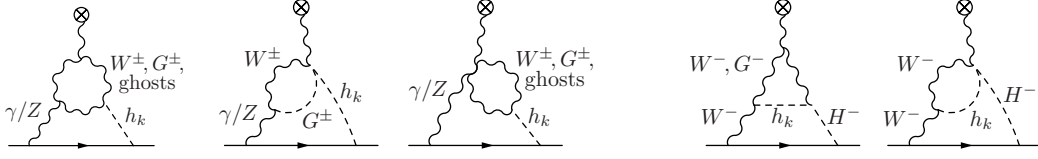
Figure 3.3: Representative W boson contributions to **left:** electromagnetic $\delta_W^{\mathrm{EM}}(\xi)$ and neutral current $\delta_W^{\mathrm{NC}}(\xi)$ Barr-Zee diagrams, and **right:** charged current $\delta_W^{\mathrm{CC}}(\xi)$ Barr-Zee diagrams. Diagrams involving the 3-point coupling of the background field $\bar{A}_\mu$ to one W gauge boson and one charged Goldstone boson are absent in the background field gauge. The third diagram with a ghost loop involving the four-point coupling in Eq. (3.21) is specific to the background field gauge.

where

$$
\begin{aligned}
G_\xi(w_k) = \; & -2\xi\big(1+\ln(\xi)\big) + \Big(\frac{(1-\xi w_k)^2}{w_k^2} - \xi\Big)\Big[\ln(\xi)\ln(\xi w_k) + 2\,\mathrm{Li}_2\Big(1-\frac{1}{\xi w_k}\Big)\Big] \\
& - \Big[\xi(1-3\xi) - \frac{1-(1+3\xi)w_k}{w_k^2} + (1-\xi)^2\xi w_k\Big]\Phi(w_k,\xi w_k)
\end{aligned}
\tag{3.37}
$$

is another mass-dependent ξ-dependent function.

Kite contributions. Representative kite Feynman diagrams are shown in Fig. 3.4. The neutral current contribution does not depend on the gauge parameter ξ and, in contrast to the neutral current Barr-Zee contributions, it is not suppressed by the weak
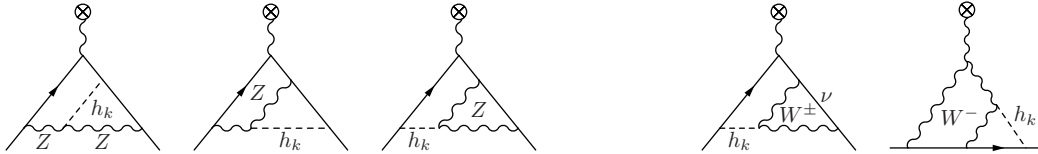
Figure 3.4: Representative contributions to **left:** neutral current kite $\delta_{\mathrm{kite}}^{\mathrm{NC}}$ and **right:** charged current $\delta_{\mathrm{kite}}^{\mathrm{CC}}(\xi)$ kite diagrams.

29

charge Q_{w}^ℓ. In agreement with [63], we find

$$\delta_{\mathrm{kite}}^{\mathrm{NC}} = -Q_{\mathrm{EM}}^\ell \frac{(Q_{\mathrm{w}}^\ell)^2 - 1}{8s_{\mathrm{w}}^2 c_{\mathrm{w}}^2} c_\ell \sum_k \mathrm{Im}(q_{k2}) q_{k1} \frac{1}{z_k^3} \Big[z_k^2 + \frac{\pi^2}{6}(1 - 4z_k) - 2z_k^2 \ln(z_k) + \frac{1 - 4z_k}{2}\ln^2(z_k)$$

$$+ 2(1 - 4z_k + z_k^2)\mathrm{Li}_2\Big(1 - \frac{1}{z_k}\Big) + \frac{1 - 6z_k + 8z_k^2}{2}\Phi(z_k) \Big]$$

$$- Q_{\mathrm{EM}}^\ell \frac{(Q_{\mathrm{w}}^\ell)^2 + 1}{24 s_{\mathrm{w}}^2 c_{\mathrm{w}}^2} c_\ell \sum_k \mathrm{Im}(q_{k2}) q_{k1} \frac{1}{z_k} \Big[2z_k(1 - 4z_k) + \frac{\pi^2}{3}(3z_k^2 + 4z_k^3) - 2z_k(1 + 4z_k)\ln(z_k)$$

$$+ 2(1 - 3z_k^2 - 4z_k^3)\mathrm{Li}_2\Big(1 - \frac{1}{z_k}\Big) + (1 - 2z_k - 8z_k^2)\Phi(z_k) \Big],$$

$$(3.38)$$

The charged current kite contribution is gauge-dependent, and is given by

$$\delta_{\mathrm{kite}}^{\mathrm{CC}}(\xi) = \delta_{\mathrm{kite}}^{\mathrm{CC}} + \frac{(-2T_3^\ell)}{4s_{\mathrm{w}}^2} c_\ell \sum_k \mathrm{Im}(q_{k2}) q_{k1} \Big[F_\xi(w_k) - G_\xi(w_k) + (1 + Q_{\mathrm{EM}}^\ell) H_\xi(w_k) \Big], \quad (3.39)$$

with

$$\delta_{\mathrm{kite}}^{\mathrm{CC}} = \frac{(-2T_3^\ell)}{4s_{\mathrm{w}}^2} c_\ell \sum_k \mathrm{Im}(q_{k2}) q_{k1} \Big[\frac{2\pi^2}{9} w_k(3 + 4w_k) + \frac{2}{3}(5 - 8w_k) - \frac{16}{3}(1 + w_k)\ln(w_k)$$

$$+ \frac{2(3 + 2w_k - 6w_k^3 - 8w_k^4)}{3w_k^2}\mathrm{Li}_2\Big(1 - \frac{1}{w_k}\Big) + \frac{(1 + 2w_k)(3 - 10w_k + w_k^2)}{3w_k^2}\Phi(w_k) \Big].$$

$$(3.40)$$

In addition to depending on $F_\xi(w_k)$ and $G_\xi(w_k)$ that appear in the W-loop Barr-Zee diagrams, it also involves a third ξ-dependent function $H_\xi(w_k)$ whose functional form is not needed since it drops out upon setting $Q_{\mathrm{EM}}^\ell = -1$. This completes the listing of contributions to the electron EDM.

Assembling a gauge-independent result. Adding together the contributions listed above, the electron EDM is given by

$$\frac{d_e}{e} = \frac{\sqrt{2}\alpha G_F m_e}{64\pi^3} \times$$

$$\Big[\sum_f (\delta_f^{\text{EM}} + \delta_f^{\text{NC}}) + (\delta_{H^+}^{\text{EM}} + \delta_{H^+}^{\text{NC}} + \delta_{H^+}^{\text{CC}})$$

$$+ (\delta_W^{\text{EM}}(\xi) + \delta_W^{\text{NC}}(\xi) + \delta_W^{\text{CC}}(\xi) + \delta_{\text{kite}}^{\text{NC}} + \delta_{\text{kite}}^{\text{CC}}(\xi))\Big], \quad (3.41)$$

where we have grouped the various contributions based on the columns of Table 3.1, corresponding to the virtual particles in the loop. Gauge-dependence is contained within the Barr-Zee W-loop contributions and charged current kite contributions. See Fig. 3.11 below for a plot of these contributions as a function of the gauge parameter. The sum of these gauge-dependent terms yields

$$\delta_W^{\text{EM}}(\xi) + \delta_W^{\text{NC}}(\xi) + \delta_W^{\text{CC}}(\xi) + \delta_{\text{kite}}^{\text{CC}}(\xi)\Big|_{\xi\text{-dep.}} =$$

$$\frac{1}{4s_{\text{W}}^2} c_\ell \sum_k \text{Im}(q_{k2}) q_{k1} \Big[(Q_{\text{W}}^\ell - 2T_3^\ell + 4Q_{\text{EM}}^\ell s_{\text{W}}^2) F_\xi(w_k)$$

$$- 2T_3^\ell (1 + Q_{\text{EM}}^\ell) H_\xi(w_k) + 8Q_{\text{EM}}^\ell s_{\text{W}}^2 \ln(\xi)$$

$$+ Q_{\text{W}}^\ell (1 - 2s_{\text{W}}^2) \Phi(\xi c_{\text{W}}^2) \Big], \quad (3.42)$$

where the ξ-dependent function $G_\xi(w_k)$ immediately cancels between the charged current Barr-Zee $\delta_W^{\text{CC}}(\xi)$ and kite $\delta_{\text{kite}}^{\text{CC}}(\xi)$ contributions. Upon inserting the electroweak relation $Q_{\text{W}}^\ell = 2T_3^\ell - 4Q_{\text{EM}}^\ell s_{\text{W}}^2$ and $Q_{\text{EM}}^\ell = -1$, the first and second terms in square brackets proportional to mass-dependent functions $F_\xi(w_k)$ and $H_\xi(w_k)$ vanish. The remaining mass-independent terms vanish after summing over k, and using the orthog-

31

onality relation $\sum_k q_{1k}q_{2k} = 0$ in (3.10). Therefore, all gauge dependent terms in (3.41) may be safely dropped so that our final result for the electron EDM is

$$\frac{d_e}{e} = \frac{\sqrt{2}\alpha G_F m_e}{64\pi^3} \times$$

$$\Big[\sum_f (\delta_f^{\text{EM}} + \delta_f^{\text{NC}}) + (\delta_{H^+}^{\text{EM}} + \delta_{H^+}^{\text{NC}} + \delta_{H^+}^{\text{CC}})$$

$$+ (\delta_W^{\text{EM}} + \delta_W^{\text{NC}} + \delta_W^{\text{CC}} + \delta_{\text{kite}}^{\text{NC}} + \delta_{\text{kite}}^{\text{CC}}) \Big] , \quad (3.43)$$

with the individual contributions given in (3.24), (3.25), (3.27), (3.28), (3.29), (3.32), (3.33), (3.36), (3.38), and (3.39). Despite their appearance, we emphasize that one should not interpret each component of the k-sum in these expressions as literally the individual contributions of the neutral Higgs to the EDM since each one by itself is gauge-dependent. Only the sum is gauge-independent.

3.4 Re-evaluation in the Feynman-'t Hooft gauge

Despite simplifications afforded by working in the background field gauge, it is still common practice to perform calculations of this kind in the conventional 't Hooft R_ξ gauge defined by

$$\mathcal{L} = -\frac{1}{2\xi} \Big[(\partial^\mu A_\mu)^2 + (\partial^\mu Z_\mu + \xi m_Z G^0)^2 + 2|\partial^\mu W_\mu^+ - i\xi m_W G^+|^2 \Big] , \quad (3.44)$$

and with $\xi = 1$ for simplicity. In order to facilitate comparison with earlier calculations of the EDM [42, 331], and also to provide additional validation of our result, we re-evaluated the electron EDM in the 't Hooft R_ξ gauge with ξ left arbitrary. In this section

32

we outline how the calculation proceeds, and the steps required to reach agreement with the background field evaluation presented above.

The electromagnetic and neutral current Barr-Zee contributions with a fermion loop δ_f^{EM}, δ_f^{NC}, or a charged Higgs loop $\delta_{H^+}^{\text{EM}}$, $\delta_{H^+}^{\text{NC}}$, along with the neutral current kite $\delta_{\text{kite}}^{\text{NC}}$ contributions are unchanged relative to the background field gauge. The differences are in the electromagnetic and neutral current Barr-Zee contributions with a W loop, $\delta_W^{\text{EM}}(\xi)$, $\delta_W^{\text{NC}}(\xi)$, and in the charged current contributions, $\delta_{H^+}^{\text{CC}}$, $\delta_W^{\text{CC}}(\xi)$ and $\delta_{\text{kite}}^{\text{CC}}(\xi)$.

Intermediate expressions are substantially more complicated due to the presence of the $\gamma W^{\pm} G^{\mp}$ vertex, which generates diagrams involving several new interaction vertices from the scalar potential. Additionally, treatment of tadpole diagrams require a multitude of *sum rules* to show that they combine with other contributions to yield a UV finite result in the end. To avoid a barrage of lengthy expressions, we give only the parts of interest for the specific case of the Feynman-'t Hooft gauge $\xi = 1$.

We start with W loop contributions to the electromagnetic Barr-Zee diagrams δ_W^{EM}. Accounting for the presence of the $\gamma W^{\pm} G^{\mp}$ vertex, there are 52 diagrams of the kinds shown on the left of Fig. 3.3. Their total is UV finite, and exhibits an apparent logarithmic singularity in the limit of vanishing electron mass

$$\delta_W^{\text{EM}}(\text{F't H}) = Q_{\text{EM}}^{\ell} c_{\ell} \sum_k \text{Im}(q_{k2}) q_{k1} \times \left[\ln\left(\frac{m_W^2}{m_e^2}\right) + \left(\begin{array}{c} \text{regular as} \\ m_e \to 0 \end{array} \right) \right]. \qquad (3.45)$$

After performing the k-sum and using the orthogonality relations in (3.10), the singularity vanishes.

Next we consider the W loop neutral current Barr-Zee contributions δ_W^{NC}.
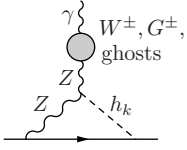
Figure 3.5: Class of diagrams additionally contributing to W loop neutral current Barr-Zee, δ_W^{NC}, in the 't Hooft R_ξ gauge.

There are 52 diagrams that sum to a UV divergent expression with the pole part in $d = 4 - 2\epsilon$ dimensions given by

$$\frac{Q_{\rm w}^\ell}{4s_{\rm w}^2} c_\ell \sum_k \mathrm{Im}(q_{k2}) q_{k1} \frac{4z_k}{(1 - z_k)^2} \left(1 - z_k + \ln(z_k)\right) \frac{1}{\epsilon} \tag{3.46}$$

that cannot be removed by performing the k-sum on account of the nontrivial m_k^2 dependence. However, there is another class of diagrams to consider, shown in Fig. 3.5, involving the γ-Z transition function mediated by gauge loops. We mention that, in the background field gauge, individual diagrams in this group are non-vanishing but sum to zero because of the property that $\Pi_{AZ}^{\mu\nu}(q^2) \to 0$ as $q^2 \to 0$ in this gauge [192]. In the 't Hooft R_ξ gauges this group does not vanish, and importantly, it supplies a UV divergent contribution equal and opposite to (3.46), yielding an overall finite neutral current contribution $\delta_W^{\rm NC}(\text{F'tH})$.

We now report on the charged current kite contribution. There are a total of 10 diagrams of the type shown in the last three diagrams of Fig. 3.4, and four additional ones involving the $\gamma W^\pm G^\mp$ vertex. Their total is nominally UV divergent

$$\delta_{\rm kite}^{\rm CC}(\text{F'tH}) = \frac{1}{4s_{\rm w}^2} c_\ell \sum_k \mathrm{Im}(q_{k2}) q_{k1} \left[-\frac{1}{2\epsilon} + \text{finite} \right]. \tag{3.47}$$

Figure 3.6: Additional charged current Barr-Zee diagrams in the 't Hooft R_ξ gauge. The R-subtracted finite parts of diagrams (a) and (b) contribute to $\delta_{H^+}^{\mathrm{CC}}$ and δ_W^{CC}, respectively. The UV-singular R-subtractions cancel against the tadpole diagrams in Fig. 3.7 and 3.8.

But after performing the k-sum, the UV divergent part vanishes by orthogonality of the rotation vectors (3.10).

Despite their finiteness, none of the three contributions $\delta_W^{\mathrm{EM}}(\mathrm{F'tH})$, $\delta_W^{\mathrm{NC}}(\mathrm{F'tH})$, nor $\delta_{\mathrm{kite}}^{\mathrm{CC}}(\mathrm{F'tH})$ so far considered coincide with their background field gauge counterparts. To find agreement, the charged current contributions $\delta_{H^+}^{\mathrm{CC}}$ and δ_W^{CC} need to be examined, which we now do.

The analysis of charged current contributions and their separation into $\delta_{H^+}^{\mathrm{CC}}$ and δ_W^{CC} appears at first obfuscated by numerous diagrams that must be considered in addition to those shown on the right of Figs. 3.2 and 3.3. A little investigation shows that to recover the charged current contributions, we only need to include the R-subtracted part of the diagrams in Fig. 3.6 (and their mirror images). The R-subtractions contain the UV singular parts of these diagrams stemming from the sub-loop Goldstone-Higgs

transition function. In d dimensions, these are given by

$$\delta_R\big[\text{Fig. 3.6(a)}\big] = \frac{c_\ell}{d\,s_{\text{W}}^2}\mathbf{\Delta}(m_W, m_{H^+})\sum_k \text{Im}(q_{k2})$$
$$\times v^2\lambda_{kH^+H^-}\big(\mathbf{A}_0(m_{H^+}) - \mathbf{A}_0(m_k)\big) \quad (3.48)$$

and

$$\delta_R\big[\text{Fig. 3.6(b)}\big] = \frac{c_\ell}{d\,s_{\text{W}}^2}\mathbf{\Delta}(m_W, m_{H^+})\sum_k \text{Im}(q_{k2})$$
$$\times q_{k1}\big(m_k^2\mathbf{A}_0(m_W) + (m_{H^+}^2 - m_k^2)\mathbf{A}_0(m_k)\big), \quad (3.49)$$

where $\mathbf{A}_0(m)$ and $\mathbf{\Delta}(m_W, m_{H^+})$ are the one-loop tadpole and triangle integrals defined by

$$\mathbf{A}_0(m) = \int (dk)\frac{1}{k^2 - m^2},$$
$$\mathbf{\Delta}(m_W, m_{H^+}) = \int (dk)\frac{1}{(k^2 - m_W^2)^3(k^2 - m_{H^+}^2)}\,.$$
$$(3.50)$$

Then upon adding the six Barr-Zee diagrams of the type shown to the right of Fig. 3.2 to the R-subtracted form of Fig. 3.6(a), we obtain a UV finite charged current charged Higgs loop contribution that also agrees with the corresponding background field gauge evaluation given in Eq. (3.29),

$$\delta_{H^+}^{\text{CC}}(\text{F'tH}) = \delta_{H^+}^{\text{CC}}. \quad (3.51)$$

Similarly, by adding the 16 Barr-Zee diagrams of the type shown on the right of Fig. 3.3 to the R-subtracted forms of Fig. 3.6(b), we obtain a UV finite result for the charged current W loop contribution $\delta_W^{\text{CC}}(\text{F'tH})$. Finally, upon combining this to

36
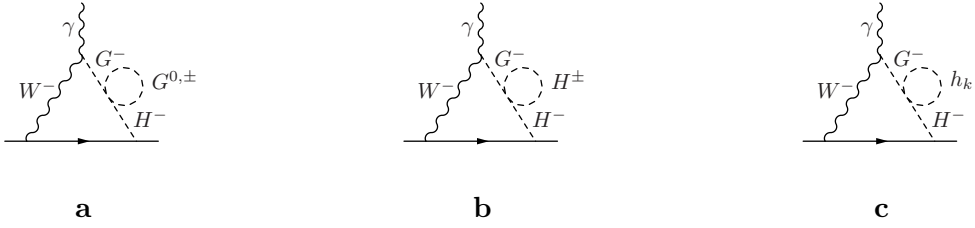
Figure 3.7: Diagrams involving the Goldstone-Higgs transition function that contribute to the electron EDM in the 't Hooft R_ξ gauge.

the electromagnetic, neutral current Barr-Zee diagrams and the charged current kite contributions in the 't Hooft R_ξ gauge computed above, we obtain a result precisely equal to the sum of corresponding contributions in the background field gauge

$$\delta_W^{\text{EM}}(\text{F'tH}) + \delta_W^{\text{NC}}(\text{F'tH}) + \delta_W^{\text{CC}}(\text{F'tH}) + \delta_{\text{kite}}^{\text{CC}}(\text{F'tH}) =$$

$$\delta_W^{\text{EM}}(\xi) + \delta_W^{\text{NC}}(\xi) + \delta_W^{\text{CC}}(\xi) + \delta_{\text{kite}}^{\text{CC}}(\xi). \quad (3.52)$$

To confirm the equivalence analytically, and especially to demonstrate ξ-independence, we found it essential to expand the 't Hooft R_ξ gauge results into partial fractions with respect to m_k^2 and to perform the k-sum dispensing of any parts that vanish by orthogonality of the rotation vectors q_{k1} and q_{k2}.

Finally, we turn to the remaining diagrams shown in Fig. 3.7 and 3.8. We aim to demonstrate a cancellation between these diagrams and the R-subtractions of Fig. 3.6, given by (3.48) and (3.49). Diagrams (a) and (b) of Fig. 3.7 are unusual in that the neutral Higgs bosons are absent and hence do not involve a k-sum. Furthermore,

37

they depend on four-point interaction vertices from the scalar potential

$$
\begin{array}{c} G^- \quad G^+ \\ \diagdown \diagup \\ \diagup \diagdown \\ H^+ \quad G^- \end{array} = 2 \left(\begin{array}{c} G^- \quad G^0 \\ \diagdown \diagup \\ \diagup \diagdown \\ H^+ \quad G^0 \end{array} \right) = -2iZ_6 \,,
$$

and

$$
\begin{array}{c} G^- \quad H^- \\ \diagdown \diagup \\ \diagup \diagdown \\ H^+ \quad H^+ \end{array} = -2iZ_7 \,,
$$

that so far have not appeared in this calculation. To put these contributions under a k-sum so that they may be brought together with other diagrams, we replace Z_6 and Z_7 by their sum rules

$$
Z_6 = \frac{1}{v^2} \sum_k q_{k2}^* q_{k1} m_k^2, \tag{3.53}
$$

$$
Z_7 = \sum_k q_{k2}^* \lambda_{kH^+H^-} \,. \tag{3.54}
$$

Respectively, these are derived by considering the double contraction of the diagonalized neutral Higgs squared-mass matrix $(R \mathcal{M}^2 R^\top)_{jk}$ in (3.6) with $q_{k2}^* q_{j1}$, and the contraction of the triple Higgs coupling $\lambda_{kH^+H^-}$ in (3.11) with q_{k2}^*. The diagram in Fig. 3.7(c) involves the four-point coupling

$$
\begin{array}{c} h_j \quad H^+ \\ \diagdown \diagup \\ \diagup \diagdown \\ h_k \quad G^- \end{array} = -i\lambda_{jkH^+G^-} \,,
$$

whose diagonal elements are given by

$$
\lambda_{kkH^+G^-} = q_{k1} \left(q_{k2}^* Z_4 + q_{k2} Z_5 + q_{k1} Z_6 \right) + |q_{k2}|^2 Z_7 \,. \tag{3.55}
$$

38

Together, the diagrams of Fig. 3.7 yield

$$
\left[\text{Fig. 3.7}\right] = \frac{-c_\ell}{d\, s_{\mathrm{W}}^2} \mathbf{\Delta}(m_W, m_{H^+}) \sum_k \left\{ \mathrm{Im}(q_{k2}) \right.
$$

$$
\times \left[q_{k1} m_k^2 \big(2\mathbf{A}_0(m_W) + \tfrac{1}{2}\mathbf{A}_0(m_Z) \big) \right.
$$

$$
\left. + 2v^2 \lambda_{kH^+ H^-} \mathbf{A}_0(m_{H^+}) \right]
$$

$$
\left. + \frac{v^2}{2} \mathrm{Im}(\lambda_{kkH^+ G^-}) \mathbf{A}_0(m_k) \right\}. \quad (3.56)
$$

Next, we consider the tadpole diagrams of Fig. 3.8. In the background field gauge, diagrams (a) and (b) cancel tadpole-by-tadpole on account of the triple-gauge vertex (3.20). In the Feynman-'t Hooft gauge, however, these diagrams give the non-zero result

$$
\left[\text{Fig. 3.8(a, b)}\right] = \frac{c_\ell}{d\, s_{\mathrm{W}}^2} \sum_k \mathrm{Im}(q_{k2}) T_k
$$

$$
\times \left[\mathbf{\Delta}(m_W, m_{H^+}) + (4-d)(2-d) \frac{\mathbf{A}_0(m_W)}{m_W^4 m_k^2} \right], \quad (3.57)
$$

where

$$
T_k = -4 \sum_f N_C^f \big(q_{k1} - 2T_3^f c_f \mathrm{Re}(q_{k2}) \big) m_f^2 \mathbf{A}_0(m_f)
$$

$$
+ q_{k1} \big(2(d-1)m_W^2 + m_k^2 \big) \mathbf{A}_0(m_W)
$$

$$
+ q_{k1} \big((d-1)m_Z^2 + \tfrac{1}{2}m_k^2 \big) \mathbf{A}_0(m_Z)
$$

$$
+ v^2 \lambda_{kH^+ H^-} \mathbf{A}_0(m_{H^+}) + \frac{v^2}{2} \sum_j \lambda_{kjj} \mathbf{A}_0(m_j) \quad (3.58)
$$

is the tadpole function to which fermions, W, Z, ghosts, $G^\pm$, G^0, $H^\pm$, and h_k contribute.

Diagram (c) of Fig. 3.8 represents an EDM contribution derived from a one-loop mag-
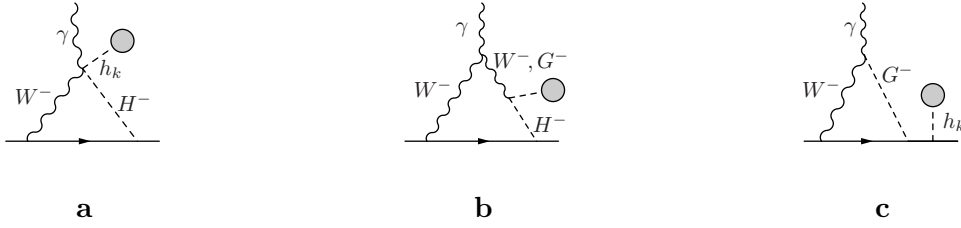
Figure 3.8: Tadpole diagrams in the 't Hooft R_ξ gauge. Diagram (c) represents a contribution due to a CP-violating shift in the residue of the electron pole.

netic moment contribution induced by a CP-violating shift in the residue of the electron propagator pole. When added to diagrams (a) and (b), this contribution exactly cancels the second term in square brackets of (3.57). Then, after performing the k-sum, all contributions to T_k proportional to q_{k1} and q_{k2} but independent of m_k^2 drop out by orthogonality, leaving just the Goldstones, charged Higgs, and neutral Higgs bosons

$$\big[\text{Fig. 3.8}\big] = \frac{c_\ell}{d\, s_\mathrm{W}^2} \mathbf{\Delta}(m_W, m_{H^+}) \sum_k \mathrm{Im}(q_{k2})$$

$$\times \left[q_{k1} m_k^2 \big(\mathbf{A}_0(m_W) + \tfrac{1}{2}\mathbf{A}_0(m_Z)\big) \right.$$

$$\left. + v^2 \lambda_{kH^+H^-} \mathbf{A}_0(m_{H^+}) + \frac{v^2}{2} \sum_j \lambda_{kjj} \mathbf{A}_0(m_j) \right]. \quad (3.59)$$

The neutral Higgs tadpole contribution is a double sum involving the triple-Higgs vertex

 $= -iv\lambda_{ijk}\,,$

40

whose diagonal elements are given by

$$\lambda_{kjj} = 3q_{k1}q_{j1}^2 Z_1$$

$$+ \left(q_{k1}|q_{j2}|^2 + 2\operatorname{Re}(q_{j1}q_{k2}q_{j2}^*)\right)(Z_3 + Z_4)$$

$$+ \operatorname{Re}\left[(q_{k1}q_{j2}^2 + q_{j1}q_{k2}q_{j2})Z_5\right.$$

$$+ 3(q_{j1}^2 q_{k2} + 2q_{j1}q_{k1}q_{j2})Z_6$$

$$\left. + (q_{k2}^* q_{j2}^2 + 2q_{k2}|q_{j2}|^2)Z_7\right]. \qquad (3.60)$$

To combine this result with (3.56), we perform the (outer) k-sum on the last term of (3.59) to exchange λ_{kjj} for $\lambda_{jjH^+G^-}$ with the help of the sum rule

$$\sum_k q_{k2}^* \lambda_{kjj} = \lambda_{jjH^+G^-}[-4mm] + 2q_{j2}^*\lambda_{jH^+H^-} - 2q_{j2}^* q_{j1}\frac{m_{H^+}^2 - m_j^2}{v^2}, \qquad (3.61)$$

which is explicitly verified by inserting the definitions (3.11), (3.55) and (3.60), and applying the orthogonality relations. Then, upon adding (3.59) to (3.56), Z-Goldstone contributions and terms proportional to $\lambda_{kkH^+G^-}$ cancel yielding

$$\left[\text{Figs. } 3.7 + 3.8\right] = \frac{-c_\ell}{d\, s_{\mathrm{W}}^2} \mathbf{\Delta}(m_W, m_{H^+}) \sum_k \operatorname{Im}(q_{k2})$$

$$\times \left[q_{k1}\left(m_k^2 \mathbf{A}_0(m_W) + (m_{H^+}^2 - m_k^2)\mathbf{A}_0(m_k)\right)\right.$$

$$\left. + v^2 \lambda_{kH^+H^-}\left(\mathbf{A}_0(m_{H^+}) - \mathbf{A}_0(m_k)\right)\right], \quad (3.62)$$

which, in turn, completely cancels the R-subtractions given in (3.48) and (3.49). This completes our evaluation of the electron EDM in the 't Hooft R_ξ gauge, thereby establishing agreement with our result in the background field gauge.

3.5 Light quark EDMs

In this section, we briefly digress to discuss how our results can be adapted to obtain EDMs of light quarks. Denoting q as a generic light quark flavor, we adopt the normalization of the quark EDM d_q as in (3.18), with the replacement $m_\ell \to m_q$. Then, our background field gauge results (3.24)–(3.39) should be modified by replacing the electron charges and couplings with the corresponding ones for quarks

$$\{Q_{\mathrm{EM}}^\ell, Q_{\mathrm{W}}^\ell, T_3^\ell, c_\ell\} \longrightarrow \{Q_{\mathrm{EM}}^q, Q_{\mathrm{W}}^q, T_3^q, c_q\}. \tag{3.63}$$

Also, there are new charged current kite contributions shown in Fig. 3.9. Including them, and putting $Q_{\mathrm{EM}}^u = +2/3$ and $Q_{\mathrm{EM}}^d = -1/3$ in the formulae gives somewhat different results for their gauge-independent parts. For EDMs of up and charm quarks,
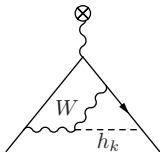
Figure 3.9: Charged current kite diagram that contributes to quark EDMs in the background field gauge. Other diagrams do not contribute at $\mathcal{O}(G_F m_q)$.

the expression in (3.40) should be replaced by

$$\delta_{\text{kite}}^{\text{CC}} = \frac{(-2T_3^u)}{4s_{\text{w}}^2} c_u \sum_k \text{Im}(q_{k2})q_{k1} \left[\frac{4\pi^2}{27} w_k(3 + 4w_k) \right.$$

$$+ \frac{2}{9}(13 - 16w_k) - \frac{4}{9}(11 + 8w_k)\ln(w_k)$$

$$+ \frac{2(9 + 4w_k - 12w_k^3 - 16w_k^4)}{9w_k^2}\text{Li}_2\left(1 - \frac{1}{w_k}\right)$$

$$\left. + \frac{(1 + 2w_k)(9 - 32w_k + 11w_k^2)}{9w_k^2}\Phi(w_k) \right], \quad (3.64)$$

and for down and strange quarks, (3.40) should be replaced by

$$\delta_{\text{kite}}^{\text{CC}} = \frac{(-2T_3^d)}{4s_{\text{w}}^2} c_d \sum_k \text{Im}(q_{k2})q_{k1} \left[\frac{2\pi^2}{27} w_k(3 + 4w_k) \right.$$

$$+ \frac{2}{9}(11 - 8w_k) - \frac{8}{9}(5 + 2w_k)\ln(w_k)$$

$$+ \frac{2(9 + 2w_k - 6w_k^3 - 8w_k^4)}{9w_k^2}\text{Li}_2\left(1 - \frac{1}{w_k}\right)$$

$$\left. + \frac{(1 + 2w_k)(9 - 34w_k + 19w_k^2)}{9w_k^2}\Phi(w_k) \right]. \quad (3.65)$$

The total quark EDM is given by (3.43) with the replacement $m_e \to m_q$.

The generalization to top and bottom quark EDMs requires a separate treatment due to their large masses and Yukawa couplings. In practice, this means the inclusion of new classes of diagrams involving multiple Higgs exchange that are suppressed for light quarks. Furthermore, since it is not justified to expand the Feynman integrals in small top quark mass, the calculation is technically more challenging. For these reasons, we have not carried out the calculation.

3.6 Comparison with literature

The electron EDM in the C2HDM has been the subject of a long history of investigations by numerous authors, consisting of efforts to identify and calculate the important two loop contributions [91, 157, 257, 331]. The original results of the gauge boson loop contributions were understood not to exhibit gauge-invariance largely due to the omission of contributions involving the charged Higgs boson or the omission of kite diagrams. An effort was undertaken relatively recently by Abe *et. al.* [42] to rectify the shortcomings of the earlier analyses to obtain a gauge-invariant result. Even though this work still does not constitute a complete calculation of the electron EDM as emphasized by the authors, their results have become a standard reference for subsequent phenomenological studies involving the electron EDM in the C2HDM [95, 158, 167, 287, 366] (see also [117, 118, 162, 166, 169, 225, 230, 303, 308] for recent related studies). Therefore in this section, we compare our results with Abe *et. al.*, and we investigate the extent to which our complete two loop result modifies predictions for the electron EDM relative to theirs.

The work of Abe *et. al.* focuses on calculating all Barr-Zee contributions, with special attention to the off shell three-point functions that enter them. They argue that in the 't Hooft R_ξ gauge (3.44) the W-loop Barr-Zee contributions δ_W^{EM}, δ_W^{NC}, and δ_W^{CC} are not gauge-invariant because the three-point functions fail to exhibit transversality with respect to the off shell leg. To obtain transverse three-point functions, they algebraically extract specific parts from the charged current kite diagrams $\delta_{\mathrm{kite}}^{\mathrm{CC}}$ using the

electroweak pinch technique [186, 378, 379], and add them to the Barr-Zee diagrams. In this way, they achieve a gauge-invariant result for the electron EDM insofar as the pinch technique leads to gauge-invariant off shell Green functions. Since results derived from the pinch technique coincide with those in the background field gauge (3.19) with $\xi = 1$ [191, 273, 388], we were able to compare our results with theirs for each of the eight contributions listed in the first three rows of Table 3.1. After careful comparison, we found exact agreement for all of them. The remainder of the kite contributions were left unevaluated.

We now explore how our inclusion of the kite contributions numerically affects the prediction of the electron EDM. To that end, we use the following input for the SM parameters [456]:

$$
\begin{aligned}
m_\tau &= & 1.777 \text{ GeV} & \qquad m_W &= & 80.34 \text{ GeV} \\
m_b &= & 2.88 \text{ GeV} & \qquad m_Z &= & 91.19 \text{ GeV} \\
m_t &= 163.0 \text{ GeV} & \qquad m_h &= 125 \text{ GeV} \\
\alpha(m_Z) &= 1/129 & \qquad v &= 246 \text{ GeV} \,,
\end{aligned}
\tag{3.66}
$$

with $c_{\mathrm{w}} = m_W/m_Z$. Additionally, we fix the C2HDM parameters to the following benchmark values

$$
\begin{aligned}
m_{H^+} &= 420 \text{ GeV} & \qquad Z_3 &= & 2.0 \\
\mathrm{Im}(\lambda_5) &= & 0.01 & \qquad Z_4 &= -0.45 \\
\mathrm{Re}(Z_5) &= -1.25 & \qquad \mathrm{Re}(Z_6) &= -0.001 \,,
\end{aligned}
\tag{3.67}
$$

and investigate the electron EDM as a function of $\tan\beta$. Note that, as discussed in the appendix, this set of 7 parameters completely fixes the Higgs potential of the C2HDM.

45

The mass spectrum at this benchmark point is

$\{m_1, m_2, m_3, m_{H^+}\} \approx \{125, 350, 450, 420\}$ GeV, and depends very mildly on $\tan\beta$.

Tree level vacuum stability is satisfied and all parameters remain perturbative at this

benchmark over the interval $0.5 \lesssim \tan\beta \lesssim 40$. Additionally, it leads to a phenomenology

that is generally in agreement with experimental bounds [246]. We mention that larger

values of $\tan\beta$ for the Type II model may already be excluded by direct searches for

heavy Higgs bosons at the LHC based on the $H \to \tau\tau$ channel [20, 409]. These bounds

are relaxed in the Type I, Flipped, or Lepton Specific models. Moreover, a charged

Higgs boson mass in the few hundred GeV mass range is liable to introduce sizable

contributions to the $b \to s\gamma$ transition. Ref. [352] showed that for the Type II model,

the lower limit on m_{H^+} is around 800 GeV, with mild dependence on $\tan\beta$. But

more recently, ref. [112] emphasized new significant theoretical uncertainties in the

determination of the $b \to s\gamma$ rate, leaving more room for new physics contributions. The

corresponding bound in the Flipped 2HDM will be similar. Type I, and Lepton Specific

models will be less constrained by the $b \to s\gamma$ rate because of the $\tan\beta$ suppression of

the down quark Yukawa couplings (3.13) and (3.15). The determination of the exact

bound on m_{H^+} is beyond the scope of this chaper.

Fig. 3.10 shows how various contributions to the electron EDM depend on

$\tan\beta$ at the benchmark point in Type I (left panel) and Type II (right panel) C2HDM.

The results for Flipped and Lepton Specific models are qualitatively similar to the ones

for Type I and Type II models respectively, and therefore we do not show them. Over

the domain of $\tan\beta$ shown, the CP-violating component of the SM-like Higgs boson,

h_1, is in the range $10^{-4} \lesssim |\text{Im}(q_{12})| \lesssim 10^{-3}$. The colored lines are the sums of all contributions within each column of Table 3.1 as labeled in the figure. The black line shows the total contribution to the electron EDM. To compare with the predictions of Abe *et. al.* [42], we also show the result of omitting the charged and neutral current kite diagrams as dashed lines.

In the Type I C2HDM, all contributions to the electron EDM are negative and their magnitudes fall with increasing $\tan \beta$ on account of the couplings in (3.13). On the other hand, in the Type II C2HDM, the electron coupling enters with an opposite sign and rises with $\tan \beta$ according to the couplings in (3.14). This causes the charged Higgs (green curve) and gauge (blue curve) contributions to grow with increasing $\tan \beta$ and to contribute to the EDM with a positive sign. As a result, cancellations due to destructive interference against the fermion contributions (red curve) can cause the predicted EDM to drop below the current and even future expected sensitivity of ACME in some regions. At our benchmark point, cancellations occur around $\tan \beta \approx 1$ and 25. These cancellations were first noticed and emphasized in [287]. However, the cancellations they found at larger $\tan \beta$ fall in regions of parameter space outside the domain of perturbativity. Our findings show that cancellations are still possible in the Type II C2HDM even when all couplings remain perturbative.

The inclusion of kite diagrams can lead to important numerical shifts in the prediction for the electron EDM. This effect is particularly pronounced in the Type II model wherein the gauge and the fermion contributions are of comparable size but enter with an opposite sign. Including the kite diagrams leads to substantial shifts of

47

the cancellation point in $\tan\beta$. Furthermore, without the kite diagrams, the remaining contributions are gauge-dependent. In Fig. 3.11, we plot the individual gauge-dependent contributions $\delta_W^{\mathrm{EM}}(\xi)$, $\delta_W^{\mathrm{NC}}(\xi)$, $\delta_W^{\mathrm{CC}}(\xi)$, and $\delta_{\mathrm{kite}}^{\mathrm{CC}}(\xi)$ in the background field gauge over a range of the gauge parameter ξ. The horizontal black line is the gauge-independent EDM obtained by including all contributions. The dashed black line is the EDM without the kite contributions. It is remarkable that without the kite contributions, even a mild variation in ξ can flip the sign of the EDM, highlighting the importance of a complete gauge-independent calculation.

3.7 Decoupling Limit and EFT analysis

In this section, we consider the possibility that the new Higgs bosons of the C2HDM are very heavy ($m_{2,3}, m_{H^+} \gg v$) by investigating the asymptotic behavior of electron EDM near the decoupling limit. We find that the electron EDM exhibits a logarithmic dependence on the heavy masses, and that its dependence on the C2HDM parameters is considerably simplified.

The decoupling limit is achieved by formally taking $Y_2 \to \infty$, with all other parameters in the Higgs basis fixed [259]. To determine the asymptotic behavior of the electron EDM in this limit, we require the large Y_2 behavior of the mixing matrix elements q_{k1}, q_{k2}, the coupling $\lambda_{kH^+H^-}$, and all the mass-dependent loop functions. In this section, we rename $Y_2 = M^2$ to emphasize its status as a large mass, since in this

limit the additional Higgs bosons of the C2HDM collectively scale as

$$m_{2,3}^2 = m_{H^+}^2 = M^2 \left[1 + \mathcal{O}(\tfrac{v^2}{M^2}) \right]. \tag{3.68}$$

The mass of the lightest Higgs boson scales as a constant

$$m_1^2 = Z_1 v^2 \left[1 + \mathcal{O}(\tfrac{v^2}{M^2}) \right] \equiv m_h^2, \tag{3.69}$$

which we therefore identify as the SM Higgs mass $m_h = 125\,\text{GeV}$. To leading order, the elements of the rotation vectors (3.8) scale as

$$q_{k1} = \begin{pmatrix} 1 \\[6pt] \frac{v^2}{M^2}\text{Re}(Z_6 e^{-i\theta_5/2}) \\[6pt] -\frac{v^2}{M^2}\text{Im}(Z_6 e^{-i\theta_5/2}) \end{pmatrix}, \quad q_{k2} = \begin{pmatrix} -\frac{v^2}{M^2} Z_6^* \\[6pt] e^{-i\theta_5/2} \\[6pt] i e^{-i\theta_5/2} \end{pmatrix}, \tag{3.70}$$

where $\theta_5 = \arg(Z_5)$, and the components of the triple Higgs coupling $\lambda_{kH^+H^-}$ in (3.11) scale as

$$\text{Im}(q_{k2}) \lambda_{kH^+H^-} \Big|_{k=1} = \mathcal{O}(\tfrac{v^2}{M^2}), \tag{3.71}$$

$$\sum_{k=2}^{3} \text{Im}(q_{k2}) \lambda_{kH^+H^-} = -\text{Im}(Z_7) + \mathcal{O}(\tfrac{v^2}{M^2}). \tag{3.72}$$

To obtain the behavior of the loop functions near the decoupling limit, the $k = 1$ and $k = 2, 3$ components of the k-sums over the neutral Higgs bosons need to be examined separately. Loop functions independent of heavy masses m_2, m_3 and m_{H^+} are necessarily $\mathcal{O}(1)$, and offer no further simplification. For loop functions containing heavy masses, we obtain the leading asymptotic behavior by directly expanding the original momentum-space Feynman integrals by regions [423], and check the results by analytically expanding the explicit expressions manually.

49

Ultimately, we find that the electron EDM is proportional to $\text{Im}(Z_{6,7}) = \pm \sin\beta \cos\beta \, \text{Im}(\lambda_5)$ and contains a logarithmically enhanced contribution near the decoupling limit that arises from the W loop Barr-Zee diagrams, yielding the leading logarithmic approximation

$$\delta_e = \frac{-3}{4c_{\text{W}}^2} \frac{v^2}{M^2} c_\ell \sin\beta \cos\beta \, \text{Im}(\lambda_5) \ln\left(\frac{M^2}{m_W^2}\right). \tag{3.73}$$

For TeV-scale Higgs masses, this logarithm is not particularly large, and may not dominate over the non-logarithmic contributions. In the following, we therefore provide the complete asymptotic expansion of the electron EDM through $\mathcal{O}(v^2/M^2)$. We find it convenient to classify each contribution as either long distance, Δ^{IR}, and short distance, Δ^{UV}, according to an effective field theory (EFT) analysis (to be discussed shortly below) to write the EDM as

$$\delta_e = \frac{v^2}{M^2} \sin\beta \cos\beta \, \text{Im}(\lambda_5) \times$$
$$\left[\sum_f c_f \Delta^{\text{IR}}_{f(\text{P})} + c_\ell \left(\sum_f \Delta^{\text{IR}}_{f(\text{S})} + \Delta^{\text{IR}}_{\text{NC kite}} + \Delta^{\text{IR}}_W\right)\right.$$
$$\left. + c_\ell (\Delta^{\text{UV}}_W + \Delta^{\text{UV}}_{H^+}) + \mathcal{O}(\tfrac{v^2}{M^2})\right]. \tag{3.74}$$

In what follows, we express squared mass ratios with respect to the mass of the SM Higgs boson $r = m_f^2/m_h^2$, $w = m_W^2/m_h^2$, and $z = m_Z^2/m_h^2$. The contributions from fermion loop Barr-Zee diagrams give

$$\Delta^{\text{IR}}_{f(\text{P})} = -4 N_C^f (Q_{\text{EM}}^f)^2 Q_{\text{EM}}^\ell r \, \Phi(r) - \frac{N_C^f Q_{\text{EM}}^f Q_{\text{W}}^f Q_{\text{W}}^\ell}{4 c_{\text{W}}^2 s_{\text{W}}^2} \frac{r}{1-z} \left(\Phi(r) - \Phi\left(\tfrac{r}{z}\right)\right), \tag{3.75}$$

and

$$\Delta^{\mathrm{IR}}_{f(\mathrm{S})} = -4N^f_C(Q^f_{\mathrm{EM}})^2 Q^\ell_{\mathrm{EM}}r\Big[4 + 2\ln(r) + (1-2r)\Phi(r)\Big]$$
$$-\frac{N^f_C Q^f_{\mathrm{EM}}Q^f_{\mathrm{W}}Q^\ell_{\mathrm{W}}}{4c^2_{\mathrm{W}}s^2_{\mathrm{W}}}\frac{r}{1-z}\Big(2\ln(z)$$
$$+ (1-2r)\Phi(r) - \big(1-\frac{2r}{z}\big)\Phi\big(\tfrac{r}{z}\big)\Big), \quad (3.76)$$

where 'S' and 'P' refer to the coupling of the Higgs boson to fermion f in the loop. The leading behavior of the neutral current kite contribution is

$$\Delta^{\mathrm{IR}}_{\mathrm{NC\ kite}} = -Q^\ell_{\mathrm{EM}}\frac{(Q^\ell_{\mathrm{W}})^2 - 1}{8s^2_{\mathrm{W}}c^2_{\mathrm{W}}z^3}\Big[z^2 + \frac{\pi^2}{6}(1-4z) - 2z^2\ln(z) + \frac{1-4z}{2}\ln^2(z)$$
$$+ 2(1-4z+z^2)\mathrm{Li}_2\Big(1-\frac{1}{z}\Big) + \frac{1-6z+8z^2}{2}\Phi(z)\Big]$$
$$-Q^\ell_{\mathrm{EM}}\frac{(Q^\ell_{\mathrm{W}})^2 + 1}{24s^2_{\mathrm{W}}c^2_{\mathrm{W}}z}\Big[2z(1-4z) + \frac{\pi^2}{3}(3z^2 + 4z^3) - 2z(1+4z)\ln(z)$$
$$+ 2(1-3z^2-4z^3)\mathrm{Li}_2\Big(1-\frac{1}{z}\Big) + (1-2z-8z^2)\Phi(z)\Big]. \tag{3.77}$$

The sum of the long distance parts of the leading behavior of the W loop Barr-Zee and the charged current kite diagrams is

$$\Delta^{\mathrm{IR}}_W = -\frac{3}{4c^2_{\mathrm{W}}}\Big[\frac{1}{2\epsilon} - \gamma_E + \ln(4\pi) + \ln\big(\frac{\mu^2}{m^2_W}\big) + \frac{7}{4}\Big]$$
$$+\frac{1}{4s^2_{\mathrm{W}}}\Big\{\Big[\frac{2\pi^2}{9}w(3+4w) + \frac{2(3+5w-(8+144s^2_{\mathrm{w}})w^2)}{3w}$$
$$-\frac{2\big(3+4(2+3s^2_{\mathrm{w}})w+8(1+9s^2_{\mathrm{w}})w^2\big)}{3w}\ln(w) + \frac{2(3+2w-6w^3-8w^4)}{3w^2}\mathrm{Li}_2\Big(1-\frac{1}{w}\Big)$$
$$+ \Big(\frac{(3-16w+12w^2)(1-4s^2_{\mathrm{w}}z)}{1-z} + \frac{3-4w-19w^2+2w^3}{3w^2}\Big)\Phi(w)\Big]$$
$$+\frac{Q^\ell_{\mathrm{W}}}{c^2_{\mathrm{W}}}\Big[\frac{1-2s^2_{\mathrm{w}}+2(5-6s^2_{\mathrm{w}})w}{(1-z)}\ln(z) + (c^2_{\mathrm{w}}-s^2_{\mathrm{w}})\ln(c^2_{\mathrm{w}}) - \frac{(1+8s^2_{\mathrm{w}}-12s^4_{\mathrm{w}})w}{(1-z)}\Phi(c^2_{\mathrm{w}})\Big]\Big\}, \tag{3.78}$$

whereas the short distance part is given by

$$\Delta^{\mathrm{UV}}_W = \frac{3}{4c^2_{\mathrm{W}}}\Big[\frac{1}{2\epsilon} - \gamma_E + \ln(4\pi) + \ln\big(\frac{\mu^2}{M^2}\big) + \frac{7}{4}\Big]. \tag{3.79}$$

51

Finally, the leading behavior of the charged Higgs Barr-Zee contributions is

$$\Delta_{H+}^{\text{UV}} = \frac{3}{4c_{\text{W}}^2}\left(\Phi(1) - 2\right),$$ (3.80)

where $\Phi(1) \approx 2.344$. Observe that when (3.78) and (3.79) are added together, the parameters of dimensional regularization $1/2\epsilon + \ln(\mu^2)$ and associated constants $-\gamma_E + \ln(4\pi) + 7/4$ cancel, and the leading logarithm of (3.73) is recovered. These unphysical parameters are introduced as a result of identifying and separating the long distance contributions derived from the Standard Model EFT, which we now discuss.

The Standard Model EFT contains higher-dimensional effective operators that parametrize new physics above the electroweak scale. In the context of the C2HDM, these operators are generated by integrating out the heavy Higgs bosons in the decoupling limit [209]. Among the CP-violating effective operators, the one relevant to the electron EDM at $\mathcal{O}(v^2/M^2)$ is the dimension-6 operator [210]

$$\mathcal{L}_6 = -\frac{y_f}{M^2}c_f Z_6(H^\dagger H)(H\bar{f}_L)f_R + \text{c.c.},$$ (3.81)

that arises by integrating out H_2 from the tree-level interaction shown in Fig. 3.12. Here, $y_f = \sqrt{2}m_f/v$ is the SM Yukawa coupling, $H \equiv H_1$ is the SM Higgs field, and f_L and f_R are the left-handed isodoublet and right-handed isosinglet fermions, respectively. From an agnostic bottom-up point of view, the only unambiguous part of the electron EDM that can be determined from the EFT in (3.81) is the leading logarithm (3.73). However, since the value of the logarithm is not particularly large unless M^2 is far above the TeV scale, it is interesting to explore the extent to which the non-logarithmic terms of the full asymptotic behavior of the electron EDM can be reproduced in the infrared.

52

There are two classes of interactions derived from the operator in (3.81) in the electroweak vacuum that contribute to the electron EDM. The first class of interactions is the pseudoscalar Yukawa interaction which is obtained by setting two of the Higgs fields to their vacuum expectation values

$$\mathcal{L}_6 \supset -i\frac{v^2}{M^2}c_f \sin\beta\cos\beta\,\mathrm{Im}(\lambda_5)\frac{m_f}{v}h\bar{f}\gamma_5 f\,. \tag{3.82}$$

In the background field gauge, the diagrams involving these interactions are essentially identical to those that are considered for the full C2HDM, but with those containing a charged Higgs boson omitted (Fig. 3.1, left of Fig. 3.3, and Fig. 3.4). We find that these contributions are UV finite as expected from power counting arguments, but also gauge-dependent. These contributions were calculated in [63] in the background field Feynman gauge, and we find agreement when we set $\xi = 1$ in our formulas.

Gauge-independence is achieved when we include the second class of interactions generated by (3.81) in the electroweak vacuum. These are the four-point interactions involving the charged Goldstone bosons obtained by setting just one Higgs field to its vacuum expectation value

$$\mathcal{L}_6 \supset -\frac{m_e}{M^2}c_\ell \sin\beta\cos\beta\,\mathrm{Im}(\lambda_5) \times \left[iG^+G^-\,\bar{e}\gamma_5 e + \left(i\sqrt{2}hG^-\,\bar{e}P_L\nu + \mathrm{c.c.}\right)\right]. \tag{3.83}$$

These interactions generate new diagrams shown in Fig. 3.13 and are essential to obtain a gauge-independent result. Furthermore, we find that they are UV divergent as expected

from power counting

$$\delta_e = \frac{v^2}{M^2} c_\ell \sin\beta \cos\beta \operatorname{Im}(\lambda_5) \Big[\frac{-3}{4c_W^2} \Big(\frac{1}{2\epsilon} - \gamma_E + \ln(4\pi)$$

$$+ \ln\big(\frac{\mu^2}{m_W^2}\big) + \frac{7}{4} \Big) + \Big(\begin{array}{c} \text{gauge dep.} \\ \text{non-log.} \end{array} \Big) \Big], \quad (3.84)$$

where the gauge-dependent non-logarithmic terms have been omitted for brevity. The appearance of a simple $1/\epsilon$ pole signals the two loop mixing of the dimension-6 operator in (3.81) into the electron dipole moment operator. This mixing effect was noted in [377] based on a model-independent systematic analysis of CP-violating dimension-6 operators, and the logarithm found there agrees with our explicit calculation in the C2HDM.

Our final result of the EFT calculation in dimensional regularization is the sum of both classes of diagrams, which we identify as the IR part of (3.74) given by (3.75)–(3.78). The appearance of the dimensional regularization parameters and regularization-dependent constants in (3.78) are understood to arise from the separation into the short distance and long distance contributions based on the EFT computation just outlined. The low energy constant associated with the electron EDM operator in the 2HDM is then given by short distance contributions $\Delta_W^{\text{UV}} + \Delta_{H^+}^{\text{UV}}$ in (3.79), (3.80), and serves as the counterterm for the EFT computation. With respect to the full C2HDM calculation, it is interesting to note that the bulk of the non-logarithmic contributions are captured in the infrared by the EFT. The only contributions that are not reproduced are those arising from the numerically small charged Higgs Barr-Zee diagrams in (3.80), and

regulator-dependent constants in the W loop contributions in (3.79).

Despite its complicated appearance, the electron EDM near the decoupling limit (3.74) depends straightforwardly on a few C2HDM parameters allowing us to provide simple numerical expressions by inserting the known values of the SM parameters (3.66):

$$\text{Type I:} \qquad d_e = -1.06 \times 10^{-27} e\,\text{cm} \times \left(\frac{1\,\text{TeV}}{M}\right)^2 \text{Im}(\lambda_5) \ \cos^2\beta \Big[1 + 0.07 \ln\left(\frac{M}{1\,\text{TeV}}\right)\Big] \qquad (3.85)$$

The leading logarithmic contribution is suppressed by a small coefficient, requiring M to be orders of magnitude above the TeV scale before it can dominate the nonlogarithmic contributions. The above expressions also reveal a numerical cancellation near $\tan\beta \approx 1$ for Type II and the Lepton Specific models, which is evident in the right panel of Fig. 3.10.

We pause to comment on a similar EFT analysis that was recently carried out in [210]. Their results differ from ours due to the omission of the diagrams of Fig. 3.13 derived from the interactions in (3.83). Consequently, their results are gauge-dependent and their formulae for the electron EDM miss the leading logarithmic contribution. The numerical effect is at the level of $\sim 25\%$ for Type I and $\sim 55\%$ for Type II at $m_{H^+} \approx 1$ TeV.

In Fig. 3.14 we numerically compare various approximations to the electron EDM as a function of m_{H^+} for the Type II C2HDM. All other parameters are fixed according to the benchmark point in (3.67) with $\tan\beta = 2$. The black line shows the result of the full two loop calculation (3.43). Its approximation near the decoupling limit (4.42) is shown in dashed red, and asymptotically approaches the full result (black

curve) as $m_{H^+} \to \infty$. The solid red curve shows the leading logarithmic approximation (3.73), and for the modest values of m_{H^+} displayed in the plot, only provides the correct order of magnitude for the electron EDM. Its approach to the black curve is slow, and good agreement is not reached until m_{H^+} is several orders of magnitude above the electroweak scale. Finally, the EFT result in the $\overline{\text{MS}}$ scheme given by the IR part of (3.74) with $\mu = M$ is shown in blue, with the shaded band obtained by varying the scale between $\mu = M/2$ and $\mu = 2M$. Because of its inability to capture the model-dependent non-logarithmic contributions in the UV, its approach to black curve is as slow as the leading logarithmic approximation (solid red). However, its difference relative to the full two loop calculation is smaller since it accounts for a significant part of the non-logarithmic contributions in the IR.

Before finishing this section, we would like to stress the limitation of the "κ framework" often used in the literature to parametrize the possible effects of a CP violating SM Higgs boson on the EDMs [63, 135, 271]. As explained below (3.82), a modified Higgs coupling of the form $-\kappa h \bar{e} i \gamma_5 e$ by itself leads to gauge-dependent contributions to the EDM and needs to be supplemented by additional interactions of the form in (3.83). However, the full gauge-independent result for the EDM that takes into account the additional interactions is found to be logarithmically divergent. The finite part of the necessary counterterm is scheme dependent and any analysis of the EDM in the EFT framework beyond the leading logarithms is therefore model dependent.

3.8 Summary

In this chaper, we presented the first complete two loop calculation of the electron EDM in the complex two-Higgs doublet model. We calculated the EDM in two separate classes of gauge, and obtained identical gauge-independent results. Our final formula is given in (3.43) which we reproduce here for reference

$$
\frac{d_e}{e} = \frac{\sqrt{2}\alpha G_F m_e}{64\pi^3} \times
$$

$$
\Big[\sum_f (\delta_f^{\mathrm{EM}} + \delta_f^{\mathrm{NC}}) + (\delta_{H^+}^{\mathrm{EM}} + \delta_{H^+}^{\mathrm{NC}} + \delta_{H^+}^{\mathrm{CC}})
$$

$$
+ (\delta_W^{\mathrm{EM}} + \delta_W^{\mathrm{NC}} + \delta_W^{\mathrm{CC}} + \delta_{\mathrm{kite}}^{\mathrm{NC}} + \delta_{\mathrm{kite}}^{\mathrm{CC}}) \Big] , \quad (3.86)
$$

The individual contributions are given in (3.24), (3.25), (3.27), (3.28), (3.29), (3.32), (3.33), (3.36), (3.38), and (3.39). We collect these expressions in a *Mathematica* notebook that is provided as ancillary material.

Compared with the most recent evaluation of the electron EDM by Abe *et. al.* [42], our calculation incorporated the kite contributions in Fig. 3.4. Generically, these new contributions lead to $\mathcal{O}(1)$ corrections to the prediction of the electron EDM (see for example Fig. 3.10), and they are particularly relevant in the Type II and Lepton Specific CHDMs. In the Type II and Lepton Specific C2HDMs there are regions in parameter space where the fermion and gauge loop contributions interfere destructively causing the electron EDM to dip below current limits established by the ACME collaboration. We found that the inclusion of the kite diagrams can significantly shift the location of these cancellations.

In addition to the full result, we derived the leading order asymptotic expansion of the electron EDM near the decoupling limit. The expressions for common types of C2HDMs are provided in Eqs. (4.41)–(**??**). We find that the electron EDM exhibits a logarithmic dependence on the heavy masses. From the point of view of an EFT, the logarithm indicates sensitivity to the UV scale implying that the precise prediction of the EDM cannot be determined in a model independent manner. However, for the case of the C2HDM we find that a large part of the electron EDM near the decoupling limit is reproduced in the infrared.

Furthermore, we have emphasized that the analysis of the electron EDM based on a simple phenomenological parameterization of CP-violating electron Yukawa coupling $-\kappa h \bar{e} i \gamma_5 e$ requires caution since the resulting prediction of the electron EDM is not gauge-invariant.

As explained in Sec. 3.5, the formulae for the electron EDM are easily adaptable for EDMs of light quarks. It would be interesting to have a calculation of EDMs for the heavier bottom and top quarks, which require separate treatment. Also, it would be interesting to perform a full calculation of the electron EDM for other types of 2HDMs without a softly broken $\mathbb{Z}_2$ symmetry, or in which CP is spontaneously broken. We leave these exercises to future work.

58

Barr-Zee	Fermion loop	Charged Higgs loop	Gauge boson loop
Electromagnetic	δ_f^{EM} (3.24)	$\delta_{H^+}^{\mathrm{EM}}$ (3.27)	$\delta_W^{\mathrm{EM}}(\xi)$ (3.30)
Neutral current	δ_f^{NC} (3.25)	$\delta_{H^+}^{\mathrm{NC}}$ (3.28)	$\delta_W^{\mathrm{NC}}(\xi)$ (3.31)
Charged current	–	$\delta_{H^+}^{\mathrm{CC}}$ (3.29)	$\delta_W^{\mathrm{CC}}(\xi)$ (3.35)
Kite			
Neutral current	–	–	$\delta_{\mathrm{kite}}^{\mathrm{NC}}$ (3.38)
Charged current	–	–	$\delta_{\mathrm{kite}}^{\mathrm{CC}}(\xi)$ (3.39)

Table 3.1: Two loop contributions to the electron EDM at $\mathcal{O}(\alpha G_F m_e)$ in the C2HDM in the background field gauge, organized by **rows:** couplings to the main lepton line and **columns:** virtual particle in the loop. Numbers in parenthesis indicate the equation number where the corresponding expression may be found.
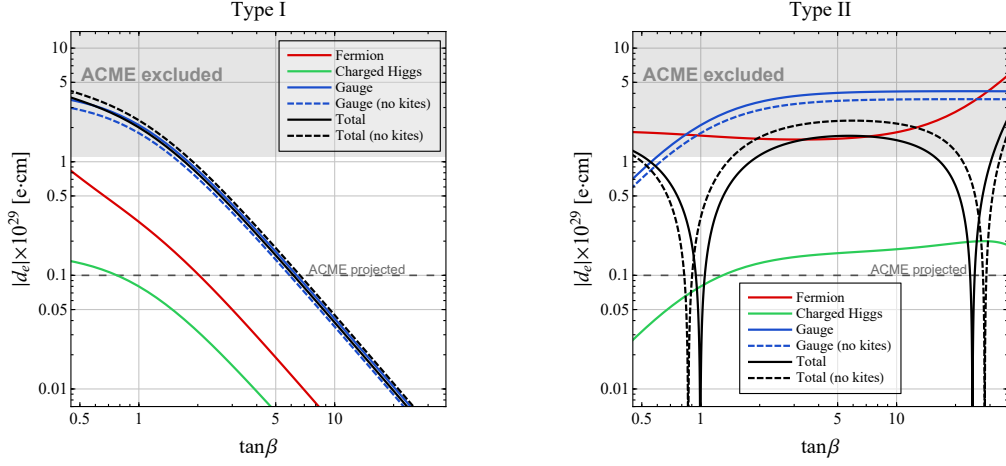
Figure 3.10: Predictions of the electron EDM in the **left:** Type I, and **right:** Type II C2HDM as a function of $\tan\beta$ for the benchmark point in (3.67). The solid black line represents the full result in (3.43). The solid red, green, and blue curves are obtained by summing all contributions within each column of Table 3.1 labeled 'Fermion loop', 'Charged Higgs loop', and 'Gauge boson loop' respectively. The dashed lines are the corresponding contributions without the charged and neutral current kite diagrams in the background field Feynman gauge, $\xi = 1$. The shaded region corresponds to the 90% C.L. exclusion limit from the ACME collaboration. In the future, ACME is expected to improve the bound by at least an order of magnitude. This is indicated by the horizontal dashed line.
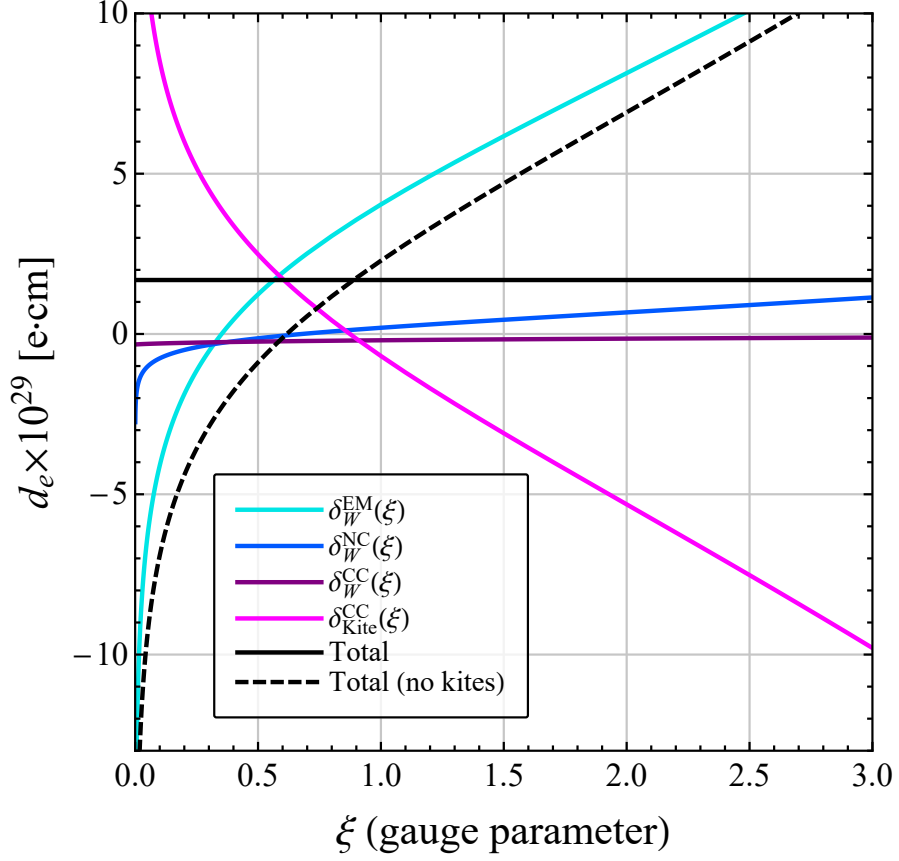
Figure 3.11: Gauge-dependence of individual contributions to the electron EDM listed in the last column of Table 3.1 in the background field gauge for the Type II model at the benchmark point in (3.67) with $\tan \beta = 5$. The horizontal black line is the total gauge-independent EDM in (3.43), and the dashed black curve is the total excluding the charged current $\delta_{\text{kite}}^{\text{CC}}(\xi)$ and neutral current $\delta_{\text{kite}}^{\text{NC}}$ kite contributions.
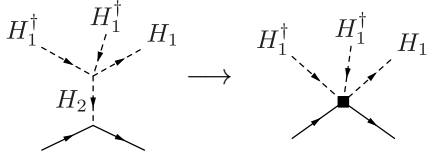
Figure 3.12: Generation of the CP-violating effective operator in (3.81) by integrating out H_2 at tree level.
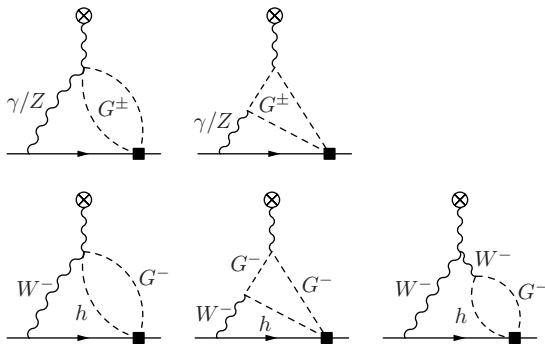
Figure 3.13: Diagrams involving the four-point interactions in (3.83) that contain the leading logarithmic contribution to the electron EDM.
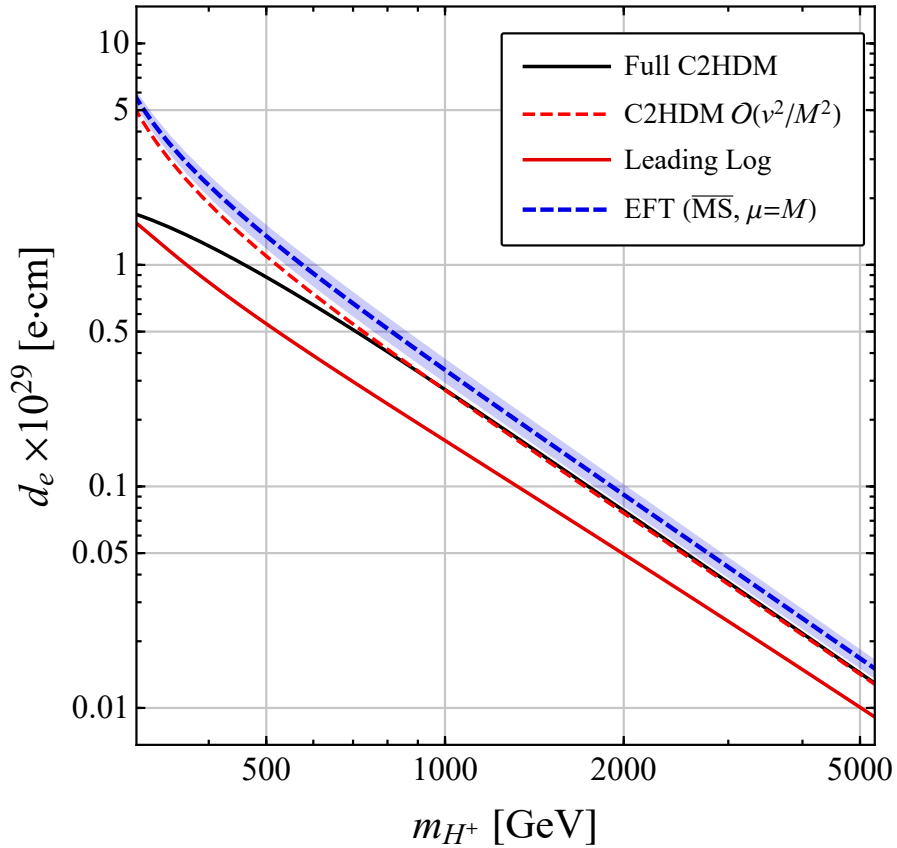
Figure 3.14: Approximations to predictions of the electron EDM in the Type II C2HDM as a function of m_{H^+}, at the benchmark point (3.67) with $\tan\beta = 2$. The black line is the full two loop result in the C2HDM (3.43). The dashed red line is its asymptotic approximation near the decoupling limit through $\mathcal{O}(v^2/M^2)$ given in (4.42). The solid red curve is the leading logarithmic approximation in (3.73) and the dashed blue curve is the EFT result in the $\overline{\mathrm{MS}}$ scheme given by the IR part of (3.74) with $\mu = M$. The shaded blue region is obtained varying the scale between $\mu = M/2$ and $\mu = 2M$.

Chapter 4

Direct and indirect tests of Higgs CP violation

This chapter is based on [401].

4.1 Introduction

Strong experimental constraints exist for the EDM of the electron, $|d_e| <$ 4.1×10^{-30} e cm [397]. Significant improvements by a few orders of magnitude can be obtained in the next one-two decades [127]. Light quark EDMs, as well as the neutron EDM are also tightly constrained by experimental data. Particularly, the neutron EDM $|d_n| < 3.6 \times 10^{-26}$ e cm and the bound is expected to improve by roughly two orders of magnitude in the next decade.

4.2   The CP violating 2HDM

4.2.1   Basics: CP violation in the Higgs potential

Two Higgs Doublet Models generically contain several sources of CPV, some in the Yukawa interactions, and some in the Higgs potential. In this chaper, we only consider new sources of CPV arising in the Higgs potential and we restrict our investigation to softly broken Z_2-symmetric models. Under these assumptions, the most generic potential is given by

$$
\begin{aligned}
V(\Phi_1, \Phi_2) \;=\;& m_{11}^2 \Phi_1^\dagger \Phi_1 + m_{22}^2 \Phi_2^\dagger \Phi_2 - \frac{1}{2}(m_{12}^2 \Phi_1^\dagger \Phi_2 + \text{h.c.}) + \frac{1}{2}\lambda_1(\Phi_1^\dagger \Phi_1)^2 \\
+\;& \frac{1}{2}\lambda_2(\Phi_2^\dagger \Phi_2)^2 + \lambda_3(\Phi_1^\dagger \Phi_1)(\Phi_2^\dagger \Phi_2) + \lambda_4(\Phi_1^\dagger \Phi_2)(\Phi_2^\dagger \Phi_1) \qquad (4.1) \\
+\;& \frac{1}{2}(\lambda_5(\Phi_1^\dagger \Phi_2)^2 + \text{h.c.}) \,, \qquad\qquad\qquad\qquad\qquad\qquad\qquad (4.2)
\end{aligned}
$$

where the two Higgs doublets read

$$
\Phi_1 = \begin{pmatrix} H_1^+ \\ \frac{1}{\sqrt{2}}(v_1 + \rho_1 + iA_1) \end{pmatrix}, \quad \Phi_2 = \begin{pmatrix} H_2^+ \\ \frac{1}{\sqrt{2}}(v_2 + \rho_2 + iA_2) \end{pmatrix}, \qquad (4.3)
$$

with $v_1^2 + v_2^2 = v^2 = 246$ GeV. The allowed complex parameters in the Higgs potential are m_{12}^2 and λ_5. In all generality, there is a phase between the two Higgs vacuum expectation values (VEVs). This phase is, however, not independent from the phases of m_{12}^2 and λ_5. In the following, we will use the freedom to re-phase the Higgs doublets, such to have real VEVs. For a rephasing invariant discussion, see Appendix B and

[260].The minimization of the Higgs potential leads to

$$2m_{11}^2 + \lambda_1 v_1^2 + (\lambda_{345})\, v_2^2 - \frac{v_2}{v_1}\,\mathrm{Re}(m_{12}^2) = 0\,,$$

$$2m_{22}^2 + \lambda_2 v_2^2 + (\lambda_{345})\, v_1^2 - \frac{v_1}{v_2}\,\mathrm{Re}(m_{12}^2) = 0\,, \qquad (4.4)$$

$$v_1 v_2 \lambda_5^i - \mathrm{Im}(m_{12}^2) = 0\,.$$

where we have denoted $\lambda_5 \equiv \lambda_5^r + i\lambda_5^i$ and $\lambda_{345} \equiv \lambda_3 + \lambda_4 + \lambda_5^r$. The last equation indicates that there is a relation between the two phases in the Higgs potential, so that there exists only one independent CPV phase in the softly broken Z_2-symmetric 2HDM.

It is convenient to work in the Higgs basis, i.e. the basis in which only one Higgs doublet acquires a non-zero VEV:

$$H_1 = \begin{pmatrix} G^+ \\ \frac{1}{\sqrt{2}}(v + S_1 + iG^0) \end{pmatrix}, \quad H_2 = \begin{pmatrix} H^+ \\ \frac{1}{\sqrt{2}}(S_2 + iA) \end{pmatrix}. \qquad (4.5)$$

The relation between the Higgs and the gauge basis is a rotation by an angle β, defined via $\tan\beta \equiv t_\beta \equiv v_2/v_1$:

$$\begin{pmatrix} H_1 \\ H_2 \end{pmatrix} = R_\beta^T \begin{pmatrix} \phi_1 \\ \phi_2 \end{pmatrix}. \qquad (4.6)$$

So for example, A is related to A_1 and A_2 in (4.3) by $A = -s_\beta A_1 + c_\beta A_2$, and the physical charged Higgs $H^\pm = -s_\beta H_1^\pm + c_\beta H_2^\pm$ ($s_\beta \equiv \sin\beta$, $c_\beta \equiv \cos\beta$). We can define a variable which characterizes the mass scale of the non-Standard Model Higgs bosons [287]:

$$\nu \equiv \frac{\mathrm{Re}(m_{12}^2)}{2v_1 v_2} = \frac{\mathrm{Re}(m_{12}^2)}{2v^2 s_\beta c_\beta}\,. \qquad (4.7)$$

66

The mass of the charged Higgs is related to this parameter as

$$m_{H^\pm}^2 = \frac{v^2}{2}(2\nu - \lambda_4 - \lambda_5^r). \tag{4.8}$$

Because of CP violation, all three neutral scalars will mix. In the (ρ_1, ρ_2, A) basis, the 3×3 neutral mass matrix is given by

$$\mathcal{M}^2 = v^2 \begin{pmatrix} \lambda_1 c_\beta^2 + \nu s_\beta^2 & (\lambda_{345} - \nu)c_\beta s_\beta & -\frac{1}{2}s_\beta \lambda_5^i \\ (\lambda_{345} - \nu)c_\beta s_\beta & \nu c_\beta^2 + \lambda_2 s_\beta^2 & -\frac{1}{2}c_\beta \lambda_5^i \\ -\frac{1}{2}s_\beta \lambda_5^i & -\frac{1}{2}c_\beta \lambda_5^i & \nu - \lambda_5^r \end{pmatrix}. \tag{4.9}$$

This mass matrix is diagonalized by a rotation matrix $\mathcal{R}$ that is given by the product of three rotations on the x, y, and z axes by the angles α_3, α_2, and $\alpha_1 \equiv \alpha + \pi/2$, respectively:

$$\mathcal{R}\mathcal{M}^2\mathcal{R}^T = \mathcal{M}_{\text{diagonal}}^2 \quad \text{with} \tag{4.10}$$

$$\mathcal{R} \equiv R_3 R_2 R_1 = R_x^T(\alpha_3) R_y(\alpha_2) R_z^T(\alpha + \pi/2)$$
$$= \begin{pmatrix} -s_\alpha c_{\alpha_2} & c_\alpha c_{\alpha_2} & s_{\alpha_2} \\ s_\alpha s_{\alpha_2} s_{\alpha_3} - c_\alpha c_{\alpha_3} & -s_\alpha c_{\alpha_3} - c_\alpha s_{\alpha_2} s_{\alpha_3} & c_{\alpha_2} s_{\alpha_3} \\ s_\alpha s_{\alpha_2} c_{\alpha_3} + c_\alpha s_{\alpha_3} & s_\alpha s_{\alpha_3} - c_\alpha s_{\alpha_2} c_{\alpha_3} & c_{\alpha_2} c_{\alpha_3} \end{pmatrix}. \tag{4.11}$$

The physical CP violating states (h_1, h_2, h_3) can be related to the gauge eigenstates (ρ_1, ρ_2, A) in (4.3) as well as to the Higgs fields in the Higgs basis (S_1, S_2, A) in (4.5) through:

$$\begin{pmatrix} h_1 \\ h_2 \\ h_3 \end{pmatrix} = \mathcal{R} \begin{pmatrix} \rho_1 \\ \rho_2 \\ A \end{pmatrix} = \mathcal{R}R_z(\beta) \begin{pmatrix} S_1 \\ S_2 \\ A \end{pmatrix}, \tag{4.12}$$

where h_1 represents the lightest Higgs with mass of 125 GeV. The 125 GeV Higgs boson has a CP odd component in the case of $\alpha_2 \neq 0$. The familiar case of CP conservation is realized for $\alpha_2 = \alpha_3 = 0$ where the two physical scalar Higgs bosons, (h, H), do not mix with the physical pseudoscalar, A, and the rotations between the Higgs, physical, and gauge bases are given by

$$
\begin{pmatrix} h \\ -H \\ A \end{pmatrix} \equiv R_z^T(\alpha + \pi/2) \begin{pmatrix} \rho_1 \\ \rho_2 \\ A \end{pmatrix} = R_z^T(\alpha + \pi/2) R_z(\beta) \begin{pmatrix} S_1 \\ S_2 \\ A \end{pmatrix}. \tag{4.13}
$$

In a generic case of CPV, $\alpha_2 \neq 0$ and $\alpha_3 \neq 0$. These angles will depend on Lagrangian parameters and will be related to each other because of the presence of only one independent CPV phase in the Higgs potential of a approximate Z_2-symmetric theory (see next section).

4.2.2 Conditions on the Higgs potential and free parameters

Depending on the quartic couplings in (4.1), the potential can be minimized by a field configuration that is different from the electroweak (EW) minimum. First we need the potential to be bounded from below, and, therefore, the potential need to be positive when $|\phi_1|, |\phi_2| \to \infty$, which lead to the following condition [198]

$$
\lambda_1 > 0, \ \lambda_2 > 0, \ \lambda_3 + \min(0, \lambda_4 - |\lambda_5|) > -\sqrt{\lambda_1 \lambda_2}. \tag{4.14}
$$

In addition, the quartic couplings cannot be too large, such to have a pertur-

bative theory. In particular, we impose[1]

$$|\lambda_i| < 4\pi. \tag{4.15}$$

Furthermore, we require the EW minimum to be the deepest minimum of the potential. Following the method developed in [289, 290] for the case of CP conservation, we compute the several minima of the potential in the most general case of CP violation. The details of our calculation are reported in Appendix B. We find the following conditions on the parameters of the potential:

$$m_{12}^2 \cos(\delta_1 + \delta_2) \cos(\delta_1) > 0, \quad -m_{12}^2 \sin(\delta_1 + \delta_2) \sin(\delta_1) > 0, \quad (m_{11}^2 - k^2 m_{22}^2)(t_\beta - k) > 0, \tag{4.16}$$

where we have used the two basis independent phases, δ_1 and δ_2 defined as $\delta_1 = \arg[m_{12}^2(\lambda_5^*)^{1/2}]$ and $\delta_2 = \arg[v_1^* v_2 (m_{12}^2)^* \lambda_5]$, and where we have defined $k \equiv \sqrt[4]{\lambda_1/\lambda_2}$.

These two conditions can be rewritten using the phase convention of our chaper as

$$|\lambda_5| \sin^2 \frac{\theta_\lambda}{2} + \nu > 0, \quad \frac{1}{2} \left(\mathrm{Re}(\lambda_5) + |\lambda_5| \right) - \nu < 0, \quad (m_{11}^2 - k^2 m_{22}^2)(t_\beta - k) > 0, \tag{4.17}$$

where we have defined $\theta_\lambda \equiv \arg(\lambda_5)$.

In the following, instead of using the quartic couplings, λ_i, we will investigate the phenomenology in terms of the more physical parameters[2]

$$m_{h_1}, m_{h_2}, m_{h_3}, m_{H^\pm}, \alpha \text{ (or } x), \alpha_2, \alpha_3, \nu, \tan\beta, \tag{4.18}$$

where, for a matter of convenience, we have defined the x mixing angle as $x = \alpha - \beta + \pi/2$. In the next section, we will show that the limit $x, \alpha_2, \alpha_3 \to 0$ corresponds to a 125 GeV

---

[1]This condition gives a rough estimate of the perturbative unitarity constraint. Depending on the relative dimension of the quartic couplings, the bound on each coupling can be more stringent. For a full recent analysis see [85].

[2]For convenience, in Sec. 4.5.1, instead of using the ν parameter, we will use the quartic coupling λ_2.

Higgs boson with SM properties. The $x \to 0$ limit is the so-called alignment limit in the case of CP conservation. In Appendix C, we report the relations between these physical parameters and the quartic couplings, λ_i. One should note that only eight of these nine parameters are independent. In fact, the CPV phases α_2, α_3 are related since there is only one independent phase in the Higgs potential in (4.1). Diagonalizing the neutral mass matrix leads to a relation between the mixing angles α_2, α_3 and the masses of the three scalars, as well as α and β, but not ν:

$$\alpha_2 = -\arcsin\left\{ \frac{\Delta m_{23}^2 \sin(2\alpha_3) \cot(\alpha + \beta)}{2(m_{h_1}^2 - m_{h_2}^2 \sin^2\alpha_3 - m_{h_3}^2 \cos^2\alpha_3)} \right\}, \tag{4.19}$$

where $\Delta m_{ij}^2 \equiv m_{h_i}^2 - m_{h_j}^2$. Our relatively good knowledge of the phenomenology of the 125 GeV Higgs boson motivates us keeping α_2 as free parameter in (4.18) and determining α_3 in terms of α_2 and the other free parameters:

$$\alpha_3 = -\arctan\left\{ \frac{\csc(\alpha_2)\csc(\alpha+\beta)}{2\Delta m_{12}^2}\left[\cos(\alpha+\beta)\Delta m_{23}^2 \right.\right.$$
$$\left.\left. \pm\sqrt{\left(\Delta m_{23}^2\right)^2 \cos^2(\alpha+\beta) - 4\Delta m_{12}^2 \Delta m_{13}^2 \sin^2(\alpha_2)\sin^2(\alpha+\beta)} \right] \right\}. $$
$$\tag{4.20}$$

The two solutions correspond to having h_2 or h_3 as mainly CP even, respectively. For the numerical analysis of our chaper (see Secs. 4.3, 4.5), we will choose the solution for which h_2 is mainly CP even. Note that not all spectra and mixing angles in (4.18) are physical, and some do not lead to a solution to the equation above.

4.2.3 Couplings of the physical Higgs bosons

The coupling of the Higgs bosons to the weak gauge bosons is given by

$$\mathcal{L}_{\text{gauge}} = \frac{g^2 v}{4} \sum_k g_{h_k VV} \left[2W_\mu^+ W^{\mu-} + \frac{1}{\cos^2\theta} Z_\mu Z^\mu \right] h_k + \frac{g}{2\cos\theta} Z_\mu \sum_{i<j} g_{Zh_i h_j} \left[h_i \partial^\mu h_j \right]$$
$$+ \frac{g}{2} \sum_i c_{iW} W_\mu^\pm (H^\mp \overleftrightarrow{\partial^\mu} h_i) \,, \tag{4.21}$$

with θ the Weinberg angle, and k denoting the several Higgs bosons, from the lightest to the heaviest, $k = 1, 2, 3$. We can express the reduced couplings in terms of the rotation matrix in (4.10):

$$g_{h_k VV} = \mathcal{R}_{kj}(R_z^\beta)_{j1} = \mathcal{R}_{k1} c_\beta + \mathcal{R}_{k2} s_\beta \,, \tag{4.22}$$

$$g_{Zh_i h_j} = \epsilon_{ijk} \, g_{h_k VV} \,, \tag{4.23}$$

$$c_{iW} = (i(\sin\beta \mathcal{R}_{i1} - \cos\beta \mathcal{R}_{i2}) + \mathcal{R}_{i3})(p_\mu^i - p_\mu^\mp) \,, \tag{4.24}$$

with ϵ_{ijk} the antisymmetric tensor with $\epsilon_{123} = 1$. p^i and $p^\pm$ are the momenta of h_i and $H^\pm$, respectively. As we will discuss in Sec. 4.5, Eq. (4.23) shows a correlation between the $g_{Zh_i h_j}$ and the $g_{h_k VV}$ couplings (e.g. $g_{Zh_2 h_3} = g_{h_1 ZZ}$). It is also interesting to note that the charged and neutral Higgs bosons share the coupling to gauge bosons, satisfying the sum rules

$$\sum_i g_{h_i VV} = 1, \quad \sum_i |\bar{c}_{iW}|^2 = 2 \,. \tag{4.25}$$

Close to the alignment and CP conserving limits $(x, \alpha_2 \to 0)$, these reduced couplings can be written as:

$$g_{h_1 VV} \simeq 1 - \frac{x^2 + \alpha_2^2}{2}, \quad g_{h_2 VV} \simeq -x - \alpha_2 \alpha_3, \quad g_{h_3 VV} \simeq -\alpha_2 + x\alpha_3.$$
$$\bar{c}_{1W} \simeq -ix + \alpha_2, \quad \bar{c}_{2W} \simeq i\left(-1 + \frac{x^2}{2}\right) + \alpha_3, \quad \bar{c}_{3W} \simeq 1 - \frac{\alpha_2^2}{2} + i\alpha_3 \,, \tag{4.26}$$

71

where we have defined $c_{iW} \equiv \bar{c}_{iW}(p_\mu^i - p_\mu^\mp)$. These expressions indicate that the most massive mostly pseudoscalar Higgs boson can couple to the W and the Z boson, thanks to CPV. CPV also allows the $h_1 W^\pm H^\mp$ and $h_2 VV$ couplings in the case of no mixing x.

The several neutral Higgs bosons couple to fermions as

$$\mathcal{L}_{\text{Yuk}} = -\frac{m_{f_i}}{v} \sum_k (\bar{f}_i \kappa_f^{(k)} f_i + i \bar{f}_i \gamma_5 \tilde{\kappa}_f^{(k)} f_i) h_k \,, \tag{4.27}$$

where i is the flavor index, $i = 1, 2, 3$. The reduced couplings $\kappa_f^{(k)}$ and $\tilde{\kappa}_f^{(k)}$ are independent on the fermion flavor and, in the Type I and II 2HDM, are given by

$$
\begin{array}{ccc}
 & \text{Type-I} & \text{Type-II} \\[6pt]
\kappa_u^{(1)} & \dfrac{c_{\alpha_2}c_\alpha}{s_\beta} & \dfrac{c_{\alpha_2}c_\alpha}{s_\beta} \\[10pt]
\kappa_{d,\ell}^{(1)} & \dfrac{c_{\alpha_2}c_\alpha}{s_\beta} & -\dfrac{c_{\alpha_2}s_\alpha}{c_\beta} \\[10pt]
\tilde{\kappa}_u^{(1)} & -\dfrac{s_{\alpha_2}}{t_\beta} & -\dfrac{s_{\alpha_2}}{t_\beta} \\[10pt]
\tilde{\kappa}_{d,\ell}^{(1)} & \dfrac{s_{\alpha_2}}{t_\beta} & -s_{\alpha_2}t_\beta \\[10pt]
\kappa_u^{(2)} & -\dfrac{c_{\alpha_3}s_\alpha + c_\alpha s_{\alpha_2}s_{\alpha_3}}{s_\beta} & -\dfrac{c_{\alpha_3}s_\alpha + c_\alpha s_{\alpha_2}s_{\alpha_3}}{s_\beta} \\[10pt]
\kappa_{d,\ell}^{(2)} & -\dfrac{c_{\alpha_3}s_\alpha + c_\alpha s_{\alpha_2}s_{\alpha_3}}{s_\beta} & \dfrac{s_{\alpha_2}s_{\alpha_3}s_\alpha - c_{\alpha_3}c_\alpha}{c_\beta} \\[10pt]
\tilde{\kappa}_u^{(2)} & -\dfrac{c_{\alpha_2}s_{\alpha_3}}{t_\beta} & -\dfrac{c_{\alpha_2}s_{\alpha_3}}{t_\beta} \\[10pt]
\tilde{\kappa}_{d,\ell}^{(2)} & \dfrac{c_{\alpha_2}s_{\alpha_3}}{t_\beta} & -c_{\alpha_2}s_{\alpha_3}t_\beta \\[10pt]
\kappa_u^{(3)} & \dfrac{s_{\alpha_3}s_\alpha - c_{\alpha_3}c_\alpha s_{\alpha_2}}{s_\beta} & \dfrac{s_{\alpha_3}s_\alpha - c_{\alpha_3}c_\alpha s_{\alpha_2}}{s_\beta} \\[10pt]
\kappa_{d,\ell}^{(3)} & \dfrac{s_{\alpha_3}s_\alpha - c_{\alpha_3}c_\alpha s_{\alpha_2}}{s_\beta} & \dfrac{c_{\alpha_3}s_{\alpha_2}s_\alpha + c_\alpha s_{\alpha_3}}{c_\beta} \\[10pt]
\tilde{\kappa}_u^{(3)} & -\dfrac{c_{\alpha_2}c_{\alpha_3}}{t_\beta} & -\dfrac{c_{\alpha_2}c_{\alpha_3}}{t_\beta} \\[10pt]
\tilde{\kappa}_{d,\ell}^{(3)} & \dfrac{c_{\alpha_2}c_{\alpha_3}}{t_\beta} & -c_{\alpha_2}c_{\alpha_3}t_\beta
\end{array}
\tag{4.28}
$$

It is straightforward to recover the common Higgs couplings to quarks and leptons in a Type-I and II 2HDM in the CP conserving case for $\alpha_2, \alpha_3 \to 0$.

For completeness, below we also report the couplings of the charged Higgs bosons to fermions. These couplings are not affected by the presence of CPV in the

Higgs potential and are given by the common expressions

$$\mathcal{L}_{yuk}^{H^\pm} = c_{ij}^d(\bar{u}_i P_R d_j)H^+ + c_{ij}^u(\bar{u}_i P_L d_j)H^+ + c_{ii}^{L\ell}(\bar{\nu}_i P_R \ell_i)H^+ + h.c., \qquad (4.29)$$

$$c_{ij}^d = -\sqrt{2}\frac{m_{d_j}}{v}V_{ij}\frac{1}{\tan\beta}, \quad c_{ij}^u = \sqrt{2}\frac{m_{u_i}}{v}V_{ij}\frac{1}{\tan\beta}, \quad c_{ii}^\ell = -\sqrt{2}\frac{m_{\ell_i}}{v}\frac{1}{\tan\beta} \quad \text{(Type-I)},$$

$$c_{ij}^d = \sqrt{2}\frac{m_{d_j}}{v}V_{ij}\tan\beta, \quad c_{ij}^u = \sqrt{2}\frac{m_{u_i}}{v}V_{ij}\frac{1}{\tan\beta}, \quad c_{ii}^\ell = \sqrt{2}\frac{m_{\ell_i}}{v}\tan\beta, \quad \text{(Type-II)},$$

where V_{ij} are the elements of the CKM matrix.

4.3 Probing the 125 GeV Higgs CP-odd component

4.3.1 Precision Higgs measurements of the Higgs couplings

Precision measurements of the Higgs rates lead to relevant insights on the CP nature of the Higgs boson. The modified Higgs couplings to fermions and gauge bosons result in Higgs rates deviating sizably from the SM predictions. In this section, we study how present and future measurements of Higgs rates can bound the parameter space of the complex 2HDM.

We perform a fit of the 125 GeV Higgs rates. All rates can be computed in a straightforward manner as a rescaling of the corresponding SM rates, except the rate of loop-induced processes for the Higgs decaying into photons and gluons and for the Higgs produced in gluon fusion. For these processes we have

$$\frac{\Gamma(h_1 \to gg)}{\Gamma(h_1 \to gg)^{\text{SM}}} \approx \frac{\sigma_{gg \to h_1}}{\sigma_{gg \to h_1}^{SM}} \approx 1.11\kappa_t^2 - 0.12\kappa_t\kappa_b + 0.008\kappa_b^2 + 2.59\tilde{\kappa}_t^2 - 0.20\tilde{\kappa}_t\tilde{\kappa}_b + 0.009\tilde{\kappa}_b^2,$$

$$\frac{\Gamma(h_1 \to \gamma\gamma)}{\Gamma(h_1 \to \gamma\gamma)^{\text{SM}}} \approx (1.28 g_{h_1 VV} - 0.28\kappa_t)^2 + 0.18\tilde{\kappa}_t^2, \qquad (4.30)$$

where, for a matter of simplicity, we have dropped the (1) on the κ couplings. The first approximate equality is only valid at NLO.

As shown by these two expressions, a CP odd coupling of the Higgs to top quarks can induce a large NP effect in the gluon fusion production cross section, as well as in the Higgs decay to two photons. The rates are symmetric under the exchange $\alpha_2 \to -\alpha_2$.

In Fig. 4.1, we show the results of our fit. For the present bound, we use up to ~ 137 fb^{-1} of proton-proton collision data collected at $\sqrt{s} = 13$ TeV. For our analysis, we naively combine the ATLAS measurements for the Higgs rates reported in Tab. 3 of [2] and the CMS measurements reported in Tab. 4 of [1]. These include VBF, gluon fusion, Vh and $t\bar{t}h$ production, followed by the decay into $\gamma\gamma, ZZ^*, WW^*, \tau\bar{\tau}, b\bar{b}$. The correlation between the several measurements has been included in our χ^2 fit, as well. The blue, yellow, and green regions shown in Fig. 4.1 represent the $1\sigma, 2\sigma, 3\sigma$ regions, respectively, as obtained from the requirement $\Delta\chi^2 \lesssim 2.3, 6, 11.8$. The first row for Type I and $\tan\beta = 1$ shows a slight preference for $x \lesssim 0$. The large-dimensional fit makes extracting a single reason difficult. Broadly speaking, small negative values of x lead to the suppression of $\mathcal{B}(h \to b\bar{b})$ and, therefore, to the enhancement of some well-measured channels like $h \to VV$. This pattern seems to be slightly favored by data (see also Appendix D). Overall, large values of CPV angle α_2 ($\lesssim 0.3$) are still allowed by the measurement of the Higgs fits, particularly at low values of $\tan\beta$ (see the left panels of the figure).

Future projections on measurements at ATLAS and CMS are reported in Tab. 35 of [153]. The darker blue region in Fig. 4.1 shows the HL constraint that we obtain combining ATLAS and CMS projections and taking the more conservative assumption

to systematic uncertainties (S1 scenario in the chaper). From the figure, we can observe that Higgs rate measurements alone allow a sizable value for the CPV angle α_2 up to ~ 0.15. Deviations from the $x \sim 0$ limit are instead more constrained with $|x| \gtrsim 0.1$ almost entirely excluded, independently on the value of $\tan \beta$.

4.3.2 LHC direct searches for a CPV Higgs component

4.3.2.1 LHC studies for CPV Higgs couplings to massive gauge bosons

So far, the ATLAS and CMS collaborations have focused on setting bounds on higher dimensional operators contributing to the Higgs-di boson interactions. In particular, searches for $h \to ZZ^* \to 4\ell$ [16, 309, 413], $h \to WW^* \to \ell\nu\ell\nu$ [16, 309], $h \to \tau\bar{\tau}$ with the Higgs produced in vector boson fusion [25], and $h \to b\bar{b}$ with the Higgs produced in association with a vector boson [310] have been used to set a bound on the Wilson coefficient of the CP conserving and CP violating operators

$$\mathcal{L}_{\text{eff}} \supset -\frac{\tilde{g}_{hZZ}}{2} h Z_{\mu\nu} \tilde{Z}^{\mu\nu} - \tilde{g}_{hWW} h W_{\mu\nu}^+ \tilde{W}^{-\mu\nu} \,, \tag{4.31}$$

where we have defined $\tilde{V}_{\mu\nu} \equiv \frac{1}{2}\epsilon_{\mu\nu\alpha\beta}V^{\alpha\beta}$. These operators are generated at one loop in our 2HDM. The Wilson coefficients will be suppressed by the CP-odd component of the Higgs boson. We have computed the top loop contribution to the Wilson coefficients in the $m_t \gg m_h, m_{Z,W}$ limit. We find that in both Type I and II 2HDMs

$$\tilde{g}_{hZZ} = \frac{\sin\alpha_2}{\tan\beta} \frac{3e^2}{16\pi^2} \frac{1}{v} \frac{\frac{1}{12} + \frac{2}{3}\sin^2\theta_W(-\frac{1}{2} + \frac{2}{3}\sin^2\theta_W)}{\cos^2\theta_W \sin^2\theta_W} \simeq -\frac{\sin\alpha_2}{\tan\beta} \frac{1}{8 \times 10^5 \text{ GeV}} \,, \tag{4.32}$$

$$\tilde{g}_{hWW} = \frac{\sin\alpha_2}{\tan\beta} \frac{3e^2}{128\pi^2} \frac{1}{v} \frac{1}{\sin^2\theta_W} \simeq \frac{\sin\alpha_2}{\tan\beta} \frac{1}{7 \times 10^5 \text{ GeV}} \,, \tag{4.33}$$

where θ_W is the Weinberg angle. We have checked that the full calculation without the $m_t \gg m_h, m_{Z,W}$ approximation produces a similar numerical result at the $10-20\%$ level. The lighter fermions also contribute to the effective hZZ and hWW couplings. However, we cannot use the heavy quark limit to compute these contributions. In the Type II 2HDM, the tau and bottom contributions are expected to scale as $\sim \frac{m_f^2}{v^3} \frac{e^2}{4\pi^2} \sin\alpha_2 \tan\beta$, where m_f is the fermion mass. Therefore, they are subdominant in the small $\tan\beta$ regime. In the Type I 2HDM, they are always subdominant since the reduced Higgs CP odd coupling is suppressed by $\tan\beta$ ($\tilde{\kappa}_{d,\ell}^{(1)} = \frac{\sin\alpha_2}{\tan\beta}$, see (4.28)).

Several CMS and ATLAS analyses study either the decay of the Higgs to WW and ZZ [9, 14, 413] or the VBF production of the Higgs [17] to set constraints on the operators in (4.31). The CMS analysis [413] for the Higgs to 4-lepton final state combines several Higgs production (VBF, VH) and decay modes ($WW, ZZ, Z\gamma, \gamma\gamma \to 4\ell$) and sets the most stringent bound on these Wilson coefficients. The analysis is based on ~ 80 fb^{-1} 13 TeV data combined with 7 TeV and 8 TeV data. From table 7 of [413], we obtain $\tilde{g}_{hZZ} \lesssim \frac{1}{10^3 \text{ GeV}}$ at the 95% C.L. (combination of on-shell and off-shell measurements). This number is obtained combining the several channels and assuming $\tilde{g}_{hZZ} = \tilde{g}_{hWW}$. A result to the same order of magnitude is obtained from an ATLAS analysis of VBF $H \to ZZ \to 4\ell$ with 139fb^{-1} of 13 TeV data[6]. As we can observe comparing this bound to the prediction of our model in (4.32) and (4.33), the CPV 2HDM predicts an anomalous coupling that is more than two orders of magnitude smaller than what is probed experimentally.

The HL-LHC will be able to set more stringent constraints on the anomalous

77

$hZ\tilde{Z}$ and $hW\tilde{W}$ couplings by exploiting the Higgs production in association with a massive gauge boson, as well as VBF production: $\tilde{g}_{hZZ} \lesssim \frac{1}{8 \times 10^3 \text{ GeV}}$ [153]. This future bound is still not stringent enough to constraint regions of parameter space of the complex 2HDM.

4.3.2.2 LHC studies for CPV Higgs couplings to fermions

Direct searches for CP-odd couplings of the Higgs to fermions also exist [3, 24, 32, 438].

The most stringent constraint on the CP-odd coupling of the Higgs to tops comes from the ATLAS study [24] and from the recent CMS analysis [3]. The ATLAS analysis uses 139 fb^{-1} data recorded at $\sqrt{s} = 13$ TeV center-of-mass energy. Higgs bosons are identified via the di-photon decay channel and are produced with a top quark pair or single top quark. The analysis sets a bound on the CP odd Higgs-top coupling, assuming that all the other Higgs couplings are SM-like. In our 2HDM, this reads

$$\left| \frac{\tilde{\kappa}_u^{(1)}}{\kappa_u^{(1)}} \right| = \left| \frac{\tan \alpha_2 \cos \beta}{\cos \alpha} \right| \lesssim 0.93 \quad \text{at} \quad 95\% \text{ C.L.} \quad (\text{Type I,II}) . \qquad (4.34)$$

The CMS analysis [3] obtains a similar bound combining Higgs decays into $ZZ, \gamma\gamma, WW, \tau\tau$ with the Higgs produced in association with one or two tops. This bound constrains part of the parameter space of the complex 2HDM and is complementary to the bound we get from the precision measurement of Higgs rates (see Sec. 4.3.1). In particular, the blue regions in Fig. 4.1 produce a too large value for $\tilde{\kappa}_u^{(1)}$. However, we observe that this direct bound on CPV is still relatively weak if compared

to the bound from Higgs coupling measurements.

The CMS collaboration has also performed a search for a possible CP odd coupling of the Higgs to tau leptons using 137 fb^{-1} data recorded at $\sqrt{s} = 13$ TeV center-of-mass energy [438]. The study of the angular correlation between the decay planes of two taus produced in Higgs decays lead to the observed bound[3]

$$\left|\frac{\tilde{\kappa}_\ell^{(1)}}{\kappa_\ell^{(1)}}\right| = \left|\frac{\tan\alpha_2\cos\beta}{\cos\alpha}\right|, \left|\frac{\tan\alpha_2\sin\beta}{\sin\alpha}\right| \lesssim 0.87 \ \text{ at } \ 95\% \text{ C.L.} \quad (\text{Type} \ \ \text{I,II}). \quad (4.35)$$

The corresponding bound is shown in red in Fig. 4.1. For a Type II model, this CMS search for Higgs CPV sets a constraint that is comparable and complementary to the present bound from Higgs coupling measurements, as long as the value of $\tan\beta$ is not too small (middle and right panels in the figure). NP regions of parameter space that are allowed by Higgs coupling measurements are excluded by the CMS search and viceversa.

4.3.2.3 Additional channels: phenomenological studies and HL projections

Additional phenomenological studies have been performed to set a bound on the CP-odd component of the 125 GeV Higgs boson.

A promising channel is the decay $h \to \bar{\tau}\tau$. The τ decay modes studied are $\tau^\pm \to \rho^\pm\nu$, $\rho^\pm \to \pi^\pm\pi^0$ [81, 163, 272, 299] and $\tau^\pm \to \pi^\pm\nu$ [107, 265]. The ATLAS collaboration has performed a study of the performance of the $\tau^\pm \to \rho^\pm\nu$, $\rho^\pm \to \pi^\pm\pi^0$ channel at the HL-LHC [173]. The angle between the planes spanned by the pion pairs is used to determine the CP nature of the Higgs. Several scenarios for π^0 reconstruction are considered and, in the most optimistic scenario, a bound on the Higgs-tau CP

---

[3]The present observed bound is a bit weaker than the expected bound that is ~ 1.1.

violating coupling

$$\left|\frac{\tilde{\kappa}_\ell^{(1)}}{\kappa_\ell^{(1)}}\right| = \left|\frac{\tan\alpha_2\cos\beta}{\cos\alpha}\right|, \left|\frac{\tan\alpha_2\sin\beta}{\sin\alpha}\right| \lesssim 0.7 \text{ at } 95\% \text{ C.L.} \quad \text{(Type I,II)} \quad (4.36)$$

can be set. This bound has been rescaled to obtain the reach of the High-Energy (HE) LHC ($\sqrt{s} = 27$ TeV) with 15 ab^{-1} luminosity [153]: $\left|\tilde{\kappa}_\ell^{(1)}\big/\kappa_\ell^{(1)}\right| \lesssim 0.08$. Combining the several tau decay modes, the CMS collaboration shows a projected bound at the level of

$$\left|\frac{\tilde{\kappa}_\ell^{(1)}}{\kappa_\ell^{(1)}}\right| = \left|\frac{\tan\alpha_2\cos\beta}{\cos\alpha}\right|, \left|\frac{\tan\alpha_2\sin\beta}{\sin\alpha}\right| \lesssim 0.3 \text{ at } 95\% \text{ C.L.} \quad \text{(Type I,II)} \quad (4.37)$$

(see the supplementary material of [438]).

Additional channels might be considered to set a bound on the CPV component of the 125 GeV Higgs boson: **(1)** A study for $pp \to t\bar{t}h, h \to b\bar{b}$ can unveil the presence of a CPV Higgs-top coupling. [245] shows that analyzing HL-LHC boosted Higgs events with the Higgs-tagged via the BDRS algorithm [138] can lead to a bound at the level of $|\tilde{\kappa}_u^{(1)}/\kappa_u^{(1)}| \lesssim 0.7$. A similar analysis done at a 100 TeV proton collider with 30/ab data would improve the bound to $|\tilde{\kappa}_u^{(1)}/\kappa_u^{(1)}| \lesssim 0.03$. The sizable improvement is mainly due to the much larger $t\bar{t}h$ statistics at a 100 TeV proton collider. **(2)** A CPV Higgs-top coupling can affect the distribution of the jets produced in association with the Higgs boson in gluon fusion production. Ref. [203] has studied the Higgs plus two jet final state followed by the Higgs decay into a pair of tau leptons and found that $|\tilde{\kappa}_u^{(1)}/\kappa_u^{(1)}| \gtrsim 0.3$ can be excluded at the 95% C.L. with ~ 500 fb^{-1} 14 TeV data. **(3)** Furthermore, one can use kinematical distributions from the $h \to \gamma\gamma$ decay to set a bound on the CPV Higgs-photon coupling. Ref. [122] has studied the kinematic distribution of the two

electron-positron pairs produced from the photons undergoing nuclear conversion. This is a difficult measurement and CPV mixing angles of order unity can be probed at the HL-LHC. **(4)** Finally, the CPV in the $hZ\gamma$ vertex can be probed by interference between the gluon fusion Higgs production $gg \to h \to \gamma Z, \; Z \to \ell^+\ell^-$ and the background $gg \to \gamma Z, \; Z \to \ell^+\ell^-$ [219]. It can also be probed measuring the forward-backward asymmetry of the charged lepton in the three-body Higgs decay $h \to \ell^+\ell^-\gamma$ [164]. However, the two effects are un-observably small for the HL-LHC.

Several channels have been studied also in the context of future e^+e^-, muon, and photon colliders. For a recent review, see [255].

4.4 Constraints from precision measurements

4.4.1 EDM

New CPV phases are generically very well constrained by searches for electric dipole moments (EDMs). At present, the strongest bound on an elementary EDM by the JILA electron EDM experiment, comes from measurements of trapped HfF$^+$ molecular ions giving at 90% C.L. [397].

$$|d_e| < 4.1 \times 10^{-30} \, e \, \text{cm} ., \tag{4.38}$$

which is a factor of 2.4 lower than the previous strongest bound of the ACME collaboration [75].

Significant improvements by a few orders of magnitude can be obtained in the next one-two decades [127] (see also [55]). Additional bounds might come from the

81

neutron EDM, that is bounded at 90% C.L. by [43]

$$|d_n| < 1.8 \times 10^{-26}\,e\,\mathrm{cm}\,. \qquad (4.39)$$

Future experiments utilizing ultra cold neutron sources are expected to produce results with sensitivity of $\mathcal{O}(10^{-27})$ e cm in the next ~ 5 years [127, 212]. Slightly weaker constraints arise from the proton EDM and from the EDM of diamagnetic atoms and molecules like the mercury [252]

$$|d_p| < 10^{-25}\,e\,\mathrm{cm}\,, \qquad |d_{Hg}| < 7.4 \times 10^{-30}\,e\,\mathrm{cm}. \qquad (4.40)$$

Four orders of magnitude improvement in the proton EDM is may be possible in the coming decade [58].

In [67], we presented the first complete calculation of the electron EDM by systematically accounting for all Feynman diagrams that contribute at two loop order. In particular, we added the full contribution of kyte diagrams. Because of the many contributions, some of which scaling in the same way in the CPV parameters, cancellations can happen in particular regions of parameter space. The final expression for the electron EDM is rather complicated, but it simplifies to

$$\text{Type I:} \quad d_e = -1.06 \times 10^{-27} e\,\mathrm{cm} \times \left(\frac{1\,\mathrm{TeV}}{M}\right)^2 \mathrm{Im}(\lambda_5)\ c_\beta^2 \left[1 + 0.07\ln\left(\frac{M}{1\,\mathrm{TeV}}\right)\right], \qquad (4.41)$$

$$\text{Type II:} \quad d_e = \quad 0.47 \times 10^{-27} e\,\mathrm{cm} \times \left(\frac{1\,\mathrm{TeV}}{M}\right)^2 \mathrm{Im}(\lambda_5)\left\{s_\beta^2\left[1 + 0.16\ln\left(\frac{M}{1\,\mathrm{TeV}}\right)\right] - 1.26 c_\beta^2\right\}, \qquad (4.42)$$

in the decoupling limit, where M is the mass of the heavy scalars of the theory. As shown in Eq. (4.42), the Type II model has a natural cancellation of the contributions to the electron EDM for values of $\tan\beta$ not too far away from one.

In [67], we also presented the first complete calculation of the light quark EDMs

at the two-loop level. These quark EDMs contribute to the EDMs of bound states, like the neutron, proton, and mercury. The dominant contributions to the neutron EDM are from the short range QCD interactions involving quark EDMs, δ_q, cEDMs $\tilde{\delta}_q$, and the Weinberg operator. These contributions read

$$d_n = (\zeta_n^u \delta_u + \zeta_n^d \delta_d) + (\tilde{\zeta}_n^u \tilde{\delta}_u + \tilde{\zeta}_n^d \tilde{\delta}_d) + \beta_n^G W_{\tilde{G}}, \tag{4.43}$$

where the hadronic matrix elements are given by [127]:

$$\beta_n^G = (2.4 \pm 1.9) \times 10^{-24} e \cdot \text{cm}, \quad \tilde{\zeta}_n^u = (3.4 \pm 1.7) \times 10^{-26} e \cdot \text{cm},$$

$$\tilde{\zeta}_n^d = (1.6 \pm 0.8) \times 10^{-25} e \cdot \text{cm}, \quad \zeta_n^u = -5.2 \times 10^{-28} e \cdot \text{cm}, \quad \zeta_n^d = 4.8 \times 10^{-27} e \cdot \text{cm}, \tag{4.44}$$

where the last two elements have a $\mathcal{O}(10\%)$ uncertainty. δ, $\tilde{\delta}$, and $W_{\tilde{G}}$ can be found from the coefficients of the operators

$$\mathcal{L} \supset -\frac{i}{2} \sum_q d_q (\bar{q} \sigma_{\mu\nu} \gamma_5 q) F^{\mu\nu} - \frac{i}{2} \sum_q \tilde{d}_q g_s (\bar{q} \sigma_{\mu\nu} \gamma_5 T^a q) G^{a\mu\nu} - \frac{1}{6} C_{\tilde{G}} g_s f^{abc} \epsilon^{\mu\nu\rho\sigma} G_{\mu\lambda}^a G_\nu^{b\,\lambda} G_{\rho\sigma}^c \ . \tag{4.45}$$

at the hadronic scale, $\mu \sim 1$ GeV, with

$$\frac{d_q}{e} = \frac{\sqrt{2}\alpha_{\text{em}} G_F m_q}{64\pi^3} \delta_q, \quad \tilde{d}_q = \frac{\sqrt{2}\alpha_{\text{s}} G_F m_q}{64\pi^3} \tilde{\delta}_q, \quad C_{\tilde{G}} = \frac{\sqrt{2}\alpha_{\text{s}} G_F}{64\pi^3} W_{\tilde{G}}, \tag{4.46}$$

where we used $\alpha_s \sim 0.189$, $m_u \sim 2$ MeV, $m_d \sim 4.8$ MeV. For the scope of this chaper, we neglect the running of quark dipole moments from the electroweak scale to the hadronic scale, since the neglected logarithm of order $\alpha_s \log(m_H^2/m_n^2) \sim 1.5$ leads to corrections which are small compared to the relevant hadronic uncertainties discussed shown above. For a full discussion of the running, see e.g., [166]. The expressions for all contributions to δ_q can be found in [67]. For the contributions to cEDM and Weinberg

operator, we have [166]

$$\tilde{\delta}_q = -2 \sum_{i=1}^{3} \left[f(z_t^i) \kappa_u^{(i)} \tilde{\kappa}_q^{(i)} + g(z_t^i) \tilde{\kappa}_u^{(i)} \kappa_q^{(i)} \right] , \qquad (4.47)$$

$$W_{\tilde{G}} = = \frac{1}{4} \sum_{i=1}^{3} W(z_t^i) \kappa_u^{(i)} \tilde{\kappa}_u^{(i)} , \qquad (4.48)$$

where we are summing over the several Higgs contributions and $z_t^i = m_t^2/m_{H_i}^2$, and the two-loop functions f, g, W are given in e.g., [166].

Similar expressions are valid for the proton EDM, after a proper replacement of the hadronic matrix elements in (4.44). Modulo cancelations, the prediction for the proton EDM will be of the same order of magnitude as the neutron EDM. Considering that the experimental bound on the proton EDM is roughly an order of magnitude weaker than the experimental bound on the neutron EDM (see Eqs. (4.39), (4.40)), the proton EDM will not put additional constraints on the parameter space of our model.

As we discuss in Sec. 4.5.1, the current large uncertainties in the hadronic matrix elements in the light quark CEDMs and in the Weinberg operator in (4.44) make the constraint from the neutron EDM relatively easy to be satisfied.

The main contributions to diamagnetic atom EDMs, like the mercury, come from the CP-odd nuclear Schiff moment that can be related to the CP-even and CP-odd pion-nucleus couplings, $g_{\pi NN}$ and $\bar{g}_{\pi NN}$. Additional contributions can come from nucleon EDMs. For a detailed discussion, especially in the context of a 2HDM, see [301]. Often in the literature, the latter contributions are neglected. However, it is interesting to note that a neutron EDM, d_n, of the order of its current constraint contributes to d_{Hg} at the order of its current constraint. One can write these two main contributions

to the mercury EDM as [170, 199, 301, 389],

$$d_{Hg} = - g_{\pi NN} \left((0.07 \pm 0.06) \, \bar{g}^{(0)}_{\pi NN} + (0.08 \pm 0.15) \, \bar{g}^{(1)}_{\pi NN} \right) \cdot 10^{-17} e \, \text{cm} +$$

$$- (2.6 \pm 0.5) \cdot 10^{-4} \times 1.9 d_n, \tag{4.49}$$

where the last term is the neutron EDM contribution to the Schiff moment. The CP-even coefficient is given by $g_{\pi NN} = 13.17 \pm 0.06$, and if we only keep the pieces that depend on the light quark CEDMs, the CP-odd iso-scalar and iso-vector couplings are [389]

$$\bar{g}^{(0)}_{\pi NN} \sim (0.5 \pm 1.0) \times 10^{-12} \frac{\tilde{d}_u + \tilde{d}_d}{10^{-26} \, \text{cm}}, \tag{4.50}$$

$$\bar{g}^{(1)}_{\pi NN} \sim (2^{+4}_{-1}) \times 10^{-12} \frac{\tilde{d}_u - \tilde{d}_d}{10^{-26} \, \text{cm}}. \tag{4.51}$$

where we have approximated the value of the quark condensate $|\langle q\bar{q}\rangle| \sim (225 \text{ MeV})^3$.

The large uncertainties in the coefficients of (4.49) and in the determination of the CP-odd couplings make the constraint from the mercury EDM irrelevant in our parameter space.

4.4.2 LEP and flavor physics

Two-Higgs-Doublet-Models receive constraints from precision measurements of flavor violating and flavor conserving observables that are affected by the presence of additional Higgs bosons at around the electroweak scale.

Electroweak precision measurements, and in particular the T parameter, gener-

ically give important constraints on spectra with large mass splittings[4]. Following the discussion in [64] (see also [229]), we find that alignment models with $m_{h_2} \sim m_{H^\pm}$ or $m_{h_3} \sim m_{H^\pm}$ but with an arbitrary large mass splitting between the other scalars and the charged Higgs lead to a very small correction to the T parameter. In fact, the 2HDM contributions to T parameter can be written to first order in the mixing angles x and α_2 as [64]:

$$T \sim \frac{1}{16\pi s_W^2 M_W^2} \left[\left(-G(m_{h_2}^2, m_{h_3}^2) + G(m_{h_2}^2, m_{H^\pm}^2) + G(m_{h_3}^2, m_{H^\pm}^2) \right) \right. \tag{4.52}$$
$$+ x^2 \left(G(m_{h_2}^2, m_{h_3}^2) - G(m_{h_1}^2, m_{h_3}^2) + G(m_{h_1}^2, m_{H^\pm}^2) + G(m_{h_2}^2, m_{H^\pm}^2) \right)$$
$$\left. + \alpha_2^2 \left(G(m_{h_2}^2, m_{h_3}^2) - G(m_{h_1}^2, m_{h_2}^2) + G(m_{h_1}^2, m_{H^\pm}^2) + G(m_{h_3}^2, m_{H^\pm}^2) \right) \right],$$
$$\text{with} \quad G(x, y) = \frac{1}{2}(x + y) - \frac{xy}{x - y} \log\left(\frac{x}{y}\right).$$

Since

$$G(x, y) = G(y, x) \quad \text{and} \quad \lim_{y \to x} G(x, y) \to 0, \tag{4.53}$$

the first line of Eq. (4.52) vanishes for $m_{H^\pm} \to m_{h_2}$ or $m_{H^\pm} \to m_{h_3}$, leaving only quadratic contributions in x or α_2, which are within the experimental constraints for the benchmark that we discuss in the next section.

In the CPV 2HDM, the Yukawa couplings of the charged Higgs boson are the same as those of the CP conserving 2HDMs (see Eq. (4.29)). Therefore we can apply the same bounds on the parameter space of the $H^\pm$, as in the case of the CP conserving model. The charged Higgs boson can introduce sizable NP contributions to the $b \to s\gamma$

---

[4]In this chaper, we do not attempt to address the anomaly in the W mass, as found by the CDF collaboration [37]. See [300] for a discussion in the context of CPV 2HDMs.

transition. Refs. [352, 353] show that for a CP conserving Type II model, the lower bound on $m_{H^\pm}$ is around 800 GeV with only a mild dependence on $\tan\beta$, as long as $\tan\beta \gtrsim 1$. However, a more recent study [112] emphasized new significant theoretical uncertainties in the determination of the $b \to s\gamma$ rate, leaving more room for NP effects, and, therefore, significantly weakening the bound on $m_{H^\pm}$. Other flavor constraints $(B \to \tau\nu)$ on the mass of the charged Higgs are weaker in the regime of low $\tan\beta$ that we will discuss in the next section. Similarly, flavor constraints on the neutral Higgs bosons are weaker than LHC direct searches in the regime of low $\tan\beta$.

4.5   Looking for CPV in heavy Higgs searches

The CPV 2HDM leads to a variety of new signatures that could be searched for at the LHC. The several Higgs bosons are a CP even-CP odd admixture. For this reason, the following new decay modes will be possible, if kinematically allowed:

$$h_3 \to h_1 h_2; \qquad h_3 \to h_2 Z, h_2 \to h_1 Z. \tag{4.54}$$

These modes are not allowed in a CP conserving scenario. These signatures have not been yet searched for by the ATLAS and CMS collaboration. A phenomenological study of the first signature was presented in e.g., [339]. The second one is the focus of this section.

Beside new signatures of the heavy Higgs bosons, in the presence of CPV, the rate of standard heavy Higgs decay modes can be affected by new interference effects.

87

Examples are the decays $h_{2,3} \to \tau\bar{\tau}$, $b\bar{b}$ in the regime of large $\tan\beta$ [227], the interference between the resonant $gg \to h_{2,3} \to Zh_1$ and the non-resonant $gg \to Zh_1$ [160] or between the resonant $h_{2,3} \to t\bar{t}$ and non-resonant $gg \to t\bar{t}$ [144] at low $\tan\beta$. In our analysis, we will not keep into account these interference effects, since, as we will argue, they are not relevant for the discussion of the benchmark scenario we present in Sec. 4.5.1. Nevertheless, generically they are important for the precise assessment of the bounds on the mass of the heavy Higgs bosons.

4.5.1 CPV benchmarks for new heavy Higgs searches

As we discussed in Sec. 4.2.2, the CPV 2HDM has 7 free parameters (once we fix the mass of the 125 GeV Higgs boson). We explore the parameter space of the model via scanning the following independent set of six parameters:

$$m_{h3}, \quad \Delta \equiv m_{h3} - m_{h2}, \quad \delta \equiv m_{H^\pm} - m_{h3}, \quad x, \quad \alpha_2, \quad \lambda_2, \quad (4.55)$$

having fixed $m_{h1} = 125$ GeV and $\tan\beta$ such that the electron EDM is below the bound set by the JILA electron EDM experiemnt, $|d_e| < 4.1 \times 10^{-30}$e cm. [397]. We set $|d_e| = 4 \times 10^{-30}$e cm. The cancelation described in Sec. 4.4.1 only arises in a Type II model, and, for this reason, we focus on this model for the remaining of the section.

For the scan of the parameter space, we focus on small values of δ such to have agreement with the constraint from the T parameter, sizable values of Δ to allow the $h_3 \to Zh_2$ decay, and values of x and α_2 consistent with the Higgs coupling fits presented in Sec. 4.3.1. We choose values of $\tan\beta$ close to 1, since, as discussed in Sec. 4.4.1, the

several contributions to the electron EDM cancel at around $\tan\beta = 1$ when the 2HDM has the additional Higgs bosons in the multi-hundred GeV mass range. Finally, we trade ν for λ_2 and scan on the latter parameter, so it is easier to find benchmarks that are consistent with perturbativity requirements (see Eq. .45 for the expression of λ_2 in terms of ν and the physical parameters). The phenomenology of the model depends only very mildly on the value of λ_2, once all the other parameters are fixed.

We choose the benchmark:

$$\Delta \simeq 240 \text{ GeV}, \quad \delta = -7 \text{ GeV}, \quad x \simeq 0.005, \quad \alpha_2 = 0.125, \quad \lambda_2 \simeq 0.2. \tag{4.56}$$

and keep m_{h_3} as a free parameter. The value of $\tan\beta$ needed to satisfy the electron EDM constraint for this benchmark is very close to 1 ($\tan\beta \sim 1.05$) in the entire range of masses for h_3 that we consider for the phenomenological analysis presented in Sec. 4.5.2. The exact value is only relevant for satisfying the constraint from the electron EDM. Changing a bit the valu e of $\tan\beta$ will not affect the heavy Higgs phenomenology. We have checked that the cancelation of the electron EDM is at around three orders of magnitude.

In Fig. 4.2, we summarize these results on the parameter space in two different planes: $(m_{h_3} - \alpha_2)$ on the left panel and $(m_{h_3} - x)$ on the right panel. The other parameters have been chosen to match the benchmark model above, in the context of the LHC phenomenology. Pink regions do not satisfy the requirements of the potential bounded from below (see eqs. (4.14)). The yellow regions do not satisfy the conditions of vacuum stability (see eqs. (4.17)). Finally, the purple regions lead to too large quartic

couplings, in tension with the requirement of perturbativity. In the allowed regions, we show the value of the α_3 mixing angle. For the plots, we choose the solution with a plus sign in (4.20).

In Fig. 4.3 we show the contributions to the neutron EDM from the terms in Eq. (4.43), as calculated using the benchmark in Eq. (4.55). The several contributions only mildly depend on the heaviest Higgs mass in the range of interest, and, for this reason, we choose a representative value, $m_{h_3} = 900$ GeV. The two main contributions (Weinberg operator and down quark cEDM) have very large uncertainties from the hadronic matrix elements (see Eq. (4.44)) and they have opposite signs. The full prediction from the neutron EDM is consistent with the bound in (4.39) shown as a dashed line in the figure.

Overall, the benchmark in Eq. (4.56), with $\tan\beta \simeq 1$ is consistent with all theoretical, low and high energy constraints as long as $m_{h_3} \lesssim 920$ GeV (see Fig. 4.2). In the region of parameter space shown in the figure, the 125 GeV Higgs coupling predictions are also consistent with measurements (see bottom-left panel of Fig. 4.1).

4.5.2 Phenomenology of the heavy Higgs bosons

In this section, discuss the phenomenology of the heavy Higgs bosons, h_2 and h_3, in the mass range of interest ($m_{h_3} \lesssim 920$ GeV). The main branching ratios for the heavy Higgs bosons are shown in Fig. 4.4, as a function of the mass of the heaviest neutral state, h_3. Both neutral Higgs bosons have $t\bar{t}$ as main decay mode. The second most important decay mode is the decay into Zh_2 (or Zh_1 for h_2). The h_2 decay into

massive gauge bosons is suppressed because the benchmark has a small CPV phase α_3 and a small x parameter (see Eq. (4.26)). The corresponding branching ratios are smaller than the branching ratio into gluons, represented in the figure. The BR($h_3 \rightarrow ZZ$, WW) are larger because of the sizable value of α_2.

As discussed in Sec. 4.2.2, h_2 is mainly CP even and h_3 mainly CP odd. For this reason, the BR($h_2 \rightarrow Zh_1$) and BR($h_3 \rightarrow ZZ, WW$) are suppressed. It is interesting to observe that there is a correlation between BR($h_2 \rightarrow Zh_1$) and BR($h_3 \rightarrow ZZ$), due to the fact that $g_{Zh_ih_j} = \epsilon_{ijk}\, g_{h_kVV}$ (see Eq. (4.23)). We can approximate[5]

$$\frac{\mathrm{BR}(h_2 \rightarrow h_1 Z)}{\mathrm{BR}(h_3 \rightarrow ZZ)} \simeq 4 \left(\frac{\tilde{\kappa}_u^{(3)}}{\kappa_u^{(2)}}\right)^2 \left(\frac{m_{h2}}{m_{h3}}\right)^2 \frac{\lambda_{h_2Zh_1}^{3/2}}{\lambda_{h_3ZZ}} \frac{\lambda_{h_3tt}^{1/2}}{\lambda_{h_2tt}^{3/2}}, \qquad (4.57)$$

where the kinematical factors are given by

$$
\begin{aligned}
\lambda_{h_itt} &= 1 - 4\frac{m_t^2}{m_{h_i}^2}, \\
\lambda_{h_2Zh_1} &= \left(1 - \frac{m_{h_1}^2}{m_{h_2}^2} - \frac{m_Z^2}{m_{h_2}^2}\right)^2 - 4\frac{m_Z^2 m_{h_1}^2}{m_{h_2}^4}, \\
\lambda_{h_3ZZ} &= \sqrt{1 - 4\frac{m_Z^2}{m_{h_3}^2}}\left(1 - 4\frac{m_Z^2}{m_{h_3}^2} + 12\frac{m_Z^4}{m_{h_3}^4}\right).
\end{aligned}
\qquad (4.58)
$$

The ratio of branching ratios in (4.57) only depends on the ratio of h_2 and h_3 couplings with tops (in addition to kinematical factors). In our benchmark $\frac{\tilde{\kappa}_u^{(3)}}{\kappa_u^{(2)}} \simeq 1$.

For completeness, in the figure we also show the main branching ratio of the charged Higgs boson. As expected, the most dominant mode is into tb. The corresponding branching ratio is, however, smaller than one because the Wh_2 decay mode is

---

[5]In this expression, we approximate $\Gamma_{h_2}^{\mathrm{tot}} \sim \Gamma(h_2 \rightarrow t\bar{t})$ and $\Gamma_{h_3}^{\mathrm{tot}} \sim 2\Gamma(h_3 \rightarrow t\bar{t})$.

kinematically open.

4.5.3 Existing bounds and new multiboson searches for CPV heavy Higgs bosons

Based on the branching ratios in Fig. 4.4, we compute the bounds from the existing experimental searches. Many channels are probed by existing searches at the LHC, in particular decays of Higgs bosons into final states of $WW, ZZ, ZH, t\bar{t}, t\bar{t}t\bar{t}$ [5, 7, 10–12, 28, 29, 408, 414, 417–420], as well as searches for $H^{\pm} \to tb$ [27, 416]. Other existing searches apply to a 2HDM model, but do not constrain our parameter space at low values of $\tan\beta$, e.g., $h_{2,3} \to \tau\bar{\tau}, b\bar{b}$ and $H^{\pm} \to \tau\nu$ [21, 22, 410, 411].

The most relevant bound comes from a search for heavy scalars decaying into top pairs and produced in gluon fusion [419]. The analysis does not lead to a constraint on h_3 because its mass range exceeds the range considered by the experimental analysis.

Interpolating the exclusion contours of the results over the relative width of h_2 allows for a comparison. The CP-even couplings, $\kappa_u^{(2)}$, and CP-odd couplings, $\tilde{\kappa}_u^{(2)}$, are computed for the benchmark. The constraint on the benchmark comes from the scalar coupling of h_2 to tops, $\kappa_u^{(2)}$, excluding at the 95% CL below $m_{h_3} < 745$ GeV.

In Fig. 4.5, we present the rates for several bosonic decay modes of the heavy Higgses, as a function of the mass of h_3, where the Higgs bosons are produced in gluon fusion. The rates are computed by modifying the corresponding SM rates [350] where possible, and implementing the remainder of the relevant expressions [326]. Some final state channels would indicate CP violation if measured for both heavy Higgs bosons,

namely WW, ZZ, Zh_1, h_1h_1. The decay $h_3 \to Zh_2 \to ZZh_1$ would indicate CP violation on its own, which is also true for the decay $h_3 \to h_2h_1$, however that signal is negligibly small in this benchmark. There are no existing searches for the channels $h_3 \to h_2Z \, (h_2 \to WW, ZZ, h_1h_1, Zh_1)$.

Existing searches for heavy Higgs bosons in a CP conserving model could exclude the model. Decays of the heavy Higgses into ZZ are particularly relevant since the decay shares a coupling (see 4.23) with the intersting channel $h_3 \to Zh_2 \to ZZh_1$. A sizeable decay into ZZ would have been observed by the searches [28, 408]. For the benchmark, $\Gamma_{h_3} \sim 0.07 \times m_{h_3}$, the signal of $\sigma_{\mathrm{ggF}} \times \mathcal{B}(h_3 \to ZZ)$ is similar and below the constraint. The same constraint for the scalar, h_2, is weaker since the branching ratio, $\mathcal{B}(h_2 \to ZZ)$, is on the order of 10^{-3} times smaller than $\mathcal{B}(h_3 \to ZZ)$ (since $\alpha_2 \times \alpha_3 \ll x$, the ratio $(x/\alpha_2)^2$ roughly gives this factor.)

Searches for $A \to Zh$ are considered. The most relevant search is $A \to Zh \, (h \to bb)$ [414]. The corresponding signal is computed for $h_{2,3} \to Zh_1 \, (h_1 \to bb)$ with only the h_2 result being sizeable compared to the bounds. At face value, the signal predicted by our benchmark scenario is slightly higher than the constraints set by the search for $m_{h_3} \simeq 900 \mathrm{GeV}$, except for a small mass range around $m_{h_3} \simeq 750$ GeV. However, the CMS search assumes that the width of A is smaller than the experimental resolution, and, therefore, the narrow width approximation is utilized. In our case, h_2 has a width $\Gamma_{h_2} \sim (2-4)\% \, m_{h_2}$ in the mass range of interest, and, therefore, we expect the bounds to be a bit weaker.

Another search that could exclude the model is from searches of four top quark

production, $pp \to \bar{t}tH \to \bar{t}t(\bar{t}t)$. The analysis [420] shows that a minimal Type II 2HDM model with $\tan\beta = 1$ is excluded at the 95% CL for a CP even (odd) scalar of about 400 (520) GeV. In our model, the mass of h_3 exceeds the range of this analysis. h_2 can in principle be constrained by this search. However, the value of $\tan\beta$ in our benchmark ($\tan\beta \sim 1.05$) together with a BR($h_2 \to \bar{t}t$) slightly below 1 makes our model still hidden to this search in the entire mass range considered in this chaper.

Charged Higgs searches, notably searches for $H^\pm \to tb$ [27, 416], could provide constraints on the model. Type II 2HDMs with $\tan\beta = 1$ are already constrained to charged Higgs masses $m_{H^\pm} \sim 900$ GeV. In our benchmark scenario, the charged Higgs has a large branching ratio into a W and lighter neutral Higgs, $H^\pm \to W^\pm h_2$ (see fig 4.4 (c)), resulting into a reduced branching ratio into tb, BR($H^\pm \to tb$) $\simeq 0.6$. Particularly, rescaling the bound, we obtain $m_{H^\pm} \gtrsim 715$ GeV for our benchmark.
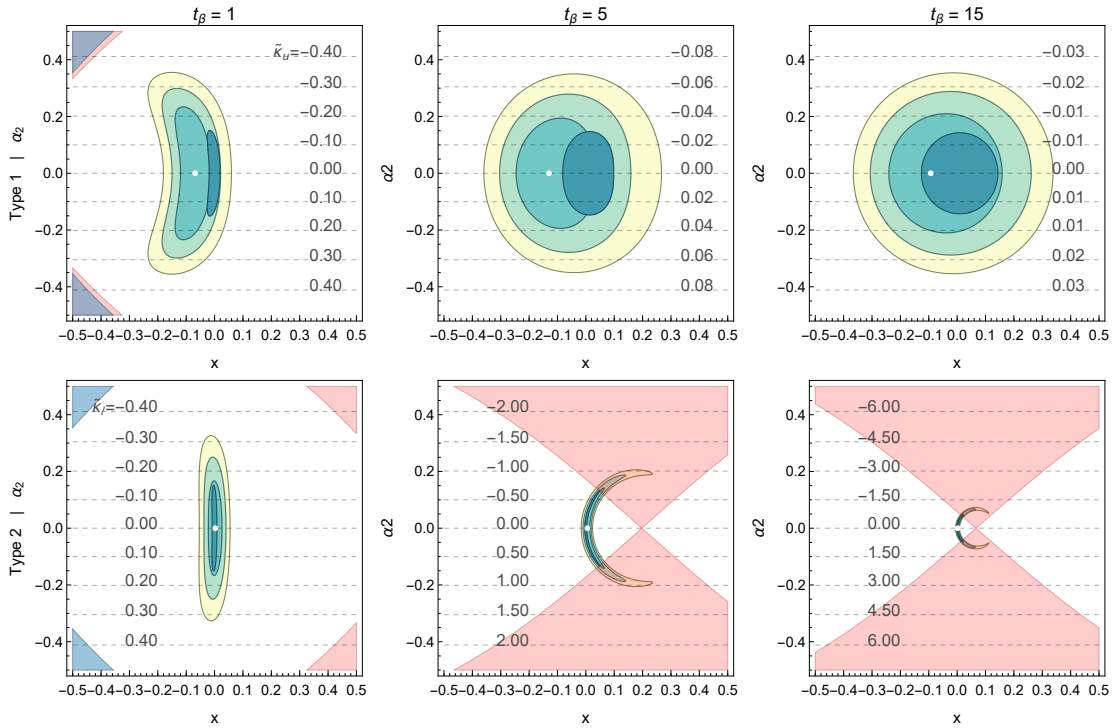
Figure 4.1: Current constraint from Higgs coupling measurements in a Type I (upper panels) and Type II (lower panels) 2HDM. We fix $\tan\beta = 1, 5, 15$ in the left, middle, and right panels, respectively. In the several panels, we indicate with white dots the best fit points. The three shaded regions from light blue to yellow correspond to the current $1, 2, 3\ \sigma$ regions obtained with a naive combination of ATLAS and CMS measurements (see text for details), while the darker blue region is the 1σ region obtained using projections with 3000/fb data. The red region is probed by the direct searches of CPV in the $h \to \bar{\tau}\tau$ decay. The blue regions are probed by the direct search of CPV in the $h\bar{t}t$ production (see Sec. 4.3.2.2 for details). The dashed horizontal lines indicate the value of the CPV couplings $\tilde{\kappa}_u$, $\tilde{\kappa}_\ell$. In the case of Type I, $\tilde{\kappa}_u = -\tilde{\kappa}_\ell$; the value of $\tilde{\kappa}_u$ is the same in both Type I and Type II.
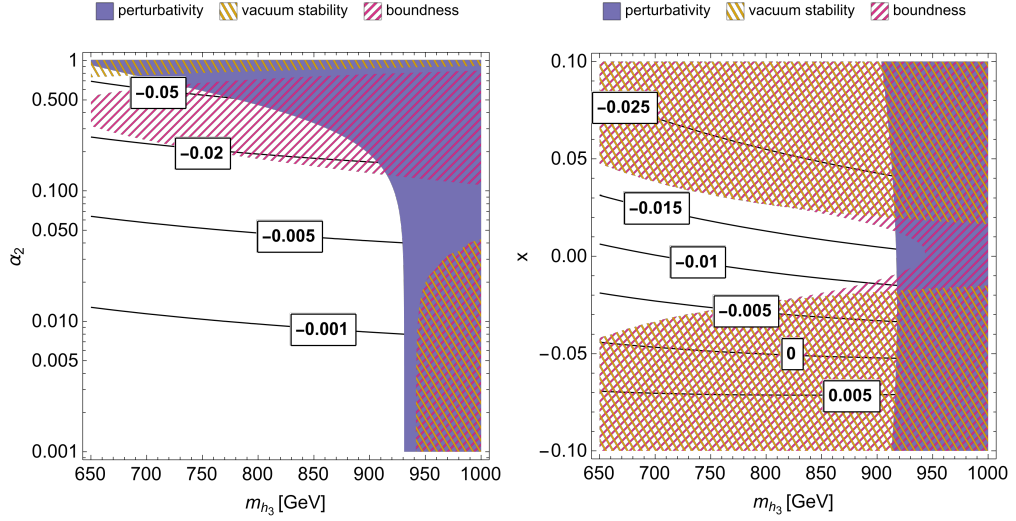
Figure 4.2: Contours for the mixing angle α_3 as predicted by the benchmark discussed in Eq. (4.56). The purple regions do not satisfy the condition of perturbativity of the quartic couplings at the electroweak scale. The yellow regions do not satisfy the conditions of vacuum stability (see eqs. (4.17)). Pink regions do not satisfy the requirements of the potential bounded from below (see eqs. (4.14)).

96
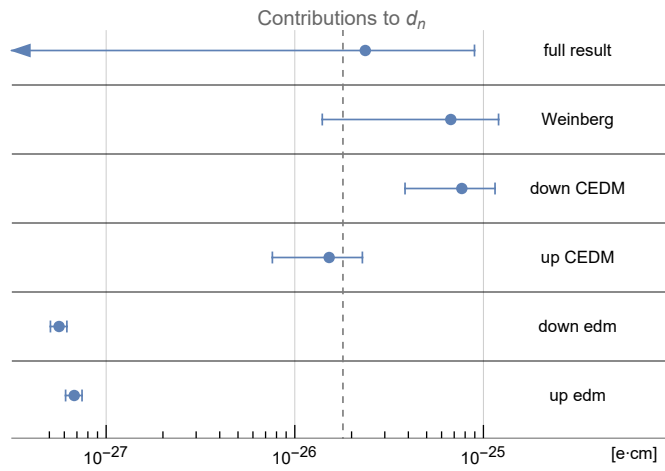
Figure 4.3: The various contributions to the neutron EDM, as presented in Eq. (4.43) using the benchmark in Eq. (4.56), and having fixed $m_{h_3} = 900\text{GeV}$. The two largest contributions combine to give a result consistent with 0. The dashed gray line indicates the experimental bound on the full result as shown in Eq. (4.39).
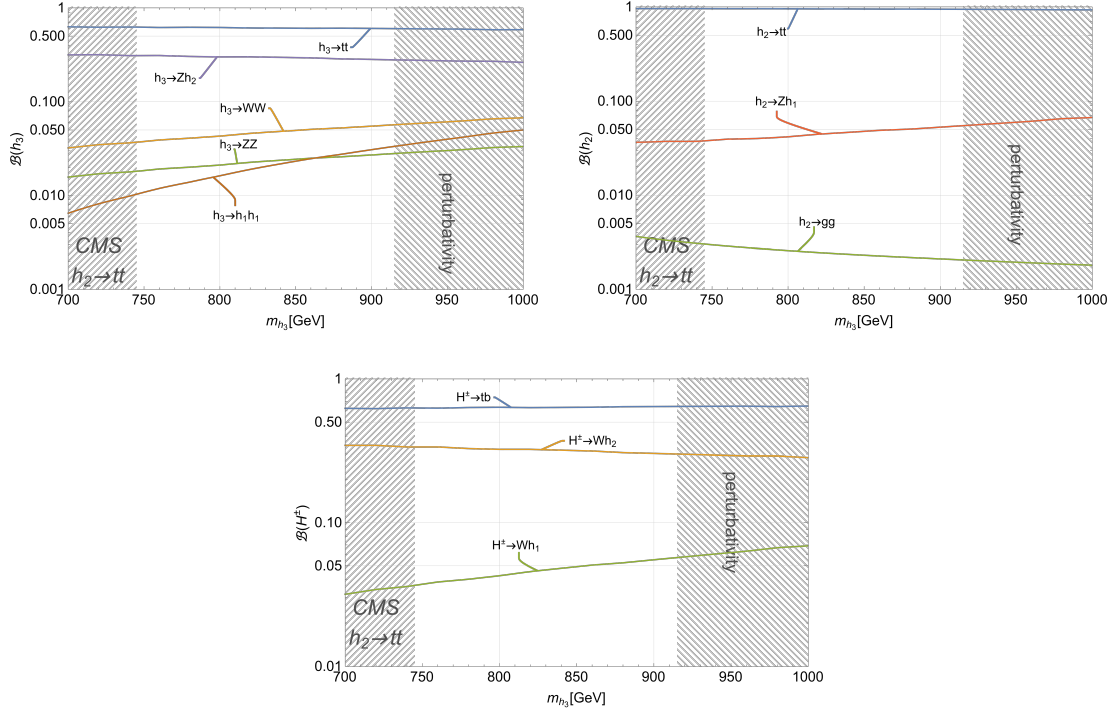
Figure 4.4: Branching ratios of h_3 (left upper panel), h_2 (right upper panel), and $H^\pm$ (lower panel) as a function of m_{h3} for a type-II 2HDM having fixed the parameters as in (4.56) and $\tan\beta = 1$. The hatched region on the left is excluded by existing searches (discussed later in this section), and the one on the right does not satisfy the perturbativity condition, $|\lambda_3| < 4\pi$.
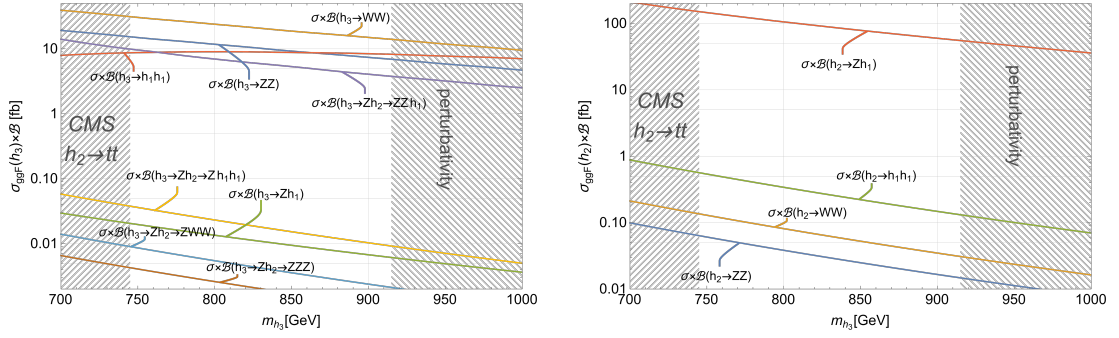
Figure 4.5: Several gluon fusion Higgs rates of the heavy Higgs bosons, h_3 (left panel) and h_2 (right panel), as a function of mass for the benchmark in (4.56) and $\tan\beta = 1$. The hatched region on the left is excluded by existing searches (discussed later in this section), and the one on the right does not satisfy the perturbativity condition, $|\lambda_3| < 4\pi$.

Part III

Astronomy interlude

Chapter 5

Introduction

A non-particle dark matter candidate exists in primordial black holes
(PBHs)[147, 148, 150, 274]. There are many propositions to populate such holes in
the universe. Many suggested mechanisms involve collapsing density fluctuations in the
early universe from a variety of sources[150, 276], others include phase transitions[311].
The hypothetical mass range of the PBHs generated by these mechanisms span a range
from asteroid mass to beyond $10^3 \, M_\odot$. Microlensing events, in which the observed
brightness of a star is altered by the transit of a body in front of it could detect PBHs,
and in fact such events (rather an excess of events) have already employed a hypothetical
PBH population to explain them [371]. Another explanation of those events could be
transits by free-floating planets (FFPs), which are planets ejected from their original star
systems. At sub-terrestrial masses, there is expected to be a much greater population
of FFPs than bound exoplanets [428, 430], which impact hypotheses of PBH-caused
microlensing events. Statistical analysis must be performed on distributions of lensing

events in order to disentangle the sources of those events.

Microlensing is a phenomenon of gravitation lensing which occurs when the lensing object has a low mass, though still high enough to have a gravitational field strong enough to distort light from background stars (sources). The result is a temporary overall apparent magnification of the background light. In contrast, a larger mass lens will generate an effect of multiple images of the source. [376]. Often, the "point-source approximation" is made where the source star is taken as a point source, a powerful simplification for lenses whose angular diameter greatly exceeds the source's. This is often the case for very distant sources. The characteristic light curve resulting from this approximation is temporally sharply peaked. Finite-source effects of microlensing come into play when the angular diameter of the source is non-negligble compared to the lens. When taken into consideration, the amplification of the apparent magnitude is decreased, but the temporal shape of the light-curve differs characteristically from true point-source events. In principle, more information can be extracted from the shape of the light-curve, though in practice it can be quite challenging. The most robust quantity for measurement of the light-curve is the event duration, making it a prudent choice for statistical analysis of events. In this section we examine such a statistical method to distinguish microlensing events which could be sourced by populations of PBHs or FFPs.

Chapter 6

Rogue worlds meet the dark side: revealing terrestrial-mass primordial black holes with the Nancy Grace Roman Space Telescope

This chapter is based on [195].

6.1 Introduction

The nature of dark matter remains one of the most pressing open questions in fundamental physics. While multiple lines of compelling evidence indicate its existence, its microphysical nature remains unknown (for a recent review and up to date references see e.g. Chapter 27 of Ref. [448]). Many models have been proposed to

explain this additional matter content, with many such models introducing new fundamental particles with suppressed interaction cross-sections to populate the dark sector [448]. However, dark matter may instead be macroscopic and potentially possess large interaction cross-sections, escaping detection due to its low number density. Primordial black holes (PBHs) are a well-motivated candidate for such a macroscopic dark matter model [147, 148, 150, 274]. There are a wide variety of mechanisms that result in the formation of PBHs, from the collapse of overdensities sourced by inflation [150, 276] to phase transitions [311] and topological defect collapse [179] in the early universe (see the discussion in Sec. 6.3.1 below). PBHs may form over a wide range of masses, from as low as asteroid masses up to thousands of solar masses and beyond.

The Earth-mass range, $\sim 10^{-6} \, M_\odot$, is of particular interest, as observations of excess short-duration microlensing events have been suggested to constitute a first hint of a population of PBHs at terrestrial masses [371]. However, there is another possible candidate to explain these events: free-floating planets (FFPs). These are planets that have been ejected from their parent star system by dynamical interactions during the chaotic early phases of system formation. Such FFPs are expected to dramatically outnumber bound exoplanets at sub-terrestrial masses [428, 430], constituting a large potential background for surveys seeking to observe PBHs at Earth masses and below.

Previously, constraints on the PBH abundance have been placed in regions of parameter space for which the expected contribution from FFPs is negligible. However, with the upcoming launch of the Nancy Grace Roman Space Telescope, this will change: over the course of its Galactic Bulge Time Domain Survey (GBTDS) [234], Roman is

expected to observe hundreds of free-floating planets at roughly Mars mass and above [298]. This unprecedented sensitivity will also provide the opportunity to search for PBHs in new regions of parameter space. In these regions, FFPs constitute an irreducible background that must be taken into account in order to constrain or claim the discovery of PBHs.

FFPs and PBHs cannot generally be discriminated on an event-by-event basis, as their light curves are degenerate for identical masses. However, FFPs and PBHs are expected to arise from different underlying mass distributions, permitting a statistical means of discrimination. In this chaper, we present a method by which a subpopulation of PBHs can be detected amidst a background of FFPs. We find that even in the presence of FFPs, Roman will be sensitive to PBHs at abundances well below existing constraints. In particular, Roman will be able to conclusively determine the nature of the Earth-mass "hint" of a PBH population claimed by [371].

The remainder of the chaper is organized as follows. In Sec. 6.2, we discuss microlensing surveys and describe the observables associated with microlensing lightcurves. In Sec. 6.3, we review mechanisms for PBH/FFP formation and provide a fiducial mass function for the abundance of each population. In Sec. 6.4, we describe the implementation of our analysis framework and the associated statistical methodology for estimating Roman sensitivity. In Sec. 6.5, we present our results and discuss their implications before concluding in Sec. 6.6.

6.2 Microlensing

Gravitational lensing is a powerful technique to observe non-luminous massive objects at astronomical distances. Light rays passing in the vicinity of a massive object are bent by the gravitational field of the object, causing the light from background stars ("sources") to be distorted by massive objects ("lenses") that lie along the line of sight. For high mass lenses, this effect produces multiple images of the source; for low mass lenses, the images cannot be individually resolved and instead contribute to an overall apparent magnification of the source. This effect is known as microlensing [376].

The duration and magnification of the source are determined by the mass of lens M, the distance to the lens and source, d_L and d_S, the relative proper motion of the source and the lens μ_{rel}, the impact parameter u, the angular diameter of the source θ_S, and the effective angular diameter of the lens θ_E. This final quantity is also known as the "Einstein angle" and is given by

$$\theta_E = \sqrt{\frac{4GM(1 - d_L/d_S)}{c^2 d_L}}. \tag{6.1}$$

When $\theta_S \ll \theta_E$, the angular extent of the source is negligible. This "point-source regime" is typical for large lens masses and distant sources, and the associated event duration is given by the time it takes for the source to cross the Einstein radius of the lens. This "Einstein crossing time" is defined as

$$t_E = \frac{\theta_E}{\mu_{\text{rel}}}. \tag{6.2}$$

In the point-source regime, the apparent magnification is given by [368]

$$A_{\rm ps}(u) = \frac{u^2 + 2}{u\sqrt{u^2 + 4}}, \qquad (6.3)$$

where $u \equiv u(t)$ is the impact parameter as a function of time. This yields a characteristic light curve consisting of a narrow peak.

When $\theta_S \gtrsim \theta_E$, however, the point-source approximation breaks down. In this finite-source regime, the light curve saturates at a lower maximum magnification and the event duration is no longer set by t_E, but rather by the time for the *lens* to cross the finite angular extent of the *source*, a timescale of $\sim 2\theta_S/\mu_{\rm rel}$. Similarly, the magnification in this regime no longer diverges as $u \to 0$ and is instead given by an integral over the source disk, specified in polar coordinates (r, ϕ) as [345, 429, 447]

$$A_{\rm finite}(u, \rho) \equiv \frac{1}{\pi\rho^2} \int_0^\rho dr \int_0^{2\pi} d\phi \; r \; A_{\rm ps}\left(\sqrt{r^2 + u^2 - 2ur\cos(\phi)}\right), \qquad (6.4)$$

where $\rho \equiv \theta_S/\theta_E$ and the origin has been chosen such that the lens center is located at a distance u from the origin along $\phi = 0$. The maximum impact parameter that produces a detectable event is defined implicitly via the relation $A_{\rm finite}(u_{\rm T}, \rho) = A_T$, where the minimum detectable magnification, A_T, is set by the photometric sensitivity of the microlensing survey, and u_T is the maximal impact parameter that results in a magnification of at least A_T. u_T defines the phase space for the expected event rate calculation (see Sec. 6.4.1) and can be calculated for a given d_L, d_S, and θ_S following the procedure given in [429].

For most events, the fundamental observable that can be measured from the light curve is the duration. We define this as the time over which the magnification is

107

above detection threshold ($A > A_T$ or equivalently $u < u_T$):

$$t_{\text{dur}} = 2\sqrt{u_T^2 - u_{\text{min}}^2}\,\frac{\theta_E}{\mu_{\text{rel}}}, \qquad (6.5)$$

where u_{min} is the impact parameter at the point of closest approach. Assuming perfect photometry, $u_T \approx \rho$ in the extreme finite-source regime and ≈ 1 in the point-source regime; hence, for a trajectory that passes through the midplane of the source, t_{dur} approaches the expected $\sim 2\theta_S/\mu_{\text{rel}}$ in the finite-source limit and $\sim 2t_E$ in the point-source regime.

Though finite-source effects reduce the peak magnification, which can reduce detectability, they introduce characteristic features in the light-curve that permit a measurement of θ_E. Coupled with a measurement of the lens distance, an estimate of the lens mass can be made. However, the extraction of θ_E is a challenge for many events, especially those that do not conform to simple single-lens models. Additionally, for low masses and short event durations, estimating d_L requires a simultaneous observation by another telescope in order to provide a parallax measurement, which is often unavailable. As such, the only observable quantity that can be robustly measured for most microlensing events is the event duration, t_{dur}, and is therefore the quantity we choose to employ to discriminate amongst various subpopulations of lenses in Sec. 6.4.

6.3   Microlensing Targets

In this section, we discuss two primary targets for microlensing surveys in the terrestrial mass range and connect them to existing observations.

6.3.1 Primordial black holes

Black holes not originating from the collapse of massive stars are generically termed "primordial" black holes and appear in many extensions of the Standard Model. Most formation mechanisms rely upon the growth of large density fluctuations in the early universe that ultimately collapse. These may be seeded by features in the inflationary potential [89, 151, 231, 237, 282, 291, 455] or by other physical processes, such as the collapse of inhomogeneities during the matter-dominated era triggered by a sudden pressure reduction [139, 294, 311], collapse of cosmic string loops [275, 280, 293], bubble collisions [179, 324], a scalar condensate collapsing to Q-balls before decay [174–177], or domain walls [188, 236, 336, 399]. (See, e.g., [147, 148] for recent reviews.)

If the overdensities are seeded by inflationary features, the resulting PBH masses are related to the redshift of formation since PBHs acquire a mass of order the total energy within a Hubble volume at the time of collapse. The resulting mass distribution is often well-described by a log-normal distribution, which is a generic prediction for PBHs forming from smooth, symmetric peaks in the power spectrum of density fluctuations in the early universe [204]. Numerical and analytical evidence for this functional form was provided in [253] and [304], see also the recent Ref. [316]. For this reason, in the following, we will consider a fiducial PBH mass function of the form

$$f(M, \sigma, M_c) = \frac{f_{\text{PBH}}}{\left(\sqrt{2\pi}\right) \sigma M} \exp\left(-\frac{\log^2\left(M/M_c\right)}{2\sigma^2}\right),$$

(6.6)

normalized such that

$$f_{\text{PBH}} = \frac{\Omega_{\text{PBH}}}{\Omega_{\text{DM}}} = \int \, \mathrm{d}M f(M, \sigma, M_c)$$

(6.7)

109

where here Ω_{PBH} and Ω_{DM} are the fractional energy density of PBHs and of all dark matter, respectively. Here M_c is the mean value of M and σ is the standard deviation of the logarithmic mass.

PBHs are a compelling candidate for dark matter and have been searched for across a wide range of masses. In the mass range of $\approx 10^{-11}\,M_\odot - 10\,M_\odot$, gravitational lensing sets some of the strongest observational constraints on their abundance [56, 57, 140, 254, 305, 371, 450, 451] limiting the fractional energy density to $f_{\mathrm{PBH}} \approx 10^{-1} - 10^{-2}$. At terrestrial masses, the strongest limits are set by observations made by the Optical Gravitational Lensing Experiment (OGLE) [371]. However, this survey also revealed an anomalous excess of six short-duration events consistent with a population of Earth-mass PBHs at $f \approx 10^{-2}$. To date, the nature of these observations has not been resolved. As we will show in Sec. 6.5, upcoming observations by the Nancy Grace Roman Space Telescope will be able to establish whether a population of PBHs truly exists at these masses or whether these events were more likely caused by, e.g., free-floating planets.

6.3.2 Free-floating planets

The term "free-floating planets" is often used to describe two different classes of astrophysical objects. At masses near and above that of Jupiter, FFPs may form *in situ* as the core of a failed star [351]. At lower masses, FFPs are expected to primarily form within young planetary systems before being ejected by dynamical processes onto unbound orbits. There is a wide variety of processes that can result in the ejection of a protoplanetary object, including stripping by nearby stars, gravitational scattering off of

planetesimals, and interactions with an inner binary star system [223, 341, 395]. Both simulations and observations suggest that FFPs may dramatically outnumber bound planets at masses $\lesssim M_\oplus$ [360, 428, 430]. FFPs are therefore an exciting observational target for existing and upcoming microlensing surveys.

Ejection processes typically yield a distribution of FFPs that are well-described by a power law [360]. Here we adopt the form

$$\frac{dN}{d\log_{10}(M)} = \mathcal{N}\Big(\frac{M}{M_{\mathrm{norm}}}\Big)^{-p} \tag{6.8}$$

where $\mathcal{N}$ is the total number of FFPs per star at mass M scaled by a normalization mass M_{norm}. Throughout the rest of the chaper, we take all logarithms to be base 10 and $M_{\mathrm{norm}} = M_\oplus$ unless otherwise noted.

At present, observational measurements of the FFP population do not place strong constraints on the values of $\mathcal{N}$ and p. Existing microlensing surveys have observed tens of FFPs, with only three events permitting a mass estimate placing the lens in the terrestrial range.[1] Based off these data, combined with the results from simulations of ejection [202, 233, 356] and observations of bound systems [325, 405, 428], the best estimates for p and $\mathcal{N}$ are of order $p \approx 1$ and $\mathcal{N} \approx 10$ with an uncertainty spanning $p \approx 0.66 - 1.33$ and $\mathcal{N} \approx 2 - 20$ [249, 360, 430]. We choose to adopt $p = 1$ and $\mathcal{N} = 10$ as our fiducial parameters and marginalize over the uncertainty on their values when computing our sensitivity (see Sec. 6.4.2).

---

[1]The associated events are OGLE-2012-BLG-1323 [362], OGLE-2016-BLG-1928 [364], and MOA-9y-5919 [321].

6.4 Detecting PBHs with Roman

In this section, we describe our statistical methodology for detecting a subpopulation of PBH lenses within a background of FFPs. The key point is that though PBH and FFP events cannot be discriminated on an event-by-event basis, the two *populations* can be distinguished by the statistical distribution of their event durations, t_{dur} (Eq. 6.5). This distribution is predominantly controlled by the underlying mass function of the lensing population, which differs significantly between FFPs and PBHs (see Secs. 6.3.1 and 6.3.2). Additionally, the t_{dur} distribution is influenced by the distribution of lens distances and transverse velocities, both of which differ between FFPs and PBHs as well (see Sec. 6.4.1). As a result, the observed distribution of t_{dur} provides a robust means of identifying multiple populations of lenses within a set of microlensing events.[2]

While existing observations have not yet yielded a sufficient number of detections at terrestrial masses to resolve the underlying distribution of t_{dur}, this will change in the coming years. The Galactic Bulge Time Domain Survey (GBTDS), one of three primary surveys to be conducted by the upcoming Nancy Grace Roman Space Telescope (set to launch in 2027), will observe seven fields tiling 2 square degrees of the Galactic bulge with a cadence of 15 minutes during six 72-day observing seasons [234]. This survey strategy has been designed specifically to meet core science requirements for the mission, including measuring the abundance of free-floating planets to within 25%. As such, the GBTDS is expected to yield hundreds of FFP microlensing events at Mars

---

[2]An alternate strategy, as suggested by Niikura et al. [371], would be to observe along different lines of sight, as FFPs and PBHs are expected to follow different spatial distributions. As this would require an additional dedicated survey, we leave the study of this topic to future work.

mass and above [298], providing the opportunity for distribution-level analyses.

In the following two subsections, we will describe our methodology for determining Roman's sensitivity to discriminating a PBH subpopulation from a background FFP population using the observed distribution of $t_{\rm dur}$ values. This is done in two steps. First, in Sec. 6.4.1, we compute the event rate for both of these populations given Roman's fiducial survey parameters to determine the $t_{\rm dur}$ distribution for both populations. Then, in Sec. 6.4.2, we perform a 2-Sample Anderson-Darling test to determine the statistical significance at which a combined FFP and PBH $t_{\rm dur}$ distribution differs from a FFP distribution without PBHs.

6.4.1 Event rate estimation

The key input to our statistical methodology is the distribution of event durations, $t_{\rm dur}$. In order to compute this, we integrate over the differential event rate given by [99, 370]

$$\frac{d\Gamma}{dM\,dd_L\,dt_{\rm dur}\,du_{\rm min}} = \frac{2}{\sqrt{u_T^2 - u_{\rm min}^2}}\frac{v_T^4}{v_c^2}\exp\Big[-\frac{v_T^2}{v_c^2}\Big]\frac{\rho_M}{M}f(M)\varepsilon(t_{\rm dur}), \qquad (6.9)$$

where $f(M)$ is the probability distribution of lens masses (Eq. 6.6 or Eq. 6.8 for PBHs and FFPs, respectively), ρ_M is the mass density of the lens population, $\varepsilon(t_{\rm dur})$ is the detection efficiency, and v_T, the transverse velocity, is given by

$$v_T = 2\theta_E d_L\sqrt{u_T^2 - u_{\rm min}^2}/t_{\rm dur}. \qquad (6.10)$$

We set u_T, the maximum impact parameter that produces a detectable event, according to the procedure discussed in Sec. 6.2, adopting $A_T = 1.34$ as our fiducial threshold

113

magnification. This choice likely underestimates Roman's sensitivity, but is in keeping with the literature [298] (see also App. E). The event rate, Γ, is then evaluated as

$$
\Gamma = 2 \int_{M_{\min}}^{M_{\max}} dM \int_0^{d_s} dd_L \int_0^{u_T} du_{\min} \int_{t_{\min}}^{t_{\max}} dt_{\mathrm{dur}}
$$
$$
\frac{1}{\sqrt{u_T^2 - u_{\min}^2}} \frac{v_T^4}{v_c^2} \exp\Big[-\frac{v_T^2}{v_c^2} \Big] \frac{\rho_M}{M} f(M) \varepsilon(t_{\mathrm{dur}}), \quad (6.11)
$$

which we calculate using `LensCalcPy`,[3] a package to semi-analytically calculate microlensing observables. We take $t_{\min}$ to be 15 min and $t_{\max}$ to be 6×72 days, corresponding to the proposed cadence and observational duration of the Roman GBTDS. By performing the integral and multiplying the resulting rate by the GBTDS observational duration, we compute the expected total number of events that Roman will detect, denoted N_{FFP} and N_{PBH} for FFPs and PBHs, respectively.

In computing the event rate, we must specify the velocity and spatial distributions of the lenses. We assume that the FFP density tracks the stellar distribution of the galaxy, for which we adopt the exponential Koshimoto parametric model described in [320]. We take the PBH mass distribution to be a Navarro-Frenk-White profile given by

$$
\rho_M = \frac{\rho_0}{(\frac{r}{r_s})(1 + \frac{r}{r_s})^2}, \quad (6.12)
$$

where $\rho_0 = 4.88 \times 10^6 \ M_\odot \ \mathrm{kpc}^{-3}$ and $r_s = 21.5$ kpc [317]. While the relative source-lens velocity depends in general on the positions of both source and lens, we take $v_c = 220$ km/s for PBHs and $v_c = 200$ km/s for FFPs. The former is a typical value for a

$\overline{}$

[3]https://github.com/NolanSmyth/LensCalcPy

virialized DM halo [317], and the latter is approximately the average transverse velocity in the stellar disk (see e.g. [371] for a more complete description). As the majority of sources are in the Galactic Bulge, finite-source effects imply that the low-mass lenses we consider must be sufficiently far from the source in order to be detectable, making this simplification appropriate for the scope of this work. Ultimately, our results are fairly insensitive to changes in these choices of parameters, as the dominant uncertainty in our analysis arises from the normalization of the FFP mass function (see Sec. 6.5). However, we have compared our yields to those computed by [298], which employ a different Galactic model and mass function, and find $\mathcal{O}(1)$ agreement (see App. E).

For the mass function of PBHs, we assume a log-normal distribution (Eq. 6.6), while for FFPs, we adopt a power-law (Eq. 6.8) truncated at $M_{\mathrm{min}} = 10^{-13}\,M_\odot$ and $M_{\mathrm{max}} = 0.1\,M_\odot$ for computational purposes. These cutoffs have been chosen to lie well outside the mass range of Roman's sensitivity ($\approx 10^{-8}\,M_\odot - 10^{-3}\,M_\odot$) and we have verified numerically that they do not have an effect on the results.

The resulting yields for PBHs and FFPs are shown in Figs. 6.1 and 6.2. Fig. 6.1 shows the number of PBH events Roman is expected to see during its proposed observational duration as a function of M_{PBH} for $f_{\mathrm{PBH}} = 1$. The various curves correspond to different widths of the log-normal distribution, σ. Note that a $f_{\mathrm{PBH}} = 1$ abundance has already been ruled out by other microlensing surveys, hence the yields in unconstrained parameter space are necessarily smaller than the values in Fig. 6.1. We see that in unconstrained parameter space ($f \lesssim 10^{-2}$), Roman is expected to observe

up to $\approx 10^4$ PBH events.[4]

Fig. 6.2 shows the number of FFP events Roman is expected to see during its proposed observational duration as a function of p, the power-law index of the FFP mass distribution. The various curves correspond to various normalizations of the power law, with $\mathcal{N} = 10$ the fiducial value. The yield is only weakly-dependent on p, with our fiducial distribution yielding ≈ 400 events for a broad range of p.

6.4.2 Subpopulation identification

Our statistical analysis relies upon discriminating between t_{dur} distributions sourced by either purely FFPs or a combination of FFPs and PBHs. We will define the true distributions from which a particular set of detected events are sampled as $\mathcal{T}_{\mathrm{dur}}^{\mathrm{FFP}}$ and $\mathcal{T}_{\mathrm{dur}}^{\mathrm{FFP+PBH}}$. These distributions depend on a complex combination of several input parameters, including the power-law index of FFPs (p), the central mass of the PBH distribution (M_{PBH}), and the overall number of observed FFPs and PBHs (N_{FFP} and N_{PBH}). As such, they cannot be computed in a closed analytic form. We therefore choose to employ a test that discriminates based purely on empirical distribution functions without relying on an underlying analytic background model. The two-sample Anderson-Darling (AD) test is an effective choice for this situation[5], as it

---

[4]We note that though distinguishing FFPs from PBHs requires a statistical characterization when the observed yields of each are comparable, there are regions of parameter space in which PBH observations would well exceed the expected FFP yield, hence an identification of this population would be much simpler. Interestingly, this includes the parameter space in which PBHs explain the short-duration OGLE events, making their interpretation as FFPs more challenging.

[5]In practice, Roman will likely perform a Bayesian analysis to estimate the parameters controlling the lens distribution, which will be more sensitive than the methodology we employ here. However, the AD test provides a robust, if conservative, estimate of Roman's sensitivity.

is non-parameteric, hence requires no model input, and outperforms the Komolgorov-Smirnov test in the amount of data required for significance, see [216].

The AD test computes the significance at which two test distributions are sampled from the same underlying distribution. Given two distributions of size m, n sampled from the true distributions $\mathcal{T}_{\mathrm{dur}}^{\mathrm{FFP}}$ and $\mathcal{T}_{\mathrm{dur}}^{\mathrm{FFP+PBH}}$, we construct two empirical distribution functions, denoted $\mathcal{T}_{\mathrm{dur},m}^{\mathrm{FFP}}$ and $\mathcal{T}_{\mathrm{dur},n}^{\mathrm{FFP+PBH}}$, respectively. In the context of our analysis, $m = N_{\mathrm{FFP}}$ and $n = N_{\mathrm{FFP}} + N_{\mathrm{PBH}}$, where N_{FFP} and N_{PBH} are calculated as described in the previous subsection. In terms of these empirical distribution functions, the AD test statistic can be written as [402]:

$$A_{mn}^2 = \frac{mn}{N} \int_{-\infty}^{\infty} \frac{(\mathcal{T}_{\mathrm{dur},m}^{\mathrm{FFP}} - \mathcal{T}_{\mathrm{dur},n}^{\mathrm{FFP+PBH}})^2}{\mathcal{K}_N(1 - \mathcal{K}_N)}\, d\mathcal{K}_N \qquad (6.13)$$

where

$$\mathcal{K}_N = \frac{1}{N}(m\mathcal{T}_{\mathrm{dur},m}^{\mathrm{FFP}} + n\mathcal{T}_{\mathrm{dur},n}^{\mathrm{FFP+PBH}}) \qquad (6.14)$$

and $N \equiv m + n$. Note that by performing this test, we do not necessarily learn the PBH mass or abundance; merely that the distributions are separable.

To determine the sensitivity, we fix $\mathcal{N}$, p, M_{PBH}, and σ and allow $r \equiv N_{\mathrm{PBH}}/N_{\mathrm{FFP}}$ to vary. We set our limit at the value of r such that the AD test rejects the null hypothesis (i.e. both distributions are sampled from a pure FFP distribution) at 95% confidence. Representative examples of distributions that are distinguishable and indistinguishable by the AD test are displayed in Figs. 6.3 and 6.4, respectively. In Fig. 6.3, the PBH distribution peaks at t_{dur} values well above the majority of FFPs, hence is readily distinguishable. In Fig. 6.4, despite having the same number of observed FFPs

and PBHs as in Fig. 6.3, the two peaks overlap and the PBH population cannot be discriminated from background.

The weakness of this test is that in the low-statistics regime, two distributions may appear to have been drawn from different underlying distributions purely due to random fluctuations. In order to mitigate this effect, we perform our analysis 10 times and take the mean of the results, which we have verified numerically is sufficient for suppressing statistical fluctuation throughout our parameter space.

The analysis described above solely sets a limit on r, the *ratio* of observed PBH yield to FFP yield. In order to connect this to a physical density, we must calculate these yields. To do so, we employ `LensCalcPy` and produce two reference yield curves. The first is the expected yield of observable PBHs as a function of M_{PBH} for $f_{\mathrm{PBH}} = 1$, which we denote $N_{\mathrm{PBH}}^{f=1}(M_{\mathrm{PBH}})$ and appears in Fig. 6.1. The second is the expected yield of observable FFPs for $\mathcal{N} = 10$ as a function of p, which we denote $N_{\mathrm{FFP}}^{\mathcal{N}=10}(p)$ and appears in Fig. 6.2. The f_{PBH} corresponding to a particular r is therefore simply given by $f_{\mathrm{PBH}}(M_{\mathrm{PBH}}, p) = r \times [N_{\mathrm{FFP}}^{\mathcal{N}=10}(p)/N_{\mathrm{PBH}}^{f=1}(M_{\mathrm{PBH}})]$.

Our results depend implicitly on $\mathcal{N}$ and p, the true values of which are unknown. Existing observations suggest possible values in the range $p \approx 0.66 - 1.33$ and $\mathcal{N} \approx 2 - 20$ [248, 298, 360, 430]. We therefore choose to marginalize over this uncertainty by determining, for a given M_{PBH} and σ, the $p \in [0.66, 1.33]$ for which our analysis is weakest and adopting the corresponding f_{PBH} as our limit. To capture the uncertainty on $\mathcal{N}$, we choose to display three results: our fiducial results ($\mathcal{N} = 10$), as well as results in which $\mathcal{N}$ has been taken to be larger/smaller than our fiducial value by an order of

magnitude. This likely dramatically overestimates the uncertainty on this parameter given current constraints. However, by adopting this range, we encapsulate both the intrinsic uncertainty on its value as well as the uncertainty induced by our Galactic model (see App. E).

6.5   Results and Discussion

We display our ultimate sensitivity curves in Fig. 6.5. Existing constraints are shown in gray [306]. Additionally, we have included a dotted region ("OGLE hint") corresponding to the parameter space in which the short-timescale events observed by OGLE can be explained by a population of PBHs [371]. The solid curves correspond to a fiducial FFP normalization of $\mathcal{N} = 10$ and varying width of the log-normal PBH distribution, while the dashed and dot-dashed curves correspond to $\mathcal{N} = 1$ and 100, respectively for a monochromatic PBH mass distribution. As described in Sec. 6.4.2, these extreme values of $\mathcal{N}$ likely significantly overestimate the uncertainty on the FFP distribution, however, as can be seen in Fig. 6.5, even these variations only induce changes to the sensitivity at the sub-magnitude level. Note that the largest number density of FFPs corresponds to the *weakest* sensitivity, as a larger FFP yield requires a correspondingly larger PBH yield to achieve the same significance of discrimination. All curves displayed have been marginalized over p via the methodology described in 6.4.2.

Roman's sensitivity to identifying a subpopulation of PBHs peaks at $f_{\mathrm{PBH}} \sim$

10^{-4} in the mass range $M_{\text{PBH}} \approx 10^{-8} \, M_\odot - 10^{-6} \, M_\odot$. Both the location of this peak and the corresponding value of f_{PBH} can be understood simply. Since the number density of PBHs scales as $1/M_{\text{PBH}}$ for fixed f_{PBH}, the location of peak sensitivity corresponds to the lowest possible mass before finite-source effects reduce detectability. As discussed in Sec. 6.2, finite-source effects become relevant when $\theta_S \approx \theta_E$, a condition that can be rewritten in terms of mass to yield [197]

$$M_{\text{finite}} \approx \frac{\theta_S^2 c^2 d_L}{4G(1 - \frac{d_L}{d_S})} \left(\frac{d_L}{d_S} \right). \tag{6.15}$$

Assuming the source to have a radius comparable to that of the Sun and taking $d_S = 8.5$ kpc and $d_L = 7.0$ kpc as typical distances for lensing events in the Galactic Bulge, one finds $M_{\text{finite}} \approx 10^{-6} M_\odot$, which corresponds with the mass at which the sensitivity peaks in Fig. 6.5.

Similarly, f_{PBH} can be estimated at this peak. We find that at terrestrial masses, a PBH yield of roughly $10\% \, N_{\text{FFP}}$ is sufficient to identify the PBH subpopulation. Figs. 6.1 and 6.2 show that Roman's expected yield for FFPs and PBHs (at $\mathcal{N} = 10$ and $f_{\text{PBH}} = 1$) are $\mathcal{O}(1000)$ and $\mathcal{O}(10^6)$, respectively. We therefore see immediately that $N_{\text{PBH}} \approx 10\% \, N_{\text{FFP}}$ corresponds to $f_{\text{PBH}} \sim 10^{-4}$, which matches onto the maximal sensitivity shown in Fig. 6.5.

In the region of peak sensitivity, we find that sensitivity weakens with increasing width of the log-normal PBH distribution. This is not due to the fact that broader PBH distributions appear more akin to the FFP power law, but rather because broadening the PBH distribution pushes PBHs outside the observable window and lowers the

120

overall yield of observable PBH events. This can be seen in Fig. 6.1, where broadening the distribution causes a monotonic decrease in the number of detected events in the region of peak sensitivity.[6] For a fixed number of PBHs required for discrimination, this reduced detection rate must be compensated for by an increase in f_{PBH}.

The small decrease in sensitivity at $M_{\mathrm{PBH}} \approx 10^{-7} \, M_{\odot}$ is due to the peak of the PBH t_{dur} distribution coinciding with the peak of the FFP t_{dur} distribution, as can be seen in Fig. 6.4. At slightly higher and lower M_{PBH}, the two distributions peak at slightly different t_{dur}, improving sensitivity. However, this effect is small, as the sensitivity is predominantly governed by the PBH yield, which decreases rapidly at masses much above $10^{-6} \, M_{\odot}$ and below $10^{-8} \, M_{\odot}$.

In summary, our results show that even under conservative assumptions about Roman's detection threshold (Sec. 6.4.1) and the underlying background of FFPs (Sec 6.4.2), the Galactic Bulge Time Domain Survey will be highly sensitive to detecting a population of PBHs in new regions of parameter space. Excitingly, these regions include the parameter space in which existing short-timescale events have been suggested to hint at a subpopulation of PBHs at terrestrial masses [371]. Roman is therefore poised not only to make the first precise measurements of the FFP mass distribution, but to possibly uncover a subpopulation of PBHs lying within it as well.

---

[6]Note that well outside this region, the opposite effect can actually improve sensitivity marginally for broad distributions by pushing events into the observable window.

6.6   Conclusions

The launch of the Nancy Grace Roman Space Telescope will open a new window into low-mass astrophysical bodies. Though its Galactic Bulge Time Domain Survey targets bound and unbound exoplanets, we have shown that it will have unprecedented sensitivity to physics beyond the Standard Model as well. In particular, it will probe the fraction of dark matter composed of primordial black holes at abundances as low as $f_{\mathrm{PBH}} \approx 10^{-4}$ at PBH masses of roughly $10^{-6}\,M_\odot$, with a sensitivity that decreases as $\approx M_{\mathrm{PBH}}^{1/3}$ towards higher masses. Its region of sensitivity extends up to three orders of magnitude below existing constraints. This region fully encompasses the parameter space in which an excess of short-duration microlensing events observed by OGLE have been suggested to hint at a population of PBHs [371]. Therefore, Roman will conclusively determine the nature of these events, whether it be rogue worlds or our first glimpse of what lies on the dark side of the universe.
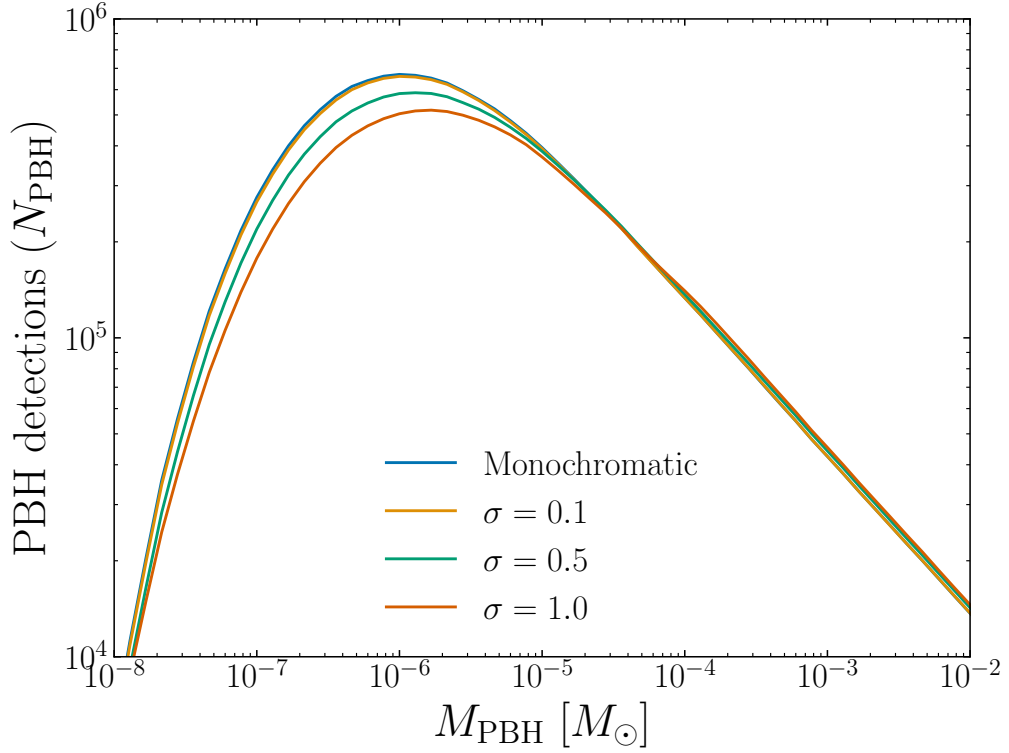
Figure 6.1: The total number of PBH microlensing events detectable by Roman for $f_{\mathrm{PBH}} = 1$ as a function of M_{PBH}. The different curves correspond to different widths of the PBH mass distribution (see Sec. 6.3.1).
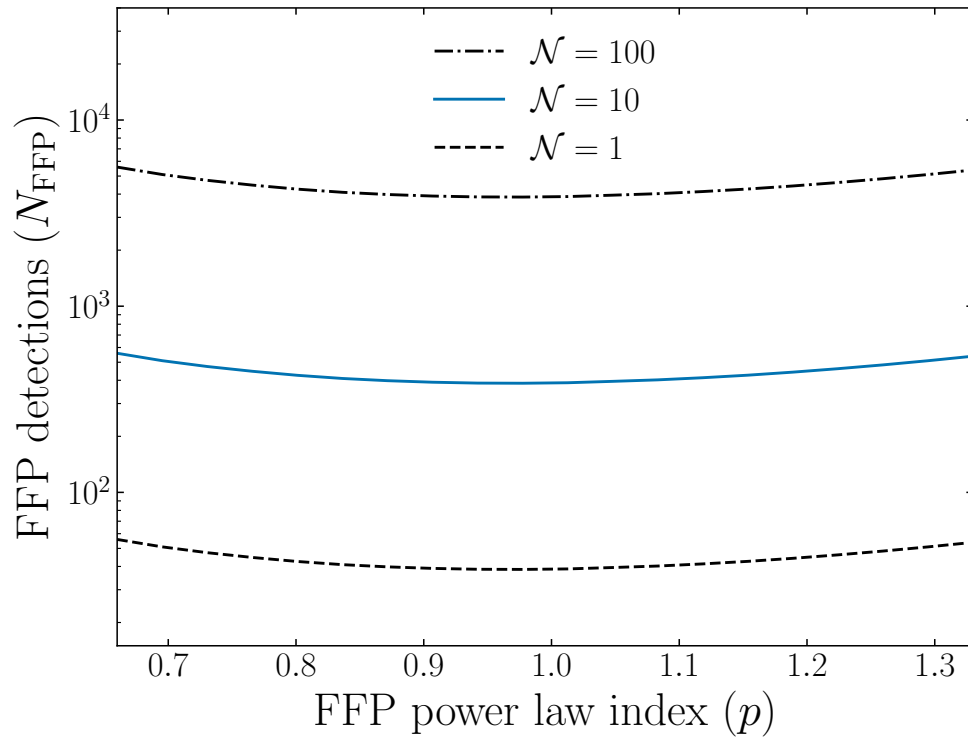
Figure 6.2: The total number of FFP microlensing events detectable by Roman as a function of p. The fiducial normalization $\mathcal{N} = 10$ is shown as a solid blue line, with $\mathcal{N} = 1$ and 100 shown as dashed and dash-dotted curves, respectively.
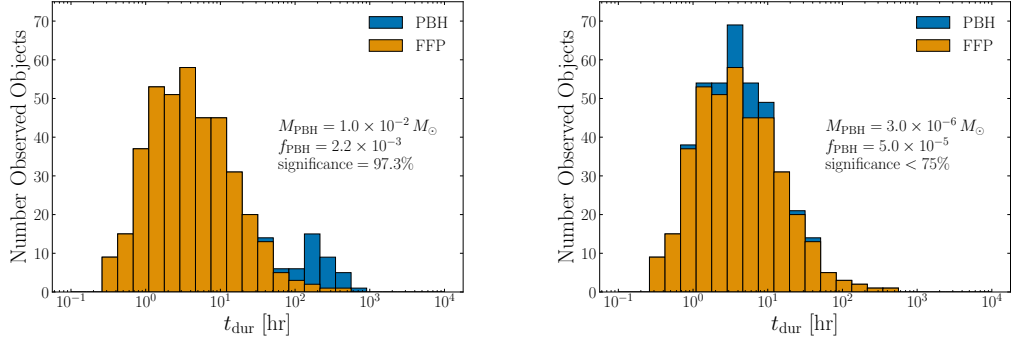
Figure 6.3: A stacked histogram of FFP and FFP+PBH distributions that are *distinguishable* at 95% confidence. These distributions correspond to parameter values of $\mathcal{N} = 10$, $p = 1.0$. The associated observable yields at this point in parameter space are $N_{\mathrm{FFP}} = 389$, $N_{\mathrm{PBH}} = 8\% \, N_{\mathrm{FFP}}$.

Figure 6.4: A stacked histogram of FFP and FFP+PBH distributions that are *indistinguishable* at 95% confidence. These distributions correspond to parameter values of $\mathcal{N} = 10$, $p = 1.0$. These parameters were chosen to yield the same observable yields as Fig. 6.3, $N_{\mathrm{FFP}} = 389$, $N_{\mathrm{PBH}} = 8\% \, N_{\mathrm{FFP}}$, however with a different location of the PBH peak.
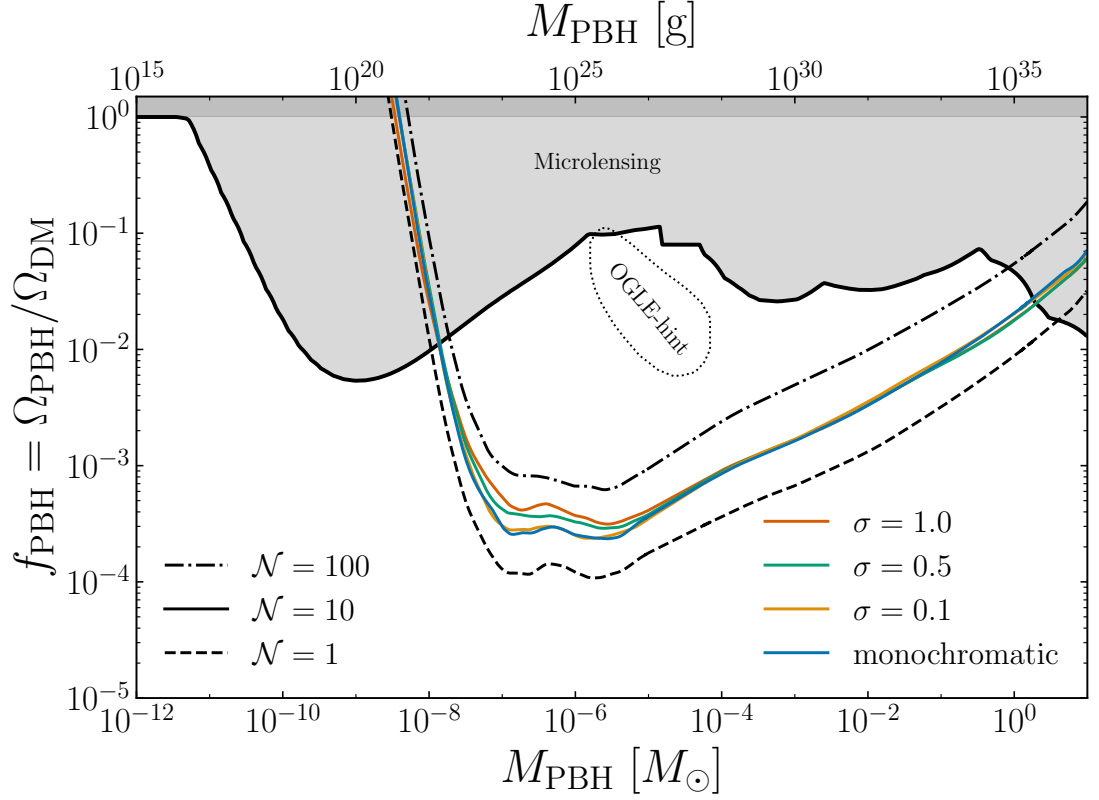
Figure 6.5: Roman sensitivity to detecting a population of PBHs in a background of FFPs. The solid curves correspond to $\mathcal{N} = 10$ and varying width σ of the log-normal PBH distribution, while the dashed and dot-dashed curves correspond to $\mathcal{N} = 1$ and 100, respectively. Existing constraints on the PBH abundance are shown in gray [306] and the region in which existing observations hint at a population of PBHs [371] is denoted "OGLE hint." See text for details.

Part IV

BSM phenomenology motivated

by the $(g-2)_\mu$ tension

Chapter 7

Introduction

As new particles can appear in loops affecting a particle's EDM, new particles in loops can affect a particle's magnetic dipole moment. Though unlike the electric dipole moment, a magnetic dipole moment is CP invariant, and so it does not rely on sources of CPV to arise. In particular, one could look to additional particles to explain a significant observed discrepancy with the SM. The anomalous magnetic moment of the muon has been measured most recently at Fermilab to be in tension with the standard model prediction to the tune of about 5σ. Specifically, the results from the Run-2/3 of the $g-2$ expriment [443] are 5.1σ from the SM prediction. This 5σ hold possibly less significance than others, however, due to open questions about the standard model prediction itself. Results from lattice gauge theory give different predictions that are only about 1σ discrepant, which is to say they aren't discrepant at all. The final chapter in that story has not been written yet, it is still under continued study.

The standard model, while outrageously good at predicting measured quanti-

ties is not without shortcomings (even ignoring the possible discrepancy of the muon magnetic moment). Descriptions of neutrino masses, dark matter, solutions to the strong CP problem all lie outside its scope [205, 313, 383]. It's best regarded as a low energy effective theory only valid below some energy cutoff Λ. Corrections to squared-masses of bosons in the low energy theory should have quadratic sensitivity to physics beyond that scale. Consider the parameter μ^2 in Eq. 1.7, which then should receive quantum corrections on the order,

$$\delta\mu^2 \sim \Lambda^2 \tag{7.1}$$

while the scalar potential of the Higgs is minimized by

$$\mu^2 = -\lambda v^2, \tag{7.2}$$

so that large fine-tuning is necessary to have a low energy theory with $v \ll \Lambda$. This is known as the hierachy problem.

On the other hands, fermion squared-masses are only logarithmically sensitive to a cutoff scale, due to a chiral symmetry of massless fermions. To avoid the large fine tuning in the Higgs sector, it is possible to introduce a symmetry between fermions and bosons, such that the quadratic sensitivity to the energy cutoff of the boson self-energy is necessarily cancelled. Such a theory is supersymmetry, precisely a theory of additional symmetry between fermions and bosons, so that each particle of the SM has a supersymmetric partner. If the SM particle is a boson, the partner is a fermion and vice versa. Since no superpartner of any SM particle with the same mass (or any mass) has ever been observed, the supersymmetric theory must be broken. For SUSY

129

breaking scales significantly above 1 TeV, this would reintroduce a lesser version of the same fine-tuning problem, called the little hierarchy problem [262].

Phenomenology of supersymmetric models depends on if a $U(1)$ symmetry of the theory is broken into a Z_2 symmetry called R-parity, in which supersymmetric partners and SM particles have opposite charge. These R-parity-conserving theories mandate that supersymmetric particles must be produced in pairs if starting from SM particles. It dictates that the lightest supersymmetric particle (LSP) cannot decay without violating momentum conservation, and thus is stable. If the LSP is electrically neutral and without color charge then it becomes a viable dark matter candidate.

New physics which can supply additional contributions to the anomalous moment of the muon could come in the form of high energy particles (multi-TeV) or much lighter particles, lighter than the muon itself. The multi-TeV range is accessible at the LHC while lighter particles can be searched for at lower energy colliders. The proposed DarkQuest experiment [78], an upgrade to the existing SpinQuest experiment at FermiLab (a fixed target experiment with a 120 GeV proton beam), would have significant reach in exploring parameter space of such new physics. In this section, we investigate phenomenology in both high energy experiments at the LHC [66] and the proposed fixed-target DarkQuest experiment at FermiLab [367].

Chapter 8

Explaining $(g-2)_\mu$ with Multi-TeV Sleptons

This chapter is based on [66].

8.1 Introduction

The Higgs discovery and the subsequent measurements of its properties at the LHC have been a crucial confirmation of the Standard Model (SM) of particle physics. Using data from Run I and Run II of the LHC, we know that the Higgs has SM-like properties and that its couplings to SM gauge bosons and third generation fermions agree with the SM predictions at the $10\% - 20\%$ level [18, 412]. Much less is known about the Higgs couplings to first and second generation fermions. Only recently, the LHC showed the first evidence for the Higgs coupling to muons [26, 422]. There is no evidence yet for the Higgs couplings to light quarks and electrons.

At the same time, the origin of the large hierarchies in the SM fermion masses, as well as the hierarchical structure of the CKM quark mixing matrix, constitute a long-standing open question in particle physics: the so-called SM flavor puzzle. One dynamical approach to this puzzle is to couple the first two generations exclusively to a new subleading source of electroweak symmetry breaking, in the form of a second Higgs doublet or some strong dynamics [68, 132, 238] (see also [125, 183, 207] for related ideas). Such a scenario adds new sources of flavor universality breaking to the SM. This is an experimentally viable option due to our lack of knowledge of the Higgs couplings to first and second generations. One concrete realization of this scenario is the Flavorful-Two-Higgs-Doublet-Model (F2HDM) [65].

Recently, new measurements involving muons have been reported by precision experiments. The LHCb collaboration has reported updated results on the ratio R_K of the rare B meson decay rates $B \to K\mu\mu$ and $B \to Kee$ [36], confirming earlier hints [31, 33, 35] for lepton flavor universality violation in rare B decays. In addition, a new measurement of the muon anomalous magnetic moment $a_\mu \equiv (g_\mu - 2)/2$ has been very recently reported by the Fermilab Muon g-2 collaboration, $a_\mu^{\mathrm{FNAL}} = 116\ 592\ 040(54) \times 10^{-11}$ [45]. This measurement is consistent with the previous measurement by the E821 experiment at BNL, $a_\mu^{\mathrm{BNL}} = 116\ 592\ 089(63) \times 10^{-11}$ [105]. The quoted combination of experimental results is $a_\mu^{\mathrm{exp}} = 116\ 592\ 061(41) \times 10^{-11}$ and deviates by 4.2σ from the SM prediction reported by the white chaper of the g-2 theory initiative, $a_\mu^{\mathrm{SM}} = 116\ 591\ 810(43) \times 10^{-11}$ [76], where the main uncertainty of the SM prediction comes

from the hadronic vacuum polarization contribution. This leads to

$$\Delta a_\mu = a_\mu^{\text{exp}} - a_\mu^{\text{SM}} = (251 \pm 59) \times 10^{-11} \,. \tag{8.1}$$

Although further scrutiny of this anomaly is needed (see e.g. [131, 171, 330]), it is interesting to ask what this anomaly may imply for new physics. In the SM, the contributions to the muon anomalous magnetic moment are chirally suppressed by the muon mass. Such a suppression can be lifted in the presence of new physics opening up the possibility to indirectly probe high new physics scales. Known examples include lepto-quark contributions that in some models can be enhanced by the ratio of top mass to muon mass, m_t/m_μ, or contributions in the minimal supersymmetric Standard Model (MSSM) that are enhanced by $\tan\beta$, the ratio of the vacuum expectation values (vevs) of the two Higgs doublets of the MSSM. Still, the typical scale of supersymmetric (SUSY) particles required to fully address the anomaly is in the few hundred GeV range. A crucial limiting factor in the MSSM is an upper bound on $\tan\beta$ that arises from demanding perturbative Yukawa couplings of the bottom quark and the tau lepton.

In this chaper, we formulate a new SUSY scenario, the flavorful supersymmetric Standard Model (FSSM). In this scenario, the contributions to a_μ can be more than an order of magnitude larger than in the MSSM. The scenario corresponds to the supersymmetrized version of the F2HDM. Its richer Higgs sector can consistently accommodate Higgsinos with $O(1)$ couplings to muons, leading to a strong enhancement of 1-loop SUSY contributions to a_μ. The chaper is organized as follows: In section 8.2, we briefly review the MSSM contributions to a_μ and show that sleptons in the few hun-

dred GeV mass range are generically preferred. In section 9.3.1, we present our model, a SUSY version of the SM with an extended scalar sector, and discuss the features most relevant in the context of $(g-2)_\mu$. In section 8.4 we detail the contributions to a_μ in our model and show that smuons as heavy as $6\,\text{TeV}$ can be responsible for the observed discrepancy. In section 8.5 we comment on further phenomenological implications of the model. We cover both indirect probes like lepton flavor violating tau decays and direct searches for electroweak SUSY particles at the LHC. Section 9.7 is reserved for conclusions and an outlook. In appendix F, we collect the loop functions entering the several contributions to $(g-2)_\mu$.

8.2 Muon Anomalous Magnetic Moment in the MSSM

We start by briefly reviewing the well known 1-loop slepton contributions to the anomalous magnetic moment of the muon in the MSSM [358]. We will neglect possible CP violating phases as they are strongly constrained by the non-observation of an electric dipole moment of the electron. We will also assume that the slepton soft masses are flavor conserving. Large flavor mixing between smuons and staus could in principle lead to chirally enhanced contributions to the anomalous magnetic moment of the muon [239, 344]. However, taking into account the stringent constraints from $\tau \to \mu\gamma$ [39, 83] it is found that flavor changing effects are negligibly small [240]. In presenting the MSSM contributions, it is convenient to distinguish loops with binos and winos. For masses of supersymmetric particles $m_{\text{SUSY}}^2 \gg m_Z^2$, one finds to a very good

134

approximation that the two contributions are given by

$$\Delta a_\mu^{\mathrm{MSSM}} = \Delta a_\mu^{\tilde{b}} + \Delta a_\mu^{\tilde{w}} , \tag{8.2}$$

$$\Delta a_\mu^{\tilde{b}} = \frac{g'^2}{192\pi^2} \frac{m_\mu^2}{m_{\tilde{\mu}_L}^2} \frac{M_1\mu}{m_{\tilde{\mu}_L}^2} \frac{t_\beta}{1 + \epsilon_\ell t_\beta} \left(2f_1(x_1, x_R) + f_2(x_1, x_\mu) - \frac{2}{x_R^2} f_2(y_1, y_\mu) \right) \tag{8.3}$$

$$\Delta a_\mu^{\tilde{w}} = \frac{5g^2}{192\pi^2} \frac{m_\mu^2}{m_{\tilde{\mu}_L}^2} \frac{M_2\mu}{m_{\tilde{\mu}_L}^2} \frac{t_\beta}{1 + \epsilon_\ell t_\beta} f_3(x_2, x_\mu) , \tag{8.4}$$

where, in the last equation, we have used the $SU(2)_L$ condition on the muon sneutrino mass $m_{\tilde{\nu}_\mu} = m_{\tilde{\mu}_L}$. The mass ratios are given by $x_1 = M_1^2/m_{\tilde{\mu}_L}^2$, $y_1 = M_1^2/m_{\tilde{\mu}_R}^2$, $x_\mu = \mu^2/m_{\tilde{\mu}_L}^2$, $y_\mu = \mu^2/m_{\tilde{\mu}_R}^2$, $x_2 = M_2^2/m_{\tilde{\mu}_L}^2$, and $x_R = m_{\tilde{\mu}_R}^2/m_{\tilde{\mu}_L}^2$. In the above expressions g and g' denote the $SU(2)_L$ and $U(1)_Y$ gauge couplings, M_2 and M_1 are the corresponding gaugino masses, μ is the Higgsino mass, and $m_{\tilde{\mu}_L}$, $m_{\tilde{\mu}_R}$ are the soft masses of the second generation slepton doublet and singlet, respectively. The parameter $\tan\beta = t_\beta = v_u/v_d$ is the ratio of the two Higgs vevs. We normalize the loop functions such that $f_1(1,1) = f_2(1,1) = f_3(1,1) = 1$. For completeness, their explicit expressions are given in the appendix F. The parameter ϵ_ℓ arises from $\tan\beta$-enhanced threshold corrections to the muon mass. It is given by [342] (see also [146, 268, 281, 387])

$$\epsilon_\ell = \frac{g'^2}{64\pi^2} \frac{M_1\mu}{m_{\tilde{\mu}_L}^2} \left(2g(x_1, x_R) + g(x_1, x_\mu) - \frac{2}{x_R} g(y_1, y_\mu) \right) - \frac{3g^2}{64\pi^2} \frac{M_2\mu}{m_{\tilde{\mu}_L}^2} g(x_2, x_\mu) , \tag{8.5}$$

where the loop function is given in the appendix F and it is normalized such that $g(1,1) = 1$. For a generic point in MSSM parameter space $\epsilon_\ell \sim 10^{-3}$, and its effect becomes relevant only for very large $\tan\beta$.

The dominant contribution to $(g - 2)_\mu$ typically comes from the wino loops. In the limit that all SUSY masses are equal and neglecting the threshold corrections,

the above expressions give

$$\Delta a_\mu^{\mathrm{MSSM}} \simeq 260 \times 10^{-11} \times \left(\frac{t_\beta}{50}\right) \times \left(\frac{500\,\mathrm{GeV}}{m_{\mathrm{SUSY}}}\right)^2 . \tag{8.6}$$

As it is evident from the above equation, even for large values of $\tan\beta \simeq 50$, the typical mass scale of the involved supersymmetric particles (sleptons and electroweakinos) is below $1\,\mathrm{TeV}$. This is confirmed by our numerical results in Figure 8.2 (see the blue and purple shaded regions). The fact that an explanation of $(g-2)_\mu$ prefers a light spectrum of sleptons and electroweakinos has been re-emphasized recently in several studies of the MSSM [47, 61, 82, 102, 155, 156, 178, 213, 256, 269, 284, 292, 441, 445, 454] and of MSSM extensions [40, 279]. It is possible to accommodate the preferred value for Δa_μ for a somewhat heavier spectrum ($m_{\mathrm{SUSY}} \gtrsim 1$ TeV) in corners of parameter space with either a very large μ term [213, 256] or with very large values of $\tan\beta$. However, for large values of μ, the MSSM scalar potential can develop charge breaking minima and vacuum stability considerations strongly constrain the parameter space. For very large values of $\tan\beta \gtrsim 70$ the bottom and tau Yukawa couplings develop Landau poles before the GUT scale, see e.g. [73].

In the following, we present a supersymmetric extension of the Standard Model that can accommodate the measured $(g-2)_\mu$ with multi-TeV sleptons. The corresponding region of parameter space is completely safe from vacuum stability constraints and all Yukawa couplings remain perturbative.

136

8.3 The MSSM with a Flavorful Higgs Sector

We supersymmetrize the flavorful 2HDM. Instead of the usual two chiral superfields $\hat{H}_u, \hat{H}_d$ of the MSSM, we introduce four chiral superfields $\hat{H}_u, \hat{H}_u', \hat{H}_d, \hat{H}_d'$ (see also [206, 217, 307] for other models with more than two Higgs doublets). Under the $SU(3)_c \times SU(2)_L \times U(1)_Y$ gauge symmetry, these superfields transform as $\hat{H}_u, \hat{H}_u' \sim (\mathbf{1}, \mathbf{2})_{+\frac{1}{2}}$ and $\hat{H}_d, \hat{H}_d' \sim (\mathbf{1}, \mathbf{2})_{-\frac{1}{2}}$. The superpotential of the model is given by

$$W = \mu_1 \hat{H}_u \hat{H}_d + \mu_2 \hat{H}_u' \hat{H}_d' + \mu_3 \hat{H}_u' \hat{H}_d + \mu_4 \hat{H}_u \hat{H}_d'$$

$$+ (Y_u \hat{H}_u + Y_u' \hat{H}_u')\hat{Q}\hat{U}^c + (Y_d \hat{H}_d + Y_d' \hat{H}_d')\hat{Q}\hat{D}^c + (Y_\ell \hat{H}_d + Y_\ell' \hat{H}_d')\hat{L}\hat{E}^c \,. \quad (8.7)$$

It contains four independent μ-terms as well as the Yukawa couplings Y_f and Y_f' of the Higgs doublets to the matter superfields. In the following we will denote this model as the flavorful supersymmetric Standard Model or FSSM.

We assume that the neutral components of the Higgs scalars acquire vevs given by v_u, v_u', v_d, and v_d', such that $v_u^2 + v_d^2 + v_u'^2 + v_d'^2 = v^2 = (246\,\mathrm{GeV})^2$. In addition to the usual vev ratio $\tan\beta = t_\beta = v_u/v_d$, we also introduce the ratios $\tan\beta_u = t_{\beta_u} = v_u/v_u'$ and $\tan\beta_d = t_{\beta_d} = v_d/v_d'$. Generic Yukawa couplings Y_f and Y_f' violate the principle of natural flavor conservation. They can lead to large neutral Higgs mediated flavor changing neutral currents and are therefore strongly constrained. In the following we will consider the "flavorful" ansatz for the Yukawa couplings as suggested in [68] that avoids the most stringent flavor constraints due to an approximate flavor symmetry [68]. In this ansatz, the doublets $\hat{H}_u, \hat{H}_d$ couple exclusively to third generation fermions, while $\hat{H}_u', \hat{H}_d'$ provide masses for the first and second generations. In the case of the leptons

we have (neglecting SUSY threshold effects)[1]

$$Y'_\ell \simeq \frac{\sqrt{2}}{v'_d} \begin{pmatrix} m_e & x_{e\mu} m_e & x_{e\tau} m_e \\ x_{\mu e} m_e & m_\mu & x_{\mu\tau} m_\mu \\ x_{\tau e} m_e & x_{\tau\mu} m_\mu & x_{\tau\tau} m_\mu \end{pmatrix}, \qquad Y_\ell \simeq \frac{\sqrt{2}}{v_d} \begin{pmatrix} 0 & 0 & 0 \\ 0 & 0 & 0 \\ 0 & 0 & m_\tau \end{pmatrix}. \quad (8.8)$$

The rank-1 Yukawa coupling Y_ℓ preserves an $SU(2)^2 = SU(2)_L \times SU(2)_E$ flavor symmetry acting of the first two generations of left-handed and right-handed lepton fields. Assuming that soft SUSY breaking is flavor universal, the $SU(2)^2$ symmetry is minimally broken by the second Yukawa coupling Y'_ℓ, implying that flavor changing effects between the second and first generation leptons are strongly suppressed. The x_{ij} parameters indicate how much the Yukawa coupling Y'_ℓ differs from a democratic ansatz. The parameters $x_{\tau\mu}$ and $x_{\mu\tau}$ can be constrained by the experimental bounds on flavor violating tau decays like $\tau \to \mu\gamma$ and $\tau \to 3\mu$, while the corresponding parameters with electrons, $x_{\tau e}$ and $x_{e\tau}$, can be constrained from data on $\tau \to e$ transitions. Due to the $SU(2)^2$ flavor symmetry, the parameters $x_{\mu e}$ and $x_{e\mu}$ are unobservable. Effects in the highly constrained $\mu \to e$ transitions like $\mu \to e\gamma$ can be expected only if the products $x_{\mu\tau} x_{\tau e}$ or $x_{e\tau} x_{\tau\mu}$ are sizable (see section 8.5 for more details).

In addition to the leptonic Yukawa couplings shown above, the most relevant ingredients for the discussion of $(g-2)_\mu$ are the smuon masses as well as the chargino and neutralino masses. For the smuon mass matrix we find after electroweak symmetry

---

[1]A similar structure can be implemented in the quark sector.

breaking

$$M_{\tilde{\mu}}^2 = \begin{pmatrix} m_{\tilde{\mu}_L}^2 & -m_\mu t_\beta t_{\beta_d}(\mu_4 + \mu_2/t_{\beta_u}) \\ -m_\mu t_\beta t_{\beta_d}(\mu_4 + \mu_2/t_{\beta_u}) & m_{\tilde{\mu}_R}^2 \end{pmatrix}, \tag{8.9}$$

where we have neglected the small D-term contributions, as well as the contributions from soft trilinear terms. Neglecting the trilinear terms is a good approximation as long as $v_d' \ll v_u$. Note that in eq. (8.9) we neglected left-right mixing between smuons and staus proportional to $x_{\tau\mu}$ and $x_{\mu\tau}$. Such mixing is of no relevance to the calculation of $(g-2)_\mu$. We will comment on its effect on $\tau \to \mu\gamma$ in section 8.5.

The model features an extended electroweakino sector, because of the additional Higgsinos. It contains three charginos and six neutralinos with the following mass matrices

$$M_{\chi^\pm} = \begin{pmatrix} M_2 & \frac{g}{\sqrt{2}}v_u & \frac{g}{\sqrt{2}}v_u' \\ \frac{g}{\sqrt{2}}v_d & \mu_1 & \mu_3 \\ \frac{g}{\sqrt{2}}v_d' & \mu_4 & \mu_2 \end{pmatrix}$$

$$M_{\chi^0} = \begin{pmatrix} M_1 & 0 & -\frac{g'}{2}v_d & \frac{g'}{2}v_u & -\frac{g'}{2}v_d' & \frac{g'}{2}v_u' \\ 0 & M_2 & \frac{g}{2}v_d & -\frac{g}{2}v_u & \frac{g}{2}v_d' & -\frac{g}{2}v_u' \\ -\frac{g'}{2}v_d & \frac{g}{2}v_d & 0 & -\mu_1 & 0 & -\mu_3 \\ \frac{g'}{2}v_u & -\frac{g}{2}v_u & -\mu_1 & 0 & -\mu_4 & 0 \\ -\frac{g'}{2}v_d' & \frac{g}{2}v_d' & 0 & -\mu_4 & 0 & -\mu_2 \\ \frac{g'}{2}v_u' & -\frac{g}{2}v_u' & -\mu_3 & 0 & -\mu_2 & 0 \end{pmatrix}, \tag{8.10}$$

where we have considered the basis $(\tilde{W}^\pm, \tilde{H}^\pm, \tilde{H}'^\pm)$ and $(\tilde{B}, \tilde{W}^0, \tilde{H}_d^0, \tilde{H}_u^0, \tilde{H}_d'^0, \tilde{H}_u'^0)$ for charginos and neutralinos, respectively. For the calculation of $(g-2)_\mu$ it is convenient

to rotate the Higgsino states to diagonalize the 2×2 Higgsino sub-matrix:

$$
\begin{pmatrix} c_d & s_d \\ -s_d & c_d \end{pmatrix} \begin{pmatrix} \mu_1 & \mu_3 \\ \mu_4 & \mu_2 \end{pmatrix} \begin{pmatrix} c_u & s_u \\ -s_u & c_u \end{pmatrix} = \begin{pmatrix} \mu & 0 \\ 0 & \tilde{\mu} \end{pmatrix} , \qquad (8.11)
$$

where we have introduced the mixing angles $c_{d,u} \equiv \cos\theta_{d,u}$, $s_{d,u} \equiv \sin\theta_{d,u}$. For gaugino and Higgsino masses sufficiently above the electroweak scale, the masses of the three charginos and of the six neutralinos are approximately $m_{\chi_i^\pm} \simeq (M_2, \mu, \tilde{\mu})$ and $m_{\chi_i^0} \simeq (M_1, M_2, \mu, \mu, \tilde{\mu}, \tilde{\mu})$. In the following section we will report the contributions to the anomalous magnetic moment of the muon in terms of the Higgsino parameters θ_u, θ_d and $\mu, \tilde{\mu}$.

8.4 FSSM Contributions to $(g-2)_\mu$

Similar to the MSSM, it is possible to split the contributions to the anomalous magnetic moment of the muon into bino mediated and wino mediated contributions. For supersymmetric particles that are sufficiently heavier than the electroweak scale,
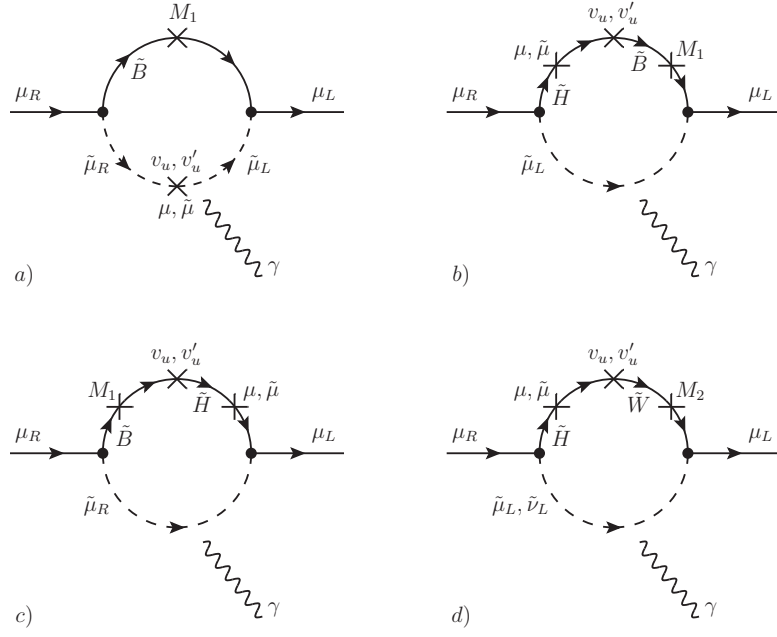
Figure 8.1: The leading 1-loop contributions to the anomalous magnetic moment of the muon. The external photon has to be attached in all possible ways to the loops. Diagrams a), b), and c) involve binos, while diagram d) involves winos. The threshold corrections to the muon mass correspond to analogous diagrams without the external photon.

$m_{\text{SUSY}}^2 \gg m_Z^2$, we find

$$\Delta a_\mu^{\text{FSSM}} = \Delta a_\mu^{\tilde{b}} + \Delta a_\mu^{\tilde{w}} \;, \tag{8.12}$$

$$\Delta a_\mu^{\tilde{b}} = \frac{g'^2}{192\pi^2} \frac{m_\mu^2}{m_{\tilde{\mu}_L}^2} \frac{t_\beta t_{\beta_d}}{1 + \epsilon_\ell t_\beta t_{\beta_d}} \tag{8.13}$$

$$\times \left[s_d \left(c_u - \frac{s_u}{t_{\beta_u}} \right) \frac{M_1\mu}{m_{\tilde{\mu}_L}^2} \left(2f_1(x_1, x_R) + f_2(x_1, x_\mu) - \frac{2}{x_R^2} f_2(y_1, y_\mu) \right) \right.$$

$$\left. + c_d \left(s_u + \frac{c_u}{t_{\beta_u}} \right) \frac{M_1\tilde{\mu}}{m_{\tilde{\mu}_L}^2} \left(2f_1(x_1, x_R) + f_2(x_1, x_{\tilde{\mu}}) - \frac{2}{x_R^2} f_2(y_1, y_{\tilde{\mu}}) \right) \right] \;,$$

$$\Delta a_\mu^{\tilde{w}} = \frac{5g^2}{192\pi^2} \frac{m_\mu^2}{m_{\tilde{\mu}_L}^2} \frac{t_\beta t_{\beta_d}}{1 + \epsilon_\ell t_\beta t_{\beta_d}} \left[s_d \left(c_u - \frac{s_u}{t_{\beta_u}} \right) \frac{M_2\mu}{m_{\tilde{\mu}_L}^2} f_3(x_2, x_\mu) \right. \tag{8.14}$$

$$141 \qquad \left. + c_d \left(s_u + \frac{c_u}{t_{\beta_u}} \right) \frac{M_2\tilde{\mu}}{m_{\tilde{\mu}_L}^2} f_3(x_2, x_{\tilde{\mu}}) \right] \;,$$

with the threshold correction parameter ϵ_ℓ given by

$$
\begin{aligned}
\epsilon_\ell = \frac{g'^2}{64\pi^2} &\left[s_d \left(c_u - \frac{s_u}{t_{\beta_u}} \right) \frac{M_1 \mu}{m_{\tilde{\mu}_L}^2} \left(2g(x_1, x_R) + g(x_1, x_\mu) - \frac{2}{x_R} g(y_1, y_\mu) \right) \right. \\
&\left. + c_d \left(s_u + \frac{c_u}{t_{\beta_u}} \right) \frac{M_1 \tilde{\mu}}{m_{\tilde{\mu}_L}^2} \left(2g(x_1, x_R) + g(x_1, x_{\tilde{\mu}}) - \frac{2}{x_R} g(y_1, y_{\tilde{\mu}}) \right) \right] \\
-\frac{3g^2}{64\pi^2} &\left[s_d \left(c_u - \frac{s_u}{t_{\beta_u}} \right) \frac{M_2 \mu}{m_{\tilde{\mu}_L}^2} g(x_2, x_\mu) + c_d \left(s_u + \frac{c_u}{t_{\beta_u}} \right) \frac{M_2 \tilde{\mu}}{m_{\tilde{\mu}_L}^2} g(x_2, x_{\tilde{\mu}}) \right] , \quad (8.15)
\end{aligned}
$$

where, similarly to x_μ and y_μ, we have defined $x_{\tilde{\mu}} = \tilde{\mu}^2/m_{\tilde{\mu}_L}^2$ and $y_{\tilde{\mu}} = \tilde{\mu}^2/m_{\tilde{\mu}_R}^2$. Note that the loop functions are identical to the MSSM case. In fact, the expressions above largely resemble the MSSM result shown in section 8.2. The relevant Feynman diagrams containing Higgsinos, binos, winos, and sleptons are shown in Figure 8.1[2]. As in the MSSM, the dominant contribution typically comes from the loops containing a wino. If all SUSY masses are set equal, the wino loops dominate over the bino loops by a factor $5g^2/g'^2 \simeq 17$. In contrast to the MSSM, we find two sets of contributions that are proportional to either one of the Higgsino mass eigenvalues μ and $\tilde{\mu}$. The main difference to the MSSM is the overall proportionality to the product of the vev ratios $\tan\beta \times \tan\beta_d = v_u/v_d'$. The additional factor $\tan\beta_d$ can increase the contributions in our setup by an order of magnitude or more compared to the MSSM. Note that the threshold correction remains of order $\epsilon_\ell \sim 10^{-3}$ in our setup. However, as it is multiplied by the product $\tan\beta \times \tan\beta_d$ (see Eqs. (8.12), (8.14)), it can have an $O(1)$ impact on the contribution to the $(g-2)_\mu$ (we show its effect explicitly in Figure 8.2 below).

A relevant bound on the size of $\tan\beta_d$ is given by perturbativity considerations.

---

[2]In addition, the model also predicts contributions from 1-loop diagrams containing leptons and Higgs bosons. However, such contributions to Δa_μ are not chirally enhanced by $\tan\beta$ factors and therefore can be neglected.

Yukawa couplings that are larger than $O(1)$ at the TeV scale develop Landau poles before reaching the GUT scale. Requiring that the muon Yukawa of the Higgs field H'_d stay perturbative up to the GUT scale, leads to the approximate bound[3]

$$Y'_{\mu\mu} \simeq \frac{\sqrt{2}m_\mu}{v} \frac{t_\beta t_{\beta_d}}{1 + \epsilon_\ell t_\beta t_{\beta_d}} \lesssim 0.7 \ . \tag{8.16}$$

Differently from the MSSM, the requirement of perturbativity of the tau and bottom Yukawa couplings sets weaker bounds on the values of $\tan\beta$ and $\tan\beta_d$. In the limit that all SUSY masses are equal and assuming $O(1)$ mixing in the Higgsino sector $s_d \sim c_d \sim s_u \sim c_u \sim 1/\sqrt{2}$ we find

$$
\begin{aligned}
\Delta a_\mu &\simeq 220 \times 10^{-11} \times \left(\frac{t_\beta}{20}\right) \times \left(\frac{t_{\beta_d}}{15}\right) \times \left(\frac{0.46}{1 + \epsilon_\ell t_\beta t_{\beta_d}}\right) \times \left(\frac{2.0\,\mathrm{TeV}}{m_{\mathrm{SUSY}}}\right)^2 \quad (8.17) \\
&\simeq 240 \times 10^{-11} \times \left(\frac{Y'_{\mu\mu}}{0.7}\right) \times \left(\frac{2.5\,\mathrm{TeV}}{m_{\mathrm{SUSY}}}\right)^2 \ . \quad (8.18)
\end{aligned}
$$

Keeping in mind the estimated bound on the muon Yukawa discussed above, we find that the generic scale of supersymmetric particles can be larger by a factor of $\simeq 5$ compared to the MSSM, while still producing the desired effect in the anomalous magnetic moment of the muon.

In Figure 8.2, we show the regions of SUSY masses that are preferred by the anomalous magnetic moment of the muon in several benchmark cases. For simplicity, we assume that the masses of the left-handed and right-handed smuons are equal, as do

---

[3]We estimate that the perturbativity bound on the muon Yukawa in our model will be similar to the bound on the tau Yukawa in the MSSM. In Eq. (8.16), we therefore quote the bound on the tau Yukawa coupling at a scale of 1 TeV that has been found in the MSSM requiring the Yukawa coupling to be smaller than $\sqrt{4\pi}$ at the GUT scale [73]. A dedicated renormalization group study of the full set of third and second generation Yukawa couplings and of the gauge couplings would be required to establish a precise bound on the muon Yukawa coupling in our model, but we do not expect the result to change significantly.

we for the masses of the bino, the wino, and the Higgsinos. In the colored bands we find agreement with (8.1) at the 1σ and 2σ level. The purple and blue bands correspond to the MSSM with $\tan\beta = 20$ and $\tan\beta = 50$, respectively. We see that for $\tan\beta = 50$, sleptons can be at most at around $1\,\text{TeV}$, if gauginos and Higgsinos are in the few hundred GeV range. The yellow and orange bands show two benchmark scenarios in the FSSM assuming a generic $O(1)$ mixing in the Higgsino sector $s_d \sim c_d \sim s_u \sim c_u \sim 1/\sqrt{2}$. The yellow band corresponds to moderate values for $\tan\beta = 20$ and $\tan\beta_d = 15$. In such a scenario the smuons can be as heavy as $3\,\text{TeV}$ while still explaining $(g-2)_\mu$. The dashed yellow lines show the region favored by $(g-2)_\mu$ in this FSSM scenario neglecting the SUSY threshold corrections to the muon mass (i.e. ϵ_ℓ is set to zero). We clearly see that the threshold corrections have an order 1 impact and cannot be neglected. Finally, the orange band shows a scenario in which we choose a large muon Yukawa coupling, $Y'_{\mu\mu} = 0.7$, that we estimate to be close to the bound from demanding perturbativity up to the GUT scale. In this case, smuons can be as heavy as $6\,\text{TeV}$.

8.5 Phenomenological Implications

In addition to the contributions to Δa_μ, the FSSM predicts contributions to the anomalous magnetic moments of the electron and of the tau, Δa_e and Δa_τ. Due to the minimally broken $SU(2)^2$ lepton symmetry, the setup predicts the relation

$$\Delta a_e \simeq \frac{m_e^2}{m_\mu^2} \Delta a_\mu \simeq 5.8 \times 10^{-14} \times \left(\frac{\Delta a_\mu}{251 \times 10^{-11}} \right) , \qquad (8.19)$$

144

which is almost an order of magnitude smaller than the uncertainties of the experimental

determination [270], as well as the uncertainties of the SM prediction that depends cru-

cially on the value of the fine structure constant [354, 381]. There is no strict correlation

of Δa_μ and Δa_τ, but generically we expect

$$\Delta a_\tau \sim \frac{m_\tau^2}{m_\mu^2} \frac{1}{t_{\beta_d}} \Delta a_\mu \simeq 4.7 \times 10^{-8} \times \left(\frac{15}{t_{\beta_d}} \right) \times \left(\frac{\Delta a_\mu}{251 \times 10^{-11}} \right) \, , \qquad (8.20)$$

which is far below foreseeable experimental sensitivities [38].

Similar to the 1-loop slepton contributions to anomalous magnetic moments,

the FSSM setup also gives contributions to the radiative lepton decays $\tau \to \mu\gamma$, $\tau \to e\gamma$,

and $\mu \to e\gamma$. While the relevant off-diagonal couplings $x_{\tau e}$, $x_{e\tau}$, $x_{\tau\mu}$, and $x_{\mu\tau}$ in the

lepton Yukawa matrix (8.8) do not enter the predictions for Δa_μ at the considered level

of accuracy, it is nonetheless interesting to explore their implications. In the limit in

which both left-handed and right-handed smuons and staus have equal masses we find

simple relations between the 1-loop slepton contributions to the anomalous magnetic

moment of the muon and the branching ratios of the decays $\tau \to \mu\gamma$, $\tau \to e\gamma$, and

145

$\mu \to e\gamma$

$$\begin{aligned}
\mathrm{BR}(\tau \to \mu\gamma) &\simeq 24\pi^3 \alpha_{\mathrm{em}} \frac{v^4}{m_\mu^4} \left(\Delta a_\mu\right)^2 \left(x_{\tau\mu}^2 + x_{\mu\tau}^2\right) \times \mathrm{BR}(\tau \to \mu\nu_\tau \bar{\nu}_\mu) \\
&\simeq 1.7 \times 10^{-8} \times \left(\frac{\Delta a_\mu}{251 \times 10^{-11}}\right)^2 \left[\left(\frac{x_{\tau\mu}}{0.01}\right)^2 + \left(\frac{x_{\mu\tau}}{0.01}\right)^2\right] , \qquad (8.21) \\
\mathrm{BR}(\tau \to e\gamma) &\simeq 24\pi^3 \alpha_{\mathrm{em}} \frac{v^4}{m_\mu^4} \frac{m_e^2}{m_\mu^2} \left(\Delta a_\mu\right)^2 \left(x_{\tau e}^2 + x_{\mu e}^2\right) \times \mathrm{BR}(\tau \to e\nu_\tau \bar{\nu}_\mu) \\
&\simeq 4.1 \times 10^{-9} \times \left(\frac{\Delta a_\mu}{251 \times 10^{-11}}\right)^2 \left[\left(\frac{x_{\tau e}}{1.0}\right)^2 + \left(\frac{x_{e\tau}}{1.0}\right)^2\right] , \qquad (8.22) \\
\mathrm{BR}(\mu \to e\gamma) &\simeq 24\pi^3 \alpha_{\mathrm{em}} \frac{v^4}{m_\mu^4} \frac{m_e^2}{m_\tau^2} \left(\Delta a_\mu\right)^2 \left(x_{e\tau}^2 x_{\tau\mu}^2 + x_{\mu\tau}^2 x_{\tau e}^2\right) \\
&\simeq 8.2 \times 10^{-15} \times \left(\frac{\Delta a_\mu}{251 \times 10^{-11}}\right)^2 \left[\left(\frac{x_{e\tau} x_{\tau\mu}}{0.01}\right)^2 + \left(\frac{x_{\mu\tau} x_{\tau e}}{0.01}\right)^2\right] \qquad (8.23)
\end{aligned}$$

where we used $\mathrm{BR}(\tau \to \mu\nu_\tau \bar{\nu}_\mu) \simeq 17.4\%$ and $\mathrm{BR}(\tau \to e\nu_\tau \bar{\nu}_\mu) \simeq 17.8\%$ [456].

We can compare these predictions to the current experimental bounds. From the bound $\mathrm{BR}(\tau \to \mu\gamma)_{\mathrm{exp}} < 4.2 \times 10^{-8}$ [39, 83] we see that the couplings $x_{\tau\mu}$ and $x_{\mu\tau}$ have to be of order 10^{-2} in order not to violate the bound from $\tau \to \mu\gamma$. The smallness of these couplings suggests that an additional lepton flavor symmetry gives structure to the lepton Yukawa coupling Y_ℓ'. If the coupling $x_{\tau e}$ or $x_{e\tau}$ is of order 1, the branching ratio of $\tau \to e\gamma$ is predicted below the current bound, $\mathrm{BR}(\tau \to e\gamma)_{\mathrm{exp}} < 3.3 \times 10^{-8}$ [39, 83], but in reach of the Belle II experiment [62]. Once the bound from $\mathrm{BR}(\tau \to \mu\gamma)$ is taken into account, the $\mu \to e\gamma$ branching ratio is predicted well below the current constraint $\mathrm{BR}(\mu \to e\gamma)_{\mathrm{exp}} < 4.2 \times 10^{-13}$ [88].

In the FSSM, we also find tree level neutral Higgs contributions to lepton flavor violating decays $\tau \to 3\mu$, $\tau \to 3e$, and $\mu \to 3e$. The most constraining decay is expected to be $\tau \to 3\mu$ as it involves the largest Yukawa couplings enhanced by the product $t_\beta t_{\beta_d}$.

Neglecting mixing among the Higgs bosons and using the results from [380], we find

$$\text{BR}(\tau \to 3\mu) \quad \simeq \quad \frac{m_\mu^4}{4m_{H_d'}^4} \frac{t_\beta^4 t_{\beta_d}^4}{(1 + \epsilon_\ell t_\beta t_{\beta_d})^4} \left(x_{\tau\mu}^2 + x_{\mu\tau}^2 \right) \times \text{BR}(\tau \to \mu\nu_\tau\bar{\nu}_\mu)$$

$$\simeq \quad 1.0 \times 10^{-9} \times \left(\frac{Y_{\mu\mu}'}{0.7} \right)^4 \times \left(\frac{1.0\,\text{TeV}}{m_{H_d'}} \right)^4 \times \left[\left(\frac{x_{\tau\mu}}{0.01} \right)^2 + \left(\frac{x_{\mu\tau}}{0.01} \right)^2 \right] . \quad (8.24)$$

Comparing to the experimental bound obtained by the Belle collaboration, $\text{BR}(\tau \to 3\mu)_{\text{exp}} < 2.1 \times 10^{-8}$ [278] (see also [34, 327]), we see that TeV scale Higgs bosons are viable and could lead to branching ratios that are accessible at Belle II and LHCb [30, 62].

Finally, we comment on the prospects of testing the SUSY parameter space favored by $(g-2)_\mu$ at the LHC. The sleptons necessary for addressing the $(g-2)_\mu$ anomaly are being searched for by the ATLAS and CMS collaborations. Particularly, the most relevant slepton signature is the slepton pair production $pp \to \tilde{\ell}\tilde{\ell}$, followed by the decay into a lepton and the lightest neutralino $\tilde{\ell}\tilde{\ell} \to (\ell\tilde{\chi}^0)(\ell\tilde{\chi}^0)$. The most stringent bounds on the slepton parameter space come from the analyses [19, 421] performed with the full Run II data set. These searches show that, in the case of degenerate left-handed and right-handed smuons, slepton masses as large as ~ 600 GeV are now generically probed if the mass splitting with the lightest neutralino $m_{\tilde{\ell}} - m_{\tilde{\chi}^0}$ is sufficiently large. In the case of a compressed spectrum, the limits are weaker and allow sleptons as light as ~ 250 GeV for mass splitting $m_{\tilde{\ell}} - m_{\tilde{\chi}^0} \lesssim 30$ GeV [23].

The existing searches probe already part of the MSSM parameter space that is able to explain the $(g-2)_\mu$ anomaly. However, depending on the specific electroweakino spectrum, sizable regions of parameter space are left unexplored. For example, for the

147

specific spectrum fixed in Figure 8.2 ($M_1 = M_2 = \mu$), the aforementioned LHC slepton

searches can only set a weak bound because of the dilution of the branching ratio of the

slepton into the lightest neutralino and a lepton. For that spectrum, additional slepton

decay modes arise including $\tilde{\mu} \to \mu\tilde{\chi}_2^0, \nu\tilde{\chi}_{1,2}^{\pm}$ with the subsequent decay of $\tilde{\chi}_2^0$ and $\tilde{\chi}_{1,2}^{\pm}$

to the lightest neutralino and jets or leptons. It will be interesting to search for these

new slepton cascade decays in the coming years at the LHC to probe further regions of

MSSM parameter space that can address the $(g-2)_\mu$ anomaly.

The slepton phenomenology in the FSSM is even richer. Due to the extended

electroweakino sector, several cascade decays are possible, giving rise to signatures with

multi-leptons (or jets) and missing energy. We leave the study of such signatures for

future work. Due to the generically heavier slepton masses in the FSSM to address the

$(g-2)_\mu$ anomaly, the sleptons that we considered in this chaper are outside the reach

of the LHC. We expect some of the scenarios favored by $(g-2)_\mu$ to be probed at a 100

TeV collider through a $pp \to \tilde{\ell}\tilde{\ell} \to (\ell\tilde{\chi}^0)(\ell\tilde{\chi}^0)$ search [87].

8.6 Conclusions and Outlook

The recent result of the Fermilab Muon g-2 collaboration confirms the long-

standing discrepancy in the anomalous magnetic moment of the muon, $(g-2)_\mu$. Moti-

vated by this result, we constructed a supersymmetric extension of the Standard Model

that can give more than an order of magnitude larger contributions to the $(g-2)_\mu$ than

the MSSM. The model, that we dub flavorful supersymmetric Standard Model (FSSM),

is based on an extended electroweak breaking sector with Yukawa couplings that follow the flavorful ansatz suggested in [68].

One set of Higgs doublets couples exclusively to the third generation through a rank-1 Yukawa coupling, while a second set of Higgs doublets couples also to the first and second generations. One of the Higgs fields can have an $O(1)$ coupling to muons. Loop contributions to $(g-2)_\mu$ that contain the corresponding Higgsino state are strongly enhanced. In contrast to the MSSM, where the SUSY particles generically have to be below the $1\,\mathrm{TeV}$ scale, in the FSSM, the $(g-2)_\mu$ result can be comfortably explained by sleptons in the multi-TeV mass range.

We explored further phenomenological implications of the model, in particular for the anomalous magnetic moments of the electron and the tau, as well as for lepton flavor violation. We found that existing bounds on $\tau \to \mu\gamma$ already give relevant constraints on the lepton flavor violating Yukawa couplings of the model. The $\tau \to 3\mu$ and $\tau \to e\gamma$ decays might be in reach of running experiments.

While LHC searches for sleptons already constrain some of the MSSM explanations of the $(g-2)_\mu$ discrepancy, directly probing the multi-TeV sleptons of the FSSM will require a future higher energy collider.

There are several possible future directions to further explore the FSSM. The rank-1 ansatz for the Yukawa couplings has been successfully implemented in the quark sector in non-supersymmetric versions of the model [65, 68, 70–72]. It has been shown that in the considered scenarios quark flavor changing neutral currents can be relatively easily in agreement with experimental bounds. In a supersymmetric version, we expect

149

interesting Higgsino mediated effects in chirality suppressed processes like $b \to s\gamma$ and $B_s \to \mu^+\mu^-$ and possibly even for the lepton flavor universality ratios R_K and R_{K^*}. A study of those effects will be presented elsewhere.

If the rank-1 ansatz for the Yukawa couplings is implemented both in the lepton and quark sectors, a scenario with $\tan\beta \sim 50$, $\tan\beta_u \sim 100$, and $\tan\beta_d \sim 10$ can address all hierarchies among the third and second generation quark and lepton masses without any pronounced hierarchy in Yukawa couplings. These are the values of $\tan\beta$ and $\tan\beta_d$ that allow multi-TeV sleptons to address the $(g-2)_\mu$ anomaly. In such a region of parameter space, third and second generation Yukawa unification might be possible at the GUT scale. For the first generation, one could entertain the possibility of radiative mass generation to explain the smallness of the up quark, down quark, and electron mass. We leave these studies to future work.
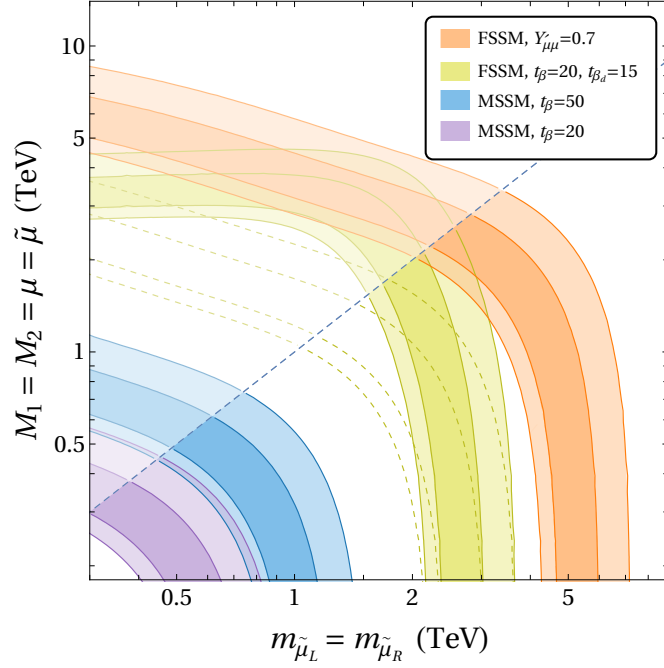
Figure 8.2: Regions of SUSY parameter space that are preferred by the anomalous magnetic moment of the muon at the 1σ and 2σ level in several benchmark models. Above the dashed diagonal line, the smuons are lighter than any of the gauginos and Higgsinos. In blue and purple, we present two MSSM scenarios; in yellow and orange two FSSM scenarios. The dashed yellow lines show the corresponding FSSM scenario neglecting the SUSY threshold corrections to the muon mass.

151

Chapter 9

Searching for Muon-philic Scalars at

DarkQuest

This chapter is based on [367].

9.1 Introduction

The measurement of anomalous magnetic moment of the muon [46, 51, 106], $a_\mu \equiv (g-2)_\mu/2$, remains in significant tension with Standard Model (SM) predictions. In particular, the difference between the Run I measurement and the calculation from the $(g-2)_\mu$ theory initiative is [76]:

$$a_\mu(\text{Exp}) - a_\mu(\text{Theory}) = (251 \pm 59) \times 10^{-11}. \tag{9.1}$$

While recent lattice QCD results may point toward a potential problem with this SM prediction [103, 128, 131], new particles beyond the SM (BSM) still provide a compelling

152

solution to this anomaly that is worth exploring further.

A large variety of new particle solutions have been proposed, including new vector bosons, and CP-even and CP-odd scalar particles. Because their effects on $(g-2)_\mu$ are through loops, this anomaly does not point to a very specific new physics scale and the viable mass range is very broad, spanning from $\sim$ MeV to several TeV [143]. Therefore many experiments running at different energies are required to comprehensively probe this parameter space.

The minimal requirement for a new particle to alleviate the $(g-2)_\mu$ problem is a non-negligible interaction with muons. Realistic models, however often contain couplings to other leptons, quarks or photons. These other interactions can provide a powerful way of testing these models; for example the minimal dark photon (A') explanation of $(g-2)_\mu$ has been excluded in both visible [100, 329] and invisible decay channels [328], mainly by virtue of the A' coupling to electrons and mesons. The searches utilized to probe these models, however, do not directly probe the interaction with muons which would be desirable to make robust claims about any BSM explanation of $(g-2)_\mu$ [161].

In this chaper we consider searching directly for such a coupling using secondary particle beams at the proposed proton beam dump DarkQuest [79]. At this experiment, a high energy proton impinging on a target produces a large flux of secondary mesons. If these mesons decay into muons (like $\pi^\pm$ and $K^\pm$ do), they can produce muon-coupled force carriers in two ways: the new particle can be produced in the meson decays themselves, or via bremsstrahlung as the muons propagate through

the beam dump. Finally, some mesons can also decay into photons which can also produce these particles in photonuclear reactions via a muon-loop-induced coupling.

We illustrate the sensitivity of DarkQuest in the context of the muon-philic scalar model whose only tree-level interactions are with muons;[1] loop-suppressed couplings to photons are naturally expected and give rise to scalar decays when its mass is below the dimuon threshold. Thus the model's main signature at a beam dump like DarkQuest is a displaced decay into photons when the scalar is lighter than $2m_\mu$. Ref. [226] studied the complimentary case where the scalar is kinematically allowed to decay to muon pairs promptly. Our work compliments the existing literature on proposed fixed-target probes of muon-coupled particles at NA64, Fermilab, BDX, NA62 and SHiP [111, 154, 159, 161, 244, 302, 322, 343, 396]. Compared to previous studies of similar experimental setups and models (e.g., [111] focusing on a leptophilic scalar model at DarkQuest and [396] focusing on NA64 and SHiP), we improve the modelling of known production channels (muon bremsstrahlung) and identify additional relevant channels (meson decays, $K, \pi \to \mu\nu S$, which have also been studied at kaon factories [322]) which turn out to dominate the sensitivity projections. We also provide the first more in-depth study of di-photon backgrounds at DarkQuest.

This work is organized as follows. In section 9.2 we briefly describe the Dark-Quest experiment to establish key experimental parameters that determine its sensitivity (for more details see Ref. [79]). We also estimate the fluxes of secondary particles that are relevant for signal and background production. We then specify the interactions of

---

[1]The sensitivity of DarkQuest to a variety of dark sector scenarios has been studied in Refs. [80, 96, 110, 111, 126, 201, 226, 232, 435].

154

the muon-philic scalar model in section 9.3 and highlight the parameter space that can explain the $(g-2)_\mu$ anomaly. section 9.4 details the modelling and simulation of signal events in three channels: muon bremsstrahlung, meson decays and photon-induced processes. The compact nature of the DarkQuest experiment enables unique sensitivity to short BSM particle lifetimes at the cost of introducing several backgrounds in the case of photon signatures, which we discuss in section 9.5. There we identify processes that can mimic our signal and describe mitigation strategies. Finally in section 9.6 we present our sensitivity projections, showing that DarkQuest can decisively probe parts of the still-allowed $(g-2)_\mu$ parameter space.

We collect more details of our analysis in the appendices. Muonphilic scalar decays and certain production channels rely on the loop-induced scalar-photon coupling which is computed in appendix G (while the corresponding on-shell amplitude/form-factor is well known, we also provide a corrected off-shell amplitude). appendix H discusses a possible ultraviolet completion of the muon-philic scalar model based on vector-like leptons, which can be constrained with high energy colliders. appendix I describes the propagation of muons through the DarkQuest dump which is a key aspect of our bremsstrahlung and muon-induced background calculations. This is the first full simulation of this type. In appendix J we present the full expression for the three-body kaon decay partial width which dominates the signal production.

9.2 The DarkQuest Experiment

9.2.1 The Experimental Setup

DarkQuest is a dark sector-focused upgrade of SpinQuest, a proton fixed-target spectrometer experiment on the neutrino-muon beamline of the Fermilab Accelerator Complex. This beamline supplies a high-intensity beam of 120 GeV protons from the Main Injector. Details of the set up are described in Refs. [54] and [79]. Here we summarize the key features relevant for our analysis.

The setup of the DarkQuest experiment is shown in fig. 9.1. A 5 m long magnetized iron block ("FMAG") is placed 1 m downstream from a thin nuclear target, serving as a focusing magnet and as a beam dump. Its magnetic field of ~ 1.8 T imparts a transverse kick of $\Delta p_T \sim 2.6$ GeV to ultrarelativistic charge-one particles traversing the entire dump on average (the actual p_T for individual particles is sensitive to multiple scattering and energy loss fluctuations in addition to the magnetic field, see appendix I).

The FMAG stops most of the primary beam and secondary particles produced by proton-iron interactions, other than neutrinos and muons; despite this, the severely attenuated fluxes of protons and kaons can still be relevant for background processes.

The detector extends for ~ 20 m after the dump and is composed of a series of tracking stations and an open-aperture magnet ("KMAG") that further sweeps away charged SM radiation thanks to a transverse kick of $\Delta p_T \sim 0.4$ GeV. The above components are already present in the SpinQuest experiment. The DarkQuest upgrade will install: an electromagnetic calorimeter ("ECal") at ~ 19 m between station 3 and

156

the muon station, additional tracking layers to improve particle identification and hodoscopes for better triggering. We will also consider modifications of this set up that include more shielding before or after the FMAG;

this is one strategy that can be used to suppress some (but not all) backgrounds as we discuss in section 9.5.

The DarkQuest experiment will collect $\sim 10^{18}$ protons on target (POT) in a two year long run. Depending on the status of the Fermilab accelerator complex [247], longer DarkQuest runs will be possible in the future. In our analysis, we will discuss the realistic scenario of 10^{18} POT and also a futuristic possibility in which DarkQuest will accumulate 10^{20} POT.
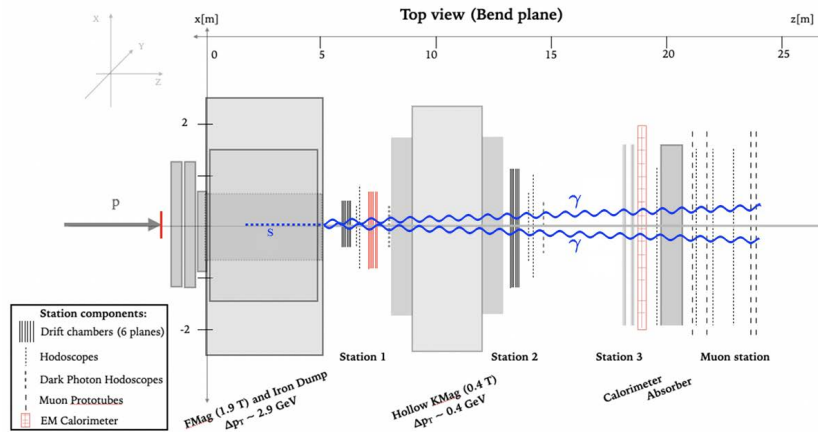
Figure 9.1: Side view of DarkQuest experiment including proposed ECal, target, and tracking detector upgrades, in red; a dark sector signature is illustrated in blue. Adapted from [79].

9.2.2 Production of SM Particles

The high intensity proton beam produces many SM particles at the beginning of the dump, including mesons, baryons, muons, and photons. These secondary particles open different production channels for the muonphilic scalar, and also produce backgrounds. In table 9.1, we summarize the average counts of the relevant mesons and hadrons produced in the first proton interaction length $\lambda_{\text{int}} = 16.77$ cm (approximately $1 - e^{-1} \approx 0.63$ of the primary proton beam interacts within this region). We estimated these yields using `Pythia` 8.306 [121].

Short-lived mesons like π^0 decay promptly after production. π^0 along with $\eta^{(\prime)}$ decays generate a flux of photons at the beginning of the FMAG. As we will discuss, decays of the long-lived mesons $\pi^{\pm}$ and $K^{\pm}$ contribute to signal production in two ways: first, through rare three body decays, and second, by generating a flux of muons that can undergo bremsstrahlung.[2] We focus on production and decay of these mesons in the first interaction length for simplicity. This allows us to neglect energy losses of hadrons that decay or interact deep in the dump. We expect this to be a good $\mathcal{O}(1)$ approximation for signal. This is because while including a longer decay region for $\pi^{\pm}$, $K^{\pm}$ would increase the muon and scalar yields linearly with the decay region size, the meson intensity falls exponentially with depth. Therefore decays in the first interaction length account for the majority of the (scalar or muon) flux that is relevant for the signal and background estimates. We estimate the muon and photon yield, and the number

---

[2]Muons are also produced in the Drell-Yan process, but the corresponding cross-section is smaller than the total pp cross-section by a factor of $\sim 10^7$, so this mechanism is subdominant to production from meson decays.

π^0	η	η'	$\pi^\pm$	$K^\pm$	K_L	K_S	Λ
1.5	0.19	0.021	3.2	0.25	0.11	0.21	0.082

Table 9.1: Average number of mesons or baryons produced in the first interaction length of the FMAG per 120 GeV proton on target. These counts are estimated using `Pythia`.

of $\pi^\pm$ and $K^\pm$ decays in the first interaction length in table 9.2. The latter counts are obtained via

$$N_{M,\,\mathrm{dec}} \simeq N_p n_M \Gamma_M \langle \gamma_M^{-1} \rangle \lambda_M \, , \tag{9.2}$$

where N_p is the number of POT, n_M is the meson yield per POT in the first interaction length from table 9.1, Γ_M and λ_M are the meson decay rate and interaction length, respectively. The average over inverse boosts $\langle \gamma_M^{-1} \rangle$ is performed using Monte Carlo samples from `Pythia`.

For certain backgrounds the attenuated proton beam or secondary K_L and Λ fluxes *are* an important source, and we will comment on them in section 9.5.

9.2.3 Di-photon mass resolution

As we will discuss in section 9.5, di-photon signatures are not background-free at DarkQuest. The most important backgrounds is π^0 and η production at the end of the dump produced either from the attenuated proton beam or from the secondary muon beam undergoing deep inelastic scattering. One experimental handle that can disentangle these events from the signal are selections on diphoton invariant mass.

$\mu^{\pm}$	γ	prompt $\pi^{\pm}$ dec.	prompt $K^{\pm}$ dec.
1.0×10^{16}	3.8×10^{18}	8.6×10^{15}	1.9×10^{15}

Table 9.2: Average counts for particles that are produced or decay near the front of FMAG for 10^{18} POT. The first two columns contain the number of muons and photons produced in the first proton interaction length of the FMAG, while the last two columns contain the number of prompt $\pi^{\pm}$ and $K^{\pm}$ decays as estimated via eq. (9.2). Here "prompt" refers to decays within the first meson interaction length.

Having a good mass resolution will improve the discrimination between signal and background. The resolution can be estimated using the energy and position resolution of the ECAL [79]. In particular, we take a position resolution of 3 cm and an energy resolution of $1\% + 7\%/\sqrt{E(\text{GeV})}$.

By simulating π^0, $\eta^{(\prime)}$ production and their decays at the back of the dump we find that the mass resolution varies between 10% and 30% for typical meson energies, with a better resolution for the η, if compared to the π^0.[3] We will find that even taking the optimistic 10% figure, selections of diphoton invariant mass can reduce background rates by a factor of a few, but not completely eliminate them. Other mitigation strategies will still be required (see section 9.6).

---

[3] We thank Yongbin Feng for useful discussions regarding these calculations.

9.3   The Scalar Singlet Model

9.3.1   The Lagrangian of the Muon-philic Scalar

We focus on minimal scalar model that at the renormalizable level contains only the interaction with muons

$$L \supset \frac{1}{2}(\partial S)^2 - \frac{1}{2}m_S^2 S^2 - g_S S\bar{\mu}\mu. \qquad (9.3)$$

We emphasize that this scenario does not have a coupling to electrons at tree level; in the parlance of Ref. [161] this is "Model B". The effective theory also contains interactions with photons at dimension five

$$L \supset -\frac{1}{4}g_{S\gamma\gamma}S F_{\mu\nu}F^{\mu\nu}. \qquad (9.4)$$

The coupling $g_{S\gamma\gamma}$ receives contributions from ultraviolet (UV) physics and from loops of muons:

$$g_{S\gamma\gamma} = g_{S\gamma\gamma}^{(\mathrm{UV})} + \frac{\alpha g_S}{2\pi m_\mu}f_{1/2}\left(\frac{4m_\mu^2}{m_S^2}, 0\right), \qquad (9.5)$$

where in writing the loop function $f_{1/2}$ we took S and the photons to be on-shell. We will neglect the UV contribution in what follows in order to be consistent with previous studies; the usual explanation given for this is that one naively expects $g_{S\gamma\gamma}^{(\mathrm{UV})}$ to be smaller by a factor of m_μ/M where M is the UV scale, see appendix G. However, in realistic UV completions S coupling to muons (i.e., g_S) and heavy physics at scale M are independent, so the UV and infrared (IR) contributions to $S\gamma\gamma$ can potentially compete for some choices of parameters, as discussed in appendix H. This photon interaction

gives rise to S decays into photons with rate:

$$\Gamma_S = \frac{\alpha^2 g_S^2 m_S^3}{256\pi^3 m_\mu^2} \left| f_{1/2}\left(\frac{4m_\mu^2}{m_S^2}, 0\right)\right|^2,$$

(9.6)

where the loop function $f_{1/2} \to 4/3$ as $m_S/m_\mu \ll 1$ (the full result is given in appendix G). The muon loop also generates couplings of off-shell photons to S which are relevant for, e.g., the photon fusion and Primakoff S production. The $S\gamma\gamma^*$ amplitude needed for this calculation is given in appendix G.

Clearly the model in eq. (9.3) is not electroweak gauge-invariant. From the point of view of UV completions, the inclusion of couplings to electrons and taus is natural in minimal models with Higgs portal interactions or extra Higgs doublets above the electroweak scale [98]. However, these models have recently been excluded as solutions of $(g-2)_\mu$ [329]. The *flavor-specific* interaction in eq. (9.3), while more minimal in the infrared, requires more engineering in the UV. Ref. [97] delineated the conditions under which couplings to specific SM fermion mass eigenstates (the muon in our case) are obtained in a technically-natural and experimentally-viable way. As a first step, the flavor-specific coupling to muons can be obtained from the electroweak-invariant effective operator

$$-\frac{S}{M}H^\dagger L\mathbf{c}_S \ell_R^c + \text{h.c.},$$

(9.7)

where H (L) is the Higgs (lepton) $SU(2)_L$ doublet, ℓ_R^c is $SU(2)_L$ singlet lepton (in Weyl notation), M is a UV scale and $\mathbf{c}_S$ is a matrix in flavor space. In order for this interaction to reduce to eq. (9.3), $\mathbf{c}_S$ has to obey two conditions: 1) it must be diagonal in the lepton mass basis (i.e., $\mathbf{c}_S$ is simultaneously diagonalizable with the lepton Yukawa

162

matrix) and 2) $\mathbf{c}_S = \mathrm{diag}(0, c_S, 0)$ in the charged lepton mass basis. This structure generates the desired coupling to muons with $g_S = c_S v/(\sqrt{2}M)$, where $v = 246$ GeV, and it minimizes flavor-changing neutral currents. In general, c_S is complex, but its imaginary part shifts $(g-2)_\mu$ in the wrong direction [97]. We therefore focus on purely real c_S. The spurion analysis of Ref. [97] reveals that the intricate structure of $\mathbf{c}_S$ is radiatively stable.[4]

The electroweak-invariant interaction in eq. (9.7) is still non-renormalizable and therefore requires a UV completion. This is easily achieved by adding a pair of vector-like leptons with mass M [97], in which case $\mathbf{c}_S$ is proportional to the Yukawa couplings of these new particles with the SM Higgs and with S. We explore such a UV completion in appendix H, which allows us to connect the low energy muon and photon couplings to UV parameters, and to consider naturalness and direct experimental bounds that must be satisfied. This scenario still does not explain the flavor alignment of $\mathbf{c}_S$ and the SM lepton Yukawa matrices.

9.3.2 The New Physics contribution to $(g-2)_\mu$

The model in eq. (9.3) is one of the few available minimal explanations of the $(g-2)_\mu$ anomaly with new physics at or below the several GeV scale [143]. The contribution of S to $(g-2)_\mu$ is [98]

$$\Delta a_\mu^S = \frac{g_S^2}{8\pi^2} \int_0^1 dz \frac{(1+z)(1-z)^2}{(1-z)^2 + z(m_S/m_\mu)^2}. \tag{9.8}$$

---

[4] The parity $S \to -S$ ensures that corrections to c_S are always proportional to c_S, while any off-diagonal elements can only arise from the non-diagonal neutrino mass matrix.

The anomaly in eq. (9.1) is explained if $g_S \sim 4 \times 10^{-4}$ for $m_S \lesssim 2m_\mu$.

9.4   Signal Production and Simulations

The dark scalar can be produced in several processes enabled by secondary muons, mesons and photons present in the beam dump. The energy and transverse momentum spectra of these particles are shown in fig. 9.2. We find that muon bremsstrahlung and meson decays dominate the dark scalar yield in interesting regions of parameter space, while the rate of photon-initiated reactions is loop-suppressed. We discuss these processes in more detail below.

9.4.1   Muon Bremsstrahlung

The primary proton collisions with the dump lead to a large flux of secondary muons. These muons are generated from meson decays ($\pi^\pm$ and $K^\pm$ in particular), and from Drell-Yan production. These can then interact within the dump, radiating a scalar. The scalar bremsstrahlung cross-section has been computed exactly in [337, 436, 437], but most recent works use the Weiszacker-Williams (WW) approximation, see, e.g., Ref. [159, 396]. This cross-section enters the signal prediction calculation in two important ways: first, it normalizes the overall rate and, second, its differential is used to generate S kinematics. We have compared three ways of evaluating the overall cross-section: (1) using the WW approximation; (2) numerically computing it in `MadGraph` [74]; (3) integrating the exact results of Ref. [337] using `VEGAS` [332, 333].
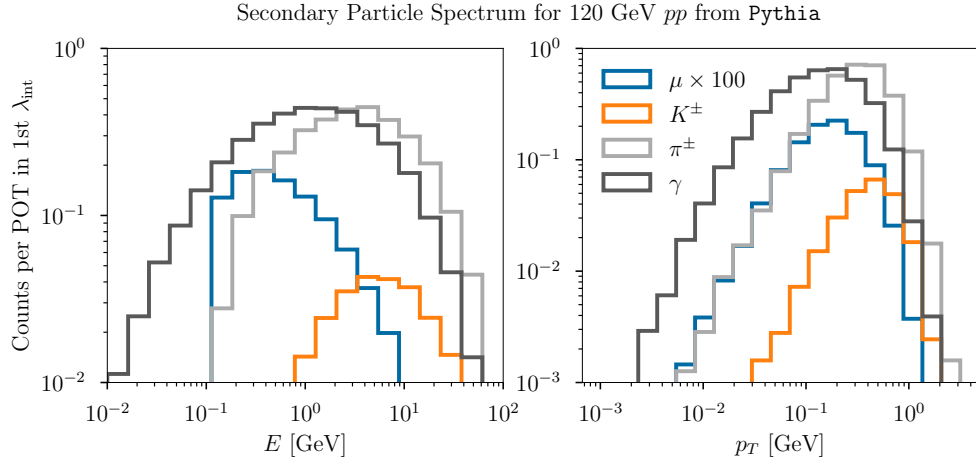
Figure 9.2: Counts of secondary particles per 120 GeV proton on target as a function of energy (left panel) and transverse momentum (right panel). The $\pi^{\pm}$, $K^{\pm}$ (γ, $\mu^{\pm}$) spectra sum to the average yields in the first interaction length of the dump given in table 9.1 (table 9.2, divided by 10^{18}). Note that the muon spectrum includes the probability for the parent particles (mostly $\pi^{\pm}$ and $K^{\pm}$) to decay in the first interaction length (this spectrum is also multiplied by 100 for convenient visualization).

In principle the latter two methods should give very similar results, but in practice we find that the custom `VEGAS` implementation yields results that are more numerically stable.[5] The result of this calculation is illustrated in fig. 9.3 for several values of m_S - we find excellent agreement with results of Ref. [343] which used a different numerical method, which is also based on the integration of the full matrix element squared. For the main results in this work we use the `VEGAS` calculation of the total cross-section, noting that the WW approximation predicts scalar yields that are a factor of 2-5 larger

---

[5]The difficulty of simulating light-particle bremsstrahlung using off-the-shelf Monte Carlo tools has been noted in, e.g., [152, 226].
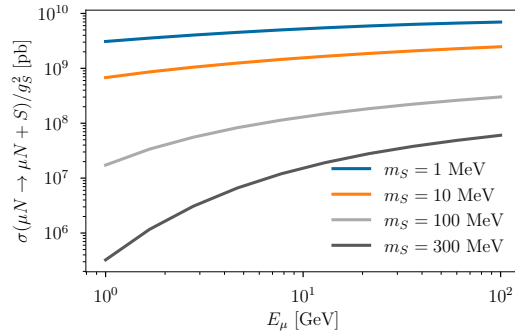
Figure 9.3: Scalar bremsstrahlung ($\mu N \to \mu N S$) cross-section, in iron as a function of muon energy for several choices of m_S. Note that to obtain a realistic scalar yield at DarkQuest for this process one must convolve these cross-sections against the muon spectrum and account for muon propagation effects.

for $m_S \lesssim 2m_\mu$ (such discrepancies were also observed in Refs. [337, 396]). We will use `MadGraph` to generate final state scalar and muon kinematics.

Most of the muons are produced near the front of the dump, so they can propagate a significant distance before undergoing bremsstrahlung. During this propagation they experience energy losses, multiple Coulomb scattering and their trajectory is bent in the magnetic field. There have been two different approaches to modelling these effects. First, input muon spectrum can be used to predict the signal yield by convolving it with the differential cross-section [111, 396]

$$N_{\text{signal}} \simeq n_{\text{atom}} \int dE_\mu^0 \frac{dN_\mu}{dE_\mu^0} \int_{E_\mu^{\text{min}}}^{E_\mu^0} dE_\mu \frac{\sigma_{\text{Brem.}}(E_\mu)}{|dE_\mu/dz_\mu|} \int_{z_{\text{min}}-z_\mu}^{z_{\text{max}}-z_\mu} dz \frac{1}{N_{\text{MC}}} \sum_{\text{events} \in \text{geom.}} \frac{e^{-z/(\gamma_S c\tau_S)}}{\gamma_S c\tau_S}. \quad (9.9)$$

where $z_{\text{min}} \simeq 5$ m, $z_{\text{max}} \simeq 19$ m and N_{MC} is the total number of simulated events. The sum is performed over only those events that remain within the geometry of the DarkQuest spectrometer. Here E_μ^0 is the initial energy of the muon at production, and E_μ is the muon energy after traversing some finite distance, z_μ, in the FMAG before

166

radiating the scalar; γ_S and τ_S are the boost and the lifetime of the scalar, respectively; dN_μ/dE_μ^0 is the total number of muons produced per initial energy bin within the first meson interaction length (output of `Pythia`); $n_{\text{atom}} = 8.5 \times 10^{22}/\text{cm}^3$ is the number density of target iron nuclei and $\sigma_{\text{Brem.}}$ is the muon bremsstrahlung cross-section. Note that in this approach muon propagation is simply encoded in the dE_μ integration, and the effect of a magnetic field is applied "by hand" as a shift in p_T of each muon. Multiple scattering is not included.

Alternatively, each muon can be tracked through the dump using its equations of motion, until it undergoes a bremsstrahlung event. At this point S kinematics is sampled from the differential cross-section. This approach makes it easier to include the effects of multiple Coulomb scattering, energy loss fluctuations, and magnetic fields. In Ref. [343] this method was implemented within `GEANT4` [50, 59, 60]. Here we follow a similar approach, but instead model the propagation in a custom `Python` program described in appendix I.

Finally, we note that muon bremsstrahlung in a thick target has the peculiar feature that scalar particles can be produced anywhere in the dump with similar probability, including very close to the end. This can be easily seen from eq. (9.9) in the limit of large muon energy (such that one can neglect energy losses) and short scalar lifetime ($\gamma_S c \tau_S \ll z_{\text{min}}$); in this case the probability of the scalar to be produced in the

dump and decay beyond it is approximately

$$n_{\text{atom}} \sigma_{\text{Brem.}}(E_\mu) \int_0^{z_{\text{min}}} dz_\mu e^{-(z_{\text{min}} - z_\mu)/(\gamma_S c \tau_S)}$$

$$\approx n_{\text{atom}} \sigma_{\text{Brem.}}(E_\mu) \gamma_S c \tau_S,$$

(9.10)

where we assumed that the cross-section and energy loss rates are constant. This shows that the signal yield will be dominated by scalar production in the last S decay length of the shield. In contrast, if the scalar was produced near the front of the dump, the rate would be proportional to $e^{-z_{\text{min}}/(\gamma_S c \tau_S)}$. Therefore the projected sensitivity of this channel extends to large couplings, which is qualitatively different to many other long-lived-particle (LLP) searches which feature a very thick shield. For example, the proton beam experiment CHARM [108, 109, 242] had a shield thickness of $\sim$ 480 m so that the LLP signal in the large coupling/short lifetime regime is exponentially suppressed despite the higher beam energy of 400 GeV.

9.4.2 Meson Decays

Dark scalars are also produced from the charged current meson decays $\pi^+ \rightarrow \mu^+ \nu S$ and $K^+ \rightarrow \mu^+ \nu S$. Using the leading-order chiral perturbation theory Lagrangian

$$L_{\chi\text{PT}} \supset \sqrt{2} G_F f_P V_{q_1 q_2} \partial_\alpha P^- \bar{\mu} \gamma^\alpha P_L \nu_\mu + \text{h.c.},$$

(9.11)

we find the partial width for meson $P = \pi, K$

$$\Gamma(P \rightarrow \mu \nu S) \approx \frac{g_S^2 f_P^2 G_F^2 |V_{q_1 q_2}|^2 m_P^3}{768 \pi^3}$$

(9.12a)

$$\approx \frac{g_S^2 m_P^2}{96 \pi^2 m_\mu^2} \Gamma(P \rightarrow \mu \nu),$$

(9.12b)

in the $m_P \gg m_S, m_\mu$ limit (the full expression is given in appendix J). Here f_P is the meson decay constant ($f_\pi = 130$ MeV and $f_K = 156$ MeV in our conventions); $V_{q_1 q_2}$ is the relevant CKM matrix element: $|V_{ud}| \approx 0.9737$ ($|V_{us}| \approx 0.2246$) for π (K) decay. These are the most important meson production modes for the scalar thanks to their sizable branching ratio into a muon and a neutrino.

An additional production mode is $K_L \to \pi^\pm \mu^\mp \nu_\mu S$. The contribution from this process, however, is generically smaller than from the meson three body decays discussed above.

9.4.3   Photon-induced Processes

The scalar-photon interaction in eq. (9.4) enables several production mechanisms that are analogous to axion-like particle production in beam dumps. These include the Primakoff process $\gamma + N \to S + N$ and photon fusion $\gamma^* \gamma^* \to S$, where γ^* are virtual photons corresponding to the electromagnetic fields of a beam proton and target nucleus. Primakoff production was shown to dominate over photon fusion in thick targets due to the large secondary photon flux [126]. The scalar-photon interaction needed to evaluate the Primakoff cross-section is described in appendix G. A potential difference of the present model with respect to axion-like particles is that the photon coupling is generated by muons, leading to a non-trivial energy dependence of that coupling (because the muon mass is not much larger than other experimental energy scales). We have estimated the yield of dark scalars from this process, finding that it is 1–2 orders of magnitude smaller than for bremsstrahlung in the mass range

169

of interest. Moreover, there is no on-shell muon in the final state which may be an important event selection designed to reduce diphoton backgrounds as we discuss in the next two sections.

9.5 Backgrounds

The compact geometry of DarkQuest enables searches for particles with short decay lengths (especially if they are radiated by muons propagating though the dump). This unique feature leads to a complementary reach compared to other experiments with a larger dump and smaller angular acceptance. The comparatively short shield also means that potential signals must contend with backgrounds. There is a variety of SM processes that can mimic the production and decay of a BSM long-lived particle into photons. The three types of potentially problematic SM events are: 1) production of genuine SM long-lived particles, such as K_L; 2) neutral mesons (π^0, $\eta^{(\prime)}$) produced at the very back of the dump from the attenuated proton beam; and 3) production of neutral mesons (π^0, $\eta^{(\prime)}$) via Deep-Inelastic Scattering (DIS) of muons towards the end of the dump. We will show that the events of the third kind are the most dangerous, but that they can be mitigated with several event selections, while preserving experimental coverage of the most interesting $(g-2)_\mu$ band at $m_S \lesssim 2m_\mu$. These backgrounds and potential mitigation strategies are summarized in table 9.3 – they will be discussed in more detail below and in section 9.6.

	Raw counts	ECAL hit	γ sep.	μ hit	$m_{\gamma\gamma}$	Extra Shielding
p-induced K_L	6×10^4	✓	✓	✓	✓	✓
p-induced π^0, $\eta^{(\prime)}$	2×10^4	✓		✓	✓	✓
μ-DIS-induced π^0, $\eta^{(\prime)}$	10^6	✓			✓	

Table 9.3: Summary of SM background events that can mimic the signal $S \to \gamma\gamma$ and experimental techniques that can reduce or eliminate them. The first two rows correspond to mesons produced by the primary proton beam. The last row corresponds to mesons produced deep in the dump by a secondary muon beam via deep-inelastic-scattering. The columns to the right of the double-line divider indicate whether the listed background events can be significantly reduced using the corresponding experimental handle. "ECAL hit" requires at least one photon with a sufficient energy in the ECAL; "γ sep." corresponds to exactly two well-separated photons in the ECAL; "μ hit" is the requirement of detecting a muon; "$m_{\gamma\gamma}$" is a selection based on the diphoton invariant mass potentially measurable with the ECAL; "Extra shielding" corresponds to adding additional material behind the FMAG. The impact of these selections on the background yield is quantified in section 9.5 and section 9.6.

171

9.5.1 SM Long-Lived Particles

Standard Model LLPs, such as K_L and Λ, which decay into neutral pions can produce signal-like photons. We will focus on K_L decays in the fiducial region $z > 5$ m and $z < 19$ m (before the ECal). Λ's have a shorter attenuation length compared to mesons, so their contribution to background ends up being two orders of magnitude smaller. The number of LLP background events can be estimated as

$$
\begin{aligned}
n_{K_L} N_p \mathrm{BR}(K_L \to 3\pi^0) & e^{-z_{\text{shield}}/\lambda_{K \text{ int}}} \\
& \times \left[e^{-z_{\text{shield}}/(\gamma c \tau_{K_L})} - e^{-z_{\text{max}}/(\gamma c \tau_{K_L})} \right] \\
& \approx 6 \times 10^4,
\end{aligned} \tag{9.13}
$$

where n_{K_L} is the number of K_L produced per POT from table 9.1, $\mathrm{BR}(K_L \to 3\pi^0) \approx 0.2$ is the branching fraction of the most problematic K_L decay channel, $z_{\text{shield}} = 5$ m is the length of shielding, $\lambda_{K \text{ int}} \approx 20$ cm is the kaon interaction length in iron. The factor on the second line is the probability of the kaons to decay after the shielding and before the ECAL. The number of events in the last line is computed for 10^{18} POT. Each of these events can lead to a ≤ 6 photons signal in our detector. Note that most K_L's are produced near the front of the dump as the incoming proton beam is exponentially attenuated.[6]

There are two approaches to deal with this background. First, one can use additional shielding in front or behind the FMAG ("Extra shielding" in table 9.3).

---

[6] K_L's produced deeper in the dump experience less attenuation before they exit which somewhat off-sets the attenuation of the beam that produced them, compared to K_L's near the front. However, because the kaon interaction length is longer than the proton interaction length, the latter K_L flux still dominates.

Using `Pythia` to estimate the median meson production rates and boosts, we find that an additional 2 m of (iron) shielding would bring the K_L background rate below 10 events for 10^{18} POT. Similar shielding requirements were discussed in Refs. [111, 126] in the context of axion-like particle searches. It is important to note that if the only goal is to close the $(g-2)_\mu$ window, we can significantly relax the shielding requirement. This is because we expect $\mathcal{O}(10^3 - 10^6)$ signal events in the currently-allowed $(g-2)_\mu$ band at $m_S \lesssim 2m_\mu$ (see fig. 9.8). The amount of extra shielding needed to bring the background below 10^3 events is only 90 cm. This can be further reduced by using a different material, such as tungsten.

The second approach to reducing SM LLP backgrounds is to select events with exactly two photons in the ECAL and a single muon hit ("γ sep." and "μ hit" in table 9.3). Both the kaon decay and muon bremsstrahlung S production mechanisms can in principle pass these cuts, while the backgrounds either have too many photons, do not have a muon in the final state or both. The leading K_L decay that leads to background events is $K_L \to 3\pi^0 \to 6\gamma$, which would be completely eliminated by such cuts, without requiring any additional shielding. In section 9.6, we will show that enough signal events pass these selections to retain sensitivity to the open $(g-2)_\mu$ region at $m_S \lesssim 2m_\mu$.

9.5.2 Secondary Mesons from the back of the dump

Another type of potentially problematic SM events is the production of π^0 and $\eta^{(\prime)}$ from the attenuated proton beam in the last radiation length of the dump. The

prompt photons from their decays would have a large probability of escaping the dump and potentially ending up in the ECAL. The number of such events is approximately

$$(n_{\pi^0} + n_\eta + n_{\eta'})N_p e^{-z_{\text{shield}}/\lambda_{p\,\text{int}}} \frac{\lambda_{\text{rl}}}{\lambda_{p\,\text{int}}}$$

$$\approx 2 \times 10^4,$$

(9.14)

where $\lambda_{p\,\text{int}} = 16.77$ cm is the nuclear interaction length for protons, n_M are given in table 9.1 and $\lambda_{\text{rl}} = 1.757$ cm is the radiation length in iron.[7] The last factor, $\lambda_{\text{rl}}/\lambda_{p\,\text{int}}$, is the probability for protons to interact in the final radiation length of the dump. The background events in the last line of eq. (9.14) can be eliminated in a few different ways. Thanks to the exponential suppression in eq. (9.14), an additional 1.8 m (70 cm) of iron shielding would suffice to reduce this background to below 1 (10^3) event for $N_p = 10^{18}$. Alternatively, as for SM LLPs, event selections requiring two photon hits in the ECAL and a muon hit would also help thanks to a requirement on the di-photon invariant mass and distributions, see section 9.6. We will investigate how such selections affect the signal yield in the next section.

9.5.3 Mesons from μ DIS

Finally we consider backgrounds generated by muons undergoing DIS at the end of the dump and producing π^0 and other mesons that can decay to photons. The reason why this reaction chain is potentially important is because muons are not exponentially attenuated by the dump, unlike the original proton beam (c.f., the secondary meson background in section 9.5.2). In order to estimate the rate, we first produce a

---

[7]The attenuated proton beam looses ~ 10 GeV of energy as it propagates through the FMAG, but the meson yields at this lower energy are approximately the same as for in original 120 GeV beam.

distribution of muons at the end of the dump as follows. We simulate the primary pp collisions in `Pythia` that produce $\pi^{\pm}$ which are then decayed to muons in the first interaction length. The muons are then propagated to the back of the dump as described in appendix I. We find that the number of muons at the back of the 5 m dump with sufficient energy to initiate DIS is $n_{\mu}^{(\text{back})} \sim 5 \times 10^{-6}$ per pp interaction. Note that this number is not sensitive to the dump thickness because the muons are not strongly attenuated. This is because the muons lose only about ~ 10 MeV/cm, so even an additional 2 m of iron does not drastically affect their spectrum at the back of the dump.

The propagated sample of muons is then fed into `Pythia` to simulate DIS, $\mu p \to \mu + X$, which is used to estimate the meson-count weighted cross-sections, $\langle \sigma(\mu p \to \mu + X) n_M \rangle$ where $M = K_L,\ \pi^0$. We find that

$$\langle \sigma(\mu p \to \mu + X) n_{\pi^0} \rangle = 2 \times 10^{-5} \text{ mb}$$

$$\langle \sigma(\mu p \to \mu + X) n_{K_L} \rangle = 5 \times 10^{-7} \text{ mb}.$$

(9.15)

We can now put all of these ingredients together. First, the expected number of μ-DIS-induced π^0 produced in the final radiation length of the dump is

$$N_p n_{\mu}^{(\text{back})} A n_A \lambda_{\text{rl}} \langle \sigma n_{\pi^0} \rangle \sim 10^6 \tag{9.16}$$

where $\langle \sigma n_{\pi^0} \rangle$ is given in eq. (9.15). The target (nucleon) density in iron is $A n_A \approx 4.7 \times 10^{24}$ cm^{-3}.

The number of kaons that are produced in a similar manner in the last kaon
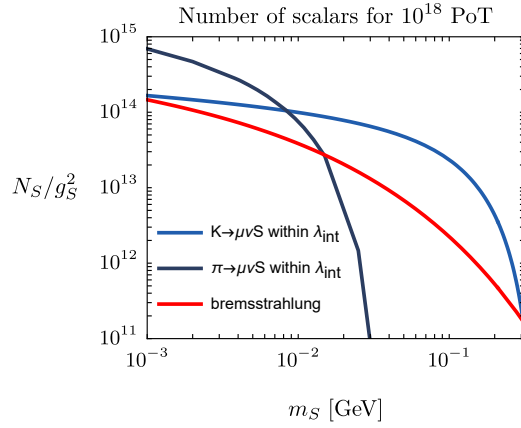
Figure 9.4: Scalar yield as a function of the mass m_S for 10^{18} POT from different production mechanisms without imposing any event selections.

interaction length, and that decay beyond the dump is

$$N_p n_\mu^{\text{(back)}} A n_A \lambda_{K \text{ int}} \langle \sigma n_{K_L} \rangle \text{Br}(K_L \to 3\pi^0)$$
$$\times \left[1 - e^{-(z_{\max} - z_{\text{dump}})/(\gamma c \tau_{K_L})} \right] \sim 10^4 \tag{9.17}$$

where the quantity the brackets is the probability of K_L produced at the back of the dump to decay between $z = z_{\text{dump}}$ and $z_{\max} = 19$ m (about 0.14 for the mean kaon energy produced in the DIS reaction).

While the raw counts for the backgrounds in eqs. (9.16) and (9.17) appear problematic, it turns out that simple selections on photon energy and angle distributions can make these backgrounds significantly smaller. Nevertheless, as we will discuss in the next section, it will be challenging to completely suppress this source of background.

176
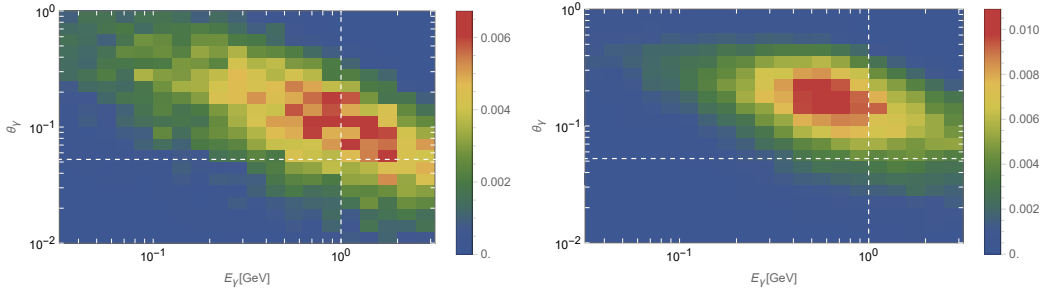
Figure 9.5: Histograms of signal photon energy and angle from $S \to \gamma\gamma$ with S produced in rare kaon decays (left panel) and muon bremsstrahlung (right panel). θ_γ is the angle between the photon and the beam axis. In both panels $m_S = 100$ MeV and the bin normalization is such that they sum to 1. The vertical dashed white line corresponds to an energy cut of 1 GeV and the horizontal line corresponds to photons being roughly in geometric acceptance of the detector.

9.6   Results and Discussion

In this section we put together our signal and background simulations to project the sensitivity of future DarkQuest searches for muonphilic scalars in the $m_S \lesssim 2m_\mu$ regime. First, we compare the raw S yields from different production channels without making any selections in fig. 9.4. We observe that production from meson decays dominates the S yield throughout our mass range. While rare π^0 decays produce the largest S flux for $m_S \lesssim m_\pi - m_\mu$, we will see that even minimal event selections make this channel less important than the other two. Kaon decays produce more S that μ-bremsstrahlung despite the initial flux of μ being larger – see table 9.2. This occurs for two related reasons: first, the spectrum-averaged muon interaction probability in

177
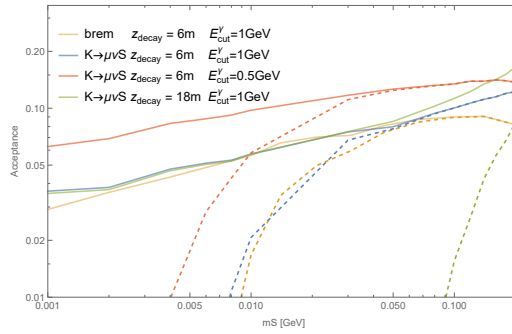
Figure 9.6: Acceptance probability of signal photons as a function of scalar mass for different S production channels, decay positions and event selections. Dashed curves indicate a further 5.5 cm separation cut was applied to the photons hitting the detector.

the dump is smaller than the $K^{\pm}$ branching fraction for the m_S of interest; second, while the bremsstrahlung cross-section grows with initial muon energy, the probability of those muons to be produced in pion decays near the front of the dump is smaller, because of their higher boost. Thus the interaction probabilities are anti-correlated with the energy-differential muon flux, which is not captured in table 9.2.

Examples of distributions of the energy and the angle between the photon and the beam axis are shown in fig. 9.5 for the two dominant production mechanisms. The probability of these photons ending up in the detector acceptance depends on the precise location of the S decay and any selections imposed on the events. In fig. 9.6 we show the effects of several simple cuts on energy and photon separation for a few fixed decay positions. We consider minimum photon energy cuts of 0.5 and 1 GeV as representative values, but looser selections are also possible [79]. Requiring photon separation will enable the selection of events with exactly two photons which may be

a useful handle for rejecting backgrounds such as $K_L \to 3\pi^0$. The choice of 5.5 cm minimum transverse separation corresponds to the transverse granularity of the ECAL towers used by DarkQuest [77, 79]. In fig. 9.6 we see that photon separation strongly reduces sensitivity to light scalars. As we discuss next this is not an issue since the novel parameter space that DarkQuest can test lies at larger masses. In fig. 9.7 we show background-free sensitivities for easy comparison with previous literature. The reach curves correspond to 10 signal event contours in the $m_S - g_S$ plane for phase 1 ($N_p \approx 10^{18}$) and phase 2 ($N_p \sim 10^{20}$). One remarkable feature of these projections is the sensitivity to relatively large couplings where the lab-frame lifetime of S is expected to be significantly shorter than the FMAG depth of 5 m. It arises due to the secondary muons' ability to interact deep in the dump, leading to S production much closer to $z = 5$ m as discussed in section 9.4. From the figure, we can see that already phase 1 could probe entirely the $(g-2)_\mu$ region at higher masses. Phase 2 will also have access to lower masses.

The projections in fig. 9.7 are valid only if the backgrounds discussed in section 9.5 are reduced or eliminated. A simple, brute-force way to achieve this for the SM LLP backgrounds and diphotons from meson decays in the back of the dump is to include substantial extra shielding. This would favour the μ bremsstrahlung production channel for shorter S lifetimes. Such a drastic modification of the DarkQuest setup may not be practically feasible so it is worth considering other mitigation strategies.

We note that while DarkQuest is sensitive to very small couplings, it does not surpass the (recasted) limits from E137 [343] in the long-lifetime regime. In fact,

N_{towers}	0	1	2	3	4	5	6
$E_{\text{cut}}^{\text{tower}} = 1.0$ GeV	55%	8%	8%	9%	10%	7%	3%

Table 9.4: Distribution of the number of distinct calorimeter towers whose total energy deposition is above $E_{\text{cut}}^{\text{towers}}$ for photons produced from the $K_L \rightarrow 3\pi^0$ background. Similar numbers are obtained using the 0.5 GeV cut on the photons.

the biggest impact of DarkQuest will be to probe the corner of parameter space with $m_S \lesssim 2m_\mu$ that can explain $(g-2)_\mu$; in this regime the couplings are substantial $g_S \lesssim 10^{-3}$, leading to signal rates of $\mathcal{O}(10^3 - 10^6)$ as we show in fig. 9.8. This suggests that the analysis can tolerate additional cuts that lower signal acceptance while still testing $(g-2)_\mu$. We delineate a few background reduction strategies below. Requiring exactly two calorimeter towers with an energy deposition of at least 1 GeV eliminates a large fraction of the $K_L \rightarrow 3\pi^0$ background (see table 9.4 with a 92% reduction). The remaining events have photon energy and p_T distributions that are drastically different from those of the signal as we show in fig. 9.9. This suggests additional selections that can further reduce this background. For example by increasing the minimum photon energy cut to 2.8 GeV one can reduce the K_L backgrounds by an order of magnitude. This selection can be further optimized by using different cuts for the lower and higher energy photons in the ECAL. For example, a lower energy photon cut of $E > 4$ GeV together with a higher energy photon cut of $E > 10$ GeV would reduce the background by a factor of 50 while reducing signal by a factor of 3.

Diphoton production in the last radiation length of the dump from the atten-

uated proton beam (section 9.5.2) and displaced decays of K_L (section 9.5.1) do not produce associated muons, while the dominant S production channels do. Thus, selecting events with a muon can be an effective way of eliminating these backgrounds. In fig. 9.10 we show how the background-free sensitivity changes with the addition of various cuts, including the muon selection. While requiring a muon in the acceptance of the detector incurs a significant penalty on the signal rate, DarkQuest remains sensitive to the parameter space that can explain $(g-2)_\mu$. The impact of the muon selection requirement was estimated by propagating each muon after it underwent bremsstrahlung in the FMAG through the remainder of the dump, through KMAG and to the muon station at ~ 21 m. The muon hit was counted if it had an energy over 1 GeV and it intersected the station 4 detectors [54] (labelled "muon station" in fig. 9.1).

Requiring a muon hit does not eliminate the muon DIS-induced neutral meson production at the back of the dump (see section 9.5.3). However, we find that simple geometric acceptance and photon energy selections reduce the estimated π^0 yield in eq. (9.16) by a factor of > 200. Similar conclusions hold for DIS-induced K_L backgrounds: requiring exactly two photons with energy above a GeV in the geometric acceptance reduces this by a factor > 1000, even before cutting on the final state muon or photon separation.

We have also explored a diphoton invariant mass cut to reduce backgrounds coming from π^0 decays. While excluding events with $m_{\gamma\gamma} \approx m_\pi$ does decrease these by a factor of at most ~ 2, the poor diphoton mass resolution discussed in section 9.2.3 means that the signal yield is also negatively affected since DarkQuest's most important

181

sensitivity lies in the window $m_\mu \lesssim m_S \lesssim 2m_\mu$, i.e., near the pion mass.

9.7 Conclusions

The proposed DarkQuest experiment offers a powerful test of scalars coupled to muons. In this chaper, we showed that it will be able to probe new regions of parameter space that address the $(g-2)_\mu$ anomaly already with 10^{18} POT, for $m_S \leq 2m_\mu$. The large number of secondary mesons and muons produced in the proton-dump collisions open multiple production channels for new light states whose displaced decays can be observed with the downstream detectors. We identified new production channels for scalars coupled to muons and background processes relevant for the displaced diphoton signatures at DarkQuest. We carefully modeled production and detection of signal and background events and outlined several strategies for achieving the projected sensitivities in fig. 9.7. Other searches (prompt $S \to \mu\mu$) using the same experiment will be able to probe higher masses [226].
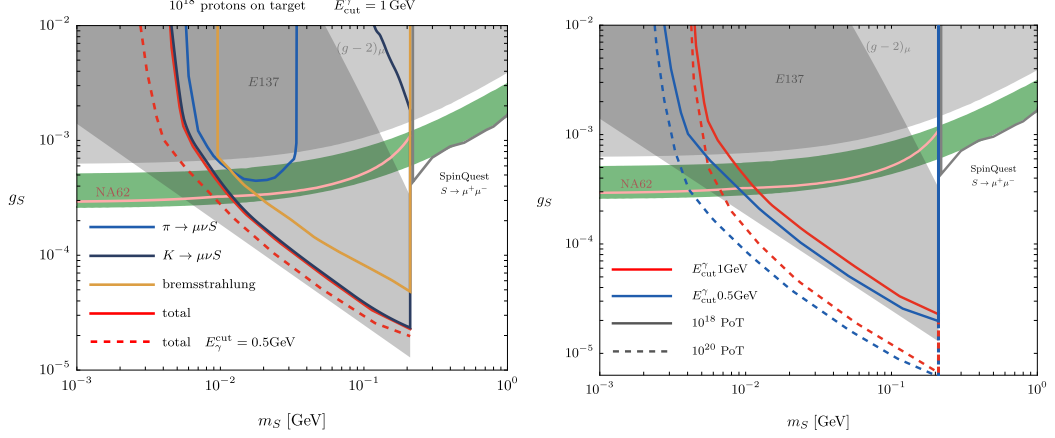
Figure 9.7: Projected sensitivity of the DarkQuest experiment to the muonphilic scalar model in the $m_S - g_S$ plane for $m_S \leq 2m_\mu$. In the left panel we show contributions of different production channels to the sensitivity for 10^{18} POT (the dashed line is for 10^{20} POT). The signal photons are required to have $E_\gamma > 1$ GeV and to be separated by more than 5.5 cm in the transverse direction when they enter the ECAL. In the right panel we show how the sensitivity changes with a lower cut on E_γ, and how the reach is improved with 10^{20} POT. In both plots the green band is the parameter space that can address the $(g-2)_\mu$ anomaly; the gray regions are excluded either by $(g-2)_\mu$ or by the recast of E137 [343]. We also show projections for the proposed resonant search at SpinQuest [226] and at NA62 [322].

183
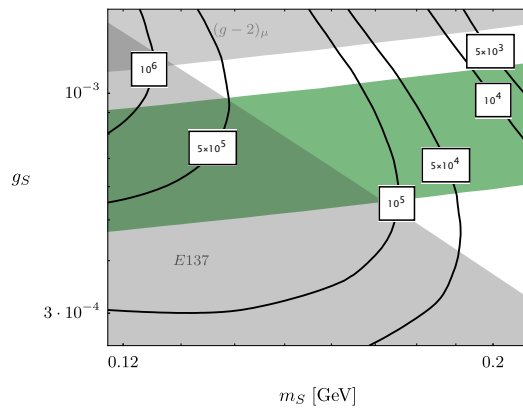
Figure 9.8: Number of signal events for 10^{18} POT, after requiring two photons with $E_\gamma > 1$ GeV each, separated by ≥ 5.5 cm .
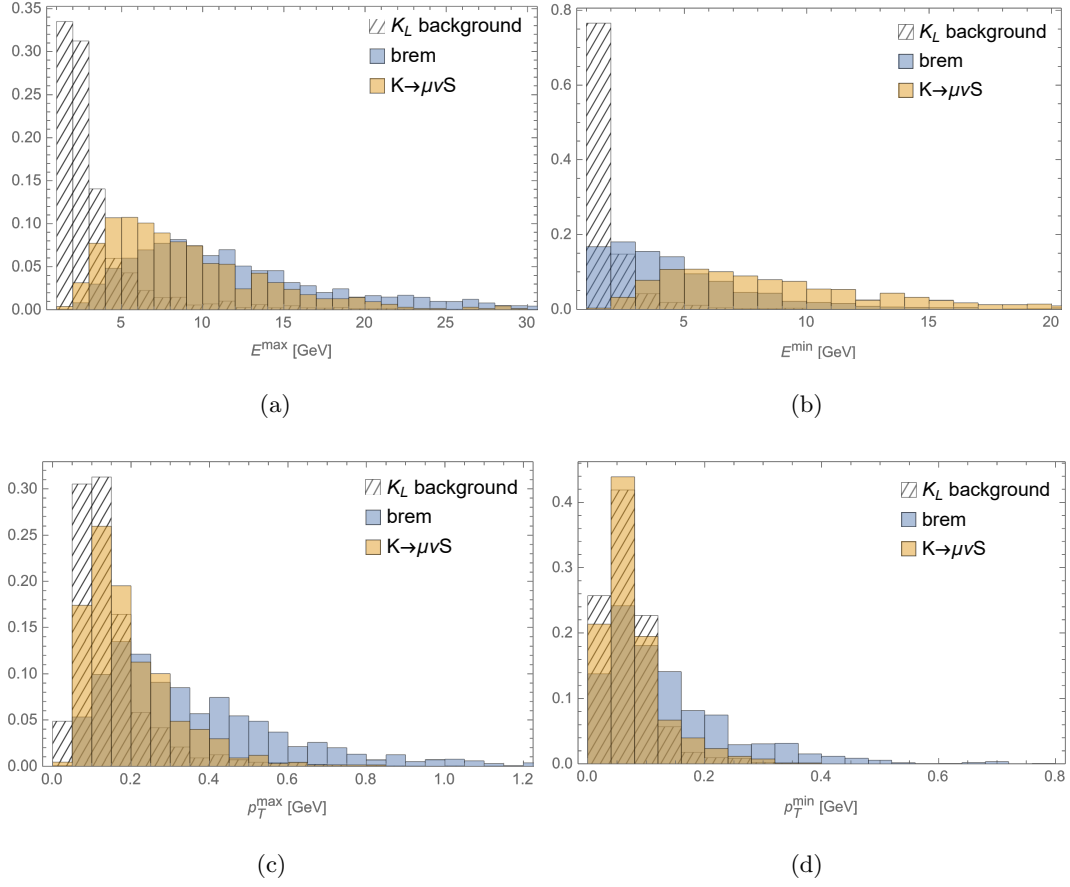
Figure 9.9: Normalized histograms of kinematic variables for a parameter point at high scalar mass, inside the $(g-2)_\mu$-favored region ($m_S = 0.14$ GeV, $g_S \sim 10^{-3}$). The bremsstrahlung and the three body kaon decay $K \to \mu\nu S$ events are selected by requiring each photon in the pair have $E_\gamma > 1$ GeV and ≥ 5.5 cm separation in the ECal. The K_L background events are selected by grouping the 6 photons into 5.5 cm square calorimeter towers and requiring that two distinct towers have a total $E_\gamma > 1$ GeV. The variables which are being plotted are then totaled for that tower.
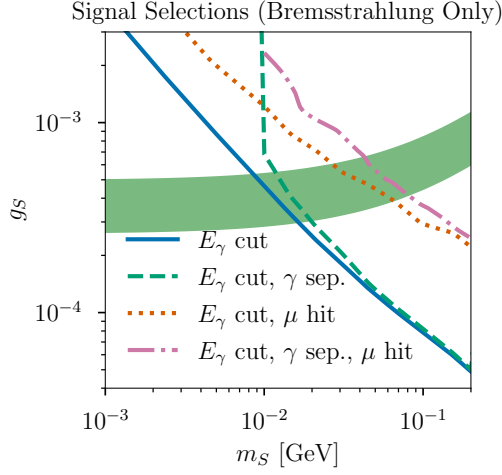
Figure 9.10: Comparison of the (background-free) experimental reach for different signal event selections for the bremsstrahlung production mechanism. All projections include a minimum photon energy cut of 1 GeV; the green dashed (orange dotted) line also requires transverse photon separation of at least 5.5 cm (a muon hit with $E_\mu > 1$ GeV in the muon station). The pink dot-dashed line combines all of these selections. Even for this more restrictive set of cuts designed to eliminate the SM LLP background, DarkQuest maintains sensitivity to the $(g-2)_\mu$ band at $m_S \lesssim 2m_\mu$.

Part V

Conclusion

This thesis has explored several models of particle physics not contained by the Standard Model. Motivations for these models come in various forms. Some are supplied by measurements in tension with the standard model, as is the case (subject to the future work by the lattice gauge theorists) for the measurement of the muon's anomalous magnetic moment. The desire to better understand existing pieces of the Standard Model, such as the Higgs boson, is motivation on its own, irrespective of departures to SM predictions. The LHC is currently in it's 'Run 3' phase, after which it will have gathered 240 fb^{-1} of data, which will soon enough be dwarfed by the HL-LHC program whose projected integrated luminosity is 3000 fb^{-1} (a more optimistic output would be 4000 fb^{-1}) at a beam energy of 14 TeV. [44]. This is a great opportunity to probe models of extra Higgs bosons, whose CPV content can be further investigated by complementary advancements in measuring electric dipole moments of elementary particles: order-of-magnitude improvements to the ACME experiment mentioned in Part 2 of this thesis are expected in the near future by the collaboration,[75]. By the end of this decade, CERN member states will have voted on whether to proceed with a proposed new collider, The Future Circular Collider (FCC). If approved, it would supply precision measurements of electroweak physics (and more) the decade thereafter (the FCC-ee stage) [49]. Much of the related physics in this thesis could be measured, and the Standard Model tested, to an exquisite and unprecedented degree.

The muon $g-2$ experiment at Fermilab, meanwhile, is preparing to release its full results, based on its entire data collection, in 2025 [443]. Possible future upgrades to the beam dump experiments at FermiLab could come online and probe dark sector

physics in a similar time frame [78]. Part IV of this thesis explored a model in the dark sector which could be studied at DarkQuest. Studying dark sectors at colliders is complemented by ongoing, and future, astrophysical searches which could explain at least a portion of the dark matter. This thesis also explored an alternative in primordial black holes, whose populations could hope to be inferred from microlensing events seen by the Nancy Grace Roman Space Telescope set to launch in 2027. This thesis optimistically describes a rich array of probes which offers many opportunities to test complementary theories of BSM physics in the present and near future.

Bibliography

[1] Combined Higgs boson production and decay measurements with up to 137 fb-1 of proton-proton collision data at sqrts = 13 TeV. Technical report, CERN, Geneva, 2020.

[2] Combined measurements of Higgs boson production and decay using up to 139 fb^{-1} of proton-proton collision data at $\sqrt{s} = 13$ TeV collected with the ATLAS experiment. Technical report, CERN, Geneva, 2021.

[3] Search for CP violation in $t\bar{t}$H and tH production in multilepton channels at $\sqrt{s} = 13$ TeV. 2022.

[4] Search for third-generation vector-like leptons in pp collisions at $\sqrt{s} = 13\,\text{TeV}$ with the ATLAS detector. 3 2023.

[5] Summary of Diboson Resonance Searches at the ATLAS experiment using full run-2 data. Technical report, CERN, Geneva, 2023. All figures including auxiliary figures are available at https://atlas.web.cern.ch/Atlas/GROUPS/PHYSICS/PUBNOTES/ATL-PHYS-PUB-2023-007.

[6] Test of cp-invariance of the higgs boson in vector-boson fusion production and its decay into four leptons. 2023.

[7] Morad Aaboud et al. Search for Heavy Higgs Bosons A/H Decaying to a Top Quark Pair in pp Collisions at $\sqrt{s} = 8$ TeV with the ATLAS Detector. *Phys. Rev. Lett.*, 119(19):191803, 2017.

[8] Morad Aaboud et al. Search for new phenomena in high-mass diphoton final states using 37 fb^{-1} of proton–proton collisions collected at $\sqrt{s} = 13$ TeV with the ATLAS detector. *Phys. Lett. B*, 775:105–125, 2017.

[9] Morad Aaboud et al. Measurement of the Higgs boson coupling properties in the $H \to ZZ^* \to 4\ell$ decay channel at $\sqrt{s} = 13$ TeV with the ATLAS detector. *JHEP*, 03:095, 2018.

[10] Morad Aaboud et al. Search for a heavy Higgs boson decaying into a Z boson and another heavy Higgs boson in the $\ell\ell bb$ final state in pp collisions at $\sqrt{s} = 13$ TeV with the ATLAS detector. *Phys. Lett. B*, 783:392–414, 2018.

[11] Morad Aaboud et al. Search for heavy resonances decaying into WW in the $e\nu\mu\nu$ final state in pp collisions at $\sqrt{s} = 13$ TeV with the ATLAS detector. *Eur. Phys. J. C*, 78(1):24, 2018.

[12] Morad Aaboud et al. Search for WW/WZ resonance production in $\ell\nu qq$ final states in pp collisions at $\sqrt{s} = 13$ TeV with the ATLAS detector. *JHEP*, 03:042, 2018.

[13] et al. Aad, G. Observation of a new particle in the search for the standard model higgs boson with the atlas detector at the lhc. *Physics Letters B*, 716(1):1–29, September 2012.

[14] Georges Aad et al. Determination of spin and parity of the Higgs boson in the $WW^* \rightarrow e\nu\mu\nu$ decay channel with the ATLAS detector. *Eur. Phys. J. C*, 75(5):231, 2015.

[15] Georges Aad et al. Search for heavy lepton resonances decaying to a Z boson and a lepton in pp collisions at $\sqrt{s} = 8$ TeV with the ATLAS detector. *JHEP*, 09:108, 2015.

[16] Georges Aad et al. Study of the spin and parity of the Higgs boson in diboson decays with the ATLAS detector. *Eur. Phys. J.*, C75(10):476, 2015. [Erratum: Eur. Phys. J.C76,no.3,152(2016)].

[17] Georges Aad et al. Test of CP Invariance in vector-boson fusion production of the Higgs boson using the Optimal Observable method in the ditau decay channel with the ATLAS detector. *Eur. Phys. J. C*, 76(12):658, 2016.

[18] Georges Aad et al. Combined measurements of Higgs boson production and decay using up to 80 fb^{-1} of proton-proton collision data at $\sqrt{s} = 13$ TeV collected with the ATLAS experiment. *Phys. Rev.*, D101(1):012002, 2020.

[19] Georges Aad et al. Search for electroweak production of charginos and sleptons decaying into final states with two leptons and missing transverse momentum in

$\sqrt{s} = 13$ TeV pp collisions using the ATLAS detector. *Eur. Phys. J.*, C80(2):123, 2020.

[20] Georges Aad et al. Search for heavy Higgs bosons decaying into two tau leptons with the ATLAS detector using pp collisions at $\sqrt{s} = 13$ TeV. *Phys. Rev. Lett.*, 125(5):051801, 2020.

[21] Georges Aad et al. Search for heavy Higgs bosons decaying into two tau leptons with the ATLAS detector using pp collisions at $\sqrt{s} = 13$ TeV. *Phys. Rev. Lett.*, 125(5):051801, 2020.

[22] Georges Aad et al. Search for heavy neutral Higgs bosons produced in association with b-quarks and decaying into b-quarks at $\sqrt{s} = 13$ TeV with the ATLAS detector. *Phys. Rev. D*, 102(3):032004, 2020.

[23] Georges Aad et al. Searches for electroweak production of supersymmetric particles with compressed mass spectra in $\sqrt{s} = 13$ TeV pp collisions with the ATLAS detector. *Phys. Rev.*, D101(5):052005, 2020.

[24] Georges Aad et al. Study of the CP properties of the interaction of the Higgs boson with top quarks using top quark associated production of the Higgs boson and its decay into two photons with the ATLAS detector at the LHC. 2020.

[25] Georges Aad et al. Test of CP invariance in vector-boson fusion production of the Higgs boson in the $H \rightarrow \tau\tau$ channel in proton$-$proton collisions at $\sqrt{s} = 13$ TeV with the ATLAS detector. 2020.

[26] Georges Aad et al. A search for the dimuon decay of the Standard Model Higgs boson with the ATLAS detector. *Phys. Lett.*, B812:135980, 2021.

[27] Georges Aad et al. Search for charged Higgs bosons decaying into a top quark and a bottom quark at $\sqrt{s} = 13$ TeV with the ATLAS detector. *JHEP*, 06:145, 2021.

[28] Georges Aad et al. Search for heavy resonances decaying into a pair of Z bosons in the $\ell^+\ell^-\ell'^+\ell'^-$ and $\ell^+\ell^-\nu\bar{\nu}$ final states using 139 fb^{-1} of proton–proton collisions at $\sqrt{s} = 13$ TeV with the ATLAS detector. *Eur. Phys. J. C*, 81(4):332, 2021.

[29] Georges Aad et al. Search for $t\bar{t}H/A \to t\bar{t}t\bar{t}$ production in the multilepton final state in proton–proton collisions at $\sqrt{s} = 13$ TeV with the ATLAS detector. *JHEP*, 07:203, 2023.

[30] R Aaij et al. Implications of LHCb measurements and future prospects. *Eur. Phys. J.*, C73(4):2373, 2013.

[31] R. Aaij et al. Test of lepton universality with $B^0 \to K^{*0}\ell^+\ell^-$ decays. *JHEP*, 08:055, 2017.

[32] Roel Aaij, Daniel Hugo Cámpora Pérez, Tommaso Colombo, Conor Fitzpatrick, Vladimir Vava Gligorov, Arthur Hennequin, Niko Neufeld, Niklas Nolte, Rainer Schwemmer, and Dorothea Vom Bruch. Evolution of the energy efficiency of LHCb's real-time processing. *EPJ Web Conf.*, 251:04009, 2021.

[33] Roel Aaij et al. Test of lepton universality using $B^+ \to K^+\ell^+\ell^-$ decays. *Phys. Rev. Lett.*, 113:151601, 2014.

[34] Roel Aaij et al. Search for the lepton flavour violating decay $\tau \to \mu\mu^+\mu$. *JHEP*, 02:121, 2015.

[35] Roel Aaij et al. Search for lepton-universality violation in $B^+ \to K^+\ell^+\ell^-$ decays. *Phys. Rev. Lett.*, 122(19):191801, 2019.

[36] Roel Aaij et al. Test of lepton universality in beauty-quark decays. 3 2021.

[37] T. Aaltonen et al. High-precision measurement of the W boson mass with the CDF II detector. *Science*, 376(6589):170–176, 2022.

[38] J. Abdallah et al. Study of tau-pair production in photon-photon collisions at LEP and limits on the anomalous electromagnetic moments of the tau lepton. *Eur. Phys. J.*, C35:159–170, 2004.

[39] A. Abdesselam et al. Search for lepton-flavor-violating tau decays to $\ell\gamma$ modes at Belle. 2021.

[40] Murat Abdughani, Yi-Zhong Fan, Lei Feng, Yue-Lin Sming Tsai, Lei Wu, and Qiang Yuan. A common origin of muon g-2 anomaly, Galaxy Center GeV excess and AMS-02 anti-proton excess in the NMSSM. 4 2021.

[41] F. Abe et al. MOA II Gravitational Microlensing Survey — A new generation microlensing survey —. In *17th Workshop on General Relativity and Gravitation in Japan*, pages 62–74, 2008.

[42] Tomohiro Abe, Junji Hisano, Teppei Kitahara, and Kohsaku Tobioka. Gauge invariant Barr-Zee type contributions to fermionic EDMs in the two-Higgs doublet models. *JHEP*, 01:106, 2014. [Erratum: JHEP 04, 161 (2016)].

[43] C. Abel et al. Measurement of the Permanent Electric Dipole Moment of the Neutron. *Phys. Rev. Lett.*, 124(8):081803, 2020.

[44] et al. Aberle, O. *High-Luminosity Large Hadron Collider (HL-LHC): Technical design report*. CERN Yellow Reports: Monographs. CERN, Geneva, 2020.

[45] B. Abi et al. Measurement of the Positive Muon Anomalous Magnetic Moment to 0.46 ppm. *Phys. Rev. Lett.*, 126:141801, 2021.

[46] B. Abi et al. Measurement of the Positive Muon Anomalous Magnetic Moment to 0.46 ppm. *Phys. Rev. Lett.*, 126(14):141801, 2021.

[47] Amin Aboubrahim, Michael Klasen, and Pran Nath. What Fermilab $(g-2)_\mu$ experiment tells us about discovering SUSY at HL-LHC and HE-LHC. 4 2021.

[48] P. Achard et al. Search for heavy neutral and charged leptons in e^+e^- annihilation at LEP. *Phys. Lett. B*, 517:75–85, 2001.

[49] I. Agapov, M. Benedikt, A. Blondel, M. Boscolo, O. Brunner, M. Chamizo Llatas, T. Charles, D. Denisov, W. Fischer, E. Gianfelice-Wendt, J. Gutleber, P. Janot, M. Koratzinos, R. Losito, S. Nagaitsev, K. Oide, T. Raubenheimer, R. Rimmer, J. Seeman, D. Shatilov, V. Shiltsev, M. Sullivan, U. Wienands, and F. Zimmermann. Future circular lepton collider fcc-ee: Overview and status, 2022.

[50] S. Agostinelli et al. GEANT4–a simulation toolkit. *Nucl. Instrum. Meth. A*, 506:250–303, 2003.

[51] D. P. Aguillard et al. Measurement of the Positive Muon Anomalous Magnetic Moment to 0.20 ppm. *Phys. Rev. Lett.*, 131(16):161802, 2023.

[52] Q. R. Ahmad, R. C. Allen, T. C. Andersen, J. D. Anglin, G. Bühler, J. C. Barton, E. W. Beier, M. Bercovitch, J. Bigu, S. Biller, R. A. Black, I. Blevis, R. J. Boardman, J. Boger, E. Bonvin, M. G. Boulay, M. G. Bowler, T. J. Bowles, S. J. Brice, M. C. Browne, T. V. Bullard, T. H. Burritt, K. Cameron, J. Cameron, Y. D. Chan, M. Chen, H. H. Chen, X. Chen, M. C. Chon, B. T. Cleveland, E. T. H. Clifford, J. H. M. Cowan, D. F. Cowen, G. A. Cox, Y. Dai, X. Dai, F. Dalnoki-Veress, W. F. Davidson, P. J. Doe, G. Doucas, M. R. Dragowsky, C. A. Duba, F. A. Duncan, J. Dunmore, E. D. Earle, S. R. Elliott, H. C. Evans, G. T. Ewan, J. Farine, H. Fergani, A. P. Ferraris, R. J. Ford, M. M. Fowler, K. Frame, E. D. Frank, W. Frati, J. V. Germani, S. Gil, A. Goldschmidt, D. R. Grant, R. L. Hahn, A. L. Hallin, E. D. Hallman, A. Hamer, A. A. Hamian, R. U. Haq, C. K. Hargrove, P. J. Harvey, R. Hazama, R. Heaton, K. M. Heeger, W. J. Heintzelman, J. Heise, R. L. Helmer, J. D. Hepburn, H. Heron, J. Hewett, A. Hime, M. Howe, J. G. Hykawy, M. C. P. Isaac, P. Jagam, N. A. Jelley, C. Jillings, G. Jonkmans, J. Karn, P. T. Keener, K. Kirch, J. R. Klein, A. B. Knox, R. J. Komar, R. Kouzes, T. Kutter, C. C. M. Kyba, J. Law, I. T. Lawson, M. Lay, H. W. Lee, K. T. Lesko, J. R. Leslie, I. Levine, W. Locke, M. M. Lowry, S. Luoma, J. Lyon, S. Majerus, H. B. Mak,

197

A. D. Marino, N. McCauley, A. B. McDonald, D. S. McDonald, K. McFarlane, G. McGregor, W. McLatchie, R. Meijer Drees, H. Mes, C. Mifflin, G. G. Miller, G. Milton, B. A. Moffat, M. Moorhead, C. W. Nally, M. S. Neubauer, F. M. Newcomer, H. S. Ng, A. J. Noble, E. B. Norman, V. M. Novikov, M. O'Neill, C. E. Okada, R. W. Ollerhead, M. Omori, J. L. Orrell, S. M. Oser, A. W. P. Poon, T. J. Radcliffe, A. Roberge, B. C. Robertson, R. G. H. Robertson, J. K. Rowley, V. L. Rusu, E. Saettler, K. K. Schaffer, A. Schuelke, M. H. Schwendener, H. Seifert, M. Shatkay, J. J. Simpson, D. Sinclair, P. Skensved, A. R. Smith, M. W. E. Smith, N. Starinsky, T. D. Steiger, R. G. Stokstad, R. S. Storey, B. Sur, R. Tafirout, N. Tagg, N. W. Tanner, R. K. Taplin, M. Thorman, P. Thornewell, P. T. Trent, Y. I. Tserkovnyak, R. Van Berg, R. G. Van de Water, C. J. Virtue, C. E. Waltham, J.-X. Wang, D. L. Wark, N. West, J. B. Wilhelmy, J. F. Wilkerson, J. Wilson, P. Wittich, J. M. Wouters, and M. Yeh. Measurement of the rate of $\nu_e + d \rightarrow p + p + e^-$ interactions produced by ^8b solar neutrinos at the sudbury neutrino observatory. *Phys. Rev. Lett.*, 87:071301, Jul 2001.

[53] Q. R. Ahmad, R. C. Allen, T. C. Andersen, J. D.Anglin, J. C. Barton, E. W. Beier, M. Bercovitch, J. Bigu, S. D. Biller, R. A. Black, I. Blevis, R. J. Boardman, J. Boger, E. Bonvin, M. G. Boulay, M. G. Bowler, T. J. Bowles, S. J. Brice, M. C. Browne, T. V. Bullard, G. Bühler, J. Cameron, Y. D. Chan, H. H. Chen, M. Chen, X. Chen, B. T. Cleveland, E. T. H. Clifford, J. H. M. Cowan, D. F. Cowen, G. A. Cox, X. Dai, F. Dalnoki-Veress, W. F. Davidson, P. J. Doe, G. Doucas, M. R.

Dragowsky, C. A. Duba, F. A. Duncan, M. Dunford, J. A. Dunmore, E. D. Earle, S. R. Elliott, H. C. Evans, G. T. Ewan, J. Farine, H. Fergani, A. P. Ferraris, R. J. Ford, J. A. Formaggio, M. M. Fowler, K. Frame, E. D. Frank, W. Frati, N. Gagnon, J. V. Germani, S. Gil, K. Graham, D. R. Grant, R. L. Hahn, A. L. Hallin, E. D. Hallman, A. S. Hamer, A. A. Hamian, W. B. Handler, R. U. Haq, C. K. Hargrove, P. J. Harvey, R. Hazama, K. M. Heeger, W. J. Heintzelman, J. Heise, R. L. Helmer, J. D. Hepburn, H. Heron, J. Hewett, A. Hime, M. Howe, J. G. Hykawy, M. C. P. Isaac, P. Jagam, N. A. Jelley, C. Jillings, G. Jonkmans, K. Kazkaz, P. T. Keener, J. R. Klein, A. B. Knox, R. J. Komar, R. Kouzes, T. Kutter, C. C. M. Kyba, J. Law, I. T. Lawson, M. Lay, H. W. Lee, K. T. Lesko, J. R. Leslie, I. Levine, W. Locke, S. Luoma, J. Lyon, S. Majerus, H. B. Mak, J. Maneira, J. Manor, A. D. Marino, N. McCauley, A. B. McDonald, D. S. McDonald, K. McFarlane, G. McGregor, R. Meijer Drees, C. Mifflin, G. G. Miller, G. Milton, B. A. Moffat, M. Moorhead, C. W. Nally, M. S. Neubauer, F. M. Newcomer, H. S. Ng, A. J. Noble, E. B. Norman, V. M. Novikov, M. O'Neill, C. E. Okada, R. W. Ollerhead, M. Omori, J. L. Orrell, S. M. Oser, A. W. P. Poon, T. J. Radcliffe, A. Roberge, B. C. Robertson, R. G. H. Robertson, S. S. E. Rosendahl, J. K. Rowley, V. L. Rusu, E. Saettler, K. K. Schaffer, M. H. Schwendener, A. Schülke, H. Seifert, M. Shatkay, J. J. Simpson, C. J. Sims, D. Sinclair, P. Skensved, A. R. Smith, M. W. E. Smith, T. Spreitzer, N. Starinsky, T. D. Steiger, R. G. Stokstad, L. C. Stonehill, R. S. Storey, B. Sur, R. Tafirout, N. Tagg, N. W. Tanner, R. K. Taplin, M. Thorman, P. M. Thornewell, P. T. Trent, Y. I. Tserkovnyak, R. Van Berg, R. G.

Van de Water, C. J. Virtue, C. E. Waltham, J.-X. Wang, D. L. Wark, N. West, J. B. Wilhelmy, J. F. Wilkerson, J. R. Wilson, P. Wittich, J. M. Wouters, and M. Yeh. Direct evidence for neutrino flavor transformation from neutral-current interactions in the sudbury neutrino observatory. *Phys. Rev. Lett.*, 89:011301, Jun 2002.

[54] C. A. Aidala et al. The SeaQuest Spectrometer at Fermilab. *Nucl. Instrum. Meth. A*, 930:49–63, 2019.

[55] Ricardo Alarcon et al. Electric dipole moments and the search for new physics. In *Snowmass 2021*, 3 2022.

[56] C. Alcock et al. The MACHO project: Microlensing results from 5.7 years of LMC observations. *Astrophys. J.*, 542:281–307, 2000.

[57] C. Alcock et al. The MACHO project: microlensing detection efficiency. *Astrophys. J. Suppl.*, 136:439–462, 2001.

[58] Jim Alexander et al. The storage ring proton EDM experiment. 4 2022.

[59] J. Allison et al. Recent developments in Geant4. *Nucl. Instrum. Meth. A*, 835:186–225, 2016.

[60] John Allison et al. Geant4 developments and applications. *IEEE Trans. Nucl. Sci.*, 53:270, 2006.

[61] Daniel Aloni, Pouya Asadi, Yuichiro Nakai, Matthew Reece, and Motoo Suzuki.

Spontaneous CP Violation and Horizontal Symmetry in the MSSM: Toward Lepton Flavor Naturalness. 4 2021.

[62] W. Altmannshofer et al. The Belle II Physics Book. *PTEP*, 2019(12):123C01, 2019. [Erratum: PTEP 2020, 029201 (2020)].

[63] Wolfgang Altmannshofer, Joachim Brod, and Martin Schmaltz. Experimental constraints on the coupling of the Higgs boson to electrons. *JHEP*, 05:125, 2015.

[64] Wolfgang Altmannshofer, Marcela Carena, Stefania Gori, and Alejandro de la Puente. Signals of CP Violation Beyond the MSSM in Higgs and Flavor Physics. *Phys. Rev.*, D84:095027, 2011.

[65] Wolfgang Altmannshofer, Joshua Eby, Stefania Gori, Matteo Lotito, Mario Martone, and Douglas Tuckler. Collider Signatures of Flavorful Higgs Bosons. *Phys. Rev.*, D94(11):115032, 2016.

[66] Wolfgang Altmannshofer, Sri Aditya Gadam, Stefania Gori, and Nick Hamer. Explaining (g 2) with multi-tev sleptons. *Journal of High Energy Physics*, 2021(7), July 2021.

[67] Wolfgang Altmannshofer, Stefania Gori, Nick Hamer, and Hiren H. Patel. Electron EDM in the complex two-Higgs doublet model. *Phys. Rev.*, D102(11):115042, 2021. [Phys. Rev.D102,115042(2020)].

[68] Wolfgang Altmannshofer, Stefania Gori, Alexander L. Kagan, Luca Silvestrini,

and Jure Zupan. Uncovering Mass Generation Through Higgs Flavor Violation. *Phys. Rev.*, D93(3):031301, 2016.

[69] Wolfgang Altmannshofer, Stefania Gori, Hiren H. Patel, Stefano Profumo, and Douglas Tuckler. Electric dipole moments in a leptoquark scenario for the B-physics anomalies. *JHEP*, 05:069, 2020.

[70] Wolfgang Altmannshofer, Stefania Gori, Dean J. Robinson, and Douglas Tuckler. The Flavor-locked Flavorful Two Higgs Doublet Model. *JHEP*, 03:129, 2018.

[71] Wolfgang Altmannshofer and Brian Maddock. Flavorful Two Higgs Doublet Models with a Twist. *Phys. Rev.*, D98(7):075005, 2018.

[72] Wolfgang Altmannshofer, Brian Maddock, and Douglas Tuckler. Rare Top Decays as Probes of Flavorful Higgs Bosons. *Phys. Rev.*, D100(1):015003, 2019.

[73] Wolfgang Altmannshofer and David M. Straub. Viability of MSSM scenarios at very large $\tan\beta$. *JHEP*, 09:078, 2010.

[74] J. Alwall, R. Frederix, S. Frixione, V. Hirschi, F. Maltoni, O. Mattelaer, H. S. Shao, T. Stelzer, P. Torrielli, and M. Zaro. The automated computation of tree-level and next-to-leading order differential cross sections, and their matching to parton shower simulations. *JHEP*, 07:079, 2014.

[75] V. Andreev et al. Improved limit on the electric dipole moment of the electron. *Nature*, 562(7727):355–360, 2018.

[76] T. Aoyama et al. The anomalous magnetic moment of the muon in the Standard Model. *Phys. Rept.*, 887:1–166, 2020.

[77] L Aphecetche et al. PHENIX calorimeter. *Nucl. Instrum. Meth. A*, 499:521–536, 2003.

[78] Aram Apyan, Brian Batell, Asher Berlin, Nikita Blinov, Caspian Chaharom, Sergio Cuadra, Zeynep Demiragli, Adam Duran, Yongbin Feng, I. P. Fernando, Stefania Gori, Philip Harris, Duc Hoang, Dustin Keller, Elizabeth Kowalczyk, Monica Leys, Kun Liu, Ming Liu, Wolfgang Lorenzon, Petar Maksimovic, Cristina Mantilla Suarez, Hrachya Marukyan, Amitav Mitra, Yoshiyuki Miyachi, Patrick McCormack, Eric A. Moreno, Yasser Corrales Morales, Noah Paladino, Mudit Rai, Sebastian Rotella, Luke Saunders, Shinaya Sawada, Carli Smith, David Sperka, Rick Tesarek, Nhan Tran, Yu-Dai Tsai, Zijie Wan, and Margaret Wynne. Darkquest: A dark sector upgrade to spinquest at the 120 gev fermilab main injector, 2022.

[79] Aram Apyan et al. DarkQuest: A dark sector upgrade to SpinQuest at the 120 GeV Fermilab Main Injector. In *2022 Snowmass Summer Study*, 3 2022.

[80] Akitaka Ariga, Reuven Balkin, Iftah Galon, Enrique Kajomovitz, and Yotam Soreq. Hunting muonic forces at emulsion detectors. *Phys. Rev. D*, 109(3):035003, 2024.

[81] Andrew Askew, Prerit Jaiswal, Takemichi Okui, Harrison B. Prosper, and Nobuo

Sato. Prospect for measuring the CP phase in the $h\tau\tau$ coupling at the LHC. *Phys. Rev.*, D91(7):075014, 2015.

[82] Peter Athron, Csaba Balázs, Douglas Hj Jacob, Wojciech Kotlarski, Dominik Stöckinger, and Hyejung Stöckinger-Kim. New physics explanations of a_μ in light of the FNAL muon $g - 2$ measurement. 4 2021.

[83] Bernard Aubert et al. Searches for Lepton Flavor Violation in the Decays $\tau^\pm \to e^\pm \gamma$ and $\tau^\pm \to \mu^\pm \gamma$. *Phys. Rev. Lett.*, 104:021802, 2010.

[84] E. Bachelet, D. Specht, M. Penny, M. Hundertmark, S. Awiphan, J.-P. Beaulieu, M. Dominik, E. Kerins, D. Maoz, E. Meade, A. A. Nucita, R. Poleski, C. Ranc, J. Rhodes, and A. C. Robin. ieuclid-roman/i joint microlensing survey: Early mass measurement, free floating planets, and exomoons. *Astronomy &amp Astrophysics*, 664:A136, aug 2022.

[85] Henning Bahl, Marcela Carena, Nina M. Coyle, Aurora Ireland, and Carlos E. M. Wagner. New tools for dissecting the general 2HDM. *JHEP*, 03:165, 2023.

[86] J. F. Bak, A. Burenkov, J. B. B. Petersen, E. Uggerhoj, S. P. Moller, and P. Siffert. Large Departures From Landau Distributions for High-energy Particles Traversing Thin Si and Ge Targets. *Nucl. Phys. B*, 288:681–716, 1987.

[87] Michael J. Baker and Andrea Thamm. Leptonic WIMP Coannihilation and the Current Dark Matter Search Strategy. *JHEP*, 10:187, 2018.

[88] A. M. Baldini et al. Search for the lepton flavour violating decay $\mu^+ \to e^+\gamma$ with the full dataset of the MEG experiment. *Eur. Phys. J. C*, 76(8):434, 2016.

[89] Guillermo Ballesteros and Marco Taoso. Primordial black hole dark matter from single field inflation. *Phys. Rev. D*, 97(2):023501, 2018.

[90] Jacob Baron et al. Order of Magnitude Smaller Limit on the Electric Dipole Moment of the Electron. *Science*, 343:269–272, 2014.

[91] Stephen M. Barr and A. Zee. Electric Dipole Moment of the Electron and of the Neutron. *Phys. Rev. Lett.*, 65:21–24, 1990. [Erratum: Phys.Rev.Lett. 65, 2920 (1990)].

[92] A. Barroso, P. M. Ferreira, I. P. Ivanov, and Rui Santos. Metastability bounds on the two Higgs doublet model. *JHEP*, 06:045, 2013.

[93] A. Barroso, P. M. Ferreira, I. P. Ivanov, and Rui Santos. Metastability bounds on the two higgs doublet model. *Journal of High Energy Physics*, 2013(6), Jun 2013.

[94] A. Barroso, P. M. Ferreira, and R. Santos. Charge and CP symmetry breaking in two Higgs doublet models. *Phys. Lett.*, B632:684–687, 2006.

[95] Philipp Basler, Margarete Mühlleitner, and Jonas Wittbrodt. The CP-Violating 2HDM in Light of a Strong First Order Electroweak Phase Transition and Implications for Higgs Pair Production. *JHEP*, 03:061, 2018.

[96] Brian Batell, Jared A. Evans, Stefania Gori, and Mudit Rai. Dark Scalars and Heavy Neutral Leptons at DarkQuest. *JHEP*, 05:049, 2021.

205

[97] Brian Batell, Ayres Freitas, Ahmed Ismail, and David Mckeen. Flavor-specific scalar mediators. *Phys. Rev. D*, 98(5):055026, 2018.

[98] Brian Batell, Nicholas Lange, David McKeen, Maxim Pospelov, and Adam Ritz. Muon anomalous magnetic moment through the leptonic Higgs portal. *Phys. Rev. D*, 95(7):075003, 2017.

[99] Virginie Batista, A. Gould, S. Dieters, Subo Dong, I. Bond, J. P. Beaulieu, D. Maoz, B. Monard, G. W. Christie, J. McCormick, M. D. Albrow, K. Horne, Y. Tsapras, M. J. Burgdorf, S. Calchi Novati, J. Skottfelt, J. Caldwell, S. Kozlowski, D. Kubas, B. S. Gaudi, C. Han, D. P. Bennett, J. An, the MOA Collaboration, the PLANET Collaboration, the MicroFUN Collaboration, the MiND-STEp Consortium, and the RoboNet Collaboration. MOA-2009-BLG-387Lb: A massive planet orbiting an M dwarf. *Astronomy & Astrophysics*, 529:A102, May 2011. arXiv:1102.0558 [astro-ph].

[100] J. R. Batley et al. Search for the dark photon in π^0 decays. *Phys. Lett. B*, 746:178–185, 2015.

[101] James M. Bauer, Tommy Grav, Yanga R. Fernández, A. K. Mainzer, Emily A. Kramer, Joseph R. Masiero, Timothy Spahr, C. R. Nugent, Rachel A. Stevenson, Karen J. Meech, Roc M. Cutri, Carey M. Lisse, Russell Walker, John W. Dailey, Joshua Rosser, Phillip Krings, Kinjal Ruecker, Edward L. Wright, and the NE-OWISE Team. Debiasing the neowise cryogenic mission comet populations. *The Astronomical Journal*, 154(2):53, jul 2017.

206

[102] Sebastian Baum, Marcela Carena, Nausheen R. Shah, and Carlos E. M. Wagner. The Tiny (g-2) Muon Wobble from Small-μ Supersymmetry. 4 2021.

[103] Alexei Bazavov et al. Light-quark connected intermediate-window contributions to the muon $g - 2$ hadronic vacuum polarization from lattice QCD. 1 2023.

[104] Nicola Bellomo, José Luis Bernal, Alvise Raccanelli, and Licia Verde. Primordial Black Holes as Dark Matter: Converting Constraints from Monochromatic to Extended Mass Distributions. *Journal of Cosmology and Astroparticle Physics*, 2018(01):004–004, January 2018. arXiv:1709.07467 [astro-ph].

[105] G. W. Bennett et al. Final Report of the Muon E821 Anomalous Magnetic Moment Measurement at BNL. *Phys. Rev. D*, 73:072003, 2006.

[106] G. W. Bennett et al. Final Report of the Muon E821 Anomalous Magnetic Moment Measurement at BNL. *Phys. Rev. D*, 73:072003, 2006.

[107] S. Berge, W. Bernreuther, B. Niepelt, and H. Spiesberger. How to pin down the CP quantum numbers of a Higgs boson in its tau decays at the LHC. *Phys. Rev.*, D84:116003, 2011.

[108] F. Bergsma et al. A Search for Decays of Heavy Neutrinos. *Phys. Lett. B*, 128:361, 1983.

[109] F. Bergsma et al. A Search for Decays of Heavy Neutrinos in the Mass Range 0.5-GeV to 2.8-GeV. *Phys. Lett. B*, 166:473–478, 1986.

[110] Asher Berlin, Nikita Blinov, Stefania Gori, Philip Schuster, and Natalia Toro. Cosmology and Accelerator Tests of Strongly Interacting Dark Matter. *Phys. Rev. D*, 97(5):055033, 2018.

[111] Asher Berlin, Stefania Gori, Philip Schuster, and Natalia Toro. Dark Sectors at the Fermilab SeaQuest Experiment. *Phys. Rev. D*, 98(3):035011, 2018.

[112] Florian U. Bernlochner, Heiko Lacker, Zoltan Ligeti, Iain W. Stewart, Frank J. Tackmann, and Kerstin Tackmann. Precision Global Determination of the $B \to X_s\gamma$ Decay Rate. 2020.

[113] Jérémy Bernon, John F. Gunion, Howard E. Haber, Yun Jiang, and Sabine Kraml. Scrutinizing the alignment limit in two-higgs-doublet models. *Physical Review D*, 93(3), February 2016.

[114] Saloni Bhatiani, Xinyu Dai, and Eduardo Guerras. Confirmation of Planet-mass Objects in Extragalactic Systems. *The Astrophysical Journal*, 885(1):77, November 2019.

[115] Saloni Bhatiani, Xinyu Dai, and Eduardo Guerras. Confirmation of planet-mass objects in extragalactic systems. *The Astrophysical Journal*, 885(1):77, nov 2019.

[116] Prudhvi N. Bhattiprolu and Stephen P. Martin. Prospects for vectorlike leptons at future proton-proton colliders. *Phys. Rev. D*, 100(1):015033, 2019.

[117] Ligong Bian and Ning Chen. Cancellation mechanism in the predictions of electric dipole moments. *Phys. Rev. D*, 95(11):115029, 2017.

[118] Ligong Bian, Tao Liu, and Jing Shu. Cancellations Between Two-Loop Contributions to the Electron Electric Dipole Moment with a CP-Violating Higgs Sector. *Phys. Rev. Lett.*, 115:021801, 2015.

[119] Hans Bichsel. Straggling in Thin Silicon Detectors. *Rev. Mod. Phys.*, 60:663–699, 1988.

[120] Anke Biekoetter, Raquel Gomez-Ambrosio, Parisa Gregg, Frank Krauss, and Marek Schoenherr. Constraining SMEFT operators with associated $h\gamma$ production in Weak Boson Fusion. 2020.

[121] Christian Bierlich et al. A comprehensive guide to the physics and usage of PYTHIA 8.3. 3 2022.

[122] Fady Bishara, Yuval Grossman, Roni Harnik, Dean J. Robinson, Jing Shu, and Jure Zupan. Probing CP Violation in $h \to \gamma\gamma$ with Converted Photons. *JHEP*, 04:084, 2014.

[123] Joss Bland-Hawthorn and Ortwin Gerhard. The galaxy in context: Structural, kinematic, and integrated properties. *Annual Review of Astronomy and Astrophysics*, 54(1):529–596, 2016.

[124] Gianluca Blankenburg, John Ellis, and Gino Isidori. Flavour-Changing Decays of a 125 GeV Higgs-like Particle. *Phys. Lett.*, B712:386–390, 2012.

[125] Andrew E. Blechman, Alexey A. Petrov, and Gagik Yeghiyan. The Flavor puzzle in multi-Higgs models. *JHEP*, 11:075, 2010.

[126] Nikita Blinov, Elizabeth Kowalczyk, and Margaret Wynne. Axion-like particle searches at DarkQuest. *JHEP*, 02:036, 2022.

[127] T. Blum et al. Fundamental Physics in Small Experiments. 9 2022.

[128] T. Blum et al. An update of Euclidean windows of the hadronic vacuum polarization. 1 2023.

[129] N.N. Bogoliubov and O.S. Parasiuk. On the Multiplication of the causal function in the quantum theory of fields. *Acta Math.*, 97:227–266, 1957.

[130] G. V. Borisov and B. M. Shustov. Discovery of the First Interstellar Comet and the Spatial Density of Interstellar Objects in the Solar Neighborhood. *Solar System Research*, 55(2):124–131, March 2021.

[131] Sz. Borsanyi et al. Leading hadronic contribution to the muon magnetic moment from lattice QCD. *Nature*, 593(7857):51–55, 2021.

[132] F. J. Botella, G. C. Branco, M. N. Rebelo, and J. I. Silva-Marcos. What if the masses of the first two quark families are not generated by the standard model Higgs boson? *Phys. Rev.*, D94(11):115031, 2016.

[133] Rafael Boto, Tiago V. Fernandes, Howard E. Haber, Jorge C. Romão, and João P. Silva. Basis-independent treatment of the complex 2HDM. *Phys. Rev. D*, 101(5):055023, 2020.

[134] Jo Bovy. Stellar Inventory of the Solar Neighborhood using Gaia DR1. *Monthly*

Notices of the Royal Astronomical Society, 470(2):1360–1387, September 2017. arXiv:1704.05063 [astro-ph].

[135] Joachim Brod and Dimitrios Skodras. Electric dipole moment constraints on CP-violating light-quark Yukawas. *JHEP*, 01:233, 2019.

[136] Peter G. Brown and Jiří Borovička. On the proposed interstellar origin of the usg 20140108 fireball, 2023.

[137] A. J. Buras, P. Gambino, M. Gorbahn, S. Jager, and L. Silvestrini. Universal unitarity triangle and physics beyond the standard model. *Phys. Lett.*, B500:161–167, 2001.

[138] Jonathan M. Butterworth, Adam R. Davison, Mathieu Rubin, and Gavin P. Salam. Jet substructure as a new Higgs search channel at the LHC. *Phys. Rev. Lett.*, 100:242001, 2008.

[139] Christian T. Byrnes, Mark Hindmarsh, Sam Young, and Michael R. S. Hawkins. Primordial black holes with an accurate QCD equation of state. *JCAP*, 08:041, 2018.

[140] S. Calchi Novati, S. Mirzoyan, Ph. Jetzer, and G. Scarpetta. Microlensing towards the SMC: a new analysis of OGLE and EROS results. *Mon. Not. Roy. Astron. Soc.*, 435:1582, 2013.

[141] Rodolfo Capdevilla, David Curtin, Yonatan Kahn, and Gordan Krnjaic. Discover-

ing the physics of $(g-2)_\mu$ at future muon colliders. *Phys. Rev. D*, 103(7):075028, 2021.

[142] Rodolfo Capdevilla, David Curtin, Yonatan Kahn, and Gordan Krnjaic. No-lose theorem for discovering the new physics of (g-2)μ at muon colliders. *Phys. Rev. D*, 105(1):015028, 2022.

[143] Rodolfo Capdevilla, David Curtin, Yonatan Kahn, and Gordan Krnjaic. Systematically testing singlet models for (g − 2)$_?$. *JHEP*, 04:129, 2022.

[144] Marcela Carena and Zhen Liu. Challenges and opportunities for heavy scalar searches in the $t\bar{t}$ channel at the LHC. *JHEP*, 11:159, 2016.

[145] Marcela Carena, Zhen Liu, and Marc Riembau. Probing the electroweak phase transition via enhanced di-Higgs boson production. *Phys. Rev.*, D97(9):095032, 2018.

[146] Marcela Carena, M. Olechowski, S. Pokorski, and C. E. M. Wagner. Electroweak symmetry breaking and bottom - top Yukawa unification. *Nucl. Phys.*, B426:269–300, 1994.

[147] Bernard Carr, Kazunori Kohri, Yuuiti Sendouda, and Jun'ichi Yokoyama. Constraints on primordial black holes. *Rept. Prog. Phys.*, 84(11):116902, 2021.

[148] Bernard Carr and Florian Kuhnel. Primordial black holes as dark matter candidates. *SciPost Phys. Lect. Notes*, 48:1, 2022.

[149] Bernard Carr and Florian Kühnel. Primordial black holes as dark matter candidates. *SciPost Physics Lecture Notes*, may 2022.

[150] Bernard J. Carr and S. W. Hawking. Black holes in the early Universe. *Mon. Not. Roy. Astron. Soc.*, 168:399–415, 1974.

[151] Bernard J. Carr and James E. Lidsey. Primordial black holes and generalized constraints on chaotic inflation. *Phys. Rev. D*, 48:543–553, 1993.

[152] Andrea Celentano, Luc Darmé, Luca Marsicano, and Enrico Nardi. New production channels for light dark matter in hadronic showers. *Phys. Rev. D*, 102(7):075026, 2020.

[153] M. Cepeda et al. Higgs Physics at the HL-LHC and HE-LHC. 2019.

[154] Cari Cesarotti, Yonatan Kahn, Gordan Krnjaic, Duncan Rocha, and Joshua Spitz. New μ Forces From ν_μ Sources. 11 2023.

[155] Manimala Chakraborti, Sven Heinemeyer, and Ipsita Saha. The new "MUON G-2" Result and Supersymmetry. 4 2021.

[156] Manimala Chakraborti, Leszek Roszkowski, and Sebastian Trojanowski. GUT-constrained supersymmetry and dark matter in light of the new $(g-2)_\mu$ determination. 4 2021.

[157] D. Chang, Wai-Yee Keung, and T.C. Yuan. Two loop bosonic contribution to the electron electric dipole moment. *Phys. Rev. D*, 43:14–16, 1991.

[158] Chien-Yi Chen, S. Dawson, and Yue Zhang. Complementarity of LHC and EDMs for Exploring Higgs CP Violation. *JHEP*, 06:056, 2015.

[159] Chien-Yi Chen, Jonathan Kozaczuk, and Yi-Ming Zhong. Exploring leptophilic dark matter with NA64-μ. *JHEP*, 10:154, 2018.

[160] Chien-Yi Chen, Hao-Lin Li, and Michael Ramsey-Musolf. CP-Violation in the Two Higgs Doublet Model: from the LHC to EDMs. *Phys. Rev. D*, 97(1):015020, 2018.

[161] Chien-Yi Chen, Maxim Pospelov, and Yi-Ming Zhong. Muon Beam Experiments to Probe the Dark Sector. *Phys. Rev. D*, 95(11):115005, 2017.

[162] Ning Chen, Tong Li, Zhaolong Teng, and Yongcheng Wu. Collapsing domain walls in the two-Higgs-doublet model and deep insights from the EDM. 6 2020.

[163] Xin Chen and Yongcheng Wu. Probing the CP-Violation effects in the $h\tau\tau$ coupling at the LHC. *Phys. Lett.*, B790:332–338, 2019.

[164] Yi Chen, Adam Falkowski, Ian Low, and Roberto Vega-Morales. New Observables for CP Violation in Higgs Decays. *Phys. Rev. D*, 90(11):113006, 2014.

[165] Adriano Cherchiglia, Patrick Kneschke, Dominik Stöckinger, and Hyejung Stöckinger-Kim. The muon magnetic moment in the 2HDM: complete two-loop result. *JHEP*, 01:007, 2017.

[166] Kingman Cheung, Adil Jueid, Ying-Nan Mao, and Stefano Moretti. The 2-Higgs-

Doublet Model with Soft CP-violation Confronting Electric Dipole Moments and Colliders. 3 2020.

[167] Kingman Cheung, Jae Sik Lee, Eibun Senaha, and Po-Yan Tseng. Confronting Higgcision with Electric Dipole Moments. *JHEP*, 06:149, 2014.

[168] R. Sekhar Chivukula and Howard Georgi. Composite Technicolor Standard Model. *Phys. Lett.*, B188:99–104, 1987.

[169] Eung Jin Chun, Jongkuk Kim, and Tanmoy Mondal. Electron EDM and Muon anomalous magnetic moment in Two-Higgs-Doublet Models. *JHEP*, 12:068, 2019.

[170] Vincenzo Cirigliano, Andreas Crivellin, Wouter Dekens, Jordy de Vries, Martin Hoferichter, and Emanuele Mereghetti. *cp* violation in higgs-gauge interactions: From tabletop experiments to the lhc. *Phys. Rev. Lett.*, 123:051801, Jul 2019.

[171] Gilberto Colangelo, Martin Hoferichter, and Peter Stoffer. Constraints on the two-pion contribution to hadronic vacuum polarization. *Phys. Lett. B*, 814:136073, 2021.

[172] CMS Collaboration. Analysis of the CP structure of the Yukawa coupling between the Higgs boson and τ leptons in proton-proton collisions at $\sqrt{s} = 13$ TeV. 2020.

[173] The ATLAS collaboration. Probing the $\mathcal{CP}$ nature of the Higgs boson coupling to τ leptons at HL-LHC. 2019.

[174] Eric Cotner and Alexander Kusenko. Primordial black holes from scalar field evolution in the early universe. *Phys. Rev. D*, 96(10):103002, 2017.

[175] Eric Cotner and Alexander Kusenko. Primordial black holes from supersymmetry in the early universe. *Phys. Rev. Lett.*, 119(3):031103, 2017.

[176] Eric Cotner, Alexander Kusenko, Misao Sasaki, and Volodymyr Takhistov. Analytic Description of Primordial Black Hole Formation from Scalar Field Fragmentation. *JCAP*, 10:077, 2019.

[177] Eric Cotner, Alexander Kusenko, and Volodymyr Takhistov. Primordial Black Holes from Inflaton Fragmentation into Oscillons. *Phys. Rev. D*, 98(8):083513, 2018.

[178] Peter Cox, Chengcheng Han, and Tsutomu T. Yanagida. Muon $g-2$ and Co-annihilating Dark Matter in the MSSM. 4 2021.

[179] Matt Crawford and David N. Schramm. Spontaneous Generation of Density Perturbations in the Early Universe. *Nature*, 298:538–540, 1982.

[180] Djuna Croon, David McKeen, Nirmal Raj, and Zihui Wang. Subaru through a different lens: microlensing by extended dark matter structures. *Physical Review D*, 102(8):083021, October 2020. arXiv:2007.12697 [astro-ph, physics:hep-ph].

[181] Xinyu Dai and Eduardo Guerras. Probing extragalactic planets using quasar microlensing. *The Astrophysical Journal*, 853(2):L27, feb 2018.

[182] G. D'Ambrosio, G. F. Giudice, G. Isidori, and A. Strumia. Minimal flavor violation: An Effective field theory approach. *Nucl. Phys.*, B645:155–187, 2002.

[183] Ashok K. Das and Chung Kao. A Two Higgs doublet model for the top quark. *Phys. Lett. B*, 372:106–112, 1996.

[184] Sacha Davidson and Howard E. Haber. Basis-independent methods for the two-Higgs-doublet model. *Phys. Rev.*, D72:035004, 2005. [Erratum: Phys. Rev.D72,099902(2005)].

[185] Andrei I. Davydychev and J.B. Tausk. Two loop selfenergy diagrams with different masses and the momentum expansion. *Nucl. Phys. B*, 397:123–142, 1993.

[186] Giuseppe Degrassi and Alberto Sirlin. Gauge invariant selfenergies and vertex parts of the Standard Model in the pinch technique framework. *Phys. Rev. D*, 46:3104–3116, 1992.

[187] Durmus A. Demir, Maxim Pospelov, and Adam Ritz. Hadronic EDMs, the Weinberg operator, and light gluinos. *Phys. Rev. D*, 67:015007, 2003.

[188] Heling Deng and Alexander Vilenkin. Primordial black hole formation by vacuum bubbles. *JCAP*, 12:044, 2017.

[189] A. Denner, S. Heinemeyer, I. Puljak, D. Rebuzzi, and M. Spira. Standard Model Higgs-Boson Branching Ratios with Uncertainties. *Eur. Phys. J. C*, 71:1753, 2011.

[190] Ansgar Denner, Laura Jenniches, Jean-Nicolas Lang, and Christian Sturm. Gauge-independent $\overline{MS}$ renormalization in the 2HDM. *JHEP*, 09:115, 2016.

[191] Ansgar Denner, G. Weiglein, and S. Dittmaier. Gauge invariance of Green func-

tions: Background field method versus pinch technique. *Phys. Lett. B*, 333:420–426, 1994.

[192] Ansgar Denner, Georg Weiglein, and Stefan Dittmaier. Application of the background field method to the electroweak standard model. *Nucl. Phys. B*, 440:95–128, 1995.

[193] Radovan Dermisek, Jonathan P. Hall, Enrico Lunghi, and Seodong Shin. Limits on Vectorlike Leptons from Searches for Anomalous Production of Multi-Lepton Events. *JHEP*, 12:013, 2014.

[194] W. DeRocco, M. Kunimoto, and N. Smyth. ——, 2023.

[195] William DeRocco, Evan Frangipane, Nick Hamer, Stefano Profumo, and Nolan Smyth. Revealing terrestrial-mass primordial black holes with the Nancy Grace Roman Space Telescope. *Phys. Rev. D*, 109(2):023013, 2024.

[196] William DeRocco and Peter W. Graham. Constraining Primordial Black Hole Abundance with the Galactic 511 keV Line. *Phys. Rev. Lett.*, 123(25):251102, 2019.

[197] William DeRocco, Nolan Smyth, and Stefano Profumo. Constraints on sub-terrestrial free-floating planets from Subaru microlensing observations, August 2023. arXiv:2308.13593 [astro-ph, physics:hep-ph].

[198] Nilendra G. Deshpande and Ernest Ma. Pattern of Symmetry Breaking with Two Higgs Doublets. *Phys. Rev.*, D18:2574, 1978.

[199] V. F. Dmitriev and R. A. Sen'kov. Schiff moment of the mercury nucleus and the proton dipole moment. *Phys. Rev. Lett.*, 91:212303, Nov 2003.

[200] Aaron Do, Michael A. Tucker, and John Tonry. Interstellar interlopers: Number density and origin of 'oumuamua-like objects. *The Astrophysical Journal*, 855(1):L10, mar 2018.

[201] Babette Döbrich, Joerg Jaeckel, and Tommaso Spadaro. Light in the beam dump - ALP production from decay photons in proton beam-dumps. *JHEP*, 05:213, 2019. [Erratum: JHEP 10, 046 (2020)].

[202] J. S. Dohnanyi. Collisional Model of Asteroids and Their Debris. In Lubor Kresak and Peter Mackenzie Millman, editors, *Physics and Dynamics of Meteors*, volume 33, page 486, January 1968.

[203] Matthew J. Dolan, Philip Harris, Martin Jankowiak, and Michael Spannowsky. Constraining CP-violating Higgs Sectors at the LHC using gluon fusion. *Phys. Rev.*, D90:073008, 2014.

[204] Alexandre Dolgov and Joseph Silk. Baryon isocurvature fluctuations at small scales and baryonic dark matter. *Phys. Rev. D*, 47:4244–4255, 1993.

[205] Manuel Drees and Gilles Gerbier. Mini–review of dark matter: 2012, 2012.

[206] Bhaskar Dutta and Yukihiro Mimura. Yukawa Unification with Four Higgs Doublets in Supersymmetric GUT. *Phys. Lett.*, B790:589–594, 2019.

[207] Daniel Egana-Ugrinovic, Samuel Homiller, and Patrick Roddy Meade. Higgs bosons with large couplings to light quarks. *Phys. Rev. D*, 100(11):115041, 2019.

[208] Daniel Egana-Ugrinovic, Matthew Low, and Joshua T. Ruderman. Charged Fermions Below 100 GeV. *JHEP*, 05:012, 2018.

[209] Daniel Egana-Ugrinovic and Scott Thomas. Effective Theory of Higgs Sector Vacuum States. 12 2015.

[210] Daniel Egana-Ugrinovic and Scott Thomas. Higgs Boson Contributions to the Electron Electric Dipole Moment. 10 2018.

[211] Abdul Wahab El Kaffas, Wafaa Khater, Odd Magne Ogreid, and Per Osland. Consistency of the two Higgs doublet model and CP violation in top production at the LHC. *Nucl. Phys.*, B775:45–77, 2007.

[212] Richard Keith Ellis et al. Physics Briefing Book. 2019.

[213] Motoi Endo, Koichi Hamaguchi, Sho Iwamoto, and Teppei Kitahara. Supersymmetric Interpretation of the Muon $g-2$ Anomaly. 4 2021.

[214] Jonathan Engel, Michael J. Ramsey-Musolf, and U. van Kolck. Electric Dipole Moments of Nucleons, Nuclei, and Atoms: The Standard Model and Beyond. *Prog. Part. Nucl. Phys.*, 71:21–74, 2013.

[215] Toni Engelhardt, Robert Jedicke, Peter Vereš , Alan Fitzsimmons, Larry Denneau, Ed Beshore, and Bonnie Meinke. An observational upper limit on the interstellar

number density of asteroids and comets. *The Astronomical Journal*, 153(3):133, feb 2017.

[216] Sonja Engmann and Denis Cousineau. Comparing distributions: the two-sample anderson–darling test as an alternative to the kolmogorov–smirnov test. *Journal of Applied Quantitative Methods*, 6:1–17, 09 2011.

[217] N. Escudero, C. Munoz, and A. M. Teixeira. FCNCs in supersymmetric multi-Higgs doublet models. *Phys. Rev. D*, 73:055015, 2006.

[218] Sergio B. Fajardo-Acosta, Andreas Faisst, Carl J. Grillmair, Ranga-Ram Chary, Roberta Paladini, Ben Rusholme, and Nathaniel Stickley. Joint Survey Processing. II. Stellar Proper Motions in the COSMOS Field from Hubble Space Telescope ACS and Subaru Telescope HSC Observations. *The Astrophysical Journal*, 930(1):71, May 2022. Publisher: The American Astronomical Society.

[219] Marco Farina, Yuval Grossman, and Dean J. Robinson. Probing CP violation in $h \to Z\gamma$ with background interference. *Phys. Rev.*, D92(7):073007, 2015.

[220] Y.R. Fernández, M.S. Kelley, P.L. Lamy, I. Toth, O. Groussin, C.M. Lisse, M.F. A'Hearn, J.M. Bauer, H. Campins, A. Fitzsimmons, J. Licandro, S.C. Lowry, K.J. Meech, J. Pittichová, W.T. Reach, C. Snodgrass, and H.A. Weaver. Thermal properties, sizes, and size distribution of jupiter-family cometary nuclei. *Icarus*, 226(1):1138–1170, 2013.

[221] P. M. Ferreira, B. Grzadkowski, O. M. Ogreid, and P. Osland. Softly broken

symmetries in the 2hdm — an invariant formulation. *Journal of High Energy Physics*, 2023(1), January 2023.

[222] P. M. Ferreira, R. Santos, and A. Barroso. Stability of the tree-level vacuum in two Higgs doublet models against charge or CP spontaneous violation. *Phys. Lett.*, B603:219–229, 2004. [Erratum: Phys. Lett.B629,114(2005)].

[223] Alan Fitzsimmons, Karem Meech, Luca Matrà, and Susanne Pfalzner. Interstellar objects and exocomets, 2023.

[224] Eirik Grude Flekkøy and Renaud Toussaint. Statistical implications of the n = 1 observation of 1I/'Oumuamua. *Monthly Notices of the Royal Astronomical Society: Letters*, 523(1):L9–L14, 04 2023.

[225] Duarte Fontes, Margarete Mühlleitner, Jorge C. Romão, Rui Santos, João P. Silva, and Jonas Wittbrodt. The C2HDM revisited. *JHEP*, 02:073, 2018.

[226] Diana Forbes, Christian Herwig, Yonatan Kahn, Gordan Krnjaic, Cristina Mantilla Suarez, Nhan Tran, and Andrew Whitbeck. New searches for muonphilic particles at proton beam dump spectrometers. *Phys. Rev. D*, 107(11):116026, 2023.

[227] Elina Fuchs and Georg Weiglein. Impact of CP-violating interference effects on MSSM Higgs searches. *Eur. Phys. J.*, C78(2):87, 2018.

[228] Y. Fukuda, T. Hayakawa, E. Ichihara, K. Inoue, K. Ishihara, H. Ishino, Y. Itow, T. Kajita, J. Kameda, S. Kasuga, K. Kobayashi, Y. Kobayashi, Y. Koshio,

M. Miura, M. Nakahata, S. Nakayama, A. Okada, K. Okumura, N. Sakurai, M. Shiozawa, Y. Suzuki, Y. Takeuchi, Y. Totsuka, S. Yamada, M. Earl, A. Habig, E. Kearns, M. D. Messier, K. Scholberg, J. L. Stone, L. R. Sulak, C. W. Walter, M. Goldhaber, T. Barszczxak, D. Casper, W. Gajewski, P. G. Halverson, J. Hsu, W. R. Kropp, L. R. Price, F. Reines, M. Smy, H. W. Sobel, M. R. Vagins, K. S. Ganezer, W. E. Keig, R. W. Ellsworth, S. Tasaka, J. W. Flanagan, A. Kibayashi, J. G. Learned, S. Matsuno, V. J. Stenger, D. Takemori, T. Ishii, J. Kanzaki, T. Kobayashi, S. Mine, K. Nakamura, K. Nishikawa, Y. Oyama, A. Sakai, M. Sakuda, O. Sasaki, S. Echigo, M. Kohama, A. T. Suzuki, T. J. Haines, E. Blaufuss, B. K. Kim, R. Sanford, R. Svoboda, M. L. Chen, Z. Conner, J. A. Goodman, G. W. Sullivan, J. Hill, C. K. Jung, K. Martens, C. Mauger, C. McGrew, E. Sharkey, B. Viren, C. Yanagisawa, W. Doki, K. Miyano, H. Okazawa, C. Saji, M. Takahata, Y. Nagashima, M. Takita, T. Yamaguchi, M. Yoshida, S. B. Kim, M. Etoh, K. Fujita, A. Hasegawa, T. Hasegawa, S. Hatakeyama, T. Iwamoto, M. Koga, T. Maruyama, H. Ogawa, J. Shirai, A. Suzuki, F. Tsushima, M. Koshiba, M. Nemoto, K. Nishijima, T. Futagami, Y. Hayato, Y. Kanaya, K. Kaneyuki, Y. Watanabe, D. Kielczewska, R. A. Doyle, J. S. George, A. L. Stachyra, L. L. Wai, R. J. Wilkes, and K. K. Young. Evidence for oscillation of atmospheric neutrinos. *Phys. Rev. Lett.*, 81:1562–1567, Aug 1998.

[229] Gerhardt Funk, Deva O'Neil, and R. Michael Winters. What the Oblique Parameters S, T, and U and Their Extensions Reveal About the 2HDM: A Numerical

Analysis. *Int. J. Mod. Phys. A*, 27:1250021, 2012.

[230] Kaori Fuyuto, Wei-Shu Hou, and Eibun Senaha. Cancellation mechanism for the electron electric dipole moment connected with the baryon asymmetry of the Universe. *Phys. Rev.*, D101(1):011901, 2020.

[231] Juan Garcia-Bellido and Ester Ruiz Morales. Primordial black holes from single field models of inflation. *Phys. Dark Univ.*, 18:47–54, 2017.

[232] S. Gardner, R. J. Holt, and A. S. Tadepalli. New Prospects in Fixed Target Searches for Dark Forces with the SeaQuest Experiment at Fermilab. *Phys. Rev. D*, 93(11):115015, 2016.

[233] Andrá s Gáspár, Dimitrios Psaltis, George H. Rieke, and Feryal Özel. MODELING COLLISIONAL CASCADES IN DEBRIS DISKS: STEEP DUST-SIZE DISTRIBUTIONS. *The Astrophysical Journal*, 754(1):74, jul 2012.

[234] B. Scott Gaudi. The Roman Galactic Bulge Time Domain Survey. In *Bulletin of the American Astronomical Society*, volume 54, page 102.146, June 2022.

[235] Shao-Feng Ge, Gang Li, Pedro Pasquini, and Michael J. Ramsey-Musolf. CP-violating Higgs Di-tau Decays: Baryogenesis and Higgs Factories. *Phys. Rev. D*, 103(9):095027, 2021.

[236] Shuailiang Ge. Sublunar-Mass Primordial Black Holes from Closed Axion Domain Walls. *Phys. Dark Univ.*, 27:100440, 2020.

[237] Cristiano Germani and Tomislav Prokopec. On primordial black holes from an inflection point. *Phys. Dark Univ.*, 18:6–10, 2017.

[238] Diptimoy Ghosh, Rick Sandeepan Gupta, and Gilad Perez. Is the Higgs Mechanism of Fermion Mass Generation a Fact? A Yukawa-less First-Two-Generation Model. *Phys. Lett.*, B755:504–508, 2016.

[239] Jennifer Girrbach, Susanne Mertens, Ulrich Nierste, and Soren Wiesenfeldt. Lepton flavour violation in the MSSM. *JHEP*, 05:026, 2010.

[240] G. F. Giudice, P. Paradisi, and M. Passera. Testing new physics with the electron g-2. *JHEP*, 11:113, 2012.

[241] Sheldon L. Glashow and Steven Weinberg. Natural Conservation Laws for Neutral Currents. *Phys. Rev. D*, 15:1958, 1977.

[242] S. N. Gninenko. Constraints on sub-GeV hidden sector gauge bosons from a search for heavy neutrino decays. *Phys. Lett. B*, 713:244–248, 2012.

[243] S. N. Gninenko and N. V. Krasnikov. Probing the muon g_μ - 2 anomaly, $L_\mu - L_\tau$ gauge boson and Dark Matter in dark photon experiments. *Phys. Lett. B*, 783:24–28, 2018.

[244] S. N. Gninenko, N. V. Krasnikov, and V. A. Matveev. Muon g-2 and searches for a new leptophobic sub-GeV dark boson in a missing-energy experiment at CERN. *Phys. Rev. D*, 91:095015, 2015.

[245] Dorival Gonçalves, Jeong Han Kim, Kyoungchul Kong, and Yongcheng Wu. Direct Higgs-top CP-phase measurement with $t\bar{t}h$ at the 14 TeV LHC and 100 TeV FCC. *JHEP*, 01:158, 2022.

[246] S. Gori and N. Hamer. in preparation.

[247] Stefania Gori et al. ACE Science Workshop Report. 3 2024.

[248] Andrew Gould, Youn Kil Jung, Kyu-Ha Hwang, Subo Dong, Michael D. Albrow, Sun-Ju Chung, Cheongho Han, Yoon-Hyun Ryu, In-Gu Shin, Yossi Shvartzvald, Hongjing Yang, Jennifer C. Yee, Weicheng Zang, Sang-Mok Cha, Dong-Jin Kim, Seung-Lee Kim, Chung-Uk Lee, Dong-Joo Lee, Yongseok Lee, Byeong-Gon Park, and Richard W. Pogge. Free-Floating Planets, the Einstein Desert, and 'Oumuamua. *Journal of The Korean Astronomical Society*, 55(5):173–194, October 2022. arXiv:2204.03269 [astro-ph].

[249] Andrew Gould, JungYoun Kil, HwangKyu-Ha, DongSubo, AlbrowMichael D., ChungSun-Ju, HanCheongho, RyuYoon-Hyun, ShinIn-Gu, ShvartzvaldYossi, YangHongjing, YeeJennifer C., ZangWeicheng, ChaSang-Mok, KimDong-Jin, KimSeung-Lee, LeeChung-Uk, LeeDong-Joo, LeeYongseok, ParkByeong-Gon, and PoggeRichard W. Free-floating planets, the einstein desert, and 'oumuamua. *Journal of The Korean Astronomical Society*, 55(5):173–194, 10 2022.

[250] Andrew Gould, Yoon-Hyun Ryu, Jennifer C. Yee, Michael D. Albrow, Sun-Ju Chung, Cheongho Han, Kyu-Ha Hwang, Youn Kil Jung, In-Gu Shin, Yossi

Shvartzvald, Hongjing Yang, Weicheng Zang, Sang-Mok Cha, Dong-Jin Kim, Seung-Lee Kim, Chung-Uk Lee, Dong-Joo Lee, Yongseok Lee, Byeong-Gon Park, and Richard W. Pogge. KMT-2022-BLG-2397: Brown Dwarf at the Upper Shore of the Einstein Desert. *arXiv e-prints*, page arXiv:2306.04870, June 2023.

[251] Andrew Gould, Wei-Cheng Zang, Shude Mao, and Su-Bo Dong. Masses for free-floating planets and dwarf planets. *Research in Astronomy and Astrophysics*, 21(6):133, August 2021.

[252] B. Graner, Y. Chen, E. G. Lindahl, and B. R. Heckel. Reduced Limit on the Permanent Electric Dipole Moment of Hg199. *Phys. Rev. Lett.*, 116(16):161601, 2016. [Erratum: Phys.Rev.Lett. 119, 119901 (2017)].

[253] Anne M. Green. Microlensing and dynamical constraints on primordial black hole dark matter with an extended mass function. *Phys. Rev. D*, 94(6):063530, 2016.

[254] Kim Griest, Agnieszka M. Cieplak, and Matthew J. Lehner. New Limits on Primordial Black Hole Dark Matter from an Analysis of Kepler Source Microlensing Data. *Phys. Rev. Lett.*, 111(18):181302, 2013.

[255] A. V. Gritsan et al. Snowmass White Paper: Prospects of CP-violation measurements with the Higgs boson at future experiments. 5 2022.

[256] Yuchao Gu, Ning Liu, Liangliang Su, and Daohan Wang. Heavy Bino and Slepton for Muon g-2 Anomaly. 4 2021.

[257] J.F. Gunion and R. Vega. The Electron electric dipole moment for a CP violating neutral Higgs sector. *Phys. Lett. B*, 251:157–162, 1990.

[258] John F. Gunion and Howard E. Haber. Cp-conserving two-higgs-doublet model: The approach to the decoupling limit. *Physical Review D*, 67(7), April 2003.

[259] John F. Gunion and Howard E. Haber. The CP conserving two Higgs doublet model: The Approach to the decoupling limit. *Phys. Rev. D*, 67:075019, 2003.

[260] John F. Gunion and Howard E. Haber. Conditions for CP-violation in the general two-Higgs-doublet model. *Phys. Rev. D*, 72:095002, 2005.

[261] John F. Gunion, Howard E. Haber, Gordon L. Kane, and Sally Dawson. *The Higgs Hunter's Guide*, volume 80. 2000.

[262] Howard E. Haber and Laurel Stephenson Haskins. Supersymmetric theory and models. In *Anticipating the Next Discoveries in Particle Physics*. WORLD SCIENTIFIC, May 2018.

[263] Howard E. Haber and Yosef Nir. Multi-scalar models with a high-energy scale. *Nuclear Physics B*, 335(2):363–394, 1990.

[264] Howard E. Haber and Deva O'Neil. Basis-independent methods for the two-Higgs-doublet model. II. The Significance of $\tan\beta$. *Phys. Rev. D*, 74:015018, 2006. [Erratum: Phys.Rev.D 74, 059905 (2006)].

[265] Kaoru Hagiwara, Kai Ma, and Shingo Mori. Probing CP violation in $h \to \tau^-\tau^+$ at the LHC. *Phys. Rev. Lett.*, 118(17):171802, 2017.

[266] Thomas Hahn. Generating Feynman diagrams and amplitudes with FeynArts 3. *Comput. Phys. Commun.*, 140:418–431, 2001.

[267] L. J. Hall and Lisa Randall. Weak scale effective supersymmetry. *Phys. Rev. Lett.*, 65:2939–2942, 1990.

[268] Lawrence J. Hall, Riccardo Rattazzi, and Uri Sarid. The Top quark mass in supersymmetric SO(10) unification. *Phys. Rev.*, D50:7048–7065, 1994.

[269] Chengcheng Han. Muon g-2 and CP violation in MSSM. 4 2021.

[270] D. Hanneke, S. Fogwell, and G. Gabrielse. New Measurement of the Electron Magnetic Moment and the Fine Structure Constant. *Phys. Rev. Lett.*, 100:120801, 2008.

[271] Roni Harnik, Joachim Kopp, and Jure Zupan. Flavor Violating Higgs Decays. *JHEP*, 03:026, 2013.

[272] Roni Harnik, Adam Martin, Takemichi Okui, Reinard Primulando, and Felix Yu. Measuring CP Violation in $h \to \tau^+\tau^-$ at Colliders. *Phys. Rev.*, D88(7):076009, 2013.

[273] Shoji Hashimoto, Jiro Kodaira, Yoshiaki Yasui, and Ken Sasaki. The Background field method: Alternative way of deriving the pinch technique's results. *Phys. Rev. D*, 50:7066–7076, 1994.

[274] S. W. Hawking. Black hole explosions. *Nature*, 248:30–31, 1974.

[275] S. W. Hawking. Black Holes From Cosmic Strings. *Phys. Lett. B*, 231:237–239, 1989.

[276] Stephen Hawking. Gravitationally collapsed objects of very low mass. *Mon. Not. Roy. Astron. Soc.*, 152:75, 1971.

[277] K. Hayasaka et al. New Search for $\tau \to \mu\gamma$ and $\tau \to e\gamma$ Decays at Belle. *Phys. Lett. B*, 666:16–22, 2008.

[278] K. Hayasaka et al. Search for Lepton Flavor Violating Tau Decays into Three Leptons with 719 Million Produced Tau+Tau- Pairs. *Phys. Lett. B*, 687:139–143, 2010.

[279] Sven Heinemeyer, Essodjolo Kpatcha, Iñaki Lara, Daniel E. López-Fogliani, Carlos Muñoz, and Natsumi Nagata. The new $(g-2)_\mu$ result and the $\mu\nu$SSM. 4 2021.

[280] Thomas Helfer, Josu C. Aurrekoetxea, and Eugene A. Lim. Cosmic String Loop Collapse in Full General Relativity. *Phys. Rev. D*, 99(10):104028, 2019.

[281] Ralf Hempfling. Yukawa coupling unification with supersymmetric threshold corrections. *Phys. Rev.*, D49:6168–6172, 1994.

[282] Mark P. Hertzberg and Masaki Yamada. Primordial Black Holes from Polynomial Potentials in Single Field Inflation. *Phys. Rev. D*, 97(8):083509, 2018.

[283] Devin J. Hoover, Darryl Z. Seligman, and Matthew J. Payne. The population of interstellar objects detectable with the lsst and accessible for *In Situ* rendezvous with various mission designs, 2022.

[284] Howard Baer and Vernon Barger and Hasan Serce. Anomalous muon magnetic moment, supersymmetry, naturalness, LHC search limits and the landscape. 2021.

[285] J.J. Hudson, D.M. Kara, I.J. Smallman, B.E. Sauer, M.R. Tarbutt, and E.A. Hinds. Improved measurement of the shape of the electron. *Nature*, 473:493–496, 2011.

[286] Man-To Hui, Quan-Zhi Ye, Dora Föhring, Denise Hung, and David J. Tholen. Physical characterization of interstellar comet 2i/2019 q4 (borisov). *The Astronomical Journal*, 160(2):92, jul 2020.

[287] Satoru Inoue, Michael J. Ramsey-Musolf, and Yue Zhang. CP-violating phenomenology of flavor conserving two Higgs doublet models. *Phys. Rev. D*, 89(11):115023, 2014.

[288] Satoru Inoue, Michael J. Ramsey-Musolf, and Yue Zhang. Cpv phenomenology of flavor conserving two higgs doublet models. 2014.

[289] I. P. Ivanov. Minkowski space structure of the Higgs potential in 2HDM. *Phys. Rev.*, D75:035001, 2007. [Erratum: Phys. Rev.D76,039902(2007)].

[290] Igor P. Ivanov. Minkowski space structure of the Higgs potential in 2HDM. II. Minima, symmetries, and topology. *Phys. Rev.*, D77:015017, 2008.

[291] P. Ivanov, P. Naselsky, and I. Novikov. Inflation and primordial black holes as dark matter. *Phys. Rev. D*, 50:7173–7178, 1994.

[292] Sho Iwamoto, Tsutomu T. Yanagida, and Norimi Yokozaki. Wino-Higgsino dark matter in the MSSM from the $g - 2$ anomaly. 4 2021.

[293] Chloe James-Turner, Danton P. B. Weil, Anne M. Green, and Edmund J. Copeland. Constraints on the cosmic string loop collapse fraction from primordial black holes. *Phys. Rev. D*, 101(12):123526, 2020.

[294] Karsten Jedamzik. Primordial black hole formation during the QCD epoch. *Phys. Rev. D*, 55:5871–5875, 1997.

[295] Ross J. Jennings, James M. Cordes, and Shami Chatterjee. Detecting gravitational scattering of interstellar objects using pulsar timing. *The Astrophysical Journal*, 889(2):145, feb 2020.

[296] David Jewitt, Jane Luu, Jayadev Rajagopal, Ralf Kotulla, Susan Ridgway, Wilson Liu, and Thomas Augusteijn. Interstellar interloper 1i/2017 u1: Observations from the not and wiyn telescopes. *The Astrophysical Journal Letters*, 850(2):L36, nov 2017.

[297] David Jewitt and Darryl Z. Seligman. The interstellar interlopers, 2022.

[298] Samson A. Johnson, Matthew Penny, B. Scott Gaudi, Eamonn Kerins, Nicholas J. Rattenbury, Annie C. Robin, Sebastiano Calchi Novati, and Calen B. Henderson. Predictions of the nancy grace roman space telescope galactic exoplanet survey. II. free-floating planet detection rates. *The Astronomical Journal*, 160(3):123, aug 2020.

[299] R. Jozefowicz, E. Richter-Was, and Z. Was. Potential for optimizing the Higgs boson CP measurement in H → ττ decays at the LHC including machine learning techniques. *Phys. Rev.*, D94(9):093001, 2016.

[300] Dong-Won Jung, Yongtae Heo, and Jae Sik Lee. Mass spectrum of heavy Higgs bosons in two-Higgs-doublet model in the light of the CDF W-mass anomaly. *Phys. Rev. D*, 108(1):015027, 2023.

[301] Martin Jung and Antonio Pich. Electric dipole moments in two-higgs-doublet models. *Journal of High Energy Physics*, 2014(4), apr 2014.

[302] Yonatan Kahn, Gordan Krnjaic, Nhan Tran, and Andrew Whitbeck. M^3: a new muon missing momentum experiment to probe (g − 2)$_\mu$ and dark matter at Fermilab. *JHEP*, 09:153, 2018.

[303] Shinya Kanemura, Mitsunori Kubota, and Kei Yagyu. Aligned CP-violating Higgs sector canceling the electric dipole moment. 4 2020.

[304] Kristjan Kannike, Luca Marzola, Martti Raidal, and Hardi Veermäe. Single Field Double Inflation and Primordial Black Holes. *JCAP*, 09:020, 2017.

[305] M. Karami, A. E. Broderick, S. Rahvar, and M. Reid. Resolving Microlensing Events with Triggered VLBI. *Astrophys. J.*, 833(2):169, 2016.

[306] Bradley J. Kavanagh. bradkav/pbhbounds: Release version, November 2019.

[307] Hidetoshi Kawase. Light Neutralino Dark Matter Scenario in Supersymmetric four-Higgs Doublet Model. *JHEP*, 12:094, 2011.

[308] Venus Keus, Niko Koivunen, and Kimmo Tuominen. Singlet scalar and 2HDM extensions of the Standard Model: CP-violation and constraints from $(g-2)_\mu$ and eEDM. *JHEP*, 09:059, 2018.

[309] Vardan Khachatryan et al. Constraints on the spin-parity and anomalous HVV couplings of the Higgs boson in proton collisions at 7 and 8 TeV. *Phys. Rev.*, D92(1):012004, 2015.

[310] Vardan Khachatryan et al. Combined search for anomalous pseudoscalar HVV couplings in VH(H $\to b\bar{b}$) production and H $\to$ VV decay. *Phys. Lett.*, B759:672–696, 2016.

[311] M. Yu. Khlopov and A. G. Polnarev. PRIMORDIAL BLACK HOLES AS A COSMOLOGICAL TEST OF GRAND UNIFICATION. *Phys. Lett. B*, 97:383–387, 1980.

[312] Hyoun-Woo Kim, Kyu-Ha Hwang, Andrew Gould, Jennifer C. Yee, Yoon-Hyun Ryu, Michael D. Albrow, Sun-Ju Chung, Cheongho Han, Youn Kil Jung, Chung-Uk Lee, In-Gu Shin, Yossi Shvartzvald, Weicheng Zang, Sang-Mok Cha, Dong-Jin Kim, Seung-Lee Kim, Dong-Joo Lee, Yongseok Lee, Byeong-Gon Park, and Richard W. Pogge. Kmt-2019-blg-2073: Fourth free-floating planet candidate with e lt; 10 as. *The Astronomical Journal*, 162(1):15, jun 2021.

[313] Jihn E. Kim and Gianpaolo Carosi. Axions and the Strong CP Problem. *Rev. Mod. Phys.*, 82:557–602, 2010. [Erratum: Rev.Mod.Phys. 91, 049902 (2019)].

[314] Seung-Lee Kim, Chung-Uk Lee, Byeong-Gon Park, Dong-Jin Kim, Sang-Mok Cha, Yongseok Lee, Cheongho Han, Moo-Young Chun, and Insoo Yuk. KMTNET: A Network of 1.6 m Wide-Field Optical Telescopes Installed at Three Southern Observatories. *Journal of Korean Astronomical Society*, 49(1):37–44, February 2016.

[315] Rain Kipper, Elmo Tempel, and Peeter Tenjes. A method to calculate the local density distribution of the Galaxy from the Tycho-Gaia Astrometric Solution data. *Monthly Notices of the Royal Astronomical Society*, 473(2):2188–2197, January 2018.

[316] Matthew Kleban and Cameron E. Norton. Monochromatic Mass Spectrum of Primordial Black Holes. 10 2023.

[317] Anatoly Klypin, HongSheng Zhao, and Rachel S. Somerville. LCDM-based models for the Milky Way and M31 I: Dynamical Models, October 2001. arXiv:astro-ph/0110390.

[318] Makoto Kobayashi and Toshihide Maskawa. CP-Violation in the Renormalizable Theory of Weak Interaction. *Progress of Theoretical Physics*, 49(2):652–657, 02 1973.

[319] Mrunal Korwar and Stefano Profumo. Updated constraints on primordial black hole evaporation. *JCAP*, 05:054, 2023.

[320] Naoki Koshimoto, Junichi Baba, and David P. Bennett. A Parametric Galactic

Model toward the Galactic Bulge Based on Gaia and Microlensing Data. *The Astrophysical Journal*, 917(2):78, August 2021. arXiv:2104.03306 [astro-ph].

[321] Naoki Koshimoto, Takahiro Sumi, David P. Bennett, Valerio Bozza, Przemek Mróz, Andrzej Udalski, Nicholas J. Rattenbury, Fumio Abe, Richard Barry, Aparna Bhattacharya, Ian A. Bond, Hirosane Fujii, Akihiko Fukui, Ryusei Hamada, Yuki Hirao, Stela Ishitani Silva, Yoshitaka Itow, Rintaro Kirikawa, Iona Kondo, Yutaka Matsubara, Shota Miyazaki, Yasushi Muraki, Greg Olmschenk, Clément Ranc, Yuki Satoh, Daisuke Suzuki, Mio Tomoyoshi, Paul J. Tristram, Aikaterini Vandorou, Hibiki Yama, and Kansuke Yamashita. Terrestrial and neptune mass free-floating planet candidates from the moa-ii 9-year galactic bulge survey, 2023.

[322] Gordan Krnjaic, Gustavo Marques-Tavares, Diego Redigolo, and Kohsaku Tobioka. Probing Muonphilic Force Carriers and Dark Matter at Kaon Factories. *Phys. Rev. Lett.*, 124(4):041802, 2020.

[323] Nilanjana Kumar and Stephen P. Martin. Vectorlike Leptons at the Large Hadron Collider. *Phys. Rev. D*, 92(11):115018, 2015.

[324] Alexander Kusenko, Misao Sasaki, Sunao Sugiyama, Masahiro Takada, Volodymyr Takhistov, and Edoardo Vitagliano. Exploring Primordial Black Holes from the Multiverse with Optical Telescopes. *Phys. Rev. Lett.*, 125:181304, 2020.

[325] M. Landgraf, W. J. Baggaley, E. Grün, H. Krüger, and G. Linkert. Aspects of

the mass distribution of interstellar dust grains in the solar system from in situ measurements. *Journal of Geophysical Research: Space Physics*, 105(A5):10343–10352, may 2000.

[326] J.S. Lee, A. Pilaftsis, M. Carena, S.Y. Choi, M. Drees, J. Ellis, and C.E.M. Wagner. Cpsuperh: a computational tool for higgs phenomenology in the minimal supersymmetric standard model with explicit cp violation. *Computer Physics Communications*, 156(3):283–317, January 2004.

[327] J. P. Lees et al. Limits on tau Lepton-Flavor Violating Decays in three charged leptons. *Phys. Rev. D*, 81:111101, 2010.

[328] J. P. Lees et al. Search for Invisible Decays of a Dark Photon Produced in e^+e^- Collisions at BaBar. *Phys. Rev. Lett.*, 119(13):131804, 2017.

[329] J. P. Lees et al. Search for a Dark Leptophilic Scalar in e^+e^- Collisions. *Phys. Rev. Lett.*, 125(18):181801, 2020.

[330] Christoph Lehner and Aaron S. Meyer. Consistency of hadronic vacuum polarization between lattice QCD and the R-ratio. *Phys. Rev. D*, 101:074515, 2020.

[331] R.G. Leigh, S. Paban, and R.M. Xu. Electric dipole moment of electron. *Nucl. Phys. B*, 352:45–58, 1991.

[332] G. Peter Lepage. A New Algorithm for Adaptive Multidimensional Integration. *J. Comput. Phys.*, 27:192, 1978.

[333] G. Peter Lepage. Adaptive multidimensional integration: VEGAS enhanced. *J. Comput. Phys.*, 439:110386, 2021.

[334] LEPSUSYWG. Combined lep chargino results, up to 208 gev for large m0, 2001. `https://lepsusy.web.cern.ch/lepsusy/www/inos_moriond01/charginos_pub.html`.

[335] W. Garrett Levine, Aster G. Taylor, Darryl Z. Seligman, Devin J. Hoover, Robert Jedicke, Jennifer B. Bergner, and Gregory P. Laughlin. Interstellar comets from post-main sequence systems as tracers of extrasolar oort clouds, 2023.

[336] Jing Liu, Zong-Kuan Guo, and Rong-Gen Cai. Primordial Black Holes from Cosmic Domain Walls. *Phys. Rev. D*, 101(2):023513, 2020.

[337] Yu-Sheng Liu, David McKeen, and Gerald A. Miller. Validity of the Weizsäcker-Williams approximation and the analysis of beam dump experiments: Production of a new scalar boson. *Phys. Rev. D*, 95(3):036010, 2017.

[338] Torsten Lohne, Alexander V. Krivov, and Jens Rodmann. Long-term collisional evolution of debris disks. *The Astrophysical Journal*, 673(2):1123, feb 2008.

[339] Ian Low, Nausheen R. Shah, and Xiao-Ping Wang. Higgs alignment and novel CP-violating observables in two-Higgs-doublet models. *Phys. Rev. D*, 105(3):035009, 2022.

[340] Gerald R. Lynch and Orin I. Dahl. Approximations to multiple Coulomb scattering. *Nucl. Instrum. Meth. B*, 58:6–10, 1991.

[341] Daniel Malmberg, Melvyn B. Davies, and Douglas C. Heggie. The effects of fly-bys on planetary systems. *Monthly Notices of the Royal Astronomical Society*, 411(2):859–877, 02 2011.

[342] Schedar Marchetti, Susanne Mertens, Ulrich Nierste, and Dominik Stockinger. Tan(beta)-enhanced supersymmetric corrections to the anomalous magnetic moment of the muon. *Phys. Rev.*, D79:013010, 2009.

[343] L. Marsicano, M. Battaglieri, A. Celentano, R. De Vita, and Yi-Ming Zhong. Probing Leptophilic Dark Sectors at Electron Beam-Dump Facilities. *Phys. Rev. D*, 98(11):115022, 2018.

[344] I. Masina and Carlos A. Savoy. Sleptonarium: Constraints on the CP and flavor pattern of scalar lepton masses. *Nucl. Phys. B*, 661:365–393, 2003.

[345] Norihito Matsunaga and Kazuhiro Yamamoto. The finite source size effect and wave optics in gravitational lensing. *Journal of Cosmology and Astroparticle Physics*, 2006(01):023–023, January 2006.

[346] Thomas A. McGlynn and Robert D. Chapman. On the Nondetection of Extrasolar Comets. *The Astrophysical Journal Letters*, 346:L105, November 1989.

[347] Brian J McParland. *Medical radiation dosimetry*. Springer, 2016.

[348] Karen J. Meech, Robert Weryk, Marco Micheli, Jan T. Kleyna, Olivier R. Hain-aut, Robert Jedicke, Richard J. Wainscoat, Kenneth C. Chambers, Jacqueline V. Keane, Andreea Petric, Larry Denneau, Eugene Magnier, Travis Berger, Mark E.

Huber, Heather Flewelling, Chris Waters, Eva Schunova-Lilly, and Serge Chastel. A brief visit from a red and extremely elongated interstellar asteroid. , 552(7685):378–381, December 2017.

[349] K.J. Meech, O.R. Hainaut, and B.G. Marsden. Comet nucleus size distributions from hst and keck telescopes. *Icarus*, 170(2):463–491, 2004.

[350] Bruce Mellado Garcia, Pasquale Musella, Massimiliano Grazzini, and Robert Harlander. CERN Report 4: Part I Standard Model Predictions. 2016. `https://twiki.cern.ch/twiki/bin/view/LHCPhysics/CERNYellowReportPageBR`.

[351] Núria Miret-Roig. The origin of free-floating planets. *Astrophysics and Space Science*, 368(3), mar 2023.

[352] M. Misiak, Abdur Rehman, and Matthias Steinhauser. Towards $\overline{B} \to X_s\gamma$ at the NNLO in QCD without interpolation in m_c. *JHEP*, 06:175, 2020.

[353] Mikolaj Misiak and Matthias Steinhauser. Weak radiative decays of the B meson and bounds on $M_{H^\pm}$ in the Two-Higgs-Doublet Model. *Eur. Phys. J. C*, 77(3):201, 2017.

[354] Léo Morel, Zhibin Yao, Pierre Cladé, and Saïda Guellati-Khélifa. Determination of the fine-structure constant with an accuracy of 81 parts per trillion. *Nature*, 588(7836):61–65, 2020.

[355] Amaya Moro-Martí n. Origin of 1i/'oumuamua. i. an ejected protoplanetary disk object? *The Astrophysical Journal*, 866(2):131, oct 2018.

[356] Amaya Moro-Martín, Edwin L. Turner, and Abraham Loeb. Will the Large Synoptic Survey Telescope Detect Extra-Solar Planetesimals Entering the Solar System? *The Astrophysical Journal*, 704(1):733–742, October 2009.

[357] Amaya Moro-Martín. Origin of 1i/'oumuamua. ii. an ejected exo-oort cloud object? *The Astronomical Journal*, 157(2):86, feb 2019.

[358] Takeo Moroi. The Muon anomalous magnetic dipole moment in the minimal supersymmetric standard model. *Phys. Rev.*, D53:6565–6575, 1996. [Erratum: Phys. Rev.D56,4424(1997)].

[359] P. Mroz, M. Ban, P. Marty, and R. Poleski. Free-floating or wide-orbit? keck adaptive-optics observations reveal no host stars near free-floating planet candidates, 2023.

[360] P. Mroz and R. Poleski. Exoplanet occurrence rates from microlensing surveys, 2023.

[361] Przemek Mró z, Radosław Poleski, Cheongho Han, Andrzej Udalski, Andrew Gould, Michał K. Szymański, Igor Soszyński, Paweł Pietrukowicz, Szymon Kozłowski, Jan Skowron, Krzysztof Ulaczyk, Mariusz Gromadzki, Krzysztof Rybicki, Patryk Iwanek, Marcin Wrona, Michael D. Albrow, Sun-Ju Chung, Kyu-Ha Hwang, Yoon-Hyun Ryu, Youn Kil Jung, In-Gu Shin, Yossi Shvartzvald, Jennifer C. Yee, Weicheng Zang, Sang-Mok Cha, Dong-Jin Kim, Hyoun-Woo Kim, Seung-Lee Kim, Chung-Uk Lee, Dong-Joo Lee, Yongseok Lee, Byeong-Gon Park,

Richard W. Pogge, and and. A free-floating or wide-orbit planet in the microlensing event OGLE-2019-BLG-0551. *The Astronomical Journal*, 159(6):262, may 2020.

[362] Przemek Mróz, Andrzej Udalski, David P. Bennett, Yoon-Hyun Ryu, Takahiro Sumi, Yossi Shvartzvald, Jan Skowron, Radosław Poleski, Paweł Pietrukowicz, Szymon Kozłowski, Michał K. Szymański, Łukasz Wyrzykowski, Igor Soszyński, Krzysztof Ulaczyk, Krzysztof Rybicki, Patryk Iwanek, Michael D. Albrow, Sun-Ju Chung, Andrew Gould, Cheongho Han, Kyu-Ha Hwang, Youn Kil Jung, In-Gu Shin, Jennifer C. Yee, Weicheng Zang, Sang-Mok Cha, Dong-Jin Kim, Hyoun-Woo Kim, Seung-Lee Kim, Chung-Uk Lee, Dong-Joo Lee, Yongseok Lee, Byeong-Gon Park, Richard W. Pogge, Fumio Abe, Richard Barry, Aparna Bhattacharya, Ian A. Bond, Martin Donachie, Akihiko Fukui, Yuki Hirao, Yoshitaka Itow, Kohei Kawasaki, Iona Kondo, Naoki Koshimoto, Man Cheung Alex Li, Yutaka Matsubara, Yasushi Muraki, Shota Miyazaki, Masayuki Nagakane, Clément Ranc, Nicholas J. Rattenbury, Haruno Suematsu, Denis J. Sullivan, Daisuke Suzuki, Paul J. Tristram, Atsunori Yonehara, Dan Maoz, Shai Kaspi, and Matan Friedmann. Two new free-floating or wide-orbit planets from microlensing. *A&A*, 622:A201, February 2019.

[363] Przemek Mróz, Andrzej Udalski, Jan Skowron, Radosław Poleski, Szymon Kozłowski, Michał K. Szymański, Igor Soszyński, Łukasz Wyrzykowski, Paweł Pietrukowicz, Krzysztof Ulaczyk, Dorota Skowron, and Michał Pawlak. No large

population of unbound or wide-orbit jupiter-mass planets. *Nature*, 548(7666):183–186, jul 2017.

[364] Przemek Mróz, Radosław Poleski, Andrew Gould, Andrzej Udalski, Takahiro Sumi, , , Michał K. Szymański, Igor Soszyński, Paweł Pietrukowicz, Szymon Kozłowski, Jan Skowron, Krzysztof Ulaczyk, (OGLE Collaboration), Michael D. Albrow, Sun-Ju Chung, Cheongho Han, Kyu-Ha Hwang, Youn Kil Jung, Hyoun-Woo Kim, Yoon-Hyun Ryu, In-Gu Shin, Yossi Shvartzvald, Jennifer C. Yee, Weicheng Zang, Sang-Mok Cha, Dong-Jin Kim, Seung-Lee Kim, Chung-Uk Lee, Dong-Joo Lee, Yongseok Lee, Byeong-Gon Park, Richard W. Pogge, and (KMT Collaboration). A terrestrial-mass rogue planet candidate detected in the shortest-timescale microlensing event. *The Astrophysical Journal Letters*, 903(1):L11, oct 2020.

[365] Przemek Mróz, Y.-H. Ryu, J. Skowron, A. Udalski, A. Gould, M. K. Szymański, I. Soszyński, R. Poleski, P. Pietrukowicz, S. Kozłowski, M. Pawlak, K. Ulaczyk, (The OGLE Collaboration), M. D. Albrow, S.-J. Chung, Y. K. Jung, C. Han, K.-H. Hwang, I.-G. Shin, J. C. Yee, W. Zhu, S.-M. Cha, D.-J. Kim, H.-W. Kim, S.-L. Kim, C.-U. Lee, D.-J. Lee, Y. Lee, B.-G. Park, R. W. Pogge, and (The KMT-Net Collaboration). A neptune-mass free-floating planet candidate discovered by microlensing surveys. *The Astronomical Journal*, 155(3):121, feb 2018.

[366] Margarete Mühlleitner, Marco O. P. Sampaio, Rui Santos, and Jonas Wittbrodt.

243

Phenomenological Comparison of Models with Extended Higgs Sectors. *JHEP*, 08:132, 2017.

[367] N. Hamer N. Blinov, S. Gori. Searching for muon-philic scalars at darkquest. 2024.

[368] Takahiro T. Nakamura and Shuji Deguchi. Wave Optics in Gravitational Lensing. *Progress of Theoretical Physics Supplement*, 133:137–153, January 1999.

[369] Hiroko Niikura et al. Microlensing constraints on primordial black holes with Subaru/HSC Andromeda observations. *Nature Astron.*, 3(6):524–534, 2019.

[370] Hiroko Niikura, Masahiro Takada, Naoki Yasuda, Robert H. Lupton, Takahiro Sumi, Surhud More, Toshiki Kurita, Sunao Sugiyama, Anupreeta More, Masamune Oguri, and Masashi Chiba. Microlensing constraints on primordial black holes with the Subaru/HSC Andromeda observation. *Nature Astronomy*, 3(6):524–534, June 2019. arXiv: 1701.02151.

[371] Hiroko Niikura, Masahiro Takada, Shuichiro Yokoyama, Takahiro Sumi, and Shogo Masaki. Constraints on earth-mass primordial black holes from OGLE 5-year microlensing events. *Physical Review D*, 99(8), apr 2019.

[372] Hiroko Niikura, Masahiro Takada, Shuichiro Yokoyama, Takahiro Sumi, and Shogo Masaki. Constraints on Earth-mass primordial black holes from OGLE 5-year microlensing events. *Phys. Rev. D*, 99(8):083503, 2019.

[373] S. Calchi Novati. Pixel lensing. *General Relativity and Gravitation*, 42(9):2101–2126, dec 2009.

[374] S. Calchi Novati, V. Bozza, F. De Paolis, M. Dominik, G. Ingrosso, Ph Jetzer, L. Mancini, A. Nucita, G. Scarpetta, M. Sereno, F. Strafella, and A. Gould. CANDIDATE MICROLENSING EVENTS FROM M31 OBSERVATIONS WITH THE LOIANO ESCOPE. *The Astrophysical Journal*, 695(1):442, March 2009. Publisher: The American Astronomical Society.

[375] Stephen Lars Olsen. The curious early history of ckm matrix – miracles happen!, 2024.

[376] B. Paczynski. Gravitational Microlensing at Large Optical Depth. *ApJ*, 301:503, February 1986.

[377] Giuliano Panico, Alex Pomarol, and Marc Riembau. EFT approach to the electron Electric Dipole Moment at the two-loop level. *JHEP*, 04:090, 2019.

[378] Joannis Papavassiliou. Gauge Invariant Proper Selfenergies and Vertices in Gauge Theories with Broken Symmetry. *Phys. Rev. D*, 41:3179, 1990.

[379] Joannis Papavassiliou. Gauge independent transverse and longitudinal self energies and vertices via the pinch technique. *Phys. Rev. D*, 50:5958–5970, 1994.

[380] Paride Paradisi. Higgs-mediated $\tau \to \mu$ and $\tau \to e$ transitions in II Higgs doublet model and supersymmetry. *JHEP*, 02:050, 2006.

[381] Richard H. Parker, Chenghui Yu, Weicheng Zhong, Brian Estey, and Holger Müller. Measurement of the fine-structure constant as a test of the Standard Model. *Science*, 360:191, 2018.

[382] Hiren H. Patel. Package-X: A Mathematica package for the analytic calculation of one-loop integrals. *Comput. Phys. Commun.*, 197:276–290, 2015.

[383] C. Patrignani et al. Review of Particle Physics. *Chin. Phys. C*, 40(10):100001, 2016.

[384] J. M. Pendlebury et al. Revised experimental upper limit on the electric dipole moment of the neutron. *Phys. Rev.*, D92(9):092003, 2015.

[385] M. T. Penny, E. Kerins, N. Rattenbury, J.-P. Beaulieu, A. C. Robin, S. Mao, V. Batista, S. Calchi Novati, A. Cassan, P. Fouqué, I. McDonald, J. B. Marquette, P. Tisserand, and M. R. Zapatero Osorio. ExELS: an exoplanet legacy science proposal for the ESA Euclid mission – I. Cold exoplanets. *Monthly Notices of the Royal Astronomical Society*, 434(1):2–22, 07 2013.

[386] Matthew T. Penny, B. Scott Gaudi, Eamonn Kerins, Nicholas J. Rattenbury, Shude Mao, Annie C. Robin, and Sebastiano Calchi Novati. Predictions of the WFIRST Microlensing Survey I: Bound Planet Detection Rates. *The Astrophysical Journal Supplement Series*, 241(1):3, February 2019. arXiv:1808.02490 [astro-ph].

[387] Damien M. Pierce, Jonathan A. Bagger, Konstantin T. Matchev, and Ren-jie

Zhang. Precision corrections in the minimal supersymmetric standard model. *Nucl. Phys.*, B491:3–67, 1997.

[388] Apostolos Pilaftsis. Generalized pinch technique and the background field method in general gauges. *Nucl. Phys. B*, 487:467–491, 1997.

[389] Maxim Pospelov. Best values for the cp-odd meson–nucleon couplings from supersymmetry. *Physics Letters B*, 530(1–4):123–128, March 2002.

[390] Maxim Pospelov and Adam Ritz. Electric dipole moments as probes of new physics. *Annals of Physics*, 318(1):119–169, July 2005.

[391] Maxim Pospelov and Adam Ritz. Electric dipole moments as probes of new physics. *Annals Phys.*, 318:119–169, 2005.

[392] Maxim Pospelov and Adam Ritz. CKM benchmarks for electron electric dipole moment experiments. *Phys. Rev. D*, 89(5):056006, 2014.

[393] K. Pruett, W. Dawson, M. S. Medford, C. Lam, J. R. Lu, N. Golovich, and G. Chapline. Primordial Black Hole Dark Matter Simulations Using PopSyCLE, November 2022. arXiv:2211.06771 [astro-ph].

[394] Lisa Randall, Marin Soljacic, and Alan H. Guth. Supernatural inflation: Inflation from supersymmetry with no (very) small parameters. *Nucl. Phys. B*, 472:377–408, 1996.

[395] Frederic A. Rasio and Eric B. Ford. Dynamical instabilities and the formation of extrasolar planetary systems. *Science*, 274(5289):954–956, 1996.

[396] Claudia Rella, Babette Döbrich, and Tien-Tien Yu. Searching for muonphilic dark sectors with proton beams. *Phys. Rev. D*, 106(3):035023, 2022.

[397] Tanya S. Roussy, Luke Caldwell, Trevor Wright, William B. Cairncross, Yuval Shagam, Kia Boon Ng, Noah Schlossberger, Sun Yool Park, Anzhou Wang, Jun Ye, and Eric A. Cornell. An improved bound on the electron's electric dipole moment. *Science*, 381(6653):46–50, July 2023.

[398] Tanya S. Roussy, Luke Caldwell, Trevor Wright, William B. Cairncross, Yuval Shagam, Kia Boon Ng, Noah Schlossberger, Sun Yool Park, Anzhou Wang, Jun Ye, and Eric A. Cornell. An improved bound on the electron's electric dipole moment. *Science*, 381(6653):46–50, July 2023.

[399] Sergei G. Rubin, Alexander S. Sakharov, and Maxim Yu. Khlopov. The Formation of primary galactic nuclei during phase transitions in the early universe. *J. Exp. Theor. Phys.*, 91:921–929, 2001.

[400] Yoon-Hyun Ryu, Przemek Mróz, Andrew Gould, Kyu-Ha Hwang, Hyoun-Woo Kim, Jennifer C. Yee, Michael D. Albrow, Sun-Ju Chung, Youn Kil Jung, In-Gu Shin, Yossi Shvartzvald, Weicheng Zang, Sang-Mok Cha, Dong-Jin Kim, Seung-Lee Kim, Chung-Uk Lee, Dong-Joo Lee, Yongseok Lee, Byeong-Gon Park, Cheongho Han, Richard W. Pogge, KMTNet Collaboration, Andrzej Udalski, Radek Poleski, Jan Skowron, Michał K. Szymański, Igor Soszyński, Paweł Pietrukowicz, Szymon Kozłowski, Krzysztof Ulaczyk, Krzysztof A. Rybicki, Pa-

tryk Iwanek, and OGLE Collaboration. KMT-2017-BLG-2820 and the Nature of the Free-floating Planet Population. , 161(3):126, March 2021.

[401] N. Hamer S. Gori. Direct and indirect tests of higgs cp violation. 2024.

[402] F. W. Scholz and M. A. Stephens. K-sample anderson-darling tests. *Journal of the American Statistical Association*, 82(399):918–924, 1987.

[403] Darryl Seligman and Gregory Laughlin. Evidence that 1i/2017 u1 ('oumuamua) was composed of molecular hydrogen ice. *The Astrophysical Journal Letters*, 896(1):L8, jun 2020.

[404] A. K. Sen and N. C. Rana. On the missing interstellar comets. *A&A*, 275:298, August 1993.

[405] Amir Siraj and Abraham Loeb. Probing Extrasolar Planetary Systems with Interstellar Meteors. *arXiv e-prints*, page arXiv:1906.03270, June 2019.

[406] Amir Siraj and Abraham Loeb. The 2019 discovery of a meteor of interstellar origin, 2022.

[407] A. M. Sirunyan et al. Search for physics beyond the standard model in high-mass diphoton events from proton-proton collisions at $\sqrt{s} = 13$ TeV. *Phys. Rev. D*, 98(9):092001, 2018.

[408] Albert M Sirunyan et al. Search for a new scalar resonance decaying to a pair of Z bosons in proton-proton collisions at $\sqrt{s} = 13$ TeV. *JHEP*, 06:127, 2018. [Erratum: JHEP 03, 128 (2019)].

[409] Albert M Sirunyan et al. Search for additional neutral MSSM Higgs bosons in the $\tau\tau$ final state in proton-proton collisions at $\sqrt{s} = 13$ TeV. *JHEP*, 09:007, 2018.

[410] Albert M Sirunyan et al. Search for additional neutral MSSM Higgs bosons in the $\tau\tau$ final state in proton-proton collisions at $\sqrt{s} = 13$ TeV. *JHEP*, 09:007, 2018.

[411] Albert M Sirunyan et al. Search for beyond the standard model Higgs bosons decaying into a $b\overline{b}$ pair in pp collisions at $\sqrt{s} = 13$ TeV. *JHEP*, 08:113, 2018.

[412] Albert M Sirunyan et al. Combined measurements of Higgs boson couplings in proton-proton collisions at $\sqrt{s} = 13$ TeV. *Eur. Phys. J.*, C79(5):421, 2019.

[413] Albert M Sirunyan et al. Measurements of the Higgs boson width and anomalous HVV couplings from on-shell and off-shell production in the four-lepton final state. *Phys. Rev.*, D99(11):112003, 2019.

[414] Albert M Sirunyan et al. Search for a heavy pseudoscalar boson decaying to a Z and a Higgs boson at $\sqrt{s} = 13$ TeV. *Eur. Phys. J. C*, 79(7):564, 2019.

[415] Albert M Sirunyan et al. Search for vector-like leptons in multilepton final states in proton-proton collisions at $\sqrt{s} = 13$ TeV. *Phys. Rev. D*, 100(5):052003, 2019.

[416] Albert M Sirunyan et al. Search for a charged Higgs boson decaying into top and bottom quarks in events with electrons or muons in proton-proton collisions at $\sqrt{s} = 13$ TeV. *JHEP*, 01:096, 2020.

[417] Albert M Sirunyan et al. Search for a heavy Higgs boson decaying to a pair of W bosons in proton-proton collisions at $\sqrt{s} = 13$ TeV. *JHEP*, 03:034, 2020.

[418] Albert M Sirunyan et al. Search for a heavy pseudoscalar Higgs boson decaying into a 125 GeV Higgs boson and a Z boson in final states with two tau and two light leptons at $\sqrt{s} = 13$ TeV. *JHEP*, 03:065, 2020.

[419] Albert M Sirunyan et al. Search for heavy Higgs bosons decaying to a top quark pair in proton-proton collisions at $\sqrt{s} = 13$ TeV. *JHEP*, 04:171, 2020.

[420] Albert M Sirunyan et al. Search for production of four top quarks in final states with same-sign or multiple leptons in proton-proton collisions at $\sqrt{s} = 13$ TeV. *Eur. Phys. J. C*, 80(2):75, 2020.

[421] Albert M Sirunyan et al. Search for supersymmetry in final states with two oppositely charged same-flavor leptons and missing transverse momentum in proton-proton collisions at $\sqrt{s} = 13$ TeV. 2020.

[422] Albert M Sirunyan et al. Evidence for Higgs boson decay to a pair of muons. *JHEP*, 01:148, 2021.

[423] Vladimir A. Smirnov. Problems of the strategy of regions. *Phys. Lett. B*, 465:226–234, 1999.

[424] Nolan Smyth, Stefano Profumo, Samuel English, Tesla Jeltema, Kevin McKinnon, and Puragra Guhathakurta. Updated Constraints on Asteroid-Mass Primordial Black Holes as Dark Matter. *Phys. Rev. D*, 101(6):063005, 2020.

[425] Nolan Smyth, Stefano Profumo, Samuel English, Tesla Jeltema, Kevin McKinnon, and Puragra Guhathakurta. Updated Constraints on Asteroid-Mass Primordial

Black Holes as Dark Matter. *Physical Review D*, 101(6):063005, March 2020. arXiv:1910.01285 [astro-ph, physics:hep-th].

[426] C. Snodgrass, A. Fitzsimmons, S. C. Lowry, and P. Weissman. The size distribution of Jupiter Family comet nuclei. *Monthly Notices of the Royal Astronomical Society*, 414(1):458–469, 06 2011.

[427] Veerle J. Sterken, Andrew J. Westphal, Nicolas Altobelli, David Malaspina, and Frank Postberg. Interstellar Dust in the Solar System. , 215(7):43, October 2019.

[428] Louis E. Strigari, Matteo Barnabè , Philip J. Marshall, and Roger D. Blandford. Nomads of the galaxy. *Monthly Notices of the Royal Astronomical Society*, 423(2):1856–1865, may 2012.

[429] Sunao Sugiyama, Toshiki Kurita, and Masahiro Takada. Revisiting the wave optics effect on primordial black hole constraints from optical microlensing search. *arXiv:1905.06066 [astro-ph]*, May 2019. arXiv: 1905.06066.

[430] Takahiro Sumi, Naoki koshimoto, David P. Bennett, Nicholas J. Rattenbury, Fumio Abe, Richard Barry, Aparna Bhattacharya, Ian A. Bond, Hirosane Fujii, Akihiko Fukui, Ryusei Hamada, Yuki Hirao, Stela Ishitani Silva, Yoshitaka Itow, Rintaro Kirikawa, Iona Kondo, Yutaka Matsubara, Shota Miyazaki, Yasushi Muraki, Greg Olmschenk, Clement Ranc, Yuki Satoh, Daisuke Suzuki, Mio Tomoyoshi, Paul . J. Tristram, Aikaterini Vandorou, Hibiki Yama, and Kansuke Yamashita.

Free-floating planet mass function from moa-ii 9-year survey towards the galactic bulge, 2023.

[431] Richard Talman. On the Statistics of Particle Identification Using Ionization. *Nucl. Instrum. Meth.*, 159:189, 1979.

[432] A. Tamm, E. Tempel, P. Tenjes, O. Tihhonova, and T. Tuvikene. Stellar mass map and dark matter distribution in M 31. *Astronomy & Astrophysics*, 546:A4, October 2012.

[433] Mark Thomson. *Modern particle physics.* Cambridge University Press, New York, 2013.

[434] David E. Trilling, Tyler Robinson, Alissa Roegge, Colin Orion Chandler, Nathan Smith, Mark Loeffler, Chad Trujillo, Samuel Navarro-Meza, and Lori M. Glaspie. Implications for planetary system formation from interstellar object 1i/2017 u1 ('oumuamua). *The Astrophysical Journal*, 850(2):L38, nov 2017.

[435] Yu-Dai Tsai, Patrick deNiverville, and Ming Xiong Liu. Dark Photon and Muon $g-2$ Inspired Inelastic Dark Matter Models at the High-Energy Intensity Frontier. *Phys. Rev. Lett.*, 126(18):181801, 2021.

[436] Yung-Su Tsai. AXION BREMSSTRAHLUNG BY AN ELECTRON BEAM. *Phys. Rev. D*, 34:1326, 1986.

[437] Yung-Su Tsai. PRODUCTION OF NEUTRAL BOSONS BY AN ELECTRON BEAM. *Phys. Rev. D*, 40:760, 1989.

[438] Armen Tumasyan et al. Analysis of the CP structure of the Yukawa coupling between the Higgs boson and τ leptons in proton-proton collisions at $\sqrt{s} = 13$ TeV. 10 2021.

[439] Armen Tumasyan et al. Inclusive nonresonant multilepton probes of new phenomena at $\sqrt{s}$=13 TeV. *Phys. Rev. D*, 105(11):112007, 2022.

[440] A. Udalski, M. K. Szymański, and G. Szymański. Ogle-iv: Fourth phase of the optical gravitational lensing experiment, 2015.

[441] Melissa Van Beekveld, Wim Beenakker, Marrit Schutten, and Jeremy De Wit. Dark matter, fine-tuning and $(g-2)_\mu$ in the pMSSM. 4 2021.

[442] J. Vaubaillon. Hyperbolic meteors: is CNEOS 2014-01-08 interstellar? *WGN, Journal of the International Meteor Organization*, 50(5):140–143, October 2022.

[443] Graziano Venanzoni. New results from the muon g-2 experiment, 2023.

[444] A. C. Vutha, M. Horbatsch, and E. A. Hessels. Orientation-dependent hyperfine structure of polar molecules in a rare-gas matrix: A scheme for measuring the electron electric dipole moment. *Phys. Rev.*, A98(3):032513, 2018.

[445] Fei Wang, Lei Wu, Yang Xiao, Jin Min Yang, and Yang Zhang. GUT-scale constrained SUSY in light of E989 muon g-2 measurement. 4 2021.

[446] Harrison Winch, Jack Setford, Jo Bovy, and David Curtin. Using LSST Microlensing to Constrain Dark Compact Objects in Spherical and Disk Configurations. *The Astrophysical Journal*, 933(2):177, July 2022.

254

[447] Hans J. Witt and Shude Mao. Can lensed stars be regarded as pointlike for microlensing by MACHOs? *The Astrophysical Journal*, 430:505–510, August 1994.

[448] R. L. Workman et al. Review of Particle Physics. *PTEP*, 2022:083C01, 2022.

[449] R. L. Workman and Others. Review of Particle Physics. *PTEP*, 2022:083C01, 2022.

[450] L. Wyrzykowski et al. The OGLE View of Microlensing towards the Magellanic Clouds. III. Ruling out sub-solar MACHOs with the OGLE-III LMC data. *Mon. Not. Roy. Astron. Soc.*, 413:493, 2011.

[451] L. Wyrzykowski et al. The OGLE View of Microlensing towards the Magellanic Clouds. IV. OGLE-III SMC Data and Final Conclusions on MACHOs. *Mon. Not. Roy. Astron. Soc.*, 416:2949, 2011.

[452] Yasuhiro Yamaguchi and Nodoka Yamanaka. Large electric dipole moment of charged leptons in the standard model. 3 2020.

[453] Yasuhiro Yamaguchi and Nodoka Yamanaka. Quark level and hadronic contributions to the electric dipole moment of charged leptons in the standard model. 5 2020.

[454] Wen Yin. Muon $g - 2$ Anomaly in Anomaly Mediation. 4 2021.

[455] Jun'ichi Yokoyama. Chaotic new inflation and formation of primordial black holes. *Phys. Rev. D*, 58:083510, 1998.

[456] P. A. Zyla et al. Review of Particle Physics. *PTEP*, 2020(8):083C01, 2020.

Part VI

Appendices

A Appendix: Parameters of the Higgs Potential

In this appendix, we collect useful equations on the 2HDM scalar potential [184]. First, the conditions of minimization of the potential in (3.1)

$$
\begin{aligned}
m_{11}^2 &= \operatorname{Re}(m_{12}^2\, e^{i\zeta})\frac{v_2}{v_1} - \frac{1}{2}\left[\lambda_1 v_1^2 + \lambda_{345}\, v_2^2\right], \\
m_{22}^2 &= \operatorname{Re}(m_{12}^2\, e^{i\zeta})\frac{v_1}{v_2} - \frac{1}{2}\left[\lambda_2 v_2^2 + \lambda_{345}\, v_1^2\right], \\
&\operatorname{Im}(m_{12}^2 e^{i\zeta}) = \frac{v_1 v_2}{2}\operatorname{Im}(\lambda_5 e^{2i\zeta}),
\end{aligned}
\tag{.18}
$$

can be used to determine v_1, v_2 and ζ, where $\lambda_{345} = \lambda_3 + \lambda_4 + \operatorname{Re}(\lambda_5 e^{2i\zeta})$. Utilizing these minimization conditions, we note that the C2HDM Higgs potential is fully determined by 9 independent free parameters, for example by the set

$$\tan\beta, \operatorname{Re}(m_{12}^2), \lambda_1, \lambda_2, \lambda_3, \lambda_4, \operatorname{Re}(\lambda_5), \operatorname{Im}(\lambda_5), v(=246\ \text{GeV}).$$

The Higgs potential can also be expressed in the Higgs basis defined in (3.4). The corresponding mass terms and quartic interactions are linearly related to the λ_i, m_{ij}^2:

$$
\begin{aligned}
Y_1 &= m_{11}^2 c_\beta^2 + m_{22}^2 s_\beta^2 - \operatorname{Re}(m_{12}^2 e^{i\zeta}) s_{2\beta} \\
Y_2 &= m_{11}^2 s_\beta^2 + m_{22}^2 c_\beta^2 + \operatorname{Re}(m_{12}^2 e^{i\zeta}) s_{2\beta} \\
Y_3 e^{i\zeta} &= \tfrac{1}{2}(m_{11}^2 - m_{22}^2) s_{2\beta} + \operatorname{Re}(m_{12}^2 e^{i\zeta}) c_{2\beta} \\
&\qquad\qquad + i\operatorname{Im}(m_{12}^2 e^{i\zeta})
\end{aligned}
\tag{.19}
$$

$$Z_1 = \lambda_1 c_\beta^4 + \lambda_2 s_\beta^4 + \tfrac{1}{2}\lambda_{345} s_{2\beta}^2$$

$$Z_2 = \lambda_1 s_\beta^4 + \lambda_2 c_\beta^4 + \tfrac{1}{2}\lambda_{345} s_{2\beta}^2$$

$$Z_3 = \tfrac{1}{4} s_{2\beta}^2 \left(\lambda_1 + \lambda_2 - 2\lambda_{345}\right) + \lambda_3$$

$$Z_4 = \tfrac{1}{4} s_{2\beta}^2 \left(\lambda_1 + \lambda_2 - 2\lambda_{345}\right) + \lambda_4 \qquad (.20)$$

$$Z_5 e^{2i\zeta} = \tfrac{1}{4} s_{2\beta}^2 \left(\lambda_1 + \lambda_2 - 2\lambda_{345}\right)$$

$$+ \mathrm{Re}(\lambda_5 e^{2i\zeta}) + i c_{2\beta}\mathrm{Im}(\lambda_5 e^{2i\zeta})$$

$$Z_6 e^{i\zeta} = -\tfrac{1}{2} s_{2\beta}\left(\lambda_1 c_\beta^2 - \lambda_2 s_\beta^2 - \lambda_{345} c_{2\beta} - i\mathrm{Im}(\lambda_5 e^{2i\zeta})\right)$$

$$Z_7 e^{i\zeta} = -\tfrac{1}{2} s_{2\beta}\left(\lambda_1 s_\beta^2 - \lambda_2 c_\beta^2 + \lambda_{345} c_{2\beta} + i\mathrm{Im}(\lambda_5 e^{2i\zeta})\right).$$

The set of 9 independent parameters that we choose for our numerics that determine the Higgs potential is given by: $\tan\beta$, m_{H^+}, $\mathrm{Im}(\lambda_5 e^{2i\zeta})$, Z_3, Z_4, $\mathrm{Re}(Z_5 e^{2i\zeta})$, $\mathrm{Re}(Z_6 e^{i\zeta})$, with $\zeta = 0$, after fixing m_1 and v. For completeness, we provide the remainder of the Z_i in terms of our chosen set, having set $\zeta = 0$. From the last three equations of (.20), $\mathrm{Im}(Z_{5,6,7})$ are determined. Utilizing results in [133], with a deriviation given in the supplementary *Mathematica* notebook, the remaining quartic couplings are given by

$$\mathrm{Re}(Z_7) = \mathrm{Re}(Z_6) + \frac{\mathrm{Im}(Z_5)\mathrm{Im}[Z_6^*(Z_1 - Z_3 - Z_4 - Z_5)]}{2\,\mathrm{Im}(Z_6)^2},$$

$$Z_2 = Z_1 + (2/t_{2\beta})(Z_6 + Z_7), \qquad (.21)$$

where Z_1 is determined diagonalizing the mass matrix in (3.5) and imposing $m_h = 125$ GeV.

B   The global minimum condition

In this Appendix we discuss the details of the method we use to derive the necessary and sufficient condition for the EW minimum to be the global minimum. We follow the method proposed in [289, 290] for the case of a CP conserving scalar potential.

We introduce a covariant 4-vector, r_μ ($\mu = 0, \cdots, 3$), function of the two Higgs doublets Φ_1 and Φ_2:

$$
\begin{aligned}
r_0 &= \Phi_1^\dagger \Phi_1 + \Phi_2^\dagger \Phi_2, \\
r_1 &= -(\Phi_1^\dagger \Phi_2 + \Phi_2^\dagger \Phi_1) = -2\mathrm{Re}(\Phi_1^\dagger \Phi_2), \\
r_2 &= i(\Phi_1^\dagger \Phi_2 - \Phi_2^\dagger \Phi_1) = -2\mathrm{Im}(\Phi_1^\dagger \Phi_2), \\
r_3 &= -(\Phi_1^\dagger \Phi_1 - \Phi_2^\dagger \Phi_2),
\end{aligned}
\tag{.22}
$$

with the corresponding contravariant vector given by $r^\mu = (r_0, -r_i)$. These vectors have the useful property

$$
r^\mu r_\mu = (r_0)^2 - (r_i)^2 = 4(\Phi_1^\dagger \Phi_1)(\Phi_2^\dagger \Phi_2) - 4(|\Phi_1^\dagger \Phi_2|)^2 \geq 0
\tag{.23}
$$

and $r^\mu r_\mu = 0$ for a minimum that does not break the electric charge. As shown in [94, 222], neutral minima and charge breaking minima do not coexist. For this reason, the conditions we derive in the following for neutral minima imply the absence of charge breaking minima.

Using this vector, the potential in Eq. (4.1) can be written in the more compact form

$$
V = -M_\mu r^\mu + \frac{1}{2}\Lambda_{\mu\nu} r^\mu r^\nu,
\tag{.24}
$$

where the 4-vector M_μ and the tensor $\Lambda_{\mu\nu}$ are defined as

$$M_\mu = \frac{1}{2}\left(-m_{11}^2 - m_{22}^2,\ \mathrm{Re}(m_{12}^2),\ -\mathrm{Im}(m_{12}^2),\ -m_{11}^2 + m_{22}^2\right), \tag{.25}$$

$$\Lambda_{\mu\nu} = \frac{1}{2}\begin{pmatrix} \frac{1}{2}(\lambda_1 + \lambda_2 + 2\lambda_3) & 0 & 0 & \frac{1}{2}(\lambda_1 - \lambda_2) \\ 0 & \lambda_4 + \mathrm{Re}\,\lambda_5 & -\mathrm{Im}\,\lambda_5 & 0 \\ 0 & -\mathrm{Im}\,\lambda_5 & \lambda_4 - \mathrm{Re}\,\lambda_5 & 0 \\ \frac{1}{2}(\lambda_1 - \lambda_2) & 0 & 0 & \frac{1}{2}(\lambda_1 + \lambda_2 - 2\lambda_3) \end{pmatrix}. \tag{.26}$$

In the following, we will identify the neutral minima of this potential. Since r_μ is a null vector ($r^\mu r_\mu = 0$), the most general minimization condition reads

$$\Lambda_{\mu\nu}r^\nu - M_\mu = \zeta r_\mu, \tag{.27}$$

with ζ an arbitrary constant of proportionality.

To find all minima of our potential, it is convenient to go to a basis in which the tensor Λ is diagonal. Conditions will be expressed in terms of the eigenvalues Λ_σ given by,

$$\Lambda^{\mu\nu}\xi_\nu^{(\sigma)} = \Lambda_\sigma g^{\mu\nu}\xi_\nu^{(\sigma)} \qquad \text{(no sum over } \sigma\text{)} \tag{.28}$$

$$\hat{\Lambda}_{\mu\nu} \equiv (O^T)_{\mu\rho}\Lambda^{\rho\sigma}O_{\sigma\nu} = \mathrm{diag}(\Lambda_0, -\Lambda_1, -\Lambda_2, -\Lambda_3), \tag{.29}$$

and Λ_0 is identified with the timelike eigenvector, the Λ_i being spacelike. In this new basis, the condition of positivity of the scalar potential can be written in a straightforward way [289]:

$$\Lambda_0 > 0,\ \Lambda_0 > \Lambda_1, \Lambda_2, \Lambda_3. \tag{.30}$$

261

Then the condition (.27) becomes:

$$(\Lambda_0 - \zeta)\hat{r}_0 = \hat{M}_0, \ (\Lambda_i - \zeta)\hat{r}_i = \hat{M}_i \ (\text{for } i = 1, 2, 3) \,, \tag{.31}$$

where $\hat{M}_{0,i}$ and $\hat{r}_{0,i}$ are the mass terms and fields in the new basis. Solving these conditions, we can find all of the neutral extrema of the theory. By plugging the extrema back into the potential and comparing their vacuum energy, one can find that the necessary and sufficient condition for the electroweak minimum to be the global minimum is (for a more detailed discussion see [92]):

$$\hat{M}_0 > 0, \quad \hat{r}_i \hat{M}_i < 0 \ (\text{for } i = 1, 2, 3). \tag{.32}$$

In the rest of this Appendix, we will discuss how to read these conditions in terms of the parameters of the Higgs potential of our complex 2HDM. The matrix $\Lambda_{\mu\nu}$ is block diagonal (see (.26)), so we can diagonalize the off diagonal components Λ_{03} and Λ_{12} separately.

To get rid of a non-zero Λ_{03} term, let us define $k \equiv \sqrt[4]{\lambda_1/\lambda_2}$, and rescale the doublets

$$\Phi_1 \to k^{-\frac{1}{2}}\Phi_1, \quad \Phi_2 \to k^{\frac{1}{2}}\Phi_2. \tag{.33}$$

This rescaling can be done only on condition that $\lambda_1/\lambda_2 > 0$. This transformation does not affect the other quartic interactions, beyond the λ_1 and λ_2 terms. To get rid of a non-zero Λ_{12}, let us rotate the doublet Φ_2 with a phase, θ_λ:

$$\Phi_1 \to \Phi_1, \quad \Phi_2 \to e^{-i\theta_\lambda/2}\Phi_2, \quad \theta_\lambda = \arg(\lambda_5) \,. \tag{.34}$$

Again it is straightforward to verify that all the other quartic terms, beyond the λ_5 term, remain unchanged.

With the two transformations above, the potential in eq.(4.1) becomes

$$V(\Phi_1, \Phi_2) = k^{-1}m_{11}^2\Phi_1^\dagger\Phi_1 + k\,m_{22}^2\Phi_2^\dagger\Phi_2 - \frac{1}{2}\left(m_{12}^2 e^{-i\frac{\theta_\lambda}{2}}\Phi_1^\dagger\Phi_2 + \text{h.c.}\right)$$
$$+\frac{1}{2}\sqrt{\lambda_1\lambda_2}\left((\Phi_1^\dagger\Phi_1)^2 + (\Phi_2^\dagger\Phi_2)^2\right) + \lambda_3(\Phi_1^\dagger\Phi_1)(\Phi_2^\dagger\Phi_2) \qquad (.35)$$
$$+\lambda_4(\Phi_1^\dagger\Phi_2)(\Phi_2^\dagger\Phi_1) + \frac{1}{2}|\lambda_5|\left((\Phi_1^\dagger\Phi_2)^2 + \text{h.c.}\right).$$

This potential can be expressed in the form (.24), with a diagonal $\Lambda_{\mu\nu}$ given by

$$\Lambda_0 = \frac{1}{2}(\sqrt{\lambda_1\lambda_2}+\lambda_3),\ \Lambda_1 = -\frac{1}{2}(\lambda_4+|\lambda_5|),\ \Lambda_2 = -\frac{1}{2}(\lambda_4-|\lambda_5|),\ \Lambda_3 = -\frac{1}{2}(\sqrt{\lambda_1\lambda_2}-\lambda_3),$$

$$(.36)$$

and mass terms given by

$$\hat{M}_0 = -\frac{1}{2}(k^{-1}m_{11}^2 + k\,m_{22}^2),\ \hat{M}_1 = \frac{1}{2}\left[\text{Re}(m_{12}^2)\cos(\theta_\lambda/2) + \text{Im}(m_{12}^2)\sin(\theta_\lambda/2)\right],$$
$$\hat{M}_2 = -\frac{1}{2}\left[\text{Im}(m_{12}^2)\cos(\theta_\lambda/2) - \text{Re}(m_{12}^2)\sin(\theta_\lambda/2)\right],\ \hat{M}_3 = \frac{1}{2}(k\,m_{22}^2 - k^{-1}m_{11}^2).\ (.37)$$

Inserting the diagonal quartic couplings (.36) in the conditions for the positivity of the potential (.30), we find the well known conditions reported in eq. (4.14), namely

$$\lambda_1 > 0,\ \lambda_2 > 0,\ \lambda_3 + \min(0, \lambda_4 - |\lambda_5|) > -\sqrt{\lambda_1\lambda_2}. \qquad (.38)$$

If we now focus on the electroweak minimum $\langle\Phi_1\rangle = v\cos\beta/\sqrt{2}$,

263

$\langle \Phi_2 \rangle = v \sin \beta e^{i\theta_v}/\sqrt{2}$, the components of $\hat{r}_\mu$ vector are

$$
\begin{aligned}
\hat{r}_0 &= \frac{v^2}{2}(k \cos^2 \beta + k^{-1} \sin^2 \beta), \\
\hat{r}_1 &= -v^2 \sin \beta \cos \beta \cos \left(\theta_v + \frac{\theta_\lambda}{2} \right), \\
\hat{r}_2 &= -v^2 \sin \beta \cos \beta \sin \left(\theta_v + \frac{\theta_\lambda}{2} \right), \\
\hat{r}_3 &= \frac{v^2}{2}(k^{-1} \sin^2 \beta - k \cos^2 \beta).
\end{aligned}
\tag{.39}
$$

The conditions $\hat{r}_i \hat{M}_i < 0$ give:

$$
\begin{aligned}
\cos \left(\theta_\lambda/2 + \theta_v \right) \mathrm{Re}[m_{12}^2 e^{-i\theta_\lambda/2}] &> 0, \\
\sin \left(\theta_\lambda/2 + \theta_v \right) \mathrm{Im}[m_{12}^2 e^{-i\theta_\lambda/2}] &< 0, \\
(m_{11}^2 - k^2 m_{22}^2)(\tan \beta - k) &> 0.
\end{aligned}
\tag{.40}
$$

We note that for a CP conserving 2HDM, only the first and the third conditions need to be satisfied and they can be expressed by the known equation [92]

$$
D = m_{12}^2 (m_{11}^2 - k^2 m_{22}^2)(\tan \beta - k) > 0.
\tag{.41}
$$

The expressions in (.40) are totally general and keep into account that m_{12}^2, λ_5, as well as the Higgs VEV can be complex. However, the corresponding three phases are not independent. We can express the conditions above

(1) in terms of basis invariant quantities [289];

(2) in the basis adopted in this chapter, i.e. the basis in which the VEV phase is equal to zero.

(1) Basis invariant formulation:

The relative phases $\delta_1 = \arg[m_{12}^2(\lambda_5^*)^{1/2}]$ and $\delta_2 = \arg[v_1^* v_2 \, (m_{12}^2)^* \lambda_5]$ are invariant under rephasing of the Higgs doublets. We can express the first two conditions in (.40) in terms of these two phases:

$$\cos(\delta_1 + \delta_2) \cos(\delta_1) \;\; > \;\; 0,$$
$$\sin(\delta_1 + \delta_2) \sin(\delta_1) \;\; < \;\; 0 \,. \qquad (.42)$$

(2) Basis adopted in this chapter:

Throughout the chapter, we use the convention $\delta_1 = \arg[m_{12}^2] - \theta_\lambda/2$ and $\delta_2 = -\arg[m_{12}^2] + \theta_\lambda$. In this basis, the vacuum stability conditions read

$$\cos\frac{\theta_\lambda}{2} \cos\left(\arg[m_{12}^2] - \frac{\theta_\lambda}{2}\right) > 0,$$
$$\sin\frac{\theta_\lambda}{2} \sin\left(\arg[m_{12}^2] - \frac{\theta_\lambda}{2}\right) < 0, \qquad (.43)$$
$$(m_{11}^2 - k^2 m_{22}^2)(\tan\beta - k) > 0.$$

If we use the minimization conditions in (4.4) and the definition of ν in (4.7), the first two conditions in (.43) become

$$\frac{2v_1 v_2}{|m_{12}^2|}\left[|\lambda_5|\sin^2\left(\frac{\theta_\lambda}{2}\right) + \nu\right]\cos^2\frac{\theta_\lambda}{2} > 0, \quad \frac{2v_1 v_2}{|m_{12}^2|}\left[\frac{1}{2}(\mathrm{Re}\lambda_5 + |\lambda_5|) - \nu\right]\sin^2\frac{\theta_\lambda}{2} < 0.$$
$$(.44)$$

Note that in the CP conserving limit these two conditions lead to the trivial condition $\nu > 0$ or, equivalently, $m_{12}^2 > 0$.

C Lagrangian parameters

The quartic couplings of the Higgs potential in (4.1) can be expressed in terms of the more physical parameters in (4.18):

$$
\begin{aligned}
\lambda_1 &= \frac{m_{h_1}^2 \sin^2\alpha \cos^2\alpha_2 + m_{h_2}^2 \mathcal{R}_{21}^2 + m_{h_3}^2 \mathcal{R}_{31}^2}{v^2 \cos\beta^2} - \nu \tan^2\beta \ , \\
\lambda_2 &= \frac{m_{h_1}^2 \cos^2\alpha \cos^2\alpha_2 + m_{h_2}^2 \mathcal{R}_{22}^2 + m_{h_3}^2 \mathcal{R}_{32}^2}{v^2 \sin\beta^2} - \nu \cot^2\beta \ , \\
\mathrm{Re}\lambda_5 &= \nu - \frac{m_{h_1}^2 \sin^2\alpha_2 + \cos^2\alpha_2(m_{h_2}^2 \sin^2\alpha_3 + m_{h_3}^2 \cos^2\alpha_3)}{v^2} \ , \\
\lambda_4 &= 2\nu - \mathrm{Re}\lambda_5 - \frac{2m_{H^+}^2}{v^2} \ , \\
\lambda_3 &= \nu - \frac{m_{h_1}^2 \sin\alpha \cos\alpha \cos^2\alpha_2 - m_{h_2}^2 \mathcal{R}_{21}\mathcal{R}_{22} - m_{h_3}^2 \mathcal{R}_{31}\mathcal{R}_{32}}{v^2 \sin\beta \cos\beta} - \lambda_4 - \mathrm{Re}\lambda_5 \ , \\
\mathrm{Im}\lambda_5 &= \frac{2\cos\alpha_2 \left[(m_{h_2}^2 - m_{h_3}^2)\cos\alpha \sin\alpha_3 \cos\alpha_3 + (m_{h_1}^2 - m_{h_2}^2 \sin^2\alpha_3 - m_{h_3}^2 \cos^2\alpha_3)\sin\alpha \sin\alpha_2\right]}{v^2 \sin\beta} \ ,
\end{aligned}
\tag{.45}
$$

where $\mathcal{R}$ is the rotation matrix defined in (4.10).

D Supplementary details on the fit to Higgs data

The shapes of the regions in Fig. 4.1 come from the complicated fit of the large number of channels. The Type-I model systematically favors negative x values, with the top-left plot being the most pronounced. Setting $\tan\beta = 1$, each channel's best fit point in (x, α_2) was separately computed. Shown in Fig. .11, are the experimental results as a fraction of the SM rates with their experimental uncertainties as error bars. The color of each bar corresponds to the individual best-fit value of x for each channel. There are some channels that clearly favor negative x, such as ATLAS VBF $H \to \gamma\gamma$, and ATLAS ttH+tH $H \to bb$. There are some that favor small positive x, but fewer, and to a lesser magnitude than the negative x channels. The plots give an illustration

266

of the slight overall preference for negative x, though the intricacies of the fit to all

channels are not captured.
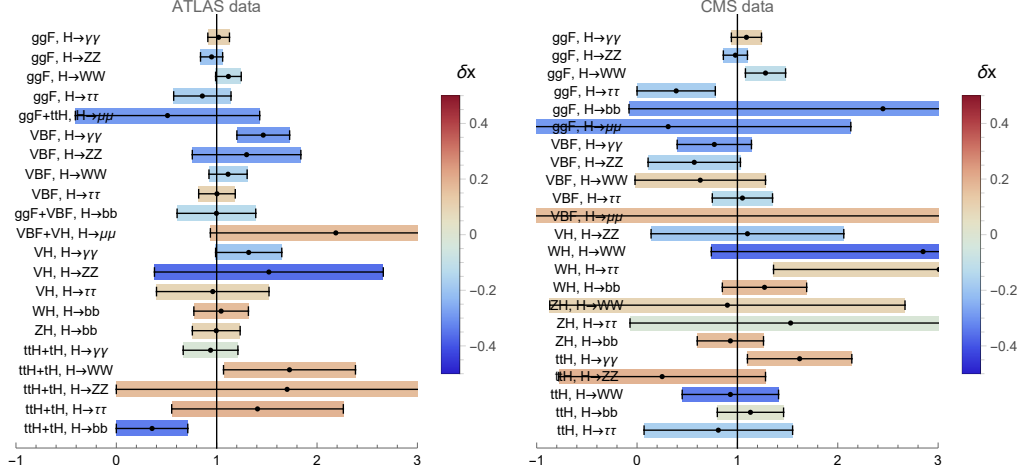
Figure .11: Observed data [1, 2] as a fraction of SM rates for the Higgs fit. Color

indicates the x value of the best fit point if only fitting to each channel individually

(with $\tan\beta = 1$), in the Type I model. Noting the presence of some deep blue channels

and the lack of deep red channels is an illustration of the slight negative-x preference

for the Type I fit in Fig. 4.1.

E Comparison of Estimated Yields

In this Appendix, we compare the fiducial FFP yield calculated in our anal-

ysis to that of [298]. The authors of [298] calculate their expected FFP yield for the

Roman GBTDS using the code *Gravitational microlensing Using Large Lensed Sources*

(GULLS) [386]. GULLS draws explicit sources and lenses from a Bescançon galactic

model (version 1106 [224]) and simulates individual microlensing events by generating

realistic photometry using synthetic images. This approach is significantly different from the semi-analytic approach we employ in the chapter. `LensCalcPy`, the code used to compute our FFP yields, is designed to provide simple estimates of lensing event rates, not to model individual events or generate associated photometry. However, its speed and flexibility makes it well-suited to population-level studies with large numbers of events.

While our approach and that of [298] differ significantly in implementation, we find that they produce very similar ultimate FFP yields. In order to see this, we compare to Table 2 of [298], where the authors have displayed their fiducial FFP yield for a log-uniform mass distribution ($\frac{dN}{d\log M} = 1$ dex^{-1}) as a function of FFP mass. Performing the equivalent analysis with `LensCalcPy` and adopting the normalization of 1 dex^{-1} results in the yields shown in Table .5. We see that at masses $> M_\oplus$, our yields differ from those of [298] by less than a factor of two. At lower masses, the discrepancy between the approaches grows, reaching a value of ≈ 6 at the lowest observable masses.

We see that our results tend to underestimate the total FFP yield compared to GULLS, particularly for low-mass objects. A primary source of this discrepancy stems from differences between the definition of maximum detectable impact parameter in the two analyses, which we compare in Fig. .12. In [298], $u_{\min}$ is drawn uniformly from $[0, \max(1, 2\rho)]$ when generating an event. This effectively sets

$$
u_T = \begin{cases} 1 & \rho < 0.5 \text{ (point-source regime)} \\ 2\rho & \rho > 0.5 \text{ (finite-source regime)} \end{cases} \tag{.46}
$$

268

Table .5: FFP yield comparison for Log-Uniform Mass distribution

Mass ($M_\oplus$)	Johnson et al. [298]	This work
0.01	0.31	0.05
0.1	4.49	1.75
1	22.1	19.0
10	87.1	72.6
100	313	234
1000	1025	744
10,000	3300	2370

resulting in the orange curve shown in Fig. .12. As described in Sec. 6.4.1, in our analysis, we instead determine the maximal impact parameter by solving the implicit equation $A_{\text{finite}}(u_T, \rho) = A_T$. This yields the blue curve in Fig. .12. We choose to adopt $A_T = 1.34$ as our fiducial threshold throughout our analysis. This agrees with [298] in the point-source regime, however in the finite-source regime (which is most relevant for low-mass objects), their approach yields generically larger values of u_T than ours, as can be seen in Fig. .12. Thus, their effective threshold magnification is < 1.34, resulting in the increased yields at low masses seen in Table .5. While we have chosen to use $A_T = 1.34$ throughout our analysis, this is likely an underestimate of Roman's ultimate detection threshold, which has been suggested to reach values of $\lesssim 1\%$ increases in flux for sufficiently bright sources [298]. We therefore note that depending on the photo-

metric sensitivity achieved by Roman, our current yield predictions may underestimate the number of detected FFP events. This uncertainty is, however, encapsulated by the range of normalizations in the mass functions considered and thus in the curves shown in Figure 6.5.

F Loop Functions

In this appendix, we collect the loop functions that enter the expressions for the SUSY contributions to $(g - 2)_\mu$ discussed in sections 8.2 and 8.4

$$
\begin{aligned}
f_1(x, y) &= \frac{6(y - 3x^2 + x(1 + y))}{(1 - x)^2 (x - y)^2} - \frac{12x(x^3 + y - 3xy + y^2) \log x}{(1 - x)^3 (x - y)^3} + \frac{12xy \log y}{(1 - y)(x - y)^3} \,, \\
f_2(x, y) &= \frac{6(x + y + xy - 3)}{(1 - x)^2 (1 - y)^2} - \frac{12x \log x}{(1 - x)^3 (x - y)} + \frac{12y \log y}{(1 - y)^3 (x - y)} \,, \\
f_3(x, y) &= \frac{6(13 - 7(x + y) + xy)}{5(1 - x)^2 (1 - y)^2} + \frac{12(2 + x) \log x}{5(1 - x)^3 (x - y)} - \frac{12(2 + y) \log y}{5(1 - y)^3 (x - y)} \,.
\end{aligned}
\tag{.47}
$$

The loop function entering the threshold corrections to the muon mass reads

$$
g(x, y) = \frac{2x \log x}{(1 - x)(y - x)} - \frac{2y \log y}{(1 - y)(y - x)} \,.
\tag{.48}
$$

G Scalar-Photon Coupling

In this section we calculate the form factor associated with the amplitude $S \to \gamma\gamma$ which gives rise to the photon coupling in eq. (9.4). This amplitude provides the main S decay channel (for $m_S < 2m_\mu$), and an S production mechanism through secondary photons in the beam dump. The former involves two on-shell photons, while

270

for the latter at least one photon is off-shell. In general, this amplitude has both UV and IR contributions (from heavy matter that generates the defining $S\bar{\mu}\mu$ interaction and from the muon loop, respectively). The one loop amplitude with a single on-shell photon, generated by a generic fermion with mass M with coupling g_f to S is

$$\mathcal{M}(S(p_S) \to \gamma(p_1)\gamma^*(p_2)) \equiv \frac{g_f \alpha Q^2}{2\pi M} f_{1/2}\left(\frac{4M^2}{m_S^2}, \frac{p_2^2}{4M^2}\right)(p_1^\mu p_2^\nu - p_1 \cdot p_2 \eta^{\mu\nu}), \qquad (.49)$$

where the form factor is

$$f_{1/2}(\tau, \rho) = \frac{\tau\left((L_1^2 - L_2^2)(\rho\tau + \tau - 1) + 4\rho\tau\left(L_1\sqrt{\frac{1-\tau}{\tau^2}}\tau - 1\right) - 4L_2\sqrt{(\rho-1)\rho\tau} + 4\right)}{2(\rho\tau - 1)^2},$$

$$(.50)$$

with

$$\tau = \frac{4M^2}{p_S^2}, \quad p_1^2 = 0, \quad \rho = \frac{p_2^2}{4M^2}, \qquad (.51)$$

and

$$L_1 = \ln\left(2\sqrt{\frac{1-\tau}{\tau^2}} - \frac{2}{\tau} + 1\right), \quad L_2 = \ln\left(-2\rho + 2\sqrt{(\rho-1)\rho} + 1\right). \qquad (.52)$$

This form factor reduces to the familiar expressions found for the fermionic contribution to $h \to \gamma\gamma$ [261], when both photons are on-shell. For muons $g_f = g_S$ and $M = m_\mu$, but we can also use this result to estimate the contribution of heavy fermions $M^2 \gg m_S^2,\ p_2^2$ to the diphoton coupling ($g_{S\gamma\gamma}^{(UV)}$ in eq. (9.5)):

$$\lim_{M \to \infty} f_{1/2}\left(\frac{4M^2}{m_S^2}, \frac{p_2^2}{4M^2}\right) = \frac{4}{3}, \qquad (.53)$$

so that

$$g_{S\gamma\gamma}^{(UV)} \sim \frac{2g_f \alpha Q^2}{3\pi M}. \qquad (.54)$$

271

Note that generally $g_f \neq g_S$ so the UV contribution to $S\gamma\gamma$ is not necessarily negligible compared to the muon one as we discuss in the next section.

H An Ultraviolet Completion

In this section we explore a simple ultraviolet completion for the effective operator in eq. (9.7), $-\frac{S}{M}H^\dagger L \mathbf{c}_S \ell_R^c$, that generates the muon-philic interaction. This will allow to discuss how the low energy couplings are related to the underlying UV parameters, and to mention additional constraints on realistic scenarios. A similar scenario was considered in the Supplementary Materials of Ref. [322].

The operator in eq. (9.7) can be generated at tree-level by a heavy vector-like lepton (VLL) pair. The simplest possibility is a VLL pair of $SU(2)_L$ singlets ψ and ψ^c, which have the same quantum numbers as the right-handed leptons ℓ_R^c in the SM (a completion with $SU(2)_L$ doublets is discussed in Ref. [97]). The allowed renormalizable terms (in two-component notation) are

$$L \supset -M\psi\psi^c - H^\dagger L^T y_\psi \psi^c - y_S' S\psi\psi^c - S\psi y_S^T \ell_R^c + \text{h.c.} \tag{.55}$$

where L and ℓ_R^c are SM leptons (with flavor index suppressed), and the transposes are in flavour space. Since we consider a single generation of VLL, M and y_S' are numbers, while y_ψ and y_S are vectors (with each entry corresponding to a SM fermion generation). In the last two terms, we assumed that ψ and ψ^c have a Yukawa interaction with a scalar

mediator S.[8] Integrating out ψ, and ψ^c yields the effective operator

$$\mathcal{L} \supset \frac{S}{M} H^\dagger L^T y_\psi y_S^T \ell_R^c + \text{h.c.} \rightarrow -\frac{v}{\sqrt{2}M} S L_L \mathbf{c}_S \ell_R^c + \text{h.c.} \qquad (.56)$$

where in the second step we transformed to the SM-lepton mass basis, which gives $\mathbf{c}_S \equiv -V_L^T y_\psi y_S^T V_R$ ($V_{L,R}$ are the left- and right-handed lepton unitary rotations that diagonalize their mass matrix). A muon-only interaction therefore requires that $\mathbf{c}_S \propto \text{diag}(0, 1, 0)$ as described in the introduction, necessitating a non-trivial flavour model. If this is realized then

$$g_S = \frac{y_S y_\psi v}{\sqrt{2}M}. \qquad (.57)$$

There are several theoretical constraints on g_S that follow from naturalness of the S mass (i.e., the desire for quantum corrections to m_S to not exceed m_S itself). These can be derived either directly from the UV completion above or from the EFT interaction as in Ref. [97]. The two most relevant quantum corrections to m_S arise from 1) a two loop contribution from a Higgs-left handed lepton-right handed lepton loop; 2) from the one loop radiatively-generated $|H|^2 S^2$ interaction. Requiring that the two corrections do not induce a mass shift larger than m_S leads to a theoretical upper bound on g_S:

$$g_S \lesssim \frac{4\pi v}{\sqrt{2}M} \min\left(\frac{\sqrt{2}m_S}{v}, 4\pi \frac{m_S}{M} \right), \qquad (.58)$$

where the first (second) term comes from the two (one) loop correction. The one loop effect dominates for $M \lesssim 4\pi v/\sqrt{2} \simeq 2$ TeV. At the same time, M cannot be too small in order to satisfy eq. (.58) in the region of interest (see [97]).

---

[8]The mass-mixing term $\mu_\ell \psi \ell_R^c \psi$ is allowed by gauge charges, but it can be rotated away by performing an orthogonal rotation on $(\ell_R^c \ \ \psi^c)$; this rotation results in redefinitions of the (unknown) parameters M, y_S', y_S, y_ψ and y_ℓ, which can then be relabelled.

We can also estimate the UV contribution to the $S\gamma\gamma$ coupling, by using eq. (.54). At one loop, only the y_S' coupling from eq. (.55) contributes, yielding

$$g_{S\gamma\gamma}^{(\text{UV})} \sim \frac{2y_S'\alpha Q^2}{3\pi M}. \tag{.59}$$

We see that $g_{S\gamma\gamma}^{(\text{UV})}$ is not necessarily correlated with g_S, and it can therefore be comparable to $g_{S\gamma\gamma}^{(\text{IR})}$ (generated by a muon loop) for $y_S' \gtrsim g_S(M/m_\mu)$.

Finally let us briefly discuss high energy collider constraints on VLL. Recent theoretical studies of these models in the context of the LHC and future machines include Refs. [116, 193, 323]. The production rate (and the resulting bounds) depend strongly on the VLL $SU(2)_L$ representation [323], with singlets usually being the least constrained. In the singlet case, the main production channel is $pp \to \gamma, Z^* \to \psi^+\psi^-$. The heavy leptons decay to SM particles via the interactions of eq. (.55). Our model differs slightly from the minimal VLL scenarios studied in these works, as it features new production and decay mechanisms involving S. For example, in addition to the "standard" decays $\psi \to W\nu$, $Z\ell$, the VLL can decay $\psi \to S\ell$. Even more interestingly, interference of SM and S-mediated channels can significantly weaken existing constraints [208]. The standard and S-mediated effects are parametrized by independent couplings, making it difficult to directly translate existing bounds on VLL models. It would therefore be interesting to carry out an dedicated study for the VLL+S model at the LHC.

With these important caveats in mind, we note some constraints on the minimal VLL model (without S) that may be relevant for the full scenario: LEP ruled out many kinds of charged particles with mass below ~ 100 GeV [48, 334]. The best current

LHC limits on the singlet VLL scenario are from ATLAS and CMS [15, 439], with M excluded in the ranges $114 - 176$ GeV ($\psi \to Z + e/\mu$) or $125 - 150$ GeV ($\psi \to Z + \tau$).

I   Muon Transport

In this Appendix, we describe our simulation of muon transport in the dump. We developed our own propagation code instead of using off-the shelf tools such as `GEANT` in order to have a simple way to incorporate rare processes relevant for signal and background events (e.g., S bremsstrahlung and muon deep inelastic scattering). Simulations of these processes are performed using other codes (e.g., `Madgraph` and `Pythia`), so having minimal muon code enables a simple interface between them.

Muons produced near the front of the beam dump can propagate a significant distance before undergoing a dark bremsstrahlung reaction. The energy and angular distributions of the resulting muon-philic scalars are sensitive to the details of muon transport through the dump. Muon propagation is also relevant for predicting the rates of some of the backgrounds, such as DIS-induced meson production at the very back of the dump (see section 9.5). Below we describe our treatment of muon production and propagation in the magnetic field, including energy loss and multiple scattering.

We generate an initial muon sample using `Pythia` to model pp collisions with incoming 120 GeV proton beam, assuming the production takes place in the first nucleon interaction length. The primary proton flux is exponentially diminished beyond the first interaction length, and the surviving protons lose energy; neglecting these protons is therefore a conservative simplifying assumption.

275

The muons come dominantly from charged pion decays. We require that the pions decay within the first pion interaction length, $\lambda_{\pi \, \text{int}}$. The fraction of decayed pions grows linearly with distance (in the long life-time regime), while their flux is exponentially suppressed by $\exp(-z/\lambda_{\pi \, \text{int}})$. As a result the total muon flux is well approximated by the first interaction length alone. This assumption allows us to neglect pion transport in the dump. The energy and transverse momentum distributions of pions and muons obtained this way are shown in fig. 9.2.

The secondary muons can undergo bremsstrahlung in the dump. Interactions close to the end of the dump are particularly interesting since they enable sensitivity to shorter scalar lifetimes. We propagate the muons through the FMAG in small steps, including the following effects:

a. The 1.8 T magnetic field of the FMAG;

b. Ionization energy loss;

c. Multiple Coulomb scattering.

The magnetic field is included by solving the relativistic equation of motion in each step. Energy loss and multiple scattering are stochastic processes, so they are applied at the end of each step. We describe our treatment of these processes below.

While dE/dx is frequently used to estimate the energy losses of particles propagating through a medium, it is important to note that dE/dx is an *average* loss, appropriate for describing very large ensembles of particles. This average is sensitive to rare, high loss collisions. This does not mean that it is an accurate representation of

276

the typical losses of individual particles [449]. Indeed, the definition of dE/dx includes large losses due to rare high-energy transfer, skewing the mean loss to larger values. For example, the most likely loss for a 5 GeV muon traversing 1 cm of iron is 10.6 MeV, while dE/dx is 14.6 MeV [449]. In practice, this means that the losses of individual particles follow a distribution where the peak of the distribution (the most probable loss) is different from the average. In our case, energy loss fluctuations can be modelled by the Landau distribution (see Refs. [86, 119, 347, 431] for helpful reviews):

$$f(\Delta) = \frac{1}{2\pi i \xi} \int_{c-i\infty}^{c+i\infty} ds \exp\left(\lambda s + s \ln s\right), \quad \lambda = \frac{\Delta - \Delta_p}{\xi} - 0.22278, \qquad (.60)$$

where c is a positive number, Δ is the energy loss, ξ and Δ_p are given by [449]:

$$\Delta_p = \xi \left[\ln \frac{2m_e \beta^2 \gamma^2}{I} + \ln \frac{\xi}{I} + 0.2 - \delta \right], \quad \xi = 0.153538 \text{ MeV cm}^2 \text{ mol}^{-1} \frac{Z}{A} \frac{t}{\beta^2}, \qquad (.61)$$

where t is the thickness in g/cm^2 of the material traversed, β the particle speed, and A and Z are the atomic mass and number, respectively. The material dependent parameters I and δ are the mean excitation energy and density correction which are evaluated using the tabulated data of Ref. [449]. The Landau distribution is an appropriate description of energy loss fluctuations when the losses are small compared to the maximum kinematically allowed loss and the initial kinetic energy ($\xi/E_{\text{max}} \ll 1$ with E_{max} given in [449]), but large compared to typical atomic binding energies ($\xi/I \gg 1$) [347]. Both conditions are easily satisfied for muon energies of $\sim$ GeV and above, and for propagation distances of a few cm. eq. (.60) is heavy-tailed with an undefined mean, implying that particles are allowed to lose arbitrarily large amounts of energy. This is of course unphysical since there is a maximum energy loss dictated by kinematics. Thus, the

distribution should be truncated, i.e., $\lambda \leq \lambda_{\max}$ for some $\lambda_{\max}$. We implement such a truncation by requiring that the mean energy loss of the truncated distribution is equal to dE/dx. Sampling from this truncated distribution is achieved using a modified version of the landaupy package. We checked that our implementation of energy losses reproduces those of `GEANT` for muons with initial energies from 1 to 100 GeV propagating through iron targets of 1 to 500 cm, covering the parameter ranges relevant for DarkQuest.

Multiple scattering is modeled by applying a transverse momentum kick drawn from a Gaussian approximation to the Moliere distribution of scattering angles. The variance σ^2 of this distribution is given in Sec. 7 of Ref. [340]:

$$\sigma^2 = \frac{\chi_c^2}{1+F}\left[\frac{1+v}{v}\log(1+v) - 1\right], \;\; \chi_c^2 = \frac{4\pi n_A t \alpha^2 Z(Z+1)}{(p\beta)^2}, v = \frac{\Omega}{2(1-F)}, \;\; F = 0.98 \qquad (.62)$$

where n_A is the atomic number density, p is the particle momentum and Ω is the mean number of scatters

$$\Omega = \frac{7800\, t\, (Z+1)Z^{1/3}}{\beta^2 A \left[1 + 3.34\left(\frac{Z\alpha}{\beta}\right)^2\right]} \qquad (.63)$$

with β, t, Z, A defined above. The Gaussian approximation provides an adequate description of multiple Coulomb scattering when $\Omega \gg 1$; this is the case for $t \gtrsim 10^{-3} X_0$, $\beta = 1$ and arbitrary Z, where X_0 is the radiation length [340].

We chose a 1 cm step size to ensure the validity of the various approximations for the treatments of ionization and multiple scattering. Specifically, 1 cm is large enough such that the number of Coulomb collisions is large and the Gaussian approximation is valid, but small enough that the losses do not significantly affect the muon trajectory in a single step. A larger step size is also desirable for computational speed.

278

We have verified that this algorithm reproduces the `GEANT4`-transported muon spectrum used in Ref. [226].[9] It also reproduces the spectra of monoenergetic muons propagated through 5 m of iron (this cross-check eliminates the convolution of propagation effects with the primary muon spectrum). Note that while [226] focused on a dimuon resonance search with a monoenergetic muon beam, here we take into account the full muon spectrum from beam-target interactions and its propagation through the dump.

The muons are thus transported until they either leave the dump or reach an energy below a GeV (in our reach estimates we always require the signal photons to each have an energy of at least 500 MeV, which implies a minimum muon energy of $\mathcal{O}(1)$ GeV). The magnetic field and energy loss are by far the most important effects: The p_T imparted by the B field is ~ 2.6 GeV for relativistic muons that traverse the entire FMAG; in practice the p_T fluctuates around this value due to multiple scattering and energy losses; it can also be substantially smaller if the muon ranges out inside the dump. The most probable energy loss (Δ_p in eq. (.61)) is ~ 7 GeV after traversing the FMAG.

The phase-space trajectories obtained using the above procedure are used to sample the momenta and interaction vertices at the interaction time. The probability distribution of the muon path length ℓ through the FMAG at interaction is given by (in the small coupling limit)

$$\frac{dP}{d\ell} \approx n_A \sigma_{\text{Brem.}}(E_\mu(\ell)), \tag{.64}$$

where n_A is the number density of target nuclei, $\sigma_{\text{Brem.}}$ is the $\mu N \to \mu N + S$ cross-section, and $E_\mu(\ell)$ is obtained from the muon trajectory. This distribution is sampled using the inverse transform method. In fig. .13 we show the energy and transverse momentum spectra of the initial muons, the muons at their interaction positions and the muons that traverse the entire FMAG without interacting. We clearly see the effects of transport, as the muons typically have a lower energy and larger p_T the more material they traverse. In our simulation, we force every generated muon to interact within the FMAG. In this approach, each event must be weighted by the probability of the muon do so:

$$n_A \int_{\text{FMAG}} \sigma_{\text{Brem.}}(E_\mu(\ell)) d\ell. \tag{.65}$$

The geometric acceptance-weighted sum of these probabilities (normalized to the total number of simulated pp collisions) gives the total S yield (see eq. (9.9)).

J Rare Meson Decays

The full result for the three-body decay of the kaon to produce a scalar is given by,[10]

---

[10]The Mathematica version of this expression can be found here.
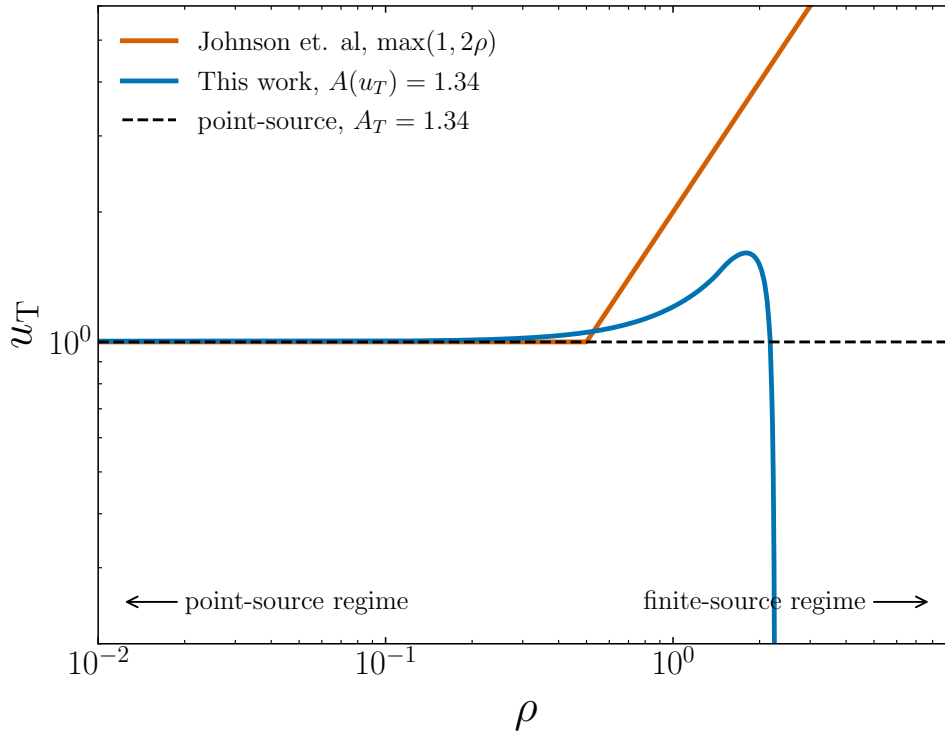
Figure .12: The threshold impact parameter as a function of $\rho = \theta_S/\theta_E$. The methodology of Johnson et al. [298] (orange) results in larger threshold impact parameters in the finite-source regime than our analysis (blue), increasing their relative yields.
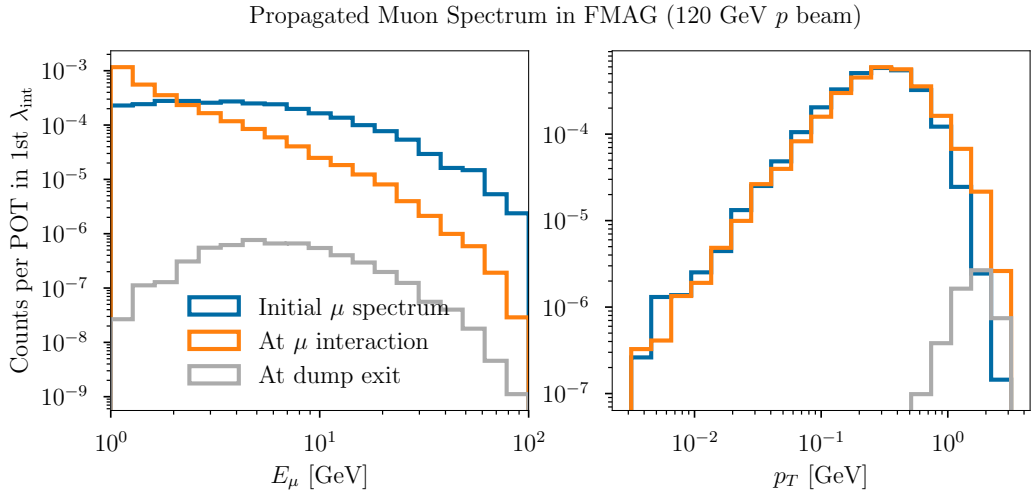
Figure .13: Muon spectra at creation (blue lines), at the $\mu N \rightarrow \mu N + S$ interaction (orange lines), and at FMAG exit (gray lines). The initial spectra are generated using `Pythia` (see fig. 9.2) and transported as described in the text. The transport includes the effects of energy loss, and multiple scattering and the magnetic field which are evident in the left and right panels, respectively. Note that blue and orange histograms sum to 0.0028 per POT, which is smaller than the total muon yield of 0.01 per POT in table 9.2 and the corresponding histogram in fig. 9.2; this is because here we impose $E_\mu > 1$ GeV. The gray histogram contains a smaller number of muons still as not all muons are able to penetrate the entire FMAG.